SMALL ANGLE NEUTRON SCATTERING STUDIES OF MAGNETIC RECORDING MEDIA

Matthew P. Wismayer

A Thesis Submitted for the Degree of PhD
at the
University of St. Andrews

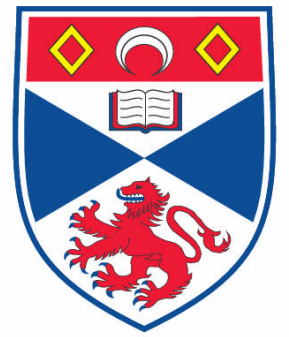

2008

Small Angle Neutron Scattering Studies of Magnetic Recording Media

By

Matthew P. Wismayer
B.Sc.Honours (York University) 1998
M.Sc. (Carleton University) 2001

University
of
St Andrews

Thesis submitted for the degree of Doctor of Philosophy of the University of St.Andrews on October 18th, 2007

Declaration

I Matthew Wismayer hereby certify that this thesis is approximately 50,000 words in length, has been written by me, that it is the record of work carried out by me and that it has not been submitted in any previous application for a higher degree

Date……signature of candidate……

I was admitted as a research student in September 2003 and as a candidate for the degree of Doctor of Philosophy in September 2004; the higher study for which this is a record was carried out in the University of St. Andrews between 2003-2007.

Date……signature of candidate……

I hereby certify that the candidate has fulfilled the conditions of the Resolution and Regulations appropriate for the degree of Doctor of Philosophy in the University of St. Andrews and that the candidate is qualified to submit this thesis in application for that degree.

Date……signature of supervisor……

In submitting this thesis to the University of St.Andrews I understand that I am giving permission for it to be made available for use in accordance with the regulations of the University Library for the time being in force, subject to any copyright vested in the work not being affected thereby. I also understand that the title and abstract will be published, and that a copy of the work may be made and supplied to any bona fide library or research worker.

Date……signature of candidate……

Acknowledgements

In the past four years, the following people have made a significant contribution to this thesis project. I would like to thank my supervisor Professor Stephen Lee, who has assisted with the project's experimental and theoretical topics. I would like to acknowledge Dr. Tom Thomson of Hitachi San Jose Research Center, who provided the project with the longitudinal and perpendicular media samples. I would like to acknowledge Dr. Feodor Ogrin of Exeter University, who has provided guidance for the micromagnetic simulations of longitudinal recording media. At the University of St. Andrews, I would like to thank the people of Stephen Lee's condensed matter physics group Stephen Lister, David Heron, Alan Drew and Ujjual Divakar.

Acknowledgements go to Dr. Charles Dewhust of D22, ILL Grenoble France, who provided guidance and analysis during the SANS experiments. In addition I would like to thank Dr. J. Kohlbrecher of SINQ, PSI Switzerland, who has assisted on the experimental and theoretical aspects of polarised SANS. Further thanks go out to the researchers Dr. Y. Peng and Dr. T.H. Shen at the University of Salford, who provided this project with the cobalt nanowire and sample holder.

I would like to acknowledge the financial support of the Gordon Chaplin Bursary Fund which has made living in St.Andrews an interesting experience. Finally I would like to thank my family and friends for their continuing academic and financial support during my stay in St.Andrews.

Abstract

In the beginning of the twenty-first century, educational and commercial institutions have driven the demand for cheap and efficient data storage. The storage medium known as magnetic recording media has remained the mainstay for most computer systems due to its large storage capacity per dollar. With the recording media's ever-increasing storage density has come reductions in the magnetic grain size per bit. At the recording bit's density threshold, the magnetic grains become more susceptible to thermal activation, which can render the storage medium unusable. An accurate characterisation of the recording layer's sub-granular structure is essential for understanding the magnetic and thermal mechanisms of high-density recording media. Small-Angle Neutron Scattering (SANS) studies have been performed to investigate the magnetic and physical properties of longitudinal and perpendicular recording grains.

The SANS studies of longitudinal magnetic recording media have probed the recording layer's magnetic grain size at a sub-nanometer resolution. In conjunction with these studies, SQUID magnetometry was used to characterise the recording grain's bulk magnetism. Measurements showed that the recording grain was composed of a ferromagnetic hard core (Co-enriched) and a weakly magnetic shell (Cr-enriched). These results provided important information on the grain's magnetic anisotropy, which determines the recording media's magnetic stability. The polarised SANS studies were used to characterise the recording layer's physical granular structure. It was shown that the physical grain size was comparable to its magnetic counterpart. These physical measurements provided insight into the recording grain's chemical composition.

The magnetic properties of perpendicular magnetic recording media were studied using SANS and VSM measurements. The neutron scattering studies revealed that the recording grain was composed of a hard ferromagnetic centre enriched with cobalt. The VSM studies showed that the magnetic recording grains exhibited a large perpendicular magnetic anisotropy. These combined studies provided information on the recording grain's ferromagnetic composition and magnetic stability. The polarised SANS measurements showed the physical grain size to be slightly smaller than its magnetic counterpart. This size difference was attributed to the non-magnetic grain boundary composed of SiO_2. The boundary thickness determined the degree of inter-granular exchange coupling. Further polarised studies investigated the recording layer's switching behaviour, which revealed more information on the grain's magnetic stability.

Contents

List of Figures

List of Tables

Abbreviations

AAO-Anodic Aluminium oxide

ADF-Advanced Disk File

AFC-Anti-Ferromagnetic Coupled

AFM-Atomic Force Microscopy

BCC-Bodied Centred Cubic

DFT-Discrete Fourier Transform

EDAXS/EDS-Energy Dispersive X-ray Analysis Spectroscopy

EELS- Electron Energy Loss Spectroscopy

ENIAC-Electrical Numerical Integrator And Calculator

FFT-Fast Fourier Transform

FMR-FerroMagnetic Resonance

GRASP- Graphical Reduction and Analysis SANS Program

HCP-Hexagonal Closed Packed

LLG-Landau-Lifshitz-Gilbert equation

LMRM-Longitudinal Magnetic Recording Media

NLS-Nonlinear Least Squares fit

NSF- Non Spin Flip state

MOKE-Magneto Optical Kerr Effect

OOMMF-Object Oriented MicroMagnetic Framework

PMRM-Perpendicular Magnetic Recording Media

POLSANS-Polarised Small Angle Neutron Scattering

RAMAC-Random Access Method of Accounting and Control

RKKY-Ruderman, Kittle, Kasuya and Yosida theory

SANS-Small Angle Neutron Scattering

SF-Spin Flip state

SNR-Signal to Noise Ratio

SUL-Soft-magnetic UnderLayer

TEM-Transmission Electron Microscopy

SEM-Surface Electron Microscopy

SQUID-Superconducting Quantum Interference Device

VSM-Vibrating Sample Magnetometer

XRD- X-Ray Diffraction

List of Symbols and Constants

Symbol	Description
U_T	magnetic recording grain's total internal energy
ρ_{areal}	areal moment density
t	recording layer/grain boundary thickness
μ_i	ith classical dipole moment
μ_T	total dipole moment
μ_L	orbital dipole moment
μ_S	atomic spin dipole moment
μ_J	total atomic dipole moment
μ_{eff}	effective atomic moment
μ_B	Bohr magneton
$\mathbf{L}$	orbital angular momentum operator
γ	gyromagnetic ratio
α	LLG damping constant
$\mathbf{S}$	total atomic spin angular momentum operator
λ	spin-orbit coupling constant
$\mathbf{J}=\mathbf{L}+\mathbf{S}$	total angular momentum operator
J	total angular momentum quantum number
$\mathbf{p}_i$	total linear momentum
$\mathbf{A}(\mathbf{r}_i)$	vector potential for an uniform magnetic field
$\mathbf{H}$	magnetic field
$\mathbf{H}_{eff}$	effective magnetic field
$\mathbf{H}_{Zeeman}$	applied Zeeman magnetic field

$\mathbf{H}_{dipolar}$	dipolar magnetic field
$\mathbf{H}_{aniso}$	magneto-crystalline anisotropy magnetic field
$\mathbf{H}_{exe}$	exchange magnetic field
H_c	coercive magnetic field
H_G	head gap magnetic field
H_F	head fringe magnetic field
$\mathscr{H}$	Hamiltonian
$\mathscr{H}_{spin}$	Heisenberg spin hamiltonian
V	atomic potential energy
χ_M	molar susceptibility
M_w	molecular weight
ρ	bulk density
n	number density
Z	atomic number
R_y	Rygburg constant
χ_{dia}	diamagnetic susceptibility
χ_{para}	paramagnetic susceptibility
χ_{Al}	Pauli susceptibility of Al
L(y)	Langevin function
$B_J(y)$	Brillouin function
M	bulk magnetisation
M_s	saturation magnetisation
M_r	remanent magnetisation
g(JLS)	Lande' g-factor
g_0	free electron g-factor

T_C	Curie temperature
J_{exe}	exchange integral
g(E)	density of state function
E_F	Fermi energy
$n_\uparrow$, $n_\downarrow$	*e*-number densities the for spin up($\uparrow$)/down($\downarrow$) band
H_M	molecular magnetic field
w	molecular field strength
ΔE_k, ΔE_{exe}	kinetic and exchange energies
S	hysteresis loop squareness
E_a	anisotropy energy
K_{u1}, K_{u2}	anisotropy energy density coefficients
ϕ	angle between magnetic moment and easy axis
λ	average neutron wavelength
m_n	mass of neutron
ψ_{in}	incident neutron wavefunction
ψ_{sc}	scattered neutron wavefunction
N	number of neutrons in incident beam
j_{in}	incident current density
j_{sc}	scattered current density
$f(\theta,\phi)$	scattering amplitude
$d\Omega$	solid angle differential
dA	surface area differential
$d\sigma/d\Omega$	differential scattering cross-section
$d\sigma_N/d\Omega$	nuclear scattering cross-section
$d\sigma_M/d\Omega$	magnetic scattering cross-section

$\|\mathbf{k}\rangle$, $\|\mathbf{k}'\rangle$	incident and scattered wave vectors
$U_i(\mathbf{x})$	ith nuclear potential energy
$\mathbf{U}_N(\mathbf{r})$	nuclear potential energy operator
$\mathbf{U}_M(\mathbf{r})$	magnetic potential energy operator
$P_{k\rightarrow k'}$	transition probability
$\rho_{k'}(E)$	energy density
b_{nuc}	nuclear scattering length
$\mathbf{B}(\mathbf{q})$	internal magnetic field
$\mathbf{B}^{\perp}(\mathbf{q})$	total interaction B-field
$\mathbf{B}_S^{\perp}(\mathbf{q})$	spin interaction B-field
$\mathbf{B}_L^{\perp}(\mathbf{q})$	orbital interaction B-field
$\boldsymbol{\sigma}_{spin}$	Pauli spin matrix
$\boldsymbol{\mu}_N$	nuclear magnetic moment
μ_N	nuclear magneton
γ_N	neutron spin g-factor
m_N	neutron spin quantum number
$\mathbf{q}=\mathbf{k}-\mathbf{k}'$	momentum transfer argument
$\rho_s(\mathbf{r})$	spin density of system
$\mathbf{M}(\mathbf{q})$	internal magnetisation field
$\mathbf{M}^{\perp}(\mathbf{q})$	total interaction M-field
$\mathbf{M}^{\perp}_L(\mathbf{q})$	orbital interaction M-field
$\mathbf{M}^{\perp}_S(\mathbf{q})$	spin interaction M-field
$\mathbf{M}_{Core}$	magnetisation of core
$\mathbf{M}_{matrix}$	magnetisation of matrix
$\Delta\mathbf{M}_{x,y}$	x, y magnetisation contrast values

$\mathbf{H}_{matrix}$	matrix field vector
$\mathbf{E}_S$, $\mathbf{E}_P$	linearly polarised EM wave in the S/P plane
$\mathbf{E}'_S$, $\mathbf{E}'_P$	elliptically polarised EM wave in the S/P plane
θ_k	Kerr rotation angle
ε_k	Kerr ellipticity factor
$f(\mathbf{q},r_i)$	scattering shape function
$F_N(\mathbf{q})$	nuclear scattering form factor
$F_M(\mathbf{q})$	magnetic scattering form factor
$S(\mathbf{q})$	structure factor
$h(\mathbf{r})$	total correlation function
$u(\mathbf{r})$	pair potential
$c(\mathbf{r})$	direct correlation function
$\tau(\mathbf{r})$	tau correlation function
$V(r)$	generic scattering potential
$\Pi(r)$	cylindrical scattering potential
$\rho(r)$	spherical scattering potential
η, *pf*	packing fraction
$d\sigma_{SF}/d\Omega$	spin flip differential cross-section
$d\sigma_{NSF}/d\Omega$	non-spin flip differential cross-section
$\pm$	neutron spin up (+) and spin down (-) states
|+>, |->	spin up and down wavefunction
$U_{ss'}$	neutron spin operator matrix element
M_{ij}	magnetisation matrix
V	volume of scattering Object
$\mathbf{x}_j$	Cartesian co-ordinate vector of ith scattering object

$\mathbf{r}_i$	spherical co-ordinate vector of ith scattering object
2θ	Bragg scattering angle.
D_1	target distance
D_2	scattering wave detector distance
Φ_0	flux quantum
I_a, I_b	super current through junction a and b
d	pair separation distance/lattice spacing
D	diameter of grain
G	grain growth rate
I	nucleation rate
λ_e	exchange interaction length
$g(r)$	gamma-Shultz distribution function
$p(E)$	Maxwell-Boltzmann distribution
R_c, R_s	grain core and shell radius
L	length of cylinder
ε	cylindrical potential decay constant
$\Delta\eta_c$, $\Delta\eta_s$	recording grain core and shell contrast
$\Delta\eta^N_c$, $\Delta\eta^N_s$	core and shell nuclear scattering contrast
$\Delta\eta^M_c$, $\Delta\eta^M_s$	core and shell magnetic scattering contrast
η_c ,η_s	nuclear scattering length density
c_i	ith atomic fraction
$<\eta>$	volume averaged scattering length density
φ_c, φ_s	grain core and shell angles
I_T	transmission intensity
$I_B(q)$	background scattering intensity

$I_F(q)$	foreground scattering intensity
$I_N(q)$	nuclear scattering intensity from sample
$I'_N(q)$	nuclear scattering intensity from instrument
$I_{NM}(q)$	nuclear-magnetic interference term from sample
$I_M^{iso}(q)$	isotropic magnetic scattering intensity from sample
$I_M^{aniso}(q)$	anisotropic magnetic scattering intensity from sample
$I_{Porod}(q)$	Porod scattering intensity
ΔI_M	magnetic difference intensity
Φ_{inc}	incident neutron flux
A	attenuation factor
S	illuminated sample area
α,θ	scattering-plane azimuthal angle
I_a	$ANCOS^2$ scattering intensity amplitude
I_b	$ANCOS^2$ scattering intensity offset
δ_c	$ANCOS^2$ phase angle
$I_M^R(q)$	recording layer magnetic scattering intensity
$I_M^U(q)$	underlayer magnetic scattering intensity
$I^{\pm}_T$	polarised transmission intensity
$I^{\pm}_B(q)$	polarised background scattering intensity
$I^{\pm}_F(q)$	polarised foreground scattering intensity
$I_{NM}(q)$	nuclear-magnetic interference term from sample
Free/*Fixed*	NLS parameter states
χ^2	chi-squared closeness of fit
v_c, v_s	core and shell volume fractions

Chapter 1

Introduction to Magnetic Recording Media

1.1 Historical Review

The history of magnetic recording begins in the late nineteenth century where the inventor Valdemar Poulsen develops the first analogue audio recorder known as the telegraphone [1]. A simplified schematic of the telegraphone is shown in Figure 1.1 [2]. An acoustic wave was generated at point (A). The sound waves were converted into electrical signals, which were then sent to an electromagnet (B). The electromagnet was the telegraphone recording head. The recording media (C) was a steel wire threaded through the centre of the electromagnet by the supply reel (E). The electrical sound signals were imprinted along the wire length as magnetisation patterns. These patterns, similar to the magnetic tape track, represented the analogue recording of the audio event. The recorded information was simply played back by the magnetic influence of the wire on the electromagnet. The telegraphone, though ahead of its time, suffered from numerous technical problems. For example the output source (A) lacked a proper amplifier which led to severe signal degradation.

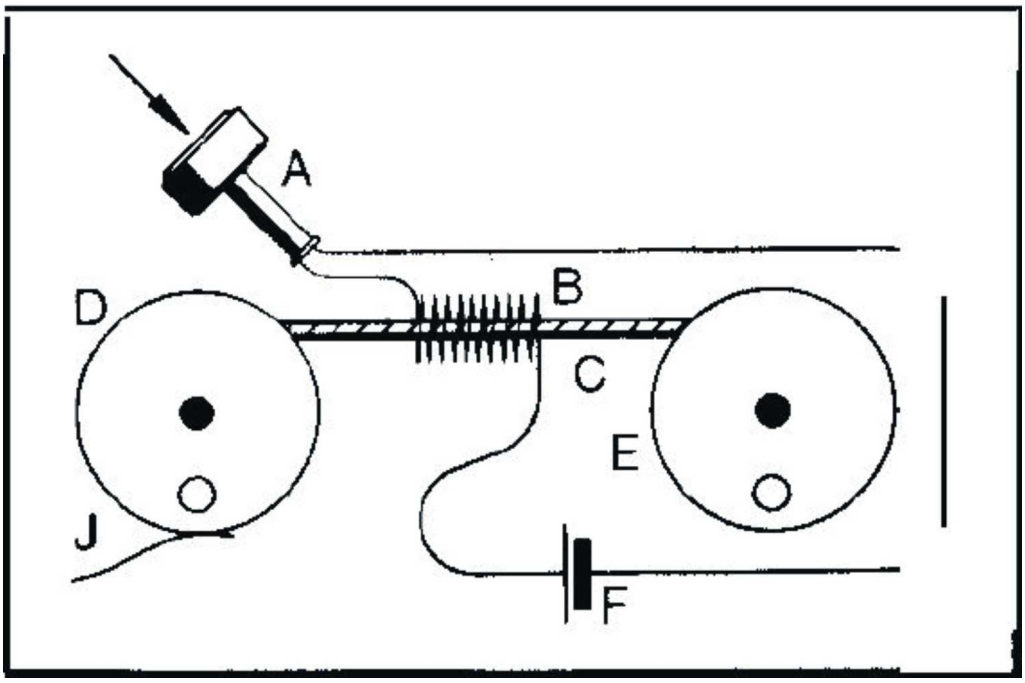

Figure 1.1: The simplified schematic shows the working components of the first telegraphone. The metallic wire is coated in a ferromagnetic oxide, which acts as the device's recording medium [2].

At the beginning of the twentieth century magnetic tape was introduced by Fitz Pfleumer [3]. The recorded information was stored into parallel tracks that ran the length of tape. The track was partitioned into cells known as longitudinal bits. The cross-section of an analogue tape is shown in Figure 1.2. The state of the magnetic bit was illustrated by an array of zeros and ones coloured grey and black respectively. The recording process involved a magnetic write head sequentially flipping $\uparrow(0) \Rightarrow \downarrow(1)$ each bit along the desired track. The recording layer was composed of a ferromagnetic coating of iron oxide (γ–Fe_2O_3) [4]. The recording grain was an elongated particle with typical dimensions of $25 \times 25 \times 100\ nm^3$ [5]. The ensemble of grains was suspended within a polymer binder that fused the recording layer to the substrate [6]. In addition the binder provided a smooth surface for tape movement. For example the binder incorporated lubricant sites, which reduced tape friction. The iron oxide was grown on an anti-static charge underlayer and a plastic substrate. The recording layer was coated with a carbon layer that protected the tape from physical damage and static-discharge.

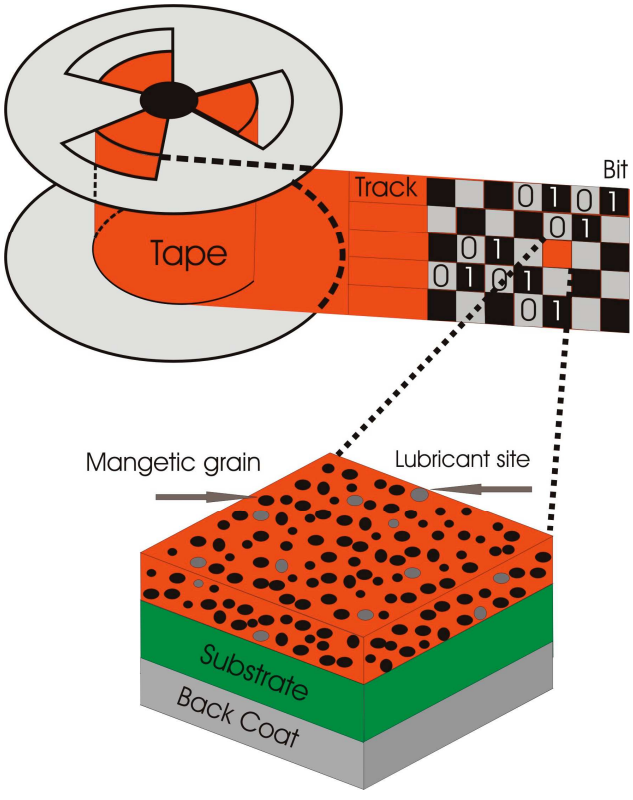

Figure 1.2: The cross-section of longitudinal magnetic recording tape. The magnetic medium is composed of a ferromagnetic oxide grown onto a thin plastic substrate. The recording grains form the recording bit, which lies along the tape track [6].

The magnetic tape medium had massive storage potential reaching into the Gigabyte regime. However the tape's main disadvantage was its sequential method of storing and reading data. The process of reading a particular section of tape required one to linearly advance the player to the desired track. This task would be time costly if the magnetic tape contained large amounts of data. Additional problems lay with the tape's durability. For example when the tape was exposed to moisture for long periods of time, the binder would undergo chemical degradation through the process of hydrolysis [7]. This process resulted in a softer binder, an increase in tape friction and a sticky tape surface.

The first computers were developed in the late 1940s. One such machine appropriately named the ENIAC (Electrical Numerical Integrator And Calculator) needed 1800 square feet of floor space and 180,000 watts of electrical power to operate [8]. Programming the ENIAC machine was a cumbersome process where the user needed to generate a series of punch cards to express a simple mathematical subroutine. As a consequence a fully sized computer program needed a library of punch cards to function. The ENIAC's disadvantage lay with the system's input medium. Any program corrections required the user to replace the faulty punch cards with a new set. These factors undoubtedly led to a strain on storage space. As recently as the late 1970s the last punch cards used in computer systems, were replaced by magnetic recording media. Figure 1.3 depicts the transfer from paper punch cards to the magnetic tape and disk media.

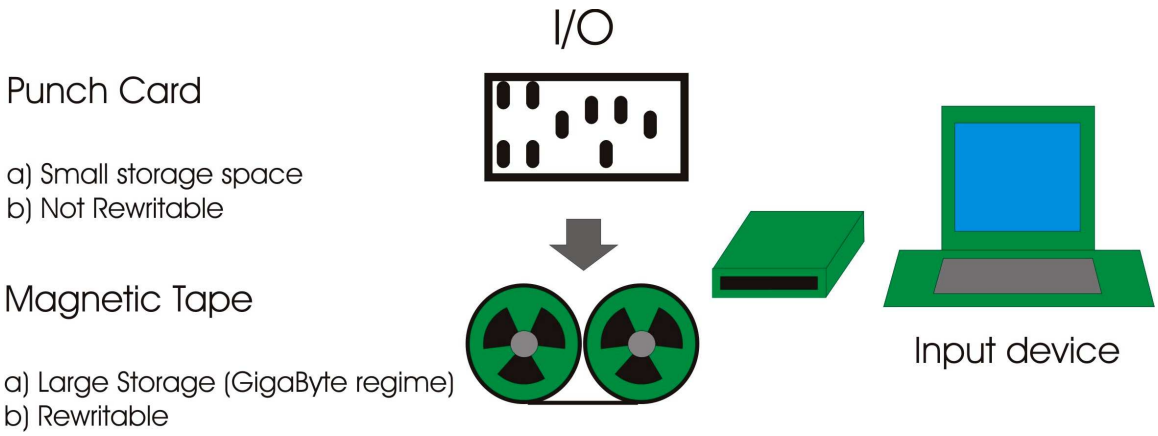

Figure 1.3: This schematic outlines the advantages from converting the storage medium to the magnetic tape.

In 1952, IBM began development of the Random Access Method of Accounting and Control (RAMAC) computer. In conjunction with this project was the development of the IBM 350 storage device which functioned using a magnetic hard disk drive [9]. The schematic of the IBM 350 disk drive unit is shown in Figure 1.4. The disk drive was constructed from a stack of 50 disks each with an approximate diameter of 61.0 cm and a thickness of 2.5 cm [10]. The drive's actuator-arm assembly could access any disk along the stack length. The disk drive's total storage capacity was approximately 5.0 Mb. The recording layer was composed of an aluminium substrate coated with a thin ferromagnetic oxide paint. The paint formed crude magnetic grains that clustered into longitudinal recording bits.

Unlike the magnetic tape, the hard disk was a random access device where the read/write head could directly scan the specified data track. This unique property solved the slow data access problems associated with the magnetic tape. However it would take many years for the hard disk drive to surpass the magnetic tape as the computer's main storage unit. The main disadvantage was the large office space needed to accommodate the storage unit. In comparision the magnetic tape drive required less operational space per Mb of storage space.

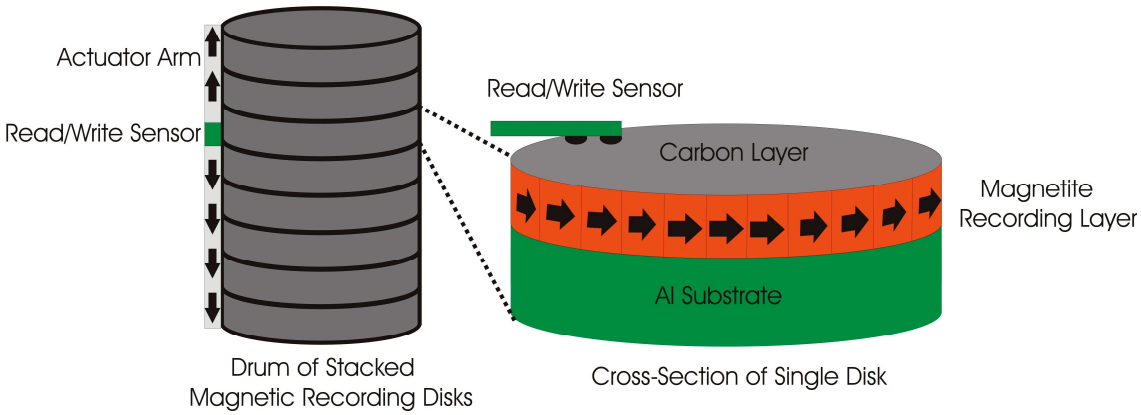

Figure 1.4: The IBM 350 hard disk drive consists of a drum of thin magnetic disks. The cross-section shows the first generation longitudinal magnetic media [9,10].

During the mid-1990s, the storage density of longitudinal recording media greatly increased through advances in sensor technology and materials physics. The first generation disk drive extracted data by using an inductive read head. These sensors exhibited poor sensitivity that limited the track size. The introduction of the magneto-resistor (AMR) and later the giant magneto-resistor read head (GMR) allowed the use of much narrower recording tracks on disk drives [11]. The recording layer was originally composed of a thin coating of ferromagnetic paint. This compound would often form into irregular shaped recording grains resulting in a reduction in the signal to noise ratio. Another problem resulted from the oxide's weak magneto-crystalline anisotropy that led to thermally active recording grains and inevitable data erasure. These technological challenges were overcame by fabricating the recording layer from a polycrystalline material composed of the cobalt-based alloys eg: CoNi and CoRe [12].

The above cobalt alloys exhibited high noise characteristics due to exchange coupling between neighbouring grains. It was demonstrated that by alloying the cobalt with the element chromium one could greatly reduce the excess noise. The reduction in noise was attributed to Cr atoms segregating to the grain boundary thus providing a physical barrier against inter-granular exchange coupling. The grain boundary was approximately 1.0-2.0 nm in thickness [13]. The Cr-segregation was more effective by doping the CoCr alloy with the element boron or tantalum. The ferromagnetic alloys CoCrPtTa and CoCrPtB were found to exhibit a favourable a signal to noise ratio [13]. Figure 1.5 illustrates a multi-layered film structure for the conventional longitudinal magnetic recording media.

The CoCrPt film also provided a strong in-plane magneto-crystalline anisotropy, which stabilised the recording grain against demagnetisation and thermal forces. It was found that the addition of the element Pt was responsible for an increase in the grain's magneto-crystalline anisotropy field [14]. Figure 1.6 illustrates the grain's internal energy as a function of magnetisation angle. The barrier height depends on the grain's magneto-crystalline anisotropy, exchange, dipolar and Zeeman fields. At zero applied field, the recording grain rests in the ground state where the easy axis of magnetisation lies at the zero angle. The energy barrier prevents the recording grain from switching to an anti-parallel state. With an increase in the grain's anisotropy energy density $K_1 \rightarrow K_3$, the barrier height gradually becomes larger. In this state, the magnetised grains are less likely to undergo switching from thermal or demagnetisation forces.

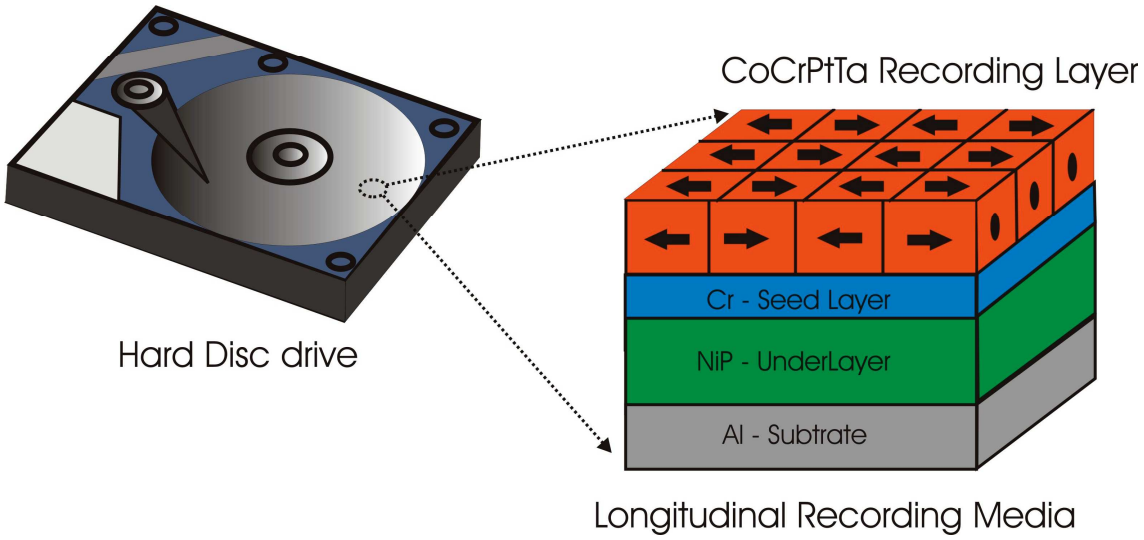

Figure 1.5: The schematic of a conventional longitudinal magnetic hard disk drive. The medium's cross-section shows the CoCrPtTa recording layer grown onto the Cr-alloy seed layer and NiP underlayer [12].

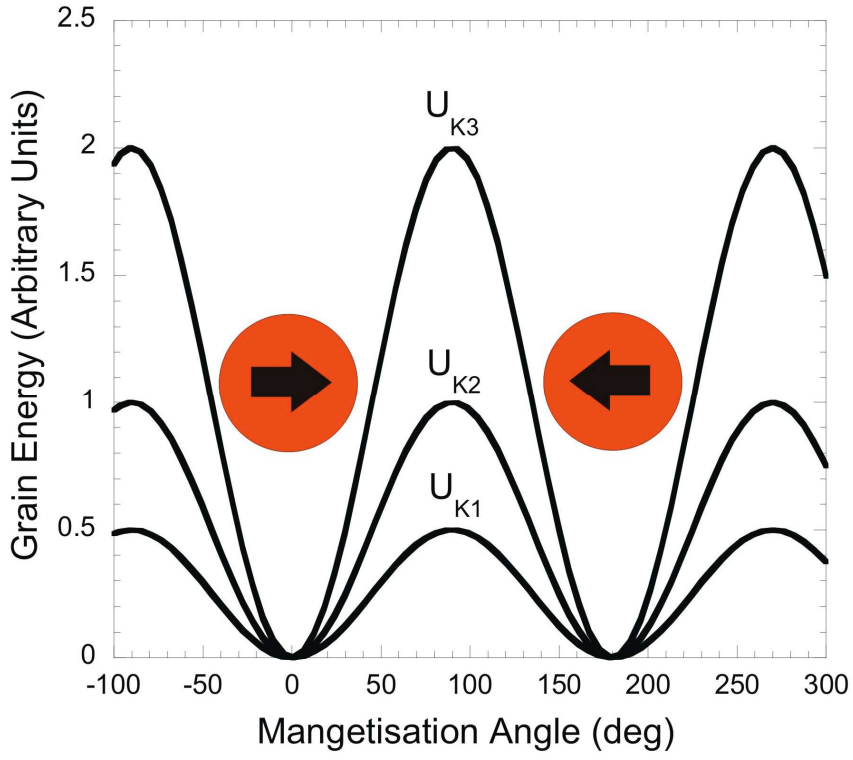

Figure 1.6: The recording grain's internal energies U_{K1}, U_{K2} and U_{K3} as a function of magnetisation angle. The energy barrier is enlarged by increasing the grain's magneto-crystalline anisotropy energy density where $K_3 > K_2 > K_1$.

In conventional longitudinal media, higher recording densities were obtained by reducing the grain volume whilst maintaining the number of grains per bit. This was accomplished by simultaneously scaling the grain's diameter and length to smaller sizes. It was found that reductions in grain volume were limited due to the increased probability of thermal activation which could lead to bit erasure. A novel type of recording media known as Anti-Ferromagnetic Coupled (AFC) media was shown to greatly improve the areal density without incurring any further thermal instabilities [15]. The cross-section of the AFC media is shown in Figure 1.7. The media was fabricated by sandwiching a thin nonmagnetic layer of Ru between two or more ferromagnetic layers. In theory the layered structure will induce RKKY exchange coupling between the top and bottom ferromagnetic layers thereby reducing the sample's remanent magnetisation [16]. This exchange coupling effectively increases the recording media's granular density by reducing the moment areal density defined by $\rho_{areal}=M_r t$. The terms M_r and t define the recording layer's remanent magnetisation and thickness respectively.

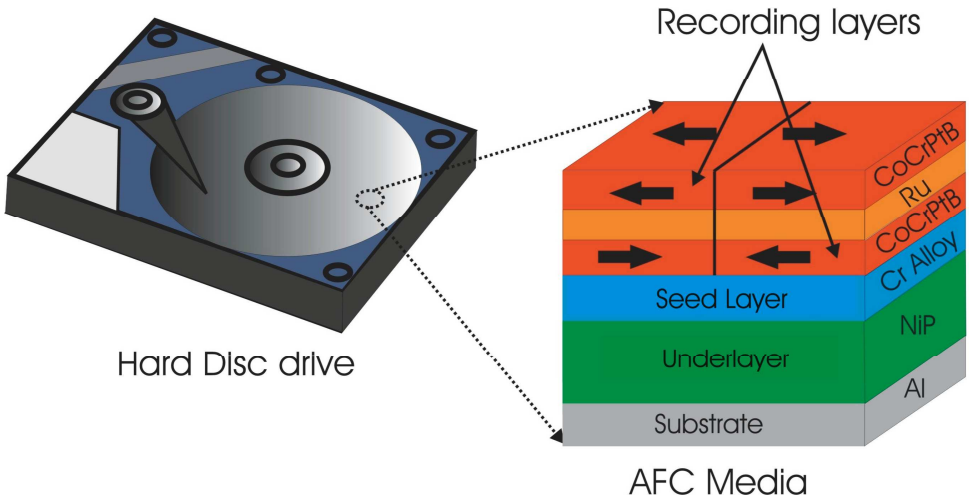

Figure 1.7: The cross-section of Anti-Ferromagnetic Coupled Media (AFC). The AFC geometry is the similar to the longitudinal media except for the non-magnetic Ru spacer between the recording layers [15].

During the development of the RAMAC hard drive, IBM instituted a parallel project known as Advanced Disk File or ADF [9]. The objective of ADF was to develop the next generation of magnetic hard drives. The recording medium was designed to store information on magnetic bits aligned perpendicular to the disk plane. The perpendicular recording media would store ten times the capacity of the RAMAC disk and improve on data access time by 10%. The ADF project for perpendicular media was abandoned due to numerous technological failures. With the development of read and write sensor technologies, the perpendicular media has once again become a viable method of storing information.

The perpendicular recording media has only recently been introduced for modern day disk drives. Figure 1.8 shows the conventional perpendicular magnetic recording system. The recording layer consists of micron-sized magnetic bits whose direction of magnetisation lies normal to the sample plane. The single bit was subdivided into multiple recording grains composed of the cobalt-based alloy CoCrPt. The grain boundary was mainly composed of a non-magnetic alloy or oxide such as SiO_2. This substance provides segregation for neighbouring grains thus reducing inter-granular exchange coupling. The recording grain has strong out of plane magneto-crystalline anisotropy, which improves the perpendicular bit's magnetic stability.

The advantage of perpendicular media over the longitudinal geometry lies with its ability to generate a sharp field gradient across the recording bit [17]. Due to this property the recording layer was fabricated with sharper track widths, which increases the storage density. In addition the recording layer was grown upon a ferromagnetic soft underlayer that greatly improves the bit's signal to noise ratio during the read/write process. Another advantage of the perpendicular geometry lies in the nature of the destabilising field generated from neighbouring bits [18]. Consider the longitudinal media where the bit boundaries form magnetostatic wall domains of equal charge. These domains generate a strong demagnetisation field, which act to destabilise the neighbouring bits. As the recording density is increased so does the number of domain walls thereby increasing the demagnetisation field. In the perpendicular geometry, the bits were arranged in anti-parallel pairs thereby forming opposite magnetostatic domain walls. This type of ordering is magnetostatically favourable and acts to reduce the system's demagnetisation field. Figure 1.9 depicts the demagnetisation field for the longitudinal and perpendicular bit.

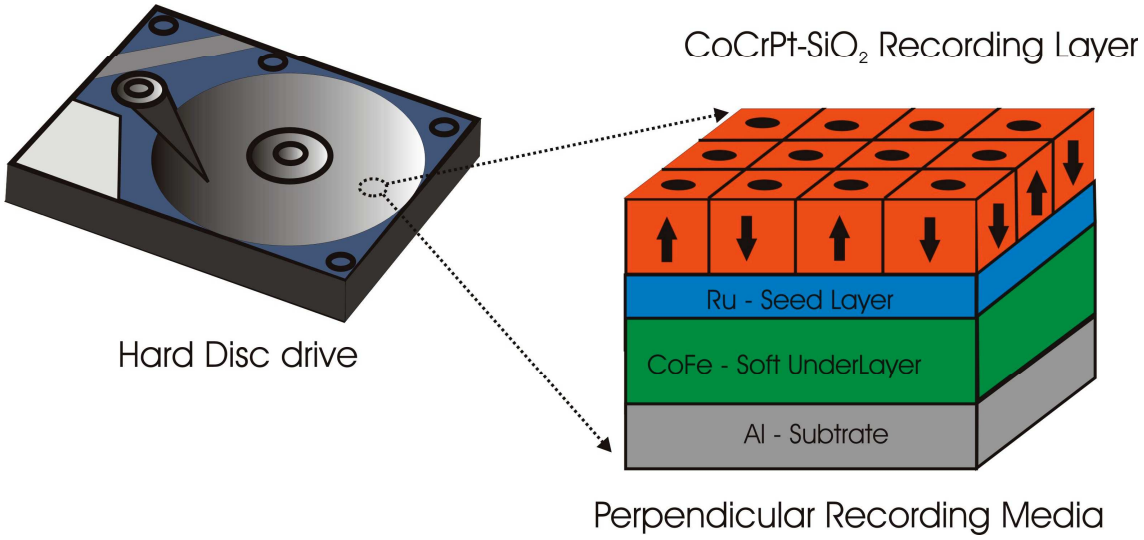

Figure 1.8: The schematic of perpendicular magnetic recording media. The cross-section shows the CoCtPt-SiO_2 recording layer grown onto a Ru seed layer and CoFe underlayer [17].

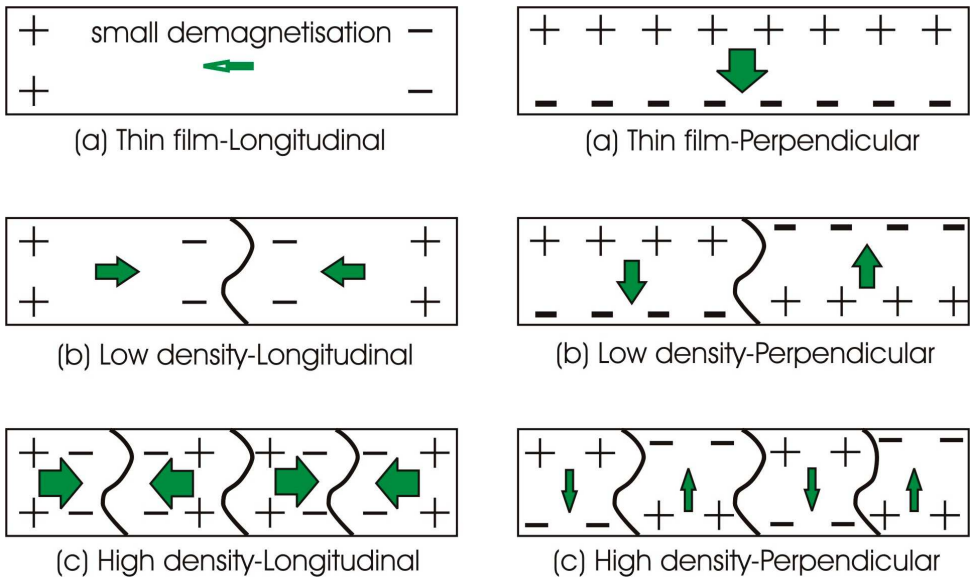

Figure 1.9: The demagnetisation field of the longitudinal and perpendicular bit for (a) thin film, (b) low density and (c) high density [18].

The recording industry is currently striving to break through the terabit/inch^2 limit. Figure 1.10 plots the recording disk's areal density as a function of production year. At the current rate perpendicular recording media should surpass the terabit regime in 2-5 years. However if the perpendicular media reaches its density limit, further research and development will be required to find a replacement for the alloy based recording media. Recently there has there been renewed interest in discrete media for applications in magnetic recording. This type of media consists of an ensemble of magnetic grains, conventionally spheres or wires, embedded in a non-magnetic matrix. Typical grain sizes are on the order of 4 nm with a grain size distribution of <5% [19,20]. The single magnetic grain represents a discrete magnetic bit with only two magnetic states. Potentially this gives the discrete medium a larger bit density than the 50-100 grains per bit of granular based media. With the quick progression of recording media technology, the discrete media may be in the application phase in 5-10 years time.

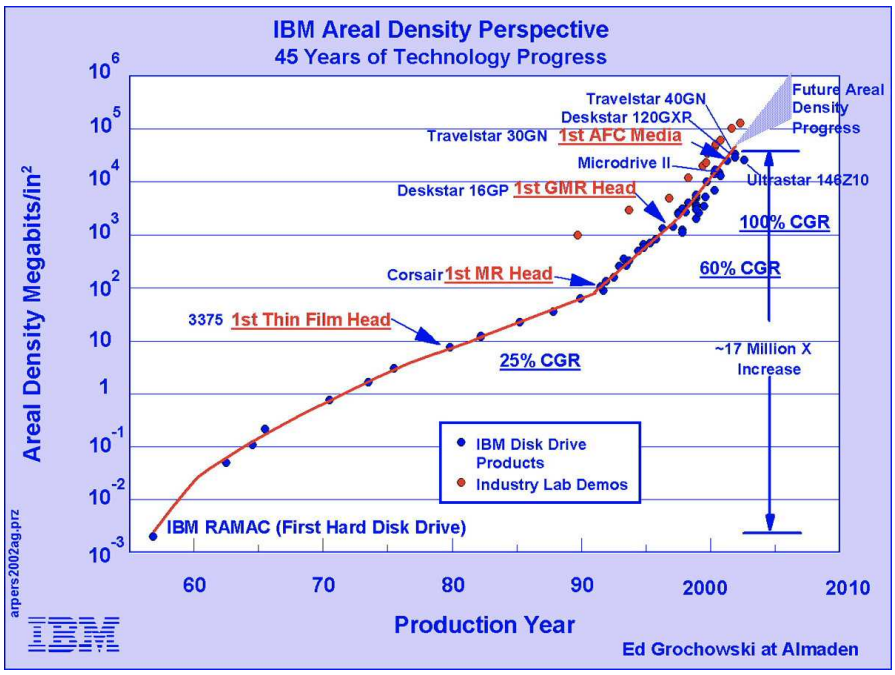

Figure 1.10: The chart follows the history of the disk drive by plotting the areal density as a function of production year.

1.2 Previous Work

Within the last few decades the field of condensed matter has developed various methods to characterise the chemical and magnetic properties of solids. These methods have led to an improved understanding of the recording media's magnetic and physical sub-granular structure. In general characterisation techniques such as transmission electron microscopy (TEM) was used to measure the physical grain size and grain size distribution of the recording layer. The physical grain size was important in determining the density of the recording media while the size distribution gives information pertaining to the grain's growth process. Another technique known as Surface Electron Microscopy (SEM) was utilised to map out the surface roughness and/or texture of intermediate seed layers. This property aids in the recording grain's nucleation rate. In addition, the technique of scanning energy filtered TEM has been used to map out the chemical structure within the recording grain and grain boundary region.

The above characterisation methods so far only measure the physical and chemical composition of the recording layer. A thorough understanding of recording media requires additional studies on its sub-granular magnetism. The characterisation technique of magnetometry was widely used to measure the sample's magnetisation. These measurements describe the recording grain's average magnetisation, however they fail to extract any spatial detail on the sub-granular magnetism. The technique known as small-angle neutron scattering (SANS) has been widely used to investigate the magnetic materials such as granular or discrete based recording media. The SANS experiment extracts the sample's magnetic and nuclear scattering components. Magnetic scattering occurs when the neutron's inherent dipole moment interacts with the sample's magnetic spin moment. The magnetic scattering intensity can be used to extract the recording layer's magnetic structure at a sub-nanometer resolution.

The following sections examine the relevant research work on longitudinal and perpendicular based recording media. In these previous experiments, the recording media's granular structure was characterised using TEM and X-ray measurements while the recording layer's sub-granular magnetism was investigated using SANS studies. The previous research work was used as a starting point for further characterisation studies of high-density recording media.

1.2.1 Longitudinal Recording Media

The research work of Futamoto et al [21] conducted a comprehensive study on the microstructure of longitudinal recording media composed of the cobalt-based alloy CoCrTa. The sample's physical grain size and chemical composition was investigated using the characterisation technique of electron energy loss spectroscopy or EEL-TEM. The TEM measurements of the $CoCr_{15}Ta_4$ longitudinal film are shown in Figure 1.11. The first TEM image shows the film's granular structure at a resolution of less than 10.0 nm. The black contrast represents the electron energy loss of zero. The recording grains have arranged themselves into an array of irregular shaped polygons, which resembled the Voronoi construction. Each grain was surrounded by a grain boundary of varying thickness. The TEM image in (b) shows the Cr core-loss pattern. The slightly faded grain indicates that the inner core was depleted of the Cr. The final image shows the Co core-loss image where the white grains indicate an enriched Co core. This TEM measurement shows that a high percentage of Cr has segregated to the grain boundaries. This physical property provides improved exchange de-coupling between the magnetic recording grains.

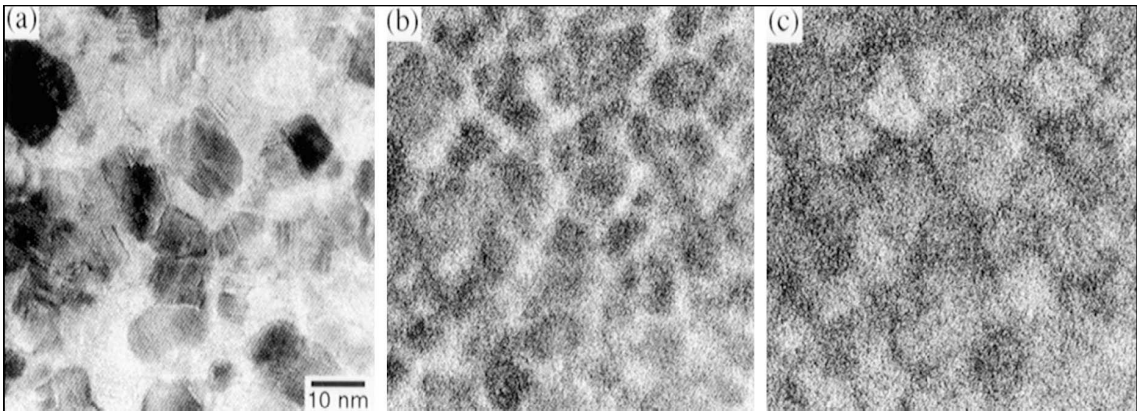

Figure 1.11: The EEL-TEM measurements of $CoCr_{15}Ta_4$ (a) zero-Loss, (b) Cr core-loss and (c) Co core-loss [21].

The chemical proportions within the grain's core and boundary regions were measured using energy dispersive x-ray analysis or EDAX-SEM spectroscopy. Figure 1.12 shows the compositional profile for grains A and B. Within either core, the atomic percentage of cobalt was approximately 90%. This indicates that the recording grain was composed of a hard ferromagnetic core. The Co percentage within the grain boundary sharply drops off to small values. The Cr within the boundary ranges from 23-26%. This high fraction of Cr renders the grain boundary non-magnetic. The Ta was uniformly distributed throughout the granular volume. The compositional profile of grain B gives a diameter of 13.2 nm with a grain boundary thickness of 1.0-5.0 nm.

The research of Wittig [22] and Grogger [23] mapped out the microstructure of longitudinal media using energy filtered TEM. Their results confirmed that a high proportion of Cr within the magnetic grain, $Co_{84}Cr_{12}Ta_4$, segregated to the grain boundaries. The research work of Kemner et al [24] investigated the microstructure of longitudinal films by using the characterisation technique of soft x-ray magnetic circular dichroism. Similarly it was found that a small fraction of Cr atoms (at least 10%) resided in the recording grain's core region.

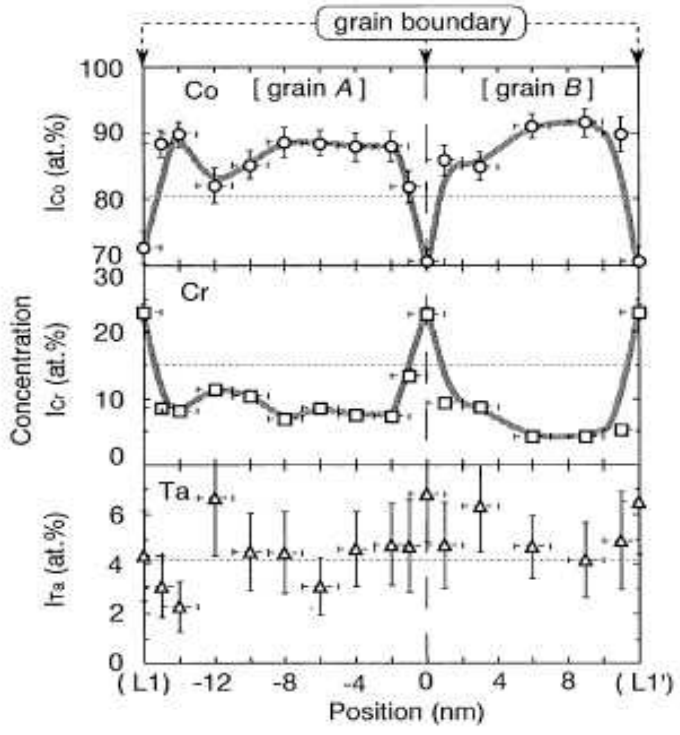

Figure 1.12: The compositional profile of the longitudinal film $CoCr_{15}Ta_4$, measured using EDAX spectroscopy. The profile plots the atomic percentage of different sized grains (A) and (B) [21].

The research work of Toney et al [25] used SANS measurements to investigate the magnetic granular structure of longitudinal recording media. The recording layer was composed of the cobalt-based thin film CoCrPt with a thickness of 25-40 nm. The film layer rests upon a nonmagnetic underlayer and a glass substrate. Three samples designated by the symbols Cy, To and So were fabricated with different grain sizes and grain size distributions. The background measurement was performed at the zero field state. The foreground intensity was measured at the magnetic field of 6.0 kOe applied parallel to the sample plane. The magnetic scattering intensity from the recording layer was extracted by calculating the difference between the foreground and background measurements. Figure 1.13(a) shows the Cy foreground and background measurements. The magnetic SANS intensity was shown in Figures 1.13(b)–(d). The magnetic SANS was due to isolated cluster particles with no inter-cluster interference scattering. TEM measurements determined that these clusters were cylindrically shaped.

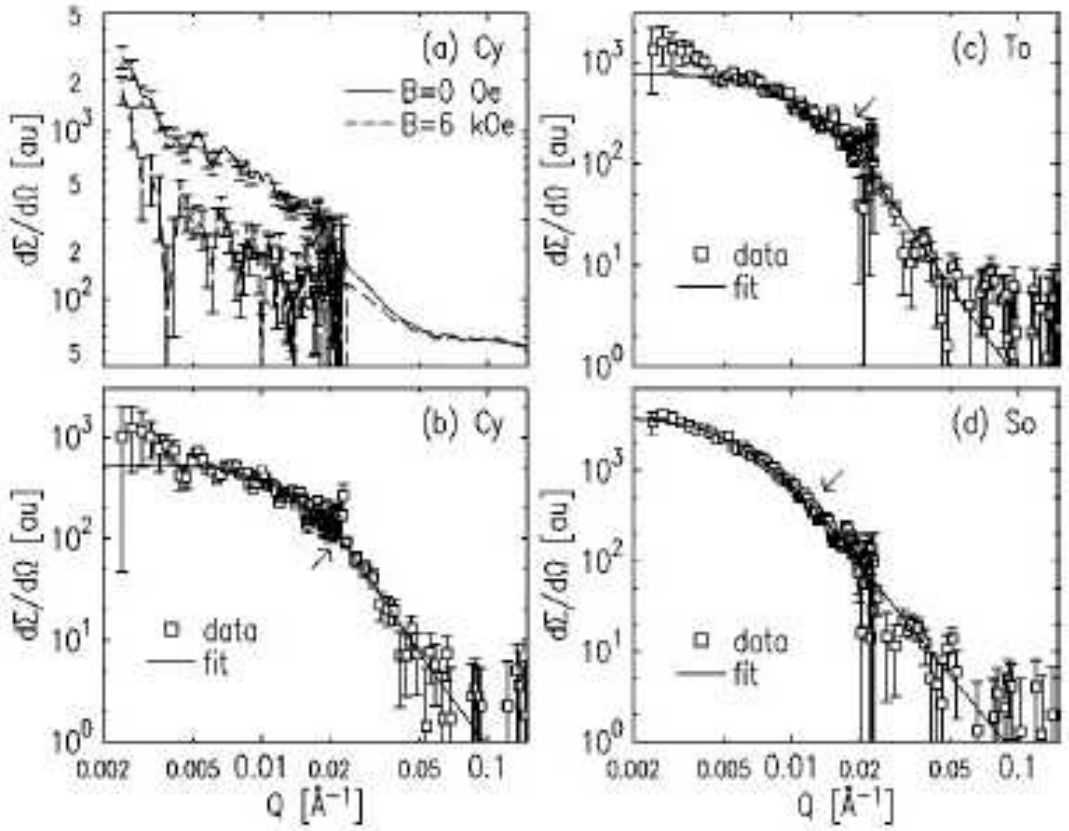

Figure 1.13: The SANS foreground (H=6.0 kOe) and background (H=0) measurements for (a) sample Cy. The magnetic scattering intensity is plotted for the samples (b) Cy, (c) To and (d) So. The scattering data is fitted with a cylindrical form factor averaged over a log-normal distribution of cluster sizes [25].

The clusters in reciprocal space were modelled using a cylindrical form factor, averaged over a lognormal distribution of cluster sizes. The scattering model fits the data quite well as shown in Figure 1.13. Results for Cy, To and So cluster sizes were 14, 16, 24 nm respectively. The lognormal distribution (number fraction) was plotted as a function of cluster diameter, see Figure 1.14. When the cluster size increased, the size distribution becomes wider. These results were consistent with x-ray measurements. The inset compared the magnetic cluster size with its physical counterpart. The average magnetic cluster size was only slightly larger than the physical grain size. This showed the inter-granular exchange interaction to be weak, which corresponds to a Cr-enriched grain boundary.

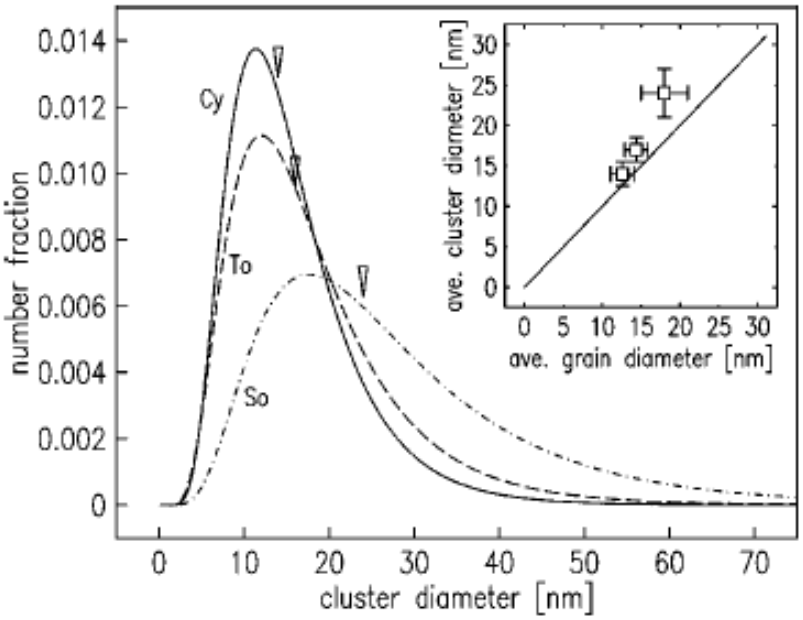

Figure 1.14: The log-distribution plot for samples Cy(—), To(--),So(- . -). The arrow marks the position of the average cluster size. The inset compares the magnetic cluster size to the physical grain size [25].

The research work of Kortright et al [26] investigated the chemical and magnetic and properties of longitudinal CoCrPt grains by using soft x–ray resonant scattering. This characterisation technique extracted the grain's physical (charge) and magnetic structure by tuning the incident x-rays to the Co/Cr excitation edge. Figure 1.15(a) shows the x-ray scattering intensities for the cobalt and chromium excitation edges of 778 eV and 574 eV respectively. The scattering intensity exhibited two peaks located at q_1=0.013 Å^{-1} and q_2=0.057 Å^{-1}. These q-positions correspond to the length scales of 48.0 nm and 11.0 nm respectively. The smaller length scale was similar to the physical grain size as measured by TEM. The larger q-position was possibly related to the magnetic inter-granular separation of adjacent domains.

The x-ray energy spectra was measured at the peak positions of 0.013 Å^{-1} and 0.057 Å^{-1}, see Figure 1.15(b). The x-ray scattering data was modelled using the charge scattering factors for Co, Cr and Pt. The scattering factors f_{Co}, f_{Cr}, and f_{Pt} are proportioned to the core and shell phase. The Co-enriched core phase was assigned the chemical ratio of Co:Cr:Pt=20:2:1. The Co-depleted shell takes the form Co:Cr=1:1. The scattering model showed that the low q-peak originated from the grain's magnetic scattering component while the high q-peak was due to its charge scattering.

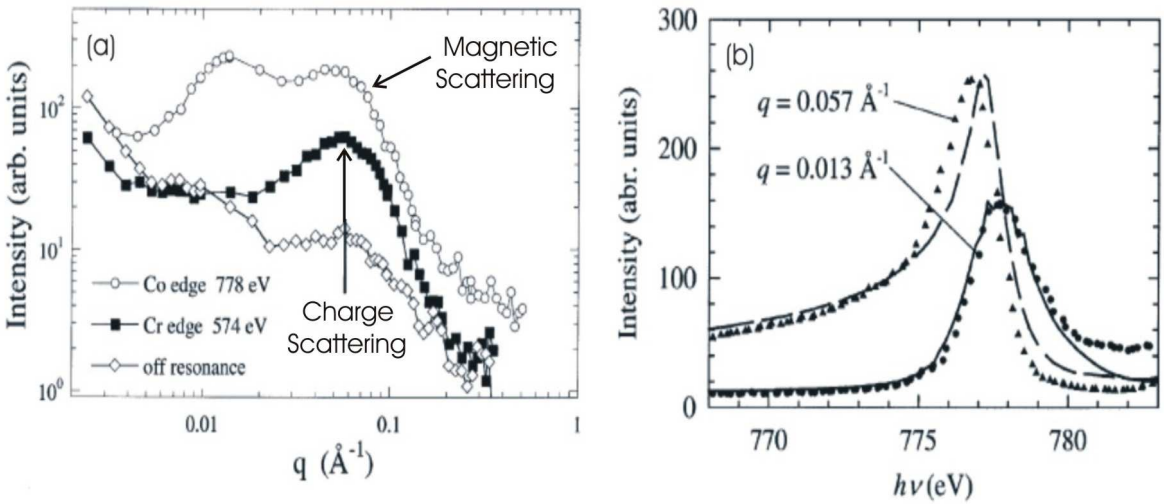

Figure 1.15: The small-angle x-ray measurements for longitudinal recording media. For plot (a) the scattering intensity as a function of q is plotted for the Co and Cr excitation edge where in (b) the spectrum is plotted for the peak positions of q=0.013 Å^{-1} and q=0.057 Å^{-1}[26].

1.2.2 Perpendicular Recording Media

One of the first magnetic SANS studies of perpendicular media based films was performed by the research group of Maeda et al [27]. The samples were fabricated from a CoCr alloy that exhibited a strong perpendicular magneto-crystalline anisotropy field. The characterisation was performed for a bulk and thin film sample. The background measurements were performed at zero field while the foreground was performed at an in-plane magnetic field of 11.6 kOe. The bulk nuclear and magnetic differential cross-section is plotted in Figure 1.16(a). The magnetic and nuclear intensities were almost identical which indicated a similarity between the magnetic and nuclear length scales. The scattering intensity for $q<0.2$ Å^{-1} was modelled using the Porod function [28]. This model shows that the bulk sample was composed of over sized granular clusters with a broad grain size distribution. Figure 1.16(b) shows the thin film SANS measurements at 11.6 kOe. In this case the cross-section exhibited scattering structure indicative of a well ordered granular ensemble with a narrow size distribution. The data was modelled using a Co-enriched spherical core form factor surrounded by a non-magnetic Cr shell.

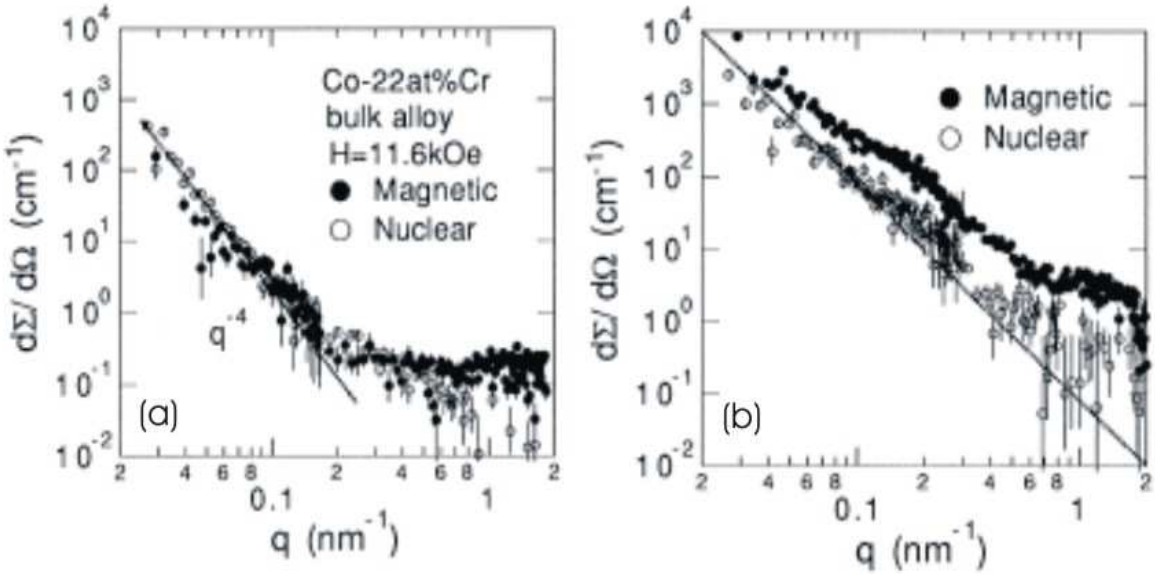

Figure 1.16: The magnetic and nuclear cross sections for (a) bulk and (b) thin film Co-Cr alloy samples. The bulk SANS data is fitted using the Porod function, while the thin film scattering is modelled using the spherical core-shell form factor [27].

The research work of Fullerton et al [29] used soft x-ray scattering to investigate the magnetic and chemical structure of perpendicular magnetised grains composed of the alloy CoCrPt. The x-ray measurements were performed in the remanent state where the granular moments lie perpendicular to the scattering plane, see Figure 1.17(a). The resonant x-ray scattering intensity was measured for the Co and Cr edges of 778 eV and 574 eV respectively, see Figure 1.17(b). The Co edge shows a magnetic scattering peak at q=0.017Å^{-1} that corresponds to the correlation length of aligned magnetic domains. The Cr edge shows a charge scattering peak occurs at q=0.065 Å^{-1}. This peak position gives the physical diameter of a single recording grain.

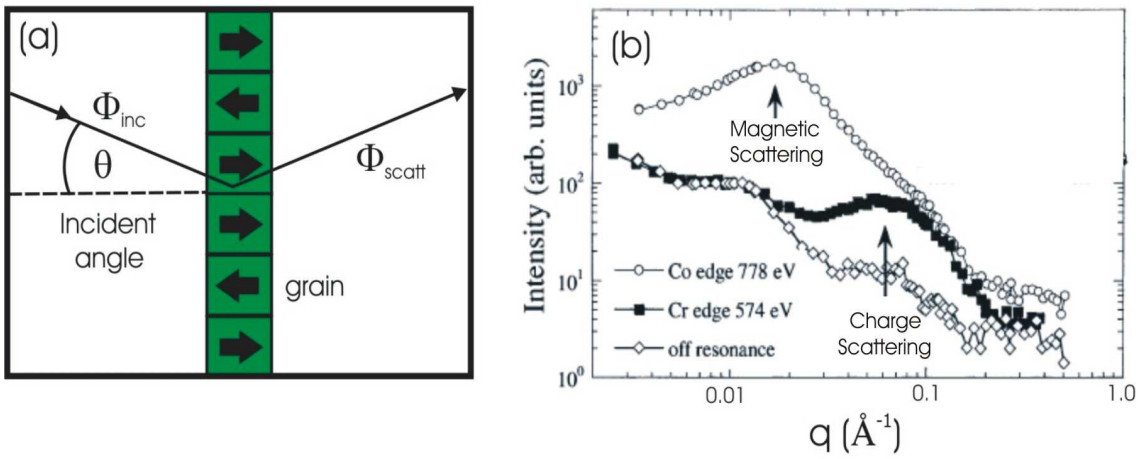

Figure 1.17 Soft x-ray resonant scattering for perpendicular orientated CoCrPt grains shown in (a). The scattering intensity (b) is extracted for the Co and Cr edges [29].

1.2.3 Summary

The above SANS, X-ray and TEM measurements were used to investigate the physical and magnetic properties of CoCrPt-based recording media. These studies have greatly expanded our knowledge on the recording layer's sub-granular magnetism. However the current research is quickly becoming dated due to improvements in sensor technology and fabrication methods. This leads to further reductions in the magnetic grain size. Currently there is a need to develop an accurate characterisation technique to study the nano-magnetism of high-density recording media. In this thesis, SANS and magnetometry studies were used to investigate the structure of longitudinal and perpendicular magnetic recording media at a sub-nanometer resolution.

Chapter 2

Theoretical Background

2.1 Magnetism

The classical theory of magnetism took shape in the mid-eighteenth century with the pioneering work of Hans Christian Oersted and Andre-Marie Ampere [30]. Oersted first demonstrated that when a compass was placed in the vicinity of a wire carrying an electrical current, the compass needle would align perpendicular to the field direction. The needle's forced response was attributed to a magnetic field generated orthogonal to the current direction. This discovery proved that there was a unique relationship between the magnetic field and direction of the current carrying wire. Ampere furthered Oersted's work by theorizing how an electrical current can excite a magnetic field (Ampere's Law). Ampere also postulated that a metallic ore's magnetism originated from an ensemble of microscopic current loops called magnetic dipoles denoted by μ_i. Figure 2.1 shows a magnification of a magnetic material where the magnetic field originates from an ensemble of Ampere current loops. This classical model of microscopic moments provided the basis for the semi-classical theory of magnetism.

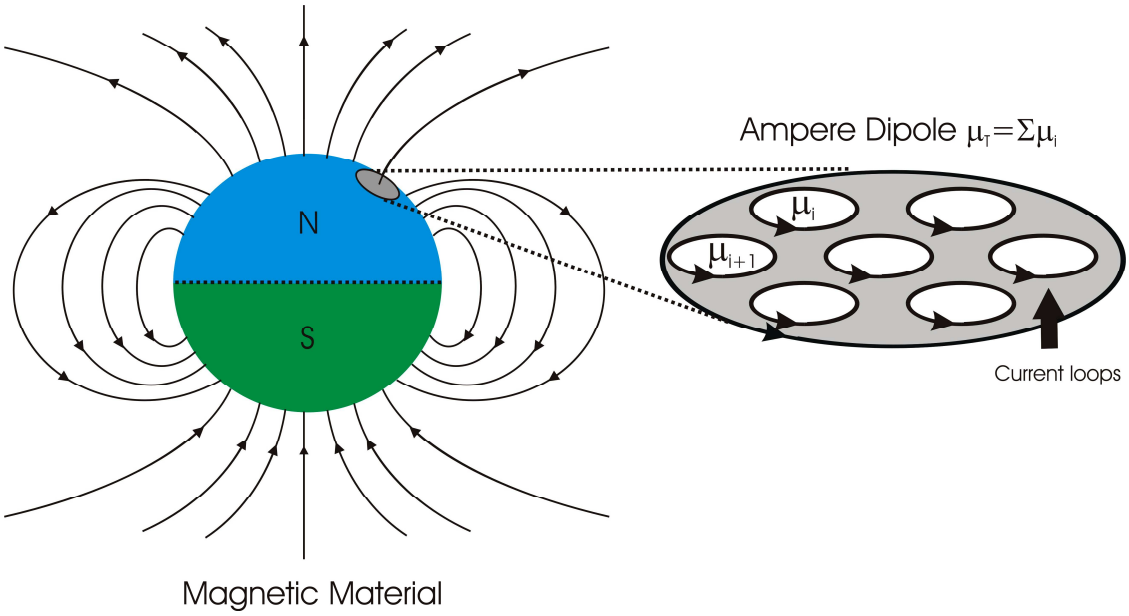

Figure 2.1: The Ampere model for classical magnetism. The total dipole moment, μ_t is the superposition of smaller current loops within the magnetic material.

The Ampere model of magnetism was formulated in part by macroscopic measurements of magnetic ores. These bulk measurements gave no clear explanation on the microscopic theory of magnetism. Experimental evidence on the origin of magnetism first came from excitation measurements of the hydrogen line spectrum. Niels Bohr postulated that the line spectra were in part due to the atom's quantized orbital angular momentum. The atom's total orbital angular momentum is defined by $\mathbf{L}=\Sigma_i\, l_i$ where l_i defines the ith electron orbital moment [31]. The magnetic dipole moment originated from orbiting electron charge. The classical equation for an atomic dipole moment is proportional to its angular momentum,

$$\mu_L = \frac{1}{2}\int (\mathbf{r}\times\mathbf{v})dq = \gamma\mathbf{L}\,. \tag{2.1}$$

The integral is calculated over the charge variable dq where the vectors **r** and **v** represent the ith electron radius and velocity respectively. The constant $\gamma=-e/2m_e$ is defined as the gyromagnetic ratio. Conventionally the atom's orbital moment is expressed as integral values of Bohr magnetons where $\mu_B=e\,\hbar/2m_e$.

The Bohr model of quantized orbital angular momentum only partially described the theory of magnetism. The Bohr model failed to predict the observed atomic line shifts when an atom was immersed in an applied magnetic field for example the Zeeman effect. These atomic line shifts where explained by the Stern-Gerlach experiment. It was observed that a beam of silver atoms, with a total orbital angular moment $\mathbf{L}=0$, exhibited a quantized magnetic moment in positive and negative directions of the applied field gradient. The origin of this moment was attributed to an intrinsic property of the electron known as spin angular momentum. The atom's magnetic moment due to electronic spin is expressed by the following,

$$\boldsymbol{\mu}_s = \gamma g_0 \mathbf{S}\,, \tag{2.2}$$

where $g_0=2.002$ is the free electron g-factor. The atomic spin is defined by summation $\mathbf{S}=\Sigma_i s_i$ where s_i is the ith electron spin moment. The magnetic fields generated by both orbit and spin moments are magnetically coupled via the spin-orbit interaction [32]. The spin-orbit Hamiltonian takes the form, $H_{SO}=\lambda\mathbf{L}\bullet\mathbf{S}$ where λ is the spin-orbit coupling constant for a particular atom. The spin-orbit coupling does not exceed the coulomb interaction between electrons therefore this effect is treated as a perturbation to the system. The spin-orbit effect is responsible for the phenomenon of magneto-crystalline anisotropy that determines a crystal's easy axis of magnetisation.

The atom's total angular momentum is expressed by the vector sum **J**=**L**+**S**. The variable J defines the quantum state of the total angular momentum. When J>0 the outer atomic shell is partially filled resulting in a non-zero total moment. At J=0 the outer shell is filled giving the atom a total moment of zero. The total magnetic moment is expressed by the summation of orbital and spin components,

$$\boldsymbol{\mu}_T=\boldsymbol{\mu}_L+\boldsymbol{\mu}_S=\gamma(\mathbf{L}+g_0\mathbf{S}). \tag{2.3}$$

Due to the g_0-factor, the total magnetic moment is no longer co-linear with the angular momentum vector **J**. In practice one does not measure the total moment but the average moment processing about the $\boldsymbol{\mu}_J$ vector. The average atomic moment is expressed as the projection of $\boldsymbol{\mu}_T$ upon $\boldsymbol{\mu}_J$ where $\mu_{ave}=g(JLS)\boldsymbol{\gamma}J$. The function g(JLS) is known as the Lande′ g-factor, which is a function of the total, orbit and spin quantum numbers [33].

When determining the magnetic behaviour of an atomic moment one must calculate the system's internal energy as a function of an externally applied magnetic field. The orbital and spin angular momentum are used to set up the canonical momentum for an ith atomic electron. Consider the equation of motion for an orbiting electron, immersed in an externally applied magnetic field,

$$\mathbf{p}_i \rightarrow \mathbf{p}_i + \frac{e}{c}\mathbf{A}(\mathbf{r}_i), \tag{2.4}$$

where $\mathbf{p}_i$ is the total momentum of the electron and $\mathbf{A}(\mathbf{r}_i)$=-1/2$\mathbf{r}\times\mathbf{H}$ is the vector potential defined for a uniform magnetic field **H**. The Hamiltonian operator is defined by $\mathscr{H}=\sum_i(\mathbf{p}_i^2/2m)$-V where V is the atomic potential energy. Through the substitution of equation 2.4 into the Hamiltonian and the inclusion of Coulomb and spin-orbit interactions the total Hamiltonian operator takes the form,

$$\mathscr{H}=\sum_i\left[\frac{p_i^2}{2m_e}-V+\sum_{ij}\frac{e^2}{r_{ij}}+\lambda\mathbf{L}\cdot\mathbf{S}\right]+\mu_B(\mathbf{L}+g_s\mathbf{S})\cdot\mathbf{H}+\frac{e^2}{8m_ec^2}H^2\sum_i(x^2{}_i+y^2{}_i). \tag{2.5}$$

The group of terms within the square brackets represents the field independent interactions. The last two terms (field dependent) describe the phenomena of paramagnetism and diamagnetism respectively. For a single atom the paramagnetic moment depends on the magnitude of J (field independent). The diamagnetic moment is induced by an applied magnetic field. These types of magnetism are characterised by the magnetic susceptibility, which defines the magnetic response to an applied field.

The magnetic susceptibility of a paramagnetic substance is positive while the diamagnetic material exhibits a negative value. The susceptibility takes the form,

$$\chi = n\frac{\partial \mu_T}{\partial H} = -n\frac{\partial^2 \mathscr{H}(H)}{\partial H^2}, \tag{2.6}$$

where μ_T is the total moment, n is the number density of the material and $\mathscr{H}(H)$ is the atomic energy state. Conventionally the material's susceptibility is expressed in terms of the molar susceptibility, $\chi_M = M_w\chi/\rho$ (cm^2/mol), where M_w is the molecular weight and ρ is the density of the material.

2.1.1 Diamagnetism

Diamagnetism is a type of magnetism, where an externally applied magnetic field perturbs the electron orbital motion of molecules thereby inducing persistent currents that oppose the applied field. The scale of the diamagnetic energy is small compared to atomic energy transitions. For example the hydrogen atom n=1 electronic energy transition is of order R_y=13.60 eV [34]. The transitional energy at the applied magnetic field of 1 Tesla (T) would be $\Delta E \approx 10^{-8}$ eV [31]. The diamagnetic susceptibility is determined using perturbation theory where the scale of the diamagnetic energy is small compared to the atomic energy shift. Through a series of mathematical manipulations the diamagnetic susceptibility takes the form,

$$\chi_{dia} = -n\frac{e^2}{8m_e c^2} Z\left\langle R^2 \right\rangle. \tag{2.7}$$

where n, Z and R are the number density, atomic number and atomic radius respectively. Equation 2.7 shows the susceptibility to be independent of the applied magnetic field and temperature. By converting to the molar susceptibility, χ_M, the mean squared average effectively cancels out. This results in a diamagnetic response linearly dependent on the atomic number Z. Molecules rather than atoms possess large diamagnetic susceptibilities where the electron charge density may span a multitude of atomic radii. For instance the substances water and ethyl alcohol are observed to have a sizeable diamagnetic susceptibility. An even larger diamagnetic susceptibility is observed for aromatic compounds such as naphthalene ($C_{10}H_8$) where one of the four bonding electrons is allowed to circulate throughout the molecule. This gives the itinerant electron a large mean square distance and hence a larger than expected diamagnetic susceptibility.

2.1.2 Paramagnetism

The magnetic phenomenon of paramagnetism occurs when an ensemble of magnetic moments, within a solid, align along the direction of an externally applied magnetic field. Classically the paramagnetic magnetisation is derived by calculating the thermal average of an ensemble of magnetic moments aligned along an arbitrary H-field direction. The magnetisation is described by the Langevin function, $L(y)=\coth(y)-1/y$ where $y=\mu H/kT$ [33]. The quantum paramagnet is described using discrete magnetic moment values, which are proportional to the system's total angular momentum. In a similar fashion, the total paramagnetic magnetisation is derived by thermally averaging the ensemble of discrete moments. The quantum paramagnet is represented by the Brillouin function $B_J(y)$. In Figure 2.2, the paramagnetic magnetisation is plotted for the quantum states J=1/2, 1, 3/2, 2 and ∞ (continuous). At the continuous limit J=∞, the Brillouin function reduces to its classical derivation. Through a series of mathematical operations the paramagnetic susceptibility takes the form,

$$\chi_{para} = n\frac{(g(JLS)\mu_B)^2}{3}\frac{J(J+1)}{k_B T}. \qquad (2.8)$$

This relation, known as Curie's Law, combines the concept of spin with the thermodynamic property of thermal disorder. Increases in temperature work to disorder the paramagnetic spin while alignment is favoured through the application of an external magnetic field. In Figure 2.3(a) the magnetic susceptibility of Cu and Au is plotted as a function of temperature. These metals exhibit a temperature independent susceptibility characteristic of a diamagnetic response. For Figure 2.3(b) the substances Al and NiAl [35,36] show a temperature dependent susceptibility characteristic of the Curie paramagnet. In most cases the diamagnetic response is small when compared to the paramagnetic component. The paramagnetic to diamagnetic susceptibility at room temperature can reach values of order $\chi_{par}/\chi_{dia}\approx 500$ [37]. Note equation 2.8 only gives a phenomenological description of the metal's paramagnetic response. The microscopic theory is properly described using Pauli paramagnetism. For a paramagnetic metal, the spin up and spin down states are partitioned in electronic bands. The band structure is described by the "density of states" function. When a magnetic field is applied to the paramagnetic metal, electrons from the spin down band are promoted to the spin up band resulting in a net magnetic moment.

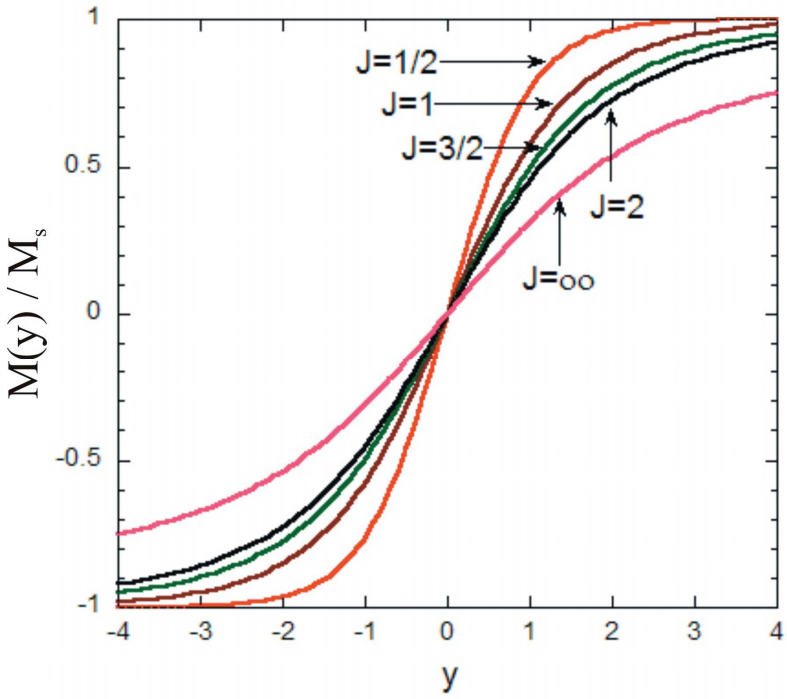

Figure 2.2: The paramagnetic magnetisation calculated using the Brillouin function B(y)=(2J+1)/2Jcoth((2J+1)/2Jy)-1/2Jcoth(2J*y) for J=1/2, 3./2, 2, ∞.

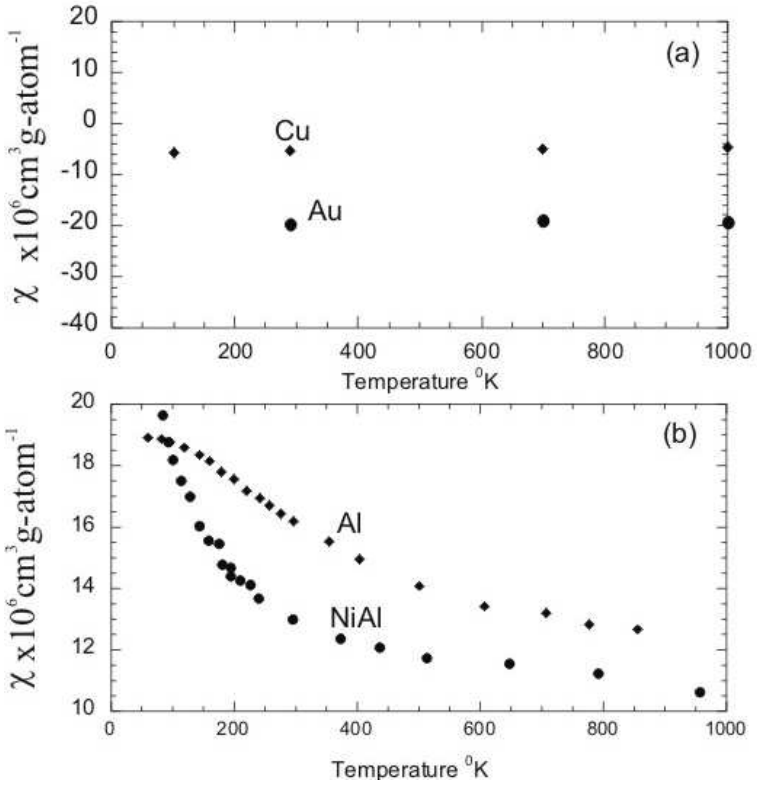

Figure 2.3: The magnetic susceptibility as a function of temperature. The metals (a) Cu and Au show a diamagnetic response while the substances (b) Al and NiAl are characteristic of a Curie paramagnet [35,36].

2.2 Spontaneous Magnetism

In the previous section the nature of induced magnetism was described for a paramagnetic solid. These materials exhibited high magnetic order when immersed in an applied magnetic field. The moment ensemble returned to a randomised state at zero field. In nature there exists a class of magnetic materials that exhibit the phenomenon of spontaneous magnetism. Classical theory first suggested that this type of magnetism could be caused by strong dipolar interactions between neighbouring atoms. However calculations showed that the dipolar field between two atoms was too small to induce permanent magnetic order. It turned out that spontaneous magnetic order was linked to the atom's exchange interaction, which was purely a quantum mechanical phenomenon.

The underlying physics of the exchange interaction is demonstrated using a pair of identical ions interacting via their unpaired electrons. Suppose the electron orbit of ion A approaches the electron orbit of ion B. If the electron spin pair is anti-parallel then the Pauli exclusion principle states that the electrons will share a common orbit thus increasing the Coulomb energy. If the spin pair is parallel then the Paul exclusion principle requires that the electrons must form separate orbits thereby decreasing the Coulomb energy. Through a series of calculations the exchange Hamiltonian for a pair of neighbouring spins, $\mathbf{S}_A$ and $\mathbf{S}_B$, takes the form,

$$\mathscr{H}_{\text{spin}} = -J_{exe}\,\mathbf{S}_A \cdot \mathbf{S}_B, \tag{2.9}$$

where J_{exe} represents the exchange or overlap integral. This equation traditionally describes the Heisenburg ferromagnet where the exchange interaction is mostly felt by its nearest neighbour spins. The magnitude of $\mathscr{H}_{\text{spin}}$ is approximately 10^3 larger than the dipole energy [37]. For $J_{exe}>0$ the exchange energy is at its lowest state when the spin pair align parallel, $\mathbf{S}_A \| \mathbf{S}_B$. This spin state is known as ferromagnetism. The lowest energy state of $J_{exe}<0$ occurs when the spin pair align anti-parallel which is known as anti-ferromagnetism. It so happens that the direct exchange mechanism fails to account for the spontaneous magnetism of solids such as metals and oxides. For example transition metals such as ^{26}Fe and ^{27}Co exhibit spontaneous magnetism via itinerant exchange interactions of the 3d band and 4s electrons. The full treatment of the exchange mechanism is beyond the scope of this thesis. However a rudimentary understanding of spontaneous magnetism is possible by briefly reviewing the class of metals known as the band ferromagnets.

2.2.1 Ferromagnetism

The phenomenon of band ferromagnetism at room is due to the metal's spin-split band structure rather than the direct overlap of localised wavefunctions. The nature of band ferromagnetism is understood in terms of the molecular mean field theory where a scalar field is used to approximate the effective exchange interaction between band electrons. The electronic band structure is represented using the "density of state" function $g(E)$ [37]. Figure 2.4 shows the spin up/down band structure for a hypothetical metal. The non-magnetic state occurs when there is an equal number of spin up $n\uparrow$ and spin down $n\downarrow$ electrons occupying their respective bands. Since there is no external or exchange field, the band electrons occupy every site below the Fermi energy E_F.

The ferromagnetic band structure becomes nontrivial due to the influence of the exchange field. For this situation, exchange interactions must be considered between the spin up/down electron bands. Figure 2.5 depicts the electronic band subdivided into a spin up (upper) and spin down (lower) band. The exchange field was approximated by the molecular field theory. In short the atom's internal molecular field promotes electrons from the lower to the upper band. When the number of electrons in the upper band exceeds the lower band then the average magnetic moment of the metal is expressed by $\mu_{ave}=\mu_B(n\uparrow-n\downarrow)$ where $n\uparrow>n\downarrow$. The net moment results in a relative energy band shift of $w\mu_B^2(n\uparrow-n\downarrow)^2$ where w represents the molecular field strength.

The above simplified band theory suggests that spontaneous magnetism could occur for any band metal with strong exchange forces. However in nature only a select few metals exhibit the state of band ferromagnetism. The ferromagnetic condition is only possible if the spin transition to the upper band is an energetically favourable state. Consider the non-magnetic metal where the upper and lower band satisfy the condition $n\uparrow=n\downarrow$. When the exchange field populates the upper band there is an increase in the system's kinetic energy $\Delta E_k>0$. The energy of the upper and lower bands change to $E_F+\delta E$ and $E_F-\delta E$ respectively. However the energy change due to the exchange field gives an energy reduction where $\Delta E_{exe}\approx -1/2 w\mu_B^2(n\uparrow-n\downarrow)^2$. Spontaneous magnetism occurs when the loss in exchange energy outweighs any increase in kinetic energy. The conditions for spontaneous magnetism is expressed simply by the Stoner criterion where $w\mu_B^2 g(E)>1$ [31]. Hence the criterion requires the ferromagnetic metal to possess a large "density of states" at the Fermi level and a large molecular exchange coupling.

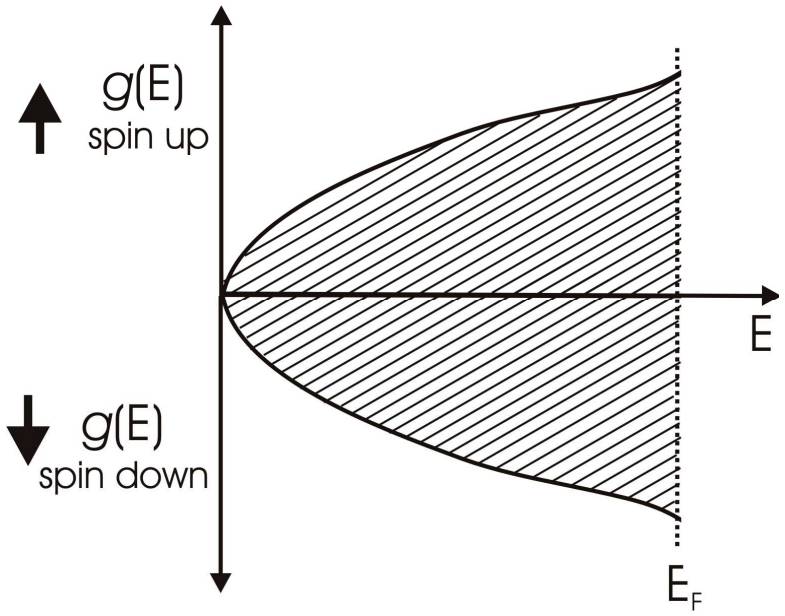

Figure 2.4: The spin up/down density of states of a non-magnetic metal. The substance exhibits paramagnetism when an applied magnetic field causes an energy shift between the spin bands [32].

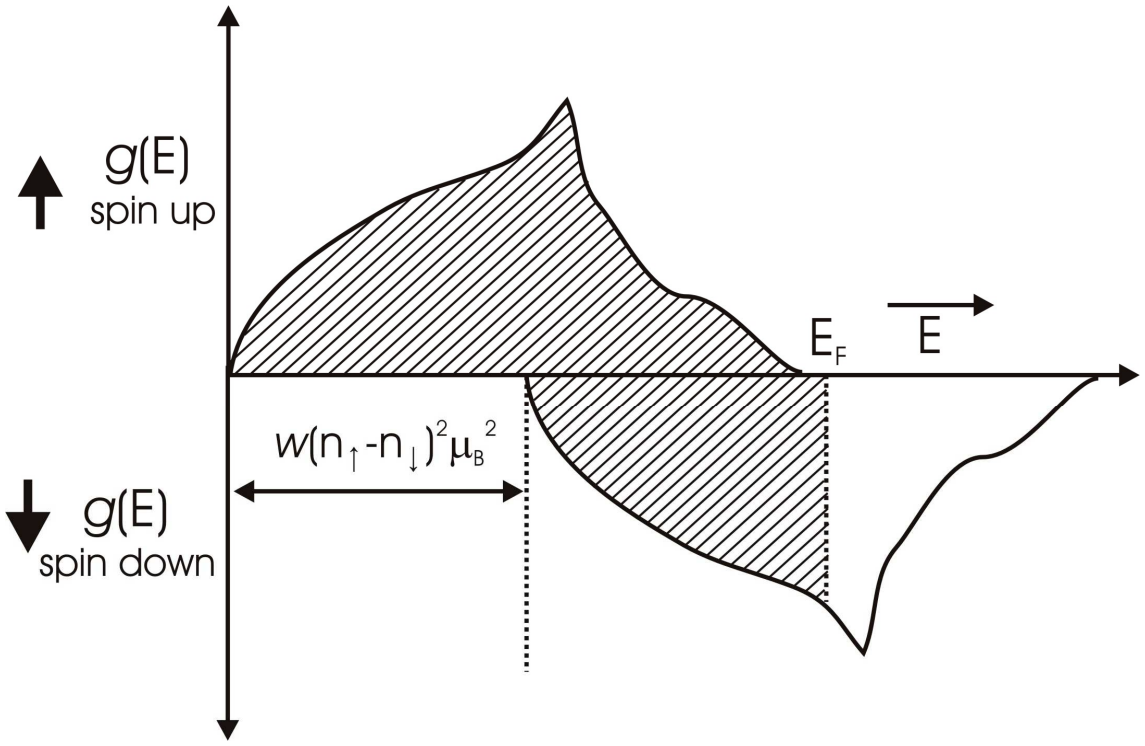

Figure 2.5: The spin up/down density of states for a band ferromagnet. At zero applied field, the shift between spin bands is due to the metal's internal molecular field *w* [32].

2.2.2 The Curie Phase Transition

The spontaneous magnetic order of a ferromagnetic metal only exists within a defined temperature range. The Curie point defines the metal's phase transition from the ferromagnetic to paramagnetic state. For the temperature range $T<T_C$ the metal exhibits ferromagnetic order. When the temperature is above the Curie temperature, $T>T_C$, the metal exhibits the phenomenon of paramagnetism. The magnetic behaviour above and below the Curie point is modelled according to the Weiss theory of ferromagnetism. In the previous section, the exchange field induces a spontaneous magnetic moment within the metal's band structure. The Weiss model approximates this exchange field by using a uniform molecular field approach. The model can be visualised as an ensemble of classical moments each generating its own molecular field. Figure 2.6 shows how the molecular field from neighbouring spins induces a spontaneous magnetic moment. The effective field on a neighbouring site takes the form $H_{eff}=H_0+H_M$ where H_0 is an applied magnetic field and $H_M=wM$ represents the molecular field. The constant w is a scaling constant and M is the metal's magnetisation.

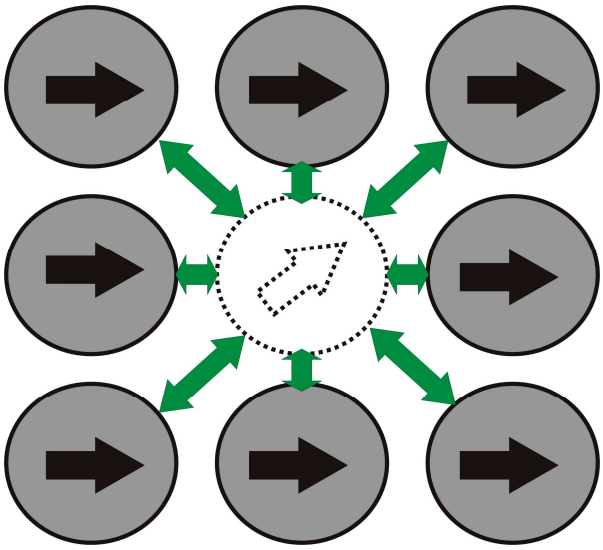

Figure 2.6: The mechanism for the Weiss theory of ferromagnetism. The centre moment is aligned by a molecular field (green arrows) generated by its nearest neighbour moments.

The spin magnetisation for an external applied field H_0 is calculated using the Brillouin function $B_J(y)$. Traditionally the Brillouin variable is modified to account for the molecular field H_M where $y=\mu_{eff}(H_0+wM)/(kT)$. The y-variable is now a function of the applied and molecular fields. The derivation is simplified by assuming that the molecular field is very much larger than the external field where $H_0=0$. The system's magnetisation is expressed by $M(y)=(kT/\mu_{eff}w)y$. The stable magnetic states resulting from the molecular field are determined by intersecting the linear function of M(y) with the Brillouin function. These equations are solved using a graphical approach whereby the magnetisation intersections are parameterised in terms of the system's temperature.

When the temperature approaches zero, the sample magnetisation intersects the Brillouin plot at three points, M=0, M>>0 and M<<0. At M=0 the system is not in magnetic equilibrium where any slight change in the y-variable will destabilise the spin state. For either M>>0 or M<<0 the magnetisation function intersects stable magnetic states where the magnetic moments exhibit spontaneous magnetism. For further temperature increases the slope of the magnetisation plot increases while still remaining in the spontaneous magnetic state. When the equation intersects at the single point M=0 there is no permanent magnetic order. This magnetic transition is known as the Curie point which is defined at $T=T_C$. Figure 2.7 plots the Brillouin intersections for four different temperatures $T<<T_C$, $T<T_C$, $T=T_C$ and $T>T_C$.

The exact form of the Curie temperature is determined by taking the derivative of $B_J(y)$ and M(y) near the origin ($y\rightarrow 0$). Through a series of substitutions, the Curie temperature is expressed by $T_C=[(J+1)/(3k)]n\mu_{eff}w$ [33]. The argument of the Brillouin function can be rewritten as $y=[3J/(J+1)](T_C/T)(M/M_s)]$. The saturation magnetisation ratio $M_s(T)/M_s(0)$ ratio is calculated for the temperature range $0<T<T_c$ at the momentum states of J=1/2, 1, 3/2, 5, 15. The ratios are solved using the graphical method outlined in Figure 2.7. At large J, the Brillouin equation simplifies to the classical Langevin derivation. Figure 2.8 compares these calculations to magnetisation data from the 3d transition elements Fe and Ni. The classical and quantum models show spontaneous magnetic ordering as the temperature approaches zero. As the temperature approaches the Curie point, the classical model diverges from the experimental data. The magnetisation data is in agreement with the quantum model for small J values rather than the classical result at J=15. For $T>T_C$ thermal agitation works to disorder the ferromagnetic state where the spontaneous magnetism vanishes.

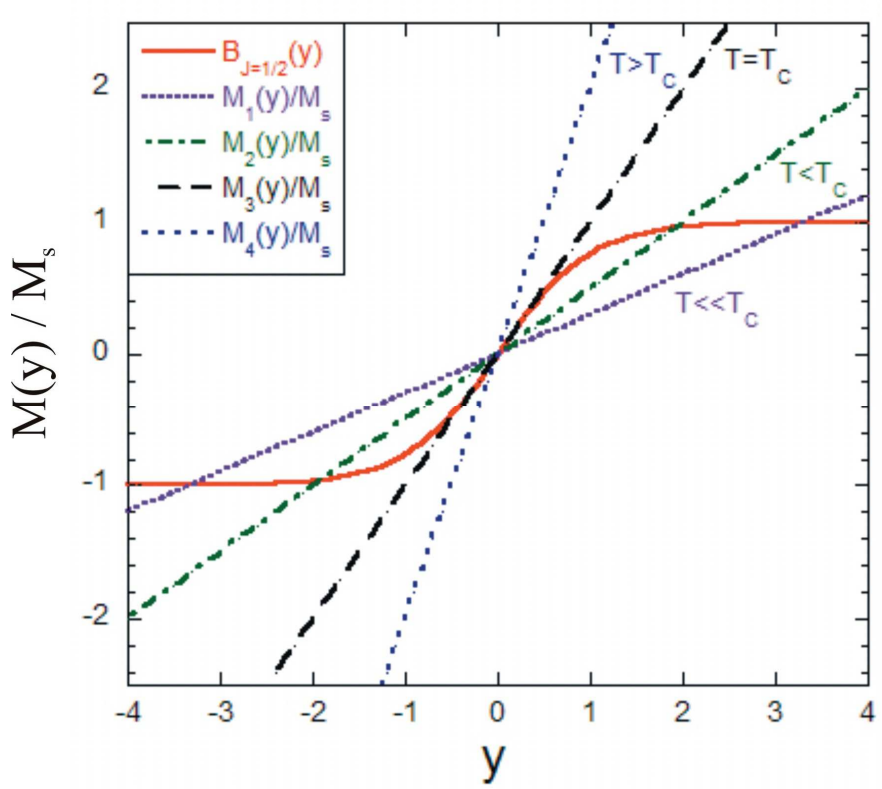

Figure 2.7: Graphical solutions to the Brillouin (intersections) function at the magnetic states $T<<T_C$, $T<T_C$, $T=T_C$ and $T>T_C$.

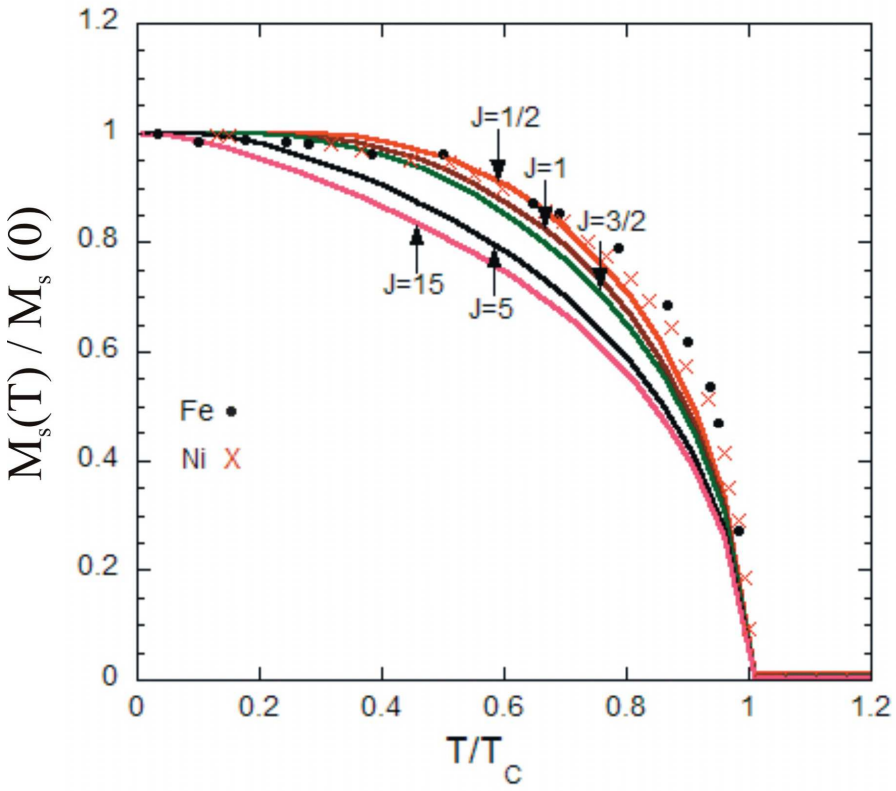

Figure 2.8: The saturation magnetisation for the Weiss ferromagnet as a function of temperature. The Weiss model at J=1/2..15 (∞) is compared to experimental data for the 3d transition elements Fe and Ni [36].

2.2.3 Domain Theory

The above discussion on ferromagnetism has described how the spin-split band structure of transition metals is responsible for inducing spontaneous magnetism. The current derivation assumes that the exchange energy is completely isotropic throughout the bulk ferromagnet. Therefore the system's exchange Hamiltonian is independent on the direction of magnetisation. In reality the bulk ferromagnet is partitioned into magnetic domains each aligned along a preferred direction of magnetisation. The formation of domains is attributed to the competition between the domain wall and dipolar field energies. The domain's preferred direction of magnetisation, known as the magnetic anisotropy, is dependent on the sample's crystalline and bulk properties.

2.2.3.1 Dipolar Field

The formation of magnetic domains is a process whereby the sample minimises its dipolar energies at the cost of creating domain walls. Figure 2.9(a) shows a single dipole moment where the dipolar energies are large at the boundary edge. The dipolar energy is reduced by the formation of domain walls via exchange forces. It is commonly observed that the domain structure is partitioned into Bloch or Neel walls. The Bloch wall separates anti-parallel domains while the Neel wall separates orthogonal pairs. Figure 2.9(b) demonstrates Bloch wall formation where the magnetic energy is reduced by factor 1/2. Further divisions lead to flux closure of the magnetic domains resulting in a zero magnetisation field. In Figures 2.9(c) and 2.9(d) the domains show a combination of Bloch and Neel wall formations [38].

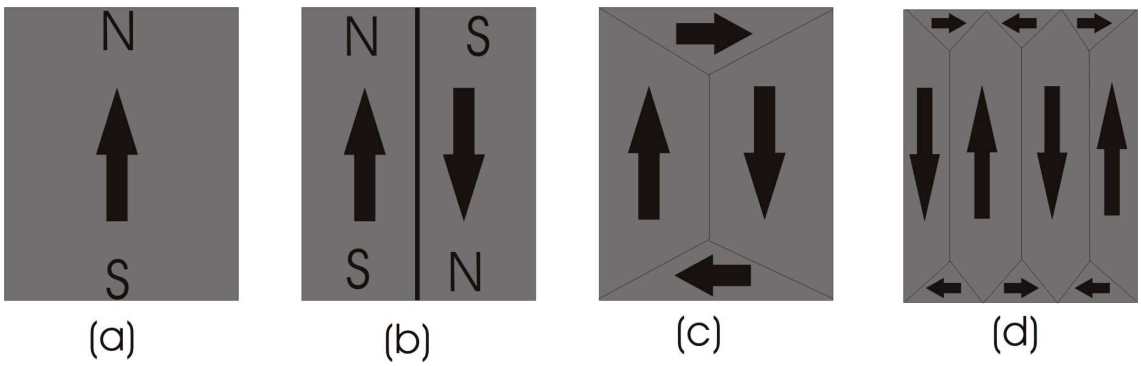

Figure 2.9: Formation of the (a) single domain, (b) anti-parallel domain, (c) multiple domains and (d) domain flux closure where the sample's net magnetisation goes to zero.

2.2.3.2 Magnetic Anisotropy

The formation of domain walls costs energy to orient the moments in anti-parallel or orthogonal pairs. If not prevented by some external force, the magnetic moments will revert back to their single domain structure. The sample's magnetic anisotropy energy is responsible for keeping the moments aligned along a preferred direction of magnetisation. The magnetic anisotropy depends on the compound's crystallographic structure and the size and shape of the magnetised body.

The energy term known as magneto-crystalline anisotropy results in a preferred direction of magnetisation along a particular crystal axis [39]. The microscopic origins of crystalline anisotropy can be linked to the Hamiltonian's spin-orbit interaction term. The orbital wave functions interact with the spin and crystallographic structure resulting in spin alignment along a particular crystal axis. Traditionally the term "easy axis" refers to the sample's preferred direction of magnetisation. The "hard axis" refers to the situation where the direction of magnetisation is not favoured. The phenomenological description of magneto-crystalline anisotropy is given for the ferromagnetic metal Tb (rare earth 4f) shown in Figure 2.10. The Tb metal forms a hexagonal closed packed (hcp) structure where the easy axis lies within the a-b plane. For hexagonal symmetry, the uniaxial anisotropy energy takes the approximate form $E_a=K_1\sin^2\phi+K_2\sin^4\phi$ where ϕ is the angle between the magnetic moment and easy axis. The coefficients K are known as the anisotropy density constants. Hysteresis measurements show that it requires a small field to align the sample moments within the a-b plane. When the field is applied along the c-axis, the moments resist the magnetic action. This resistance is so pronounced that the magnetisation at 400 kOe is only 80% of the b-axis result.

The magnetic property known as shape anisotropy is another energy term that can determine the sample's easy axis of magnetisation [40]. For a magnetised body, magnetic charges or poles are induced at the surface. This results in a surface charge distribution that generates a smaller magnetic field opposite to the applied field, also known as the demagnetisation field. The easy axis lies along the direction where the sample's demagnetisation field is weakest. In Figure 2.11 the shape anisotropy is shown for a thin film and an ensemble of cylinder objects. The demagnetisation energy of a thin film sample is expressed by $1/2\mu_0 M^2\cos^2\phi$ where ϕ is the angle between the sample normal and magnetisation M. The easy-axis of magnetisation lies within the sample plane since the demagnetisation energy is at a minimum.

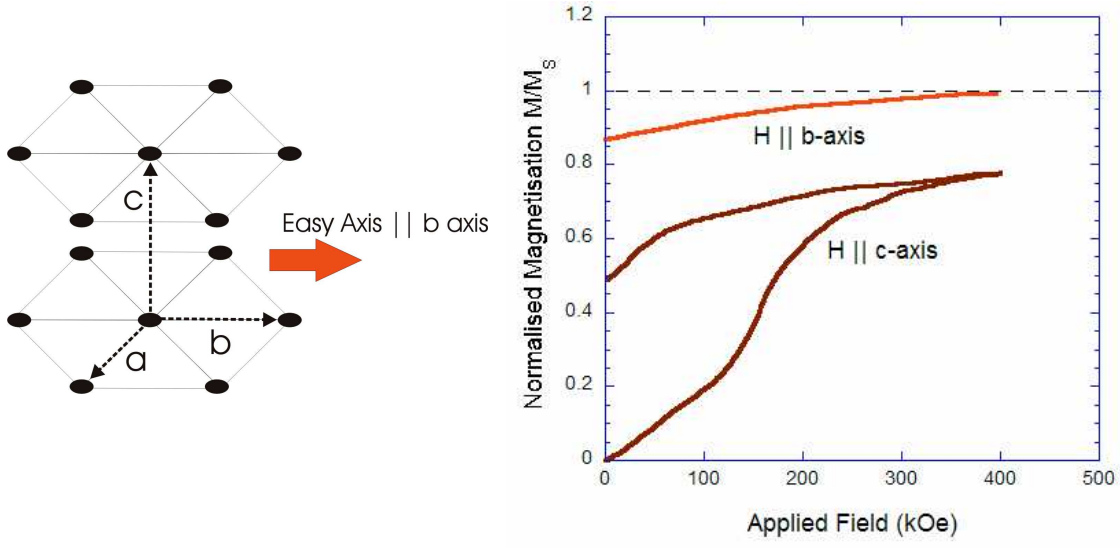

Figure 2.10: The hcp crystal structure for the ferromagnetic rare earth Tb. The crystal easy axis is directed along the b-axis. The right plot shows the Tb magnetisation measured along the c and b axes [37].

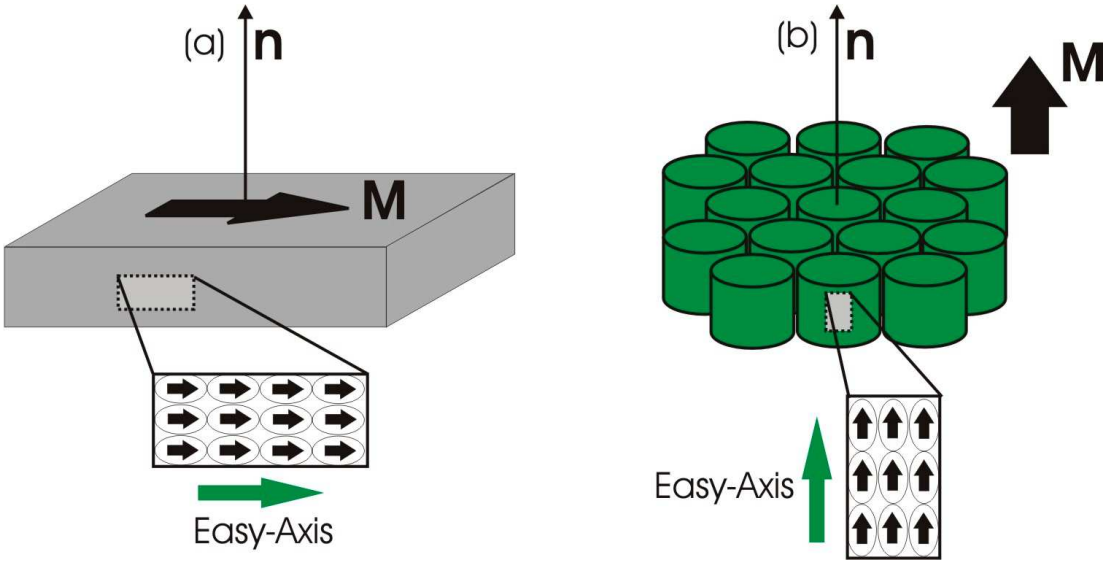

Figure 2.11: Illustrations of magnetic shape anisotropy for the (a) thin film and (b) an ensemble of infinitely long cylindrical objects. The atomic moments, shown in the rectangular box, align along the easy axis of magnetisation that turns out to be the spatial dimension of largest extent.

2.2.3.3 Magnetic Hysteresis

The energies involved in the formation of magnetic domains are characterised by measuring the sample's bulk magnetisation as a function of an applied magnetic field. For the purpose of illustration, consider a ferromagnetic sample where the easy axis of magnetisation lies within the x-y plane. Figure 2.12 shows the sample's magnetic hysteresis loop. At zero field the domain structure forms a flux closure resulting in a magnetisation of M=0. When a small magnetic field is applied in-plane, domains that are aligned favourably to the applied field will grow at the expense of the unfavourably aligned domains. If the magnetic field is ramped down to zero, the domains return to their initial magnetic state. Within this field range, the magnetic hysteresis curve exhibits reversible behaviour. At larger magnetic fields the domains begin to align along or near the easy-axis of magnetisation. When the sample is fully saturated $M(H_s)=M_s$, the domains are forced to align along the field direction regardless of the sample's easy or hard axes. When the applied magnetic field is reduced to zero, the magnetisation falls to a remanent value $M(0)=M_r$. The domains are prevented from returning to their original magnetic state. In this region the hysteresis loop exhibits irreversible behaviour which is caused by the sample defects or pinning sites. Traditionally the remanent and saturation magnetisation is expressed by the loop squareness $S=M_r/M_s$. The zero magnetisation state is now shifted to finite field values known as the coercive field H_c. Depending on the application, the magnitude of the coercive field can be controlled by metallic doping or by introducing physical inhomogeneities eg: point defects that inhibit domain boundary motion.

The area of the hysteresis loop is proportional to the amount of energy dissipated for the reversal of the applied field [41]. If the loop area is large then domain wall motion is highly restricted resulting in a hard ferromagnetic material. Figure 2.13(a) shows an example of a hard ferromagnetic loop. This type of hysteresis behaviour is desirable for permanent magnets and magnetic recording media. When the loop area becomes very small the domain structure is highly permeable resulting in a soft ferromagnetic substance. Figure 2.13(c) shows an example of a soft ferromagnetic loop. These types of materials are used for transformer cores, which minimise energy loss during AC electricity production. As the domain's anisotropy energy decreases, the loop width gradually approaches zero as shown in Figure 2.13(d). At zero width the magnetic domains exist in the superparamagnetic state.

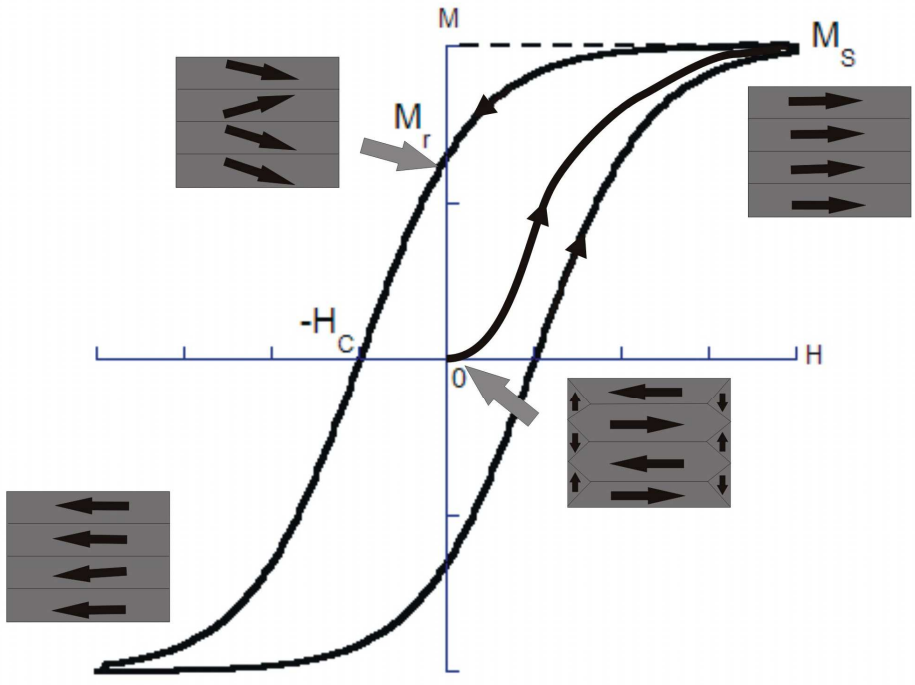

Figure 2.12: The magnetic hysteresis loop for the typical ferromagnet. The virgin state at M=0 is brought to saturation M_s. At zero the magnetisation remains finite defined by the remanent magnetisation M_r. The zero magnetisation states are defined at the coercive field H_c.

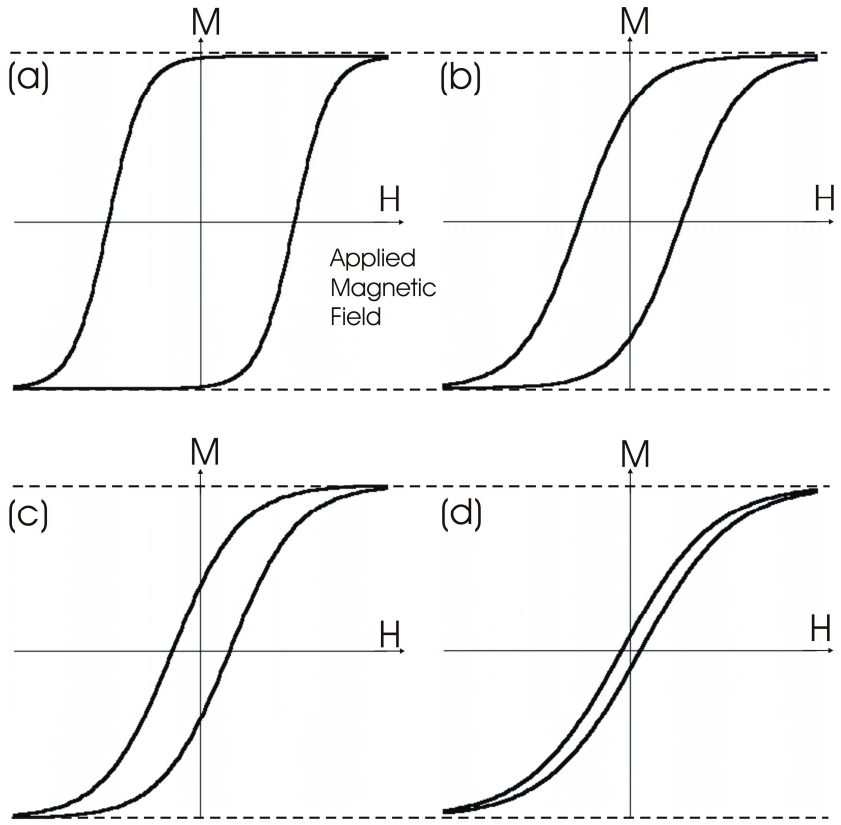

Figure 2.13: The magnetic hysteresis loop ranging from (a) hard to (d) soft ferromagnet.

2.3 Neutron Scattering

Since the introduction of nuclear reactors, thermal neutron scattering has become an invaluable characterisation technique for the study of condensed matter. The neutron's subatomic properties such as wavelength, charge and magnetic moment make it an ideal probe to investigate the sample's physical and magnetic properties on the submicron scale.

The neutron like all subatomic particles has a wavelength expressed by the de Broglie the relation $\lambda=\hbar/(m_n v)$ where m_n and v are the mass and velocity of the neutron respectively. The neutron like the soft x-ray can undergo elastic or inelastic scattering when the wavelength is comparable to the target's atomic dimensions. Figure 2.14 shows the typical scattering interaction. The incident neutron beam is represented by a travelling planar wave of wavelength λ. When the neutron beam collides with the target, a spherical scattering wave radiates out from the centre. The structure of solids and liquids are investigated using thermal neutrons where the wavelength is just a few angstroms. The energy range of thermal neutrons is of the order of 1-100 meV [42].

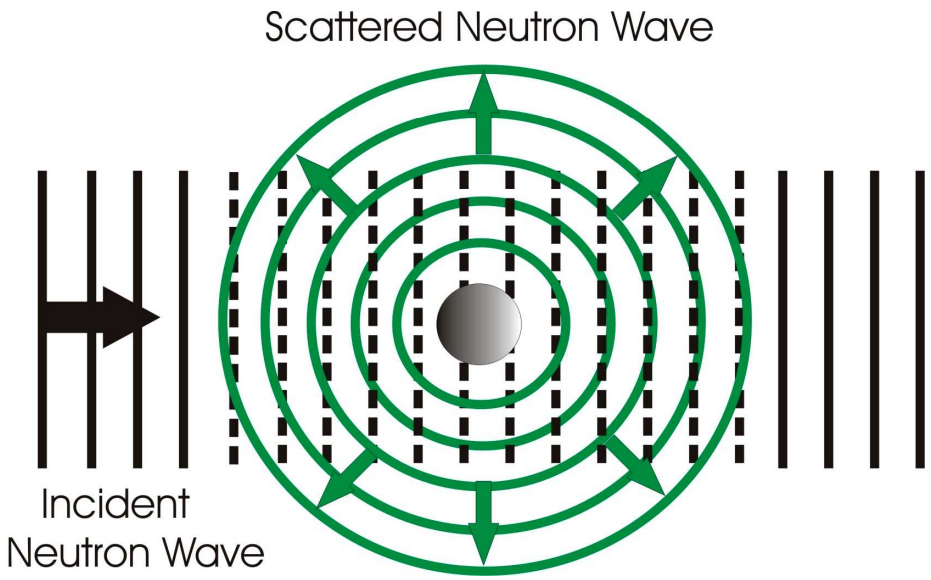

Figure 2.14: The incident neutron plane wave scattering off a spherical target [43].

The neutron exhibits a charge of zero. Due to this property there is no coulomb scattering from the positively charged nucleus. This allows the neutrons to interact with the atomic nucleus via the nuclear force. The scattering properties of neutrons and x-rays are compared in Figure 2.15 by plotting their respective scattering amplitudes as a function of atomic weight (mass). Soft x-ray scattering measures the atomic structure through photon-electron interactions. The scattering amplitude is linearly dependent on the atomic weight as shown in the x-ray plots at q=0 and q=0.5 $Å^{-1}$. Neutron scattering originates from nuclear and magnetic interactions. The nuclear scattering amplitude is erratic over all atomic weights. The nuclear amplitude is modelled using a constant nuclear potential. The differences between x-ray and nuclear scattering are apparent when measuring the scattering intensity of pure water. The x-ray scattering intensity mainly originates from the water's oxygen atoms with the scattering amplitude of 20.0 fm. However the nuclear scattering is considerably weaker with an amplitude of not less than 5.0 fm. Note this result neglects the strong incoherent scattering from the hydrogen atoms.

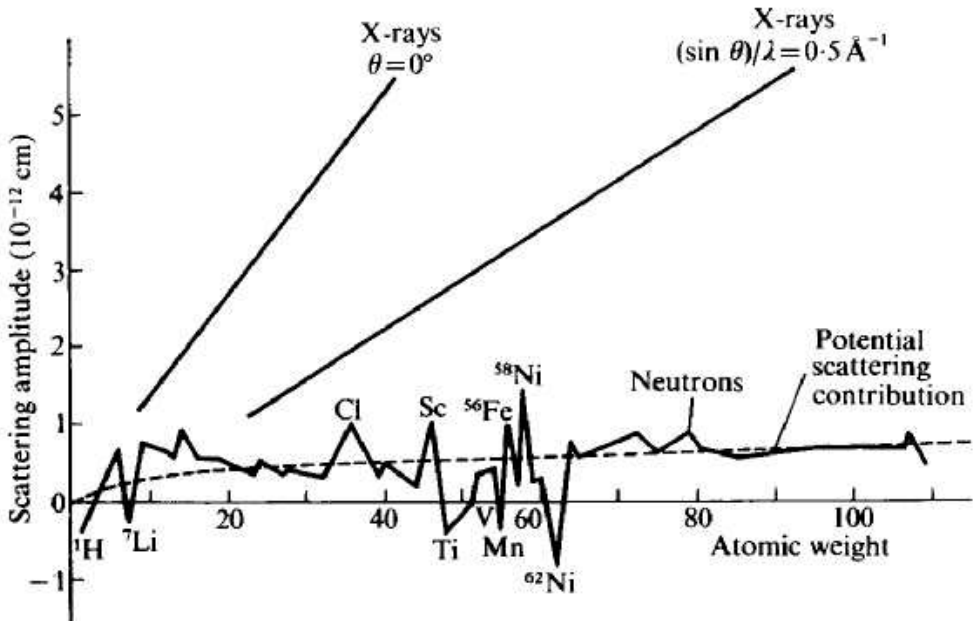

Figure 2.15: The neutron and x-ray scattering amplitudes plotted as a function of atomic weight. The solid linear plots represent the x-ray scattering amplitudes while the dashed line relates to the nuclear scattering component [44].

The neutron is a Fermion with a spin of $m_N=\pm 1/2$. This property gives the neutron an inherent magnetic dipole. An incident beam of neutrons will undergo magnetic scattering when the neutron's dipole couples to the magnetic moment of the atom. The magnetic scattering amplitude is similar in magnitude to the nuclear component. Unlike the nuclear amplitude the magnetic component will vary depending on the atom's magnetic moment density.

2.3.1 Elastic Nuclear Scattering

The spatial properties of a scattering body are determined by measuring the coherent scattering cross-section. The cross-section is derived using the following scattering experiment depicted in Figure 2.16. The neutrons travel along the co-ordinate z-axis represented by the wave function $\psi_{in}=N\exp(ikz)$ where k is the incident wave vector and N is proportional to the number of neutrons in the beam. The wave function has SI units of $m^{-3/2}$. The incident flux is expressed in terms of the current density relation where $j=\mathrm{Re}[\psi^*(\hbar/im)\nabla\psi]$. The incident current takes on the simplified form of $j_{in}=N^2(\hbar k/m)\mathbf{z}=j_0\mathbf{z}$. The neutrons elastically collide with a single target where it is assumed that the target has an infinite mass. This insures that the centre of mass remains stationary during the scattering event. The scattering wave function is given,

$$\psi_{sc}= N\frac{\exp(ikr)}{r} f(\theta,\phi)\,. \tag{2.10}$$

Equation 2.10 represents a spherical wave modulated by the scattering amplitude $f(\theta,\phi)$.

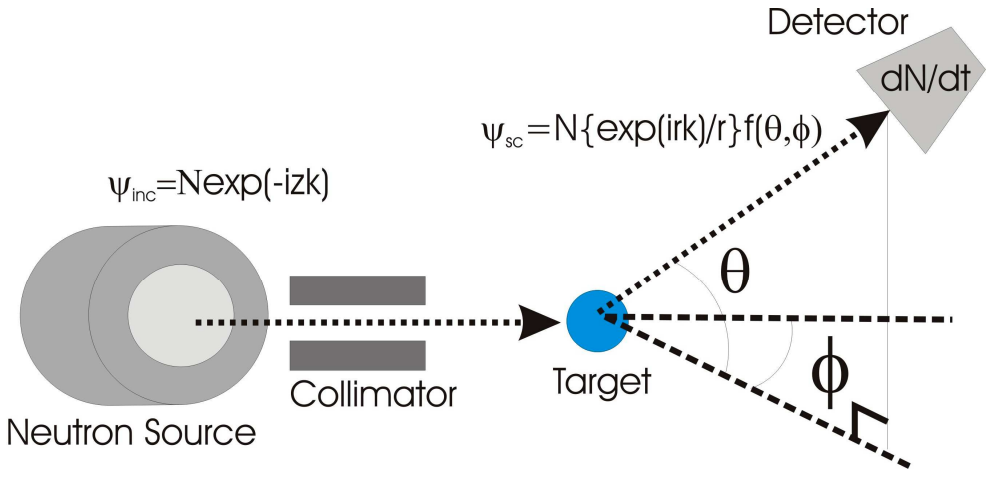

Figure 2.16: The conventional scattering experiment used to derive the nuclear scattering cross-section.

The scattering amplitude characterises the strength of the scattering event where the polar co-ordinates represent the direction of the scattered wave. By using the current density relation the scattering intensity is expressed by,

$$\mathbf{j}_{sc} \approx \frac{N^2 \hbar k}{m} \frac{|f(\theta,\phi)|^2}{r^2} \hat{\mathbf{r}} = j_{in} \frac{|f(\theta,\phi)|^2}{r^2} \hat{\mathbf{r}}. \tag{2.11}$$

The beam is scattered into a solid angle $d\Omega = 1/r^2 dA$ where dA is the projected area of the detector located at (r,θ,ϕ). The number of neutrons per second scattered into the detector is proportional to the solid angle and the incident flux,

$$\frac{dN}{dt} = j_{in} d\mathbf{\Omega} \frac{d\sigma(\theta,\phi)}{d\mathbf{\Omega}} = j_{in} \frac{dA}{r^2} \frac{d\sigma(\theta,\phi)}{d\mathbf{\Omega}}, \tag{2.12}$$

where $d\sigma(\theta,\varphi)/d\Omega$ is the differential cross-section. By dividing out the detector area of equation 2.12 one can equate the cross-section to the square of the scattering amplitude,

$$\frac{d\sigma(\theta,\phi)}{d\Omega} = |f(\theta,\phi)|^2. \tag{2.13}$$

The derivation so far has devised the scattering cross-section using elementary concepts of scattering theory. However there has been no mention on the nature of the scattering force and how it depends on the scattering cross-section.

To obtain a clearer picture of the nuclear scattering system one must utilise a quantum mechanical approach. The scattering problem can be viewed in terms of probability transitions. The incident unpolarised wave vector $|\mathbf{k}>$ undergoes a transition to another (unpolarised scattering) state $|\mathbf{k}'>$ via the nuclear potential operator $\mathbf{U}_{Nuc}(\mathbf{r})$. The transition probability is expressed by Fermi's Golden rule,

$$P_{k\to k'} = \frac{2\pi}{\hbar} \rho_{k'}(E) \left| \langle \mathbf{k}' | \mathbf{U}_{Nuc}(\mathbf{r}) | \mathbf{k} \rangle \right|^2, \tag{2.14}$$

where $\rho_{k'}(E)$ is the energy density of the final scattering state [42]. Fermi's Golden rule is based on first order perturbation theory, which requires a weak interacting potential. The bracketed term is expanded $<\mathbf{k}'|\mathbf{U}_{Nuc}(\mathbf{r})|\mathbf{k}> = \int \psi_{k'} \mathbf{U}_{Nuc}(r) \psi_k d\mathbf{r}$ where $(\psi_{k'}, \psi_k)$ represent the scattering and incident wavefunctions respectively. The scattering cross-section is determined by taking the ratio of the transition probability to the incident flux,

$$\frac{d\sigma_N}{d\Omega} = \left(\frac{m}{2\pi\hbar^2} \right)^2 \left| \langle \mathbf{k}' | \mathbf{U}_{Nuc}(\mathbf{r}) | \mathbf{k} \rangle \right|^2. \tag{2.15}$$

The nuclear operator contains the physics of the neutron-nuclear interaction. The nuclear force has interaction length of just few femtometers.

The strong nature of the nuclear force apparently violates the Fermi Golden rule where the interaction potential must be weak in nature. The apparent theoretical flaw is countered by the following argument. The nuclear length scale is much smaller than the wavelength of thermal neutrons. This fact allows one to approximate the neutron-nucleus interaction by isotropic scattering. Isotropic scattering is achieved by using the Fermi pseudo-potential $\mathbf{U}_{Nuc}=(2\pi\hbar^2/m)\delta(\mathbf{r})b_{nuc}$ where b_{nuc} is the nuclear scattering length. The nuclear scattering cross-section simplifies to the following $d\sigma_N/d\Omega=b_{nuc}^2$. Since the nuclear potential is a delta function the nuclear scattering cross-section remains a constant for all reciprocal space.

2.3.2 Elastic Magnetic Scattering

The elastic neutron scattering from a magnetic material is composed of nuclear and magnetic scattering components. The elastic magnetic scattering occurs when the neutron's magnetic moment interacts with the magnetic field of a paramagnetic or ferromagnetic atom. The magnetic interaction potential is expressed by the vector dot product of the neutron moment and the atom's total internal magnetic field **B**,

$$U_M = -\boldsymbol{\mu}_N \cdot \mathbf{B} = \gamma_N \mu_N \boldsymbol{\sigma}_{spin} \cdot \mathbf{B}, \tag{2.16}$$

where $\boldsymbol{\mu}_N=-\gamma_N\mu_N\boldsymbol{\sigma}_{spin}$ defines the neutron's magnetic moment. The constant $\gamma_N=1.91$ takes on the role of the spin g-factor. The nuclear magneton is $\mu_N=e\hbar/2m_p$ where m_p is the proton mass. The neutron's spin components are defined by the Pauli spin matrix $\boldsymbol{\sigma}_{spin}$. The total B-field, $\mathbf{B}=\mathbf{B}_L+\mathbf{B}_S$ originates from the atom's orbital and spin moments. Unlike the nuclear force the spin and orbital interactions are not central forces. This makes the task of deriving the scattering cross-section nontrivial. The derivation can be found in most texts on neutron scattering. By solving the matrix element of equation 2.16, the magnetic scattering from the ith electron takes the form,

$$\langle \mathbf{k}' \mid U_M \mid \mathbf{k} \rangle = \gamma r_0 \boldsymbol{\sigma}_{spin} \cdot \left[\hat{\mathbf{q}} \times (\mathbf{s}_i \times \hat{\mathbf{q}}) + \frac{i}{\hbar |\mathbf{q}|} (\mathbf{p}_i \times \hat{\mathbf{q}}) \right] \exp(i\mathbf{q} \cdot \mathbf{r}_i), \tag{2.17}$$

where $\mathbf{q}=\mathbf{k}-\mathbf{k}'$ is known as the momentum transfer argument [42]. The first term describes the spin interaction B-field where $\mathbf{s}_i$ is the spin vector. The following term expresses the orbital interaction B-field where $\mathbf{p}_i$ is the linear momentum vector of ith electron. The matrix elements of equation 2.17 are simplified by expressing the spin and orbital magnetic fields in terms of their respective magnetisation fields.

The spin magnetisation is expressed by $\mathbf{M}_s(\mathbf{r})=-2\mu_B\rho_s(\mathbf{r})$ where $\rho_s(\mathbf{r})=\Sigma_i\delta(\mathbf{r}-\mathbf{r}_i)\mathbf{s}_i$ defines the spin density. By inserting the Fourier transform of $\mathbf{M}_s(\mathbf{r})$ into equation 2.17 one can express the spin interaction field in terms of its reciprocal space magnetisation,

$$\mathbf{B}^{\perp}{}_S(\mathbf{q})=\frac{1}{\mu_B}\mathbf{M}^{\perp}{}_S(\mathbf{q})=\frac{1}{\mu_B}\hat{\mathbf{q}}\times(\mathbf{M}_S(\mathbf{q})\times\hat{\mathbf{q}}). \tag{2.18}$$

The orbital interaction field simplifies to the same form expressed in equation 2.18 where $\mathbf{M}^{\perp}{}_L(\mathbf{q})=\hat{\mathbf{q}}\times(\mathbf{M}_L(\mathbf{q})\times\hat{\mathbf{q}})$. Therefore the total interaction B-field is expressed by $\mathbf{B}^{\perp}(q)=\mu^{-1}{}_B(\mathbf{M}^{\perp}{}_S+\mathbf{M}^{\perp}{}_L)$. By taking the square of equation 2.17, the magnetic scattering cross-section can be expressed as

$$\frac{d\sigma_M}{d\Omega}=\left(\frac{\gamma r_0}{2\mu_B}\right)^2\left|\mathbf{M}^{\perp}(\mathbf{q})\right|^2, \tag{2.19}$$

where $\mathbf{M}^{\perp}(\mathbf{q})=\hat{\mathbf{q}}\times(\mathbf{M}(\mathbf{q})\times\hat{\mathbf{q}})$ defines the total interaction M-field. The geometric relationship between the vectors $\mathbf{M_q}$, $\mathbf{M}_{q\perp}$ and $\hat{\mathbf{q}}$ is shown in Figure 2.17. By definition $\mathbf{M}^{\perp}(\mathbf{q})=\mathbf{M}(\mathbf{q})-(\mathbf{M}(\mathbf{q})\cdot\hat{\mathbf{q}})\hat{\mathbf{q}}$ where the square of this relation is,

$$|\mathbf{M}^{\perp}(\mathbf{q})|^2=|\mathbf{M}(\mathbf{q})|^2(1-(\hat{\mathbf{m}}\cdot\hat{\mathbf{q}})^2) \tag{2.20}$$

where the unit vector $\hat{\mathbf{m}}$ expresses the direction of the magnetisation. The function $\mathbf{M}(\mathbf{q})$ is known as the magnetic form factor, which describes the atom's moment density. The second term of equation 2.20 is known as the moment orientation factor. When the direction of magnetisation lies parallel with the scattering vector, the magnetic scattering intensity will drop to zero.

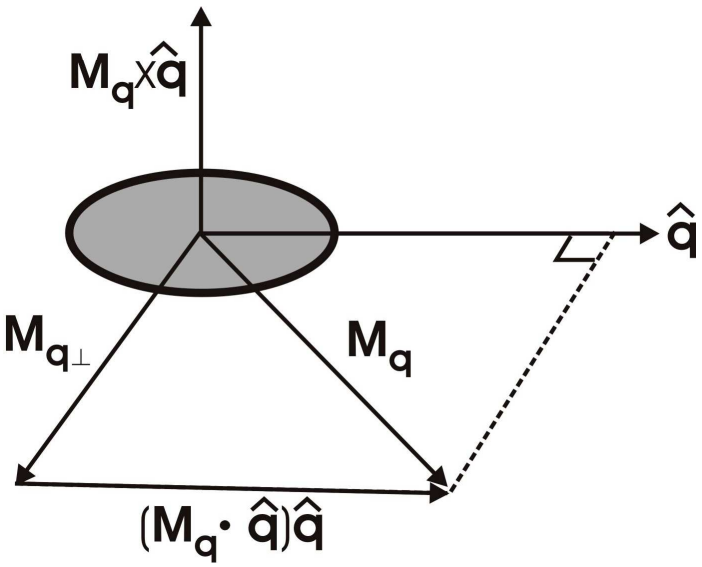

Figure 2.17: Vector plot of the interaction magnetisation field $\mathbf{M}^{\perp}(\mathbf{q})=\hat{\mathbf{q}}\times(\mathbf{M}(\mathbf{q})\times\hat{\mathbf{q}})$.

2.4 Polarised Neutron Scattering

The preceding derivation of the nuclear and magnetic scattering cross-section assumed that the neutron spin of the incident beam is unpolarised. When the incident beam is unpolarised there is an equal probability of measuring the neutron in the spin up $|s=+>$ or spin down $|s=->$ state. The complete treatment of polarised neutron scattering requires one to account for the incident and outgoing spin states within the spin matrix element. This matrix element takes the form $U_{ss'} = <s'|\mathbf{U}_{int}|s>$ where the neutron spin state undergoes a transition from s' to s [45]. The nuclear and magnetic interactions are expressed by the potential operator $\mathbf{U}_{int}=b_{nuc}-\boldsymbol{\sigma}_{spin}\bullet\mu_B^{-1}\mathbf{M}$. The operator neglects any nuclear spin interactions conventionally defined by the quantum number I. The four possible spin transitions for polarised neutron scattering are (1) $|+>\rightarrow|+>$, (2) $|->\rightarrow|->$, (3) $|->\rightarrow|+>$, (4) $|+>\rightarrow|->$. The spin equations (1) and (2) show that the incident neutron spin remains unchanged after the scattering event. The equation set (3) and (4) expresses the scattered neutron's spin flip transition. Table 2.1 lists the allowed spin transitions and their respective matrix elements.

Spin Transition	***Wave Function***	***Matrix Element***
Up-Up	$\|+>\rightarrow\|+>$	$U_{++}= b_{nuc} - \mu_B^{-1}M_{j,z}$
Down-Down	$\|->\rightarrow\|->$	$U_{--} = b_{nuc} + \mu_B^{-1}M_{j,z}$
Spin Flip Down -Up	$\|->\rightarrow\|+>$	$U_{-+} = -\mu_B^{-1}(M_{j,x}+i M_{j,y})$
Spin Flip Up-Down	$\|+>\rightarrow\|->$	$U_{+-} = -\mu_B^{-1}(M_{j,x}-i M_{j,y})$

Table 2.1: The neutron spin transitions and their respective matrix elements $U_{ss'}$ [45].

2.4.1 Nuclear-Magnetic Interference Scattering

The total spin polarised scattering cross-section is defined as a superposition of the non-spin flip (NSF) and spin flip (SF) scattering components expressed by the formula $d\sigma/d\Omega=d\sigma_{SF}/d\Omega+d\sigma_{NSF}/d\Omega$. The non-spin flip and spin flip scattering cross-sections are derived by inserting the spin matrix elements of table 2.1 into equation 2.15,

$$\frac{d\sigma_{NSF}^{\pm\pm}}{d\Omega}=\frac{1}{V}\sum_{jl}\exp(i\mathbf{q}\bullet(\mathbf{x}_j-\mathbf{x}_l))(b_{nuc,j}\mp M_{j,z})(b_{nuc,l}\mp M_{l,z}), \tag{2.21}$$

$$\frac{d\sigma_{SF}^{\pm\mp}}{d\Omega}=\frac{1}{V}\sum_{jl}\exp(i\mathbf{q}\bullet(\mathbf{x}_j-\mathbf{x}_l))\left(M_{j,x}M_{l,x}+M_{l,y}M_{j,y}\right). \tag{2.22}$$

The non-spin flip cross-section is a superposition of magnetic and nuclear scattering components. The magnetic scattering is related to an ensemble of magnetisation components (M_{jz}) aligned along a single co-ordinate axis. Due to the matrix product, there is also an interference term between the nuclear b_{nuc} and magnetic scattering M_j amplitudes. The spin flip equation expresses the magnetic scattering intensity from spin misaligned systems where $M_x=M_y\neq0$. In this thesis we consider only the non-spin flip cross-section which applies to spin aligned systems. For polarised SANS studies the non-spin flip scattering cross-section is simplified by assuming that the nuclear and magnetic scattering lengths are identical at each site. The no-spin flip cross-section is recast in the continuous form,

$$\frac{d\sigma^{\pm\pm}}{d\Omega}=\frac{1}{V}(F^2{}_N(q)\mp 2F_N(q)F_M(q)\sin^2\alpha+F^2{}_M(q)\sin^2\alpha). \tag{2.23}$$

The functions $F_N(q)=\langle k|b_{nuc}|k'\rangle$ and $F_M(q)=\langle k|M|k'\rangle$ define the nuclear and magnetic form factors for the bulk sample [46]. The product $F_N(q)F_M(q)$ represents the nuclear-magnetic interference term. The $\sin^2\alpha$ term relates to the moment orientation factor where α defines the angle between the magnetisation-**m** and scattering-**q** unit vectors.

2.5 Amorphous Scattering

The scattering cross-section derived in the previous section considered the nuclear and magnetic scattering from a single ferromagnetic atom. The scattering matrix element is solved in terms of the single body problem. When an ensemble of N atoms or particles is placed within a box of volume V at temperature T, the atom's electrostatic forces will determine the nature of the condensed state such as a gas, liquid or solid. For example a strong attractive potential results in a pseudo-crystalline solid with long range order while a weaker potential gives an amorphous solid with short range order. Traditionally the scattering problem for the condensed state is determined by considering the spatial symmetry of the lattice.

The crystalline solid has a high degree of spatial symmetry where the lattice structure is modelled using a cubic or hexagonal arrangement. By inserting the lattice parameters into Bragg's Law one can solve for the scattering cross-section. At the opposite end of the symmetry spectrum, the gaseous phase is approximated using the ideal gas model. The gaseous scattering function is modelled using single bodied matrix element where interference effects are neglected. For the liquid state there is no apparent spatial symmetry. This fact leads one to assume that the scattering model resembles the gaseous approximation. Unfortunately this is not observed in liquid scattering experiments where there exists strong spatial correlations between atomic pairs. In one particular case the liquid scattering problem is modelled using a system of hard spheres in thermal equilibrium. The total correlation function h(r) describes the degree of ordering between particle pairs. The scattering interference function known as the structure factor $S(\mathbf{q})$ is proportional to the Fourier transform of the pair distribution function.

The scattering characteristics of the solid, liquid and gas phase are shown in Figure 2.18. For the crystalline material the diffraction pattern contains information on lattice spacing and orientation of lattice plane. The peak sharpness measures the degree of lattice ordering at a particular reflection. Perfect lattice ordering is represented by a series of delta functions. The amorphous scattering pattern gives details on pair correlations between spherical particles. The peak sharpness and/or intensity are a measure of how well the atoms are packed within the ensemble. The gas or dilute liquid has a vanishing small packing fraction therefore shows no interference scattering.

The scattering problem for an amorphous material is complicated due to the ambiguous nature of the lattice structure and interaction potential. For the amorphous material the ensemble of particles form into a semi-ordered solid which exhibits the spatial characteristics of both crystalline and liquid matter. For example the amorphous structure will exhibit pair correlations indicative of the crystalline state shown in Figure 2.18. However the ensemble of particles are not arranged onto a regular lattice which results in suppression of any long-range order. The amorphous material also exhibits short-range correlations characteristic of the liquid state. This is shown by the broad interference peaks from liquid type scattering. In the following section the amorphous scattering potential is modelled as some intermediate state between a crystalline-solid and the liquid state.

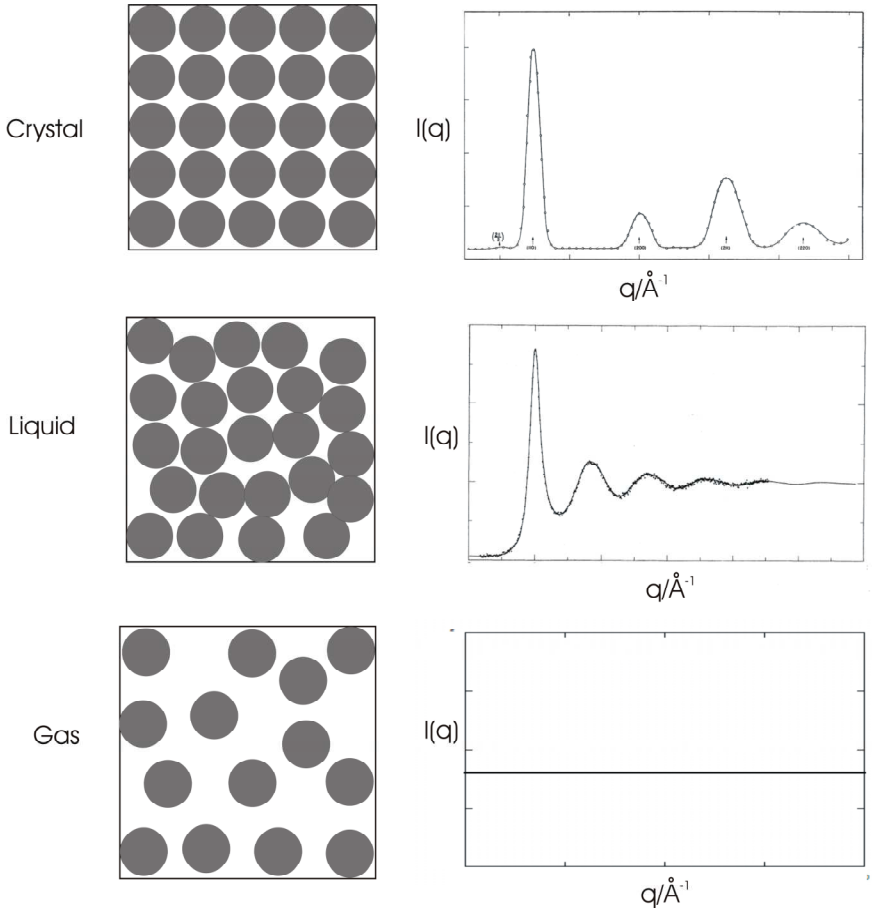

Figure 2.18: Spatial representations of the crystal, liquid and gas phase. For each phase state the elastic scattering intensity is plotted in reciprocal space [44,48].

2.5.1 Multi-Bodied Scattering

The scattering system in real space is defined by a superposition of the neutron interaction potential, $U_i(\mathbf{x}-\mathbf{x}_i)$, where $\mathbf{x}_i$ defines the vector position of the ith scattering object [49]. Figure 2.19 shows the scattering system partitioned into a closed packed system of polydisperse scattering objects. The interaction potential of each object is defined by the top-hat function. The nature of the force interaction depends on the type of neutron scattering. If for example the scattering originates from a sample's magnetic domains then the interaction potential would be proportional to the compounds magnetic scattering length. A similar situation would apply for the nuclear interaction potential. The total potential for an ensemble of scattering objects is the sum of individual potential terms of the system. The sum is expressed by $U(\mathbf{x})=\sum U_i(\mathbf{x}-\mathbf{x}_i)$ where $\mathbf{X}_i=\mathbf{x}-\mathbf{x}_i$ defines the displacement vector of the scattering system. The multi-bodied matrix element takes the form,

$$\langle \mathbf{k}' \mid \mathbf{U} \mid \mathbf{k} \rangle = \sum_i \mathbf{U}_i(\mathbf{q}) \exp(-\mathbf{q} \cdot \mathbf{x}_i) \tag{2.24}$$

where $U_i(\mathbf{q})=\int \exp(-\mathbf{q}\bullet\mathbf{X}_i)U_i(\mathbf{X}_i)d^3\mathbf{X}_i$ is the Fourier transform of the ith interaction potential.

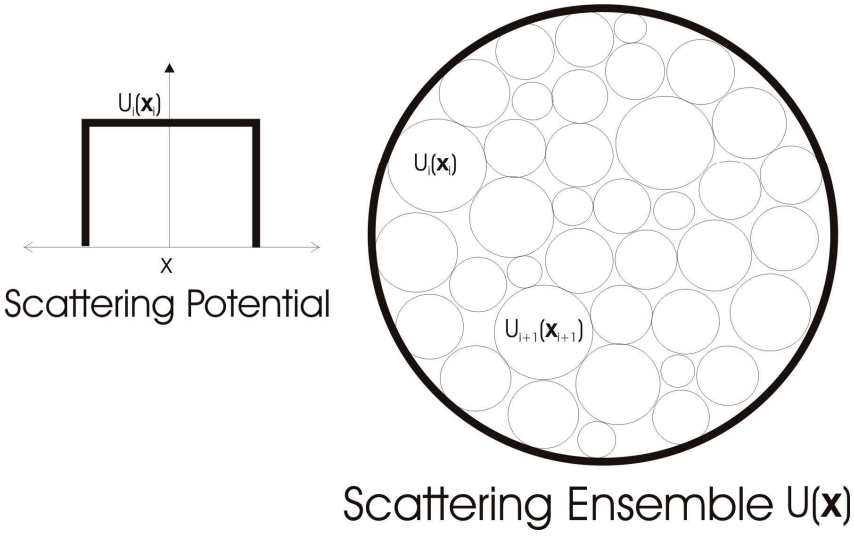

Figure 2.19: Model for an ensemble of polydisperse scattering potentials $U(\mathbf{x}_i)$.

The potential transform $U_i(\mathbf{q})$ is a function of the momentum transfer argument where $|\mathbf{q}|=|\mathbf{k}'-\mathbf{k}|=4\pi/\lambda\sin(\theta)$ [50]. The spatial dependence in reciprocal space is expressed by the transform, $U_i(\mathbf{q})=AF(\mathbf{q},\mathbf{r}_i)$ where $F(\mathbf{q},r_i)$ is the form factor for the ith scattering object and A is the normalisation constant [51]. The form factor describes the shape and size of the scattering object in reciprocal space. Due to their simple mathematical formulation, the spherical and cylindrical form factors are widely used to model the scattering objects. Figure 2.20 shows the spherical and cylindrical objects and their respective form factor intensities. The cylindrical form factor, was calculated for an orientation of $\delta=45^0$. The form factors were compared to the Porod scattering function $I(q)=Aq^{-4}$ [28], which describes scattering from a nearly homogenous medium. In general, the form factor is defined as the Fourier transform of the spherical and cylindrical top-hat functions, see derivations in sections 8.1.1 and 8.1.2 respectively.

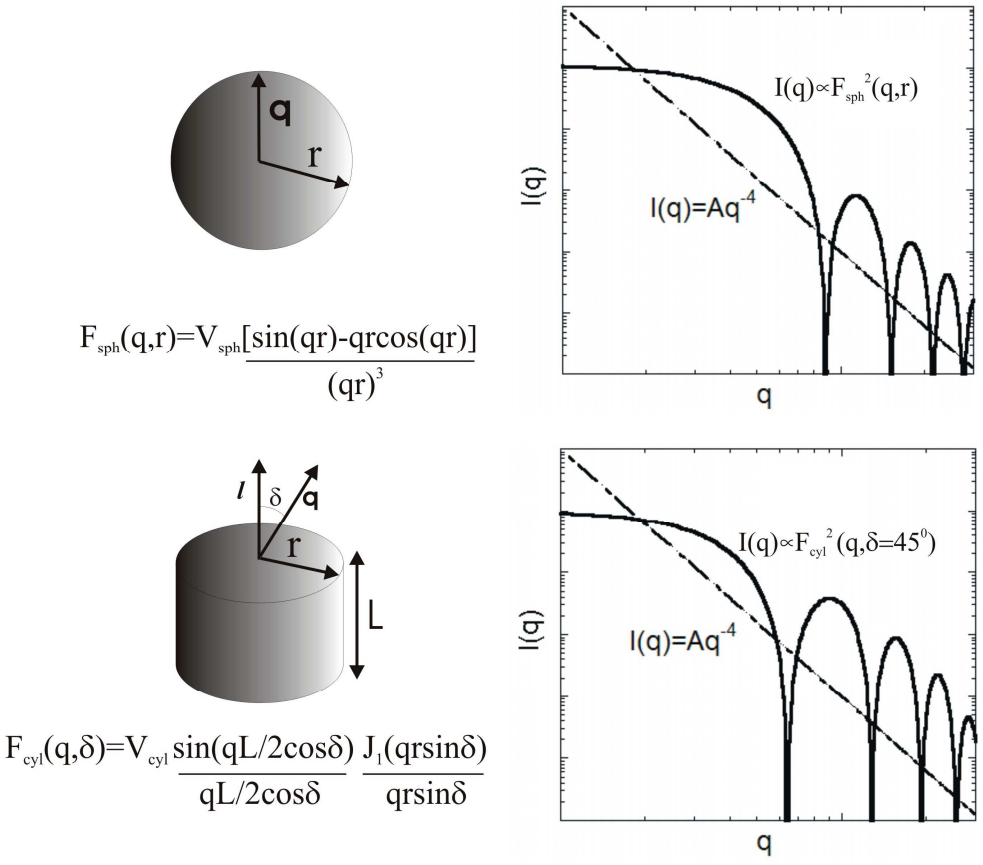

Figure 2.20: The form factors intensity plotted for the spherical and cylindrical object. The form factor intensities are compared with the Porod scattering function Aq^{-4}.

The scattering cross-section is determined by averaging the square of the matrix element over the size-distribution function g(r) [52]. The term monodisperse refers to a system of particles with a size distribution width of σ=0. The polydisperse system has a finite size distribution width. The differential scattering cross-section takes the form,

$$\frac{d\sigma}{d\Omega} = \left\langle \sum_{i \neq j} F(\mathbf{q}, \mathbf{r}_i) F(\mathbf{q}, \mathbf{r}_j) \exp(-i\mathbf{q} \cdot (\mathbf{x}_i - \mathbf{x}_j)) \right\rangle . \tag{2.25}$$

The angled bracket represents an average over the size distribution function [51]. The scattering cross-section is expanded in terms of its i=j and i≠j components,

$$\frac{d\sigma}{d\Omega} = n\{\left\langle F^2(\mathbf{q}, r_i)\right\rangle - \left\langle F(\mathbf{q}, r_i)\right\rangle^2\} + nS(\mathbf{q})\left\langle F(\mathbf{q}, r_i)\right\rangle^2 \tag{2.26}$$

where $\langle F^2\rangle = \int F^2 g(r) dr$, $\langle F\rangle = \int F g(r) dr$ and n=N/V. The difference term of equation 2.26 represents the incoherent scattering brought about by the polydisperse ensemble. The second term describes interference scattering from an ensemble. The scattering function $S(\mathbf{q}) = 1 + \langle \sum \exp[-i\mathbf{q} \bullet (\mathbf{x}_i - \mathbf{x}_j)] \rangle$ is known as the structure factor [49]. This function is derived either using simulation or analytic methods. Numerical methods such as Monte-Carlo simulations are widely used to determine an approximation to the pair distribution function and hence structure factor [54,55].

The analytic method involves solving the pair distribution for a specified geometric shape and interaction potential. The exact form of S(q) is derived using the Percus-Yevick integral method, see Appendix section 8.2. The monodisperse structure factor depends on the packing density ρ and pair separation d. The spherical packing faction is defined by $pf = \pi/6 \rho d^3$. Figure 2.21 plots the monodisperse Percus-Yevick structure factor for a series of packing fractions. The first order peak defines the interference scattering from an ensemble of particle pairs. The successive oscillations represent interference from smaller pair separations. For large packing fractions, the system approaches a pseudo-crystalline phase where perfect packing occurs at pf=0.74. Further decreases in the packing fraction results in the damping of peak intensities. In Figure 2.22, the S(q) function is solved for a polydisperse system of hard spheres [62]. The packing fraction $\langle pf \rangle = \pi/6 \rho \langle d^3 \rangle$ is averaged using the gamma-Shultz distribution function. At the size distribution of 40%, the oscillations damp out to unity leaving the primary peak. The finite size distribution reduces the packing efficiency of the system by increasing the number of possible pair separations. For large size distributions, there is a random number of pair separations resulting in the total damping of S(q).

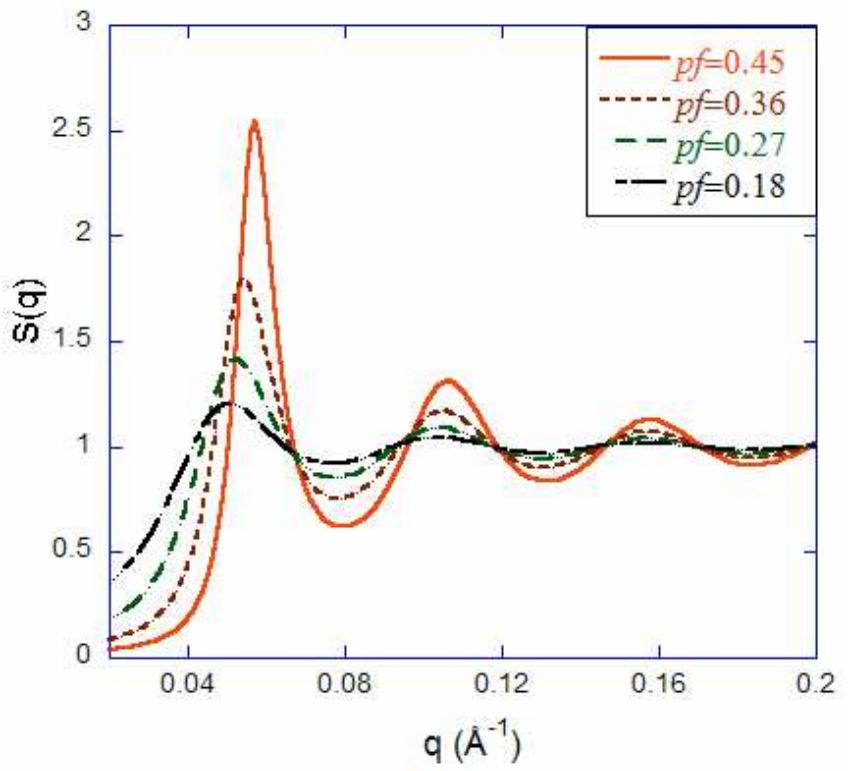

Figure 2.21: Monodisperse liquid structure factor S(q) calculated using the Percus-Yevick integral method. The structure factor is investigated by varying the packing fraction *pf*. The S(q) exhibits crystal like scattering for large *pf* value. Scattering from secondary peaks becomes weak for *pf* <0.27 [61].

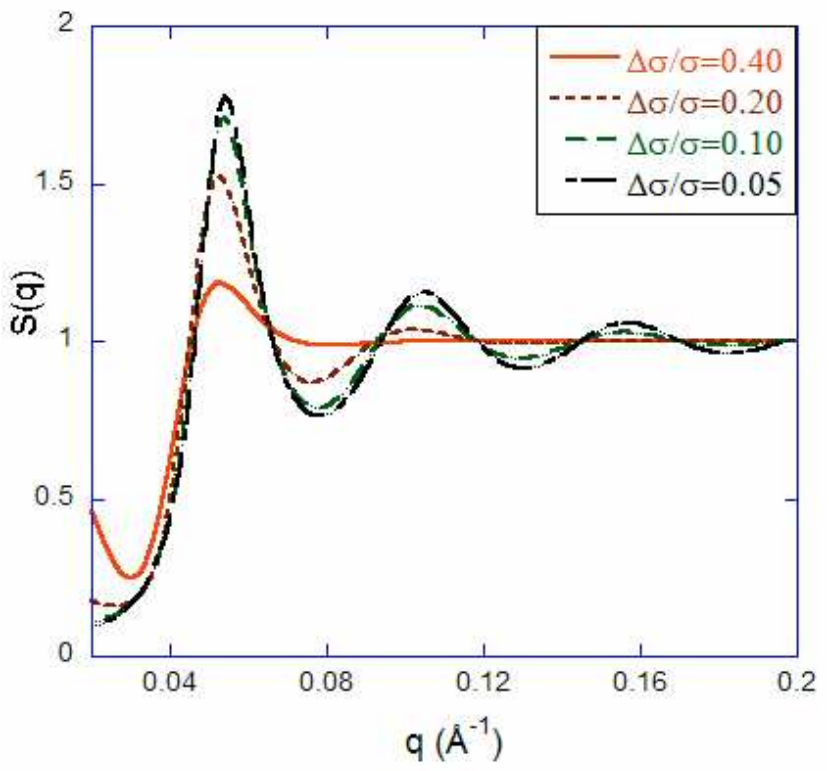

Figure 2.22: Polydisperse liquid structure factor S(q) calculated using the Percus-Yevick integral method. The S(q) distribution of hard spheres is investigated for a *pf*=0.36. At a large size distribution, the pair correlations reduce to unity [62].

Chapter 3

Experimental Techniques And Instrumentation

3.1 Small Angle Neutron Scattering

The characterisation technique of elastic neutron scattering is widely used to measure the sample's spatial structure ranging from atomic to the macroscopic length scale. The sample's lattice spacing d is related to the neutron wavelength λ by Bragg's Law $d=(\lambda/2)(\sin\theta)^{-1}$ where 2θ is the neutron scattering angle. The technique of single crystal or powder diffractometry is used to measure lattice plane separation and the phase-state for typical crystalline structures of the order of 1.0-10.0 Å [34]. According to Bragg's Law the scattering angle ranges from $70\text{-}90^0$ with a wavelength of a few angströms. The diffraction technique of small angle neutron scattering (SANS) is used to measure large-scale structures of the order of 10-200 Å. Large-scale structures are investigated using small scattering angles when compared to single crystal measurements. For example to measure the periodic length scale of 100 Å with a neutron wavelength of 4.0 Å requires a scattering angle of about 1.0^0. Figure 3.1 lists the various forms of matter as function of length scale. In this thesis, SANS studies were performed on magnetic recording media where the physical grain size is of the order of 100.0 Å.

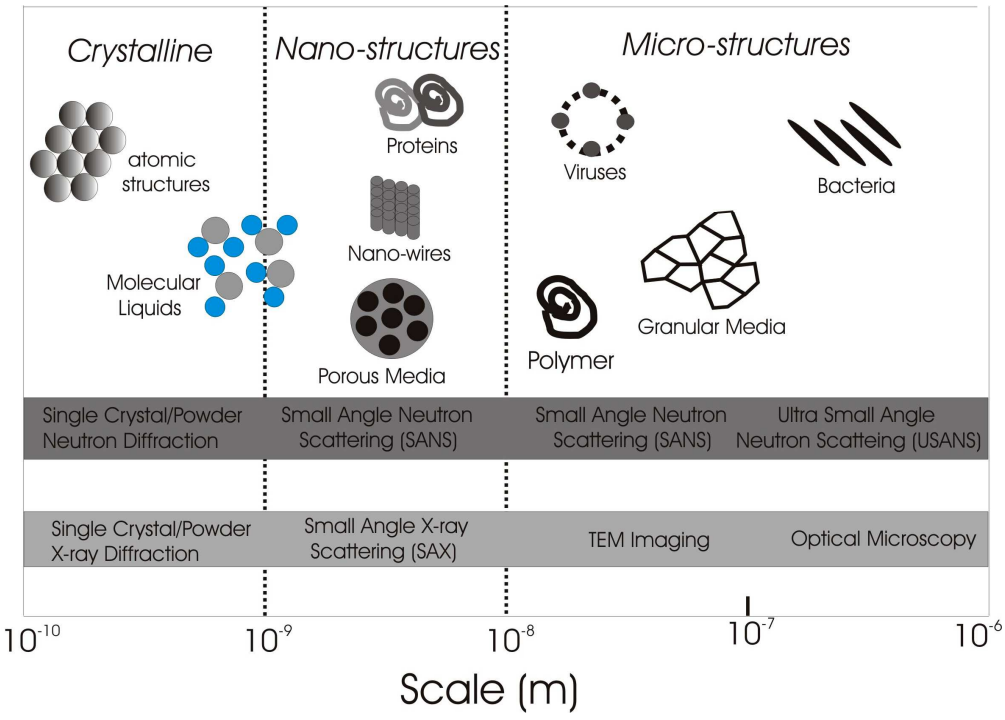

Figure 3.1: The scale diagram lists various condensed matter states alongside their respective characterisation technique.

The SANS measurements were carried out using the D11 and D22 SANS instruments located at the ILL, Grenoble France [63,64]. These instruments utilise a nuclear reactor to generate a collimated neutron beam. The reactor source provides a large neutron flux that greatly improves the scattering statistics for experiments on magnetic recording media. Another set of measurements was performed on the SANS1 instrument at PSI, Villigen, Switzerland [65]. This instrument uses a pulsed source to generate the neutron beam [66]. The incident neutron flux when compared to the D11 instrument was substantially smaller. However this downside was offset by the ability of SANS1 to measure magnetic structures using polarised neutrons. Unlike the unpolarised mode, the polarised neutron beam can give reasonable good scattering statistics for short scan times. In addition, the polarised mode has the ability to extract the sample's physical and magnetic structure through the interference of magnetic and nuclear scattering components. In the following sections the various components of the SANS instrument are briefly reviewed.

3.1.1 SANS Instrumentation

The conventional SANS instrument is set-up to measure the forward scattering from a target sample, see Figure 3.2. The neutron source is generated either by using a nuclear fission (nuclear reactor) or through proton collisions (pulsed source). Highly energetic neutrons of the order of 10-100 MeV are delivered from the reaction chamber to the SANS instrument via the exit guide tube [66]. The neutrons propagate down the guide tube through the process of specular reflection. This phenomenon is used to transport the reactor neutrons large distances without any intensity loss. At the guide's exit point, the beam of neutrons is too energetic for SANS measurements. In order to reduce the average beam energy, the guide tube is fashioned with a slight curvature along its length. This feature allows the guide tube to absorb any high-energy neutrons that fail to fulfil the total reflection condition at the guide surface. Figure 3.3 shows a cross-section of the reactor guide tube. Another method to reduce the neutron's energy is to position the guide tube with a vertical gradient. As the neutrons propagate through this section, the force of gravity will further reduce the beam's average kinetic energy.

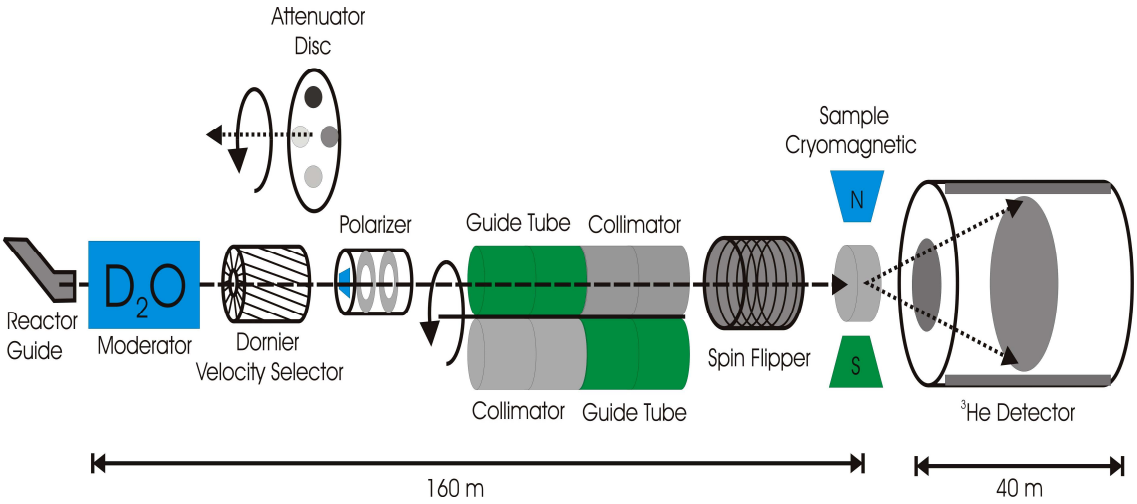

Figure 3.2: The schematic of the conventional SANS instrument. The device is set-up to measure nuclear and magnetic structures for the energy scale of 10^{-2} eV.

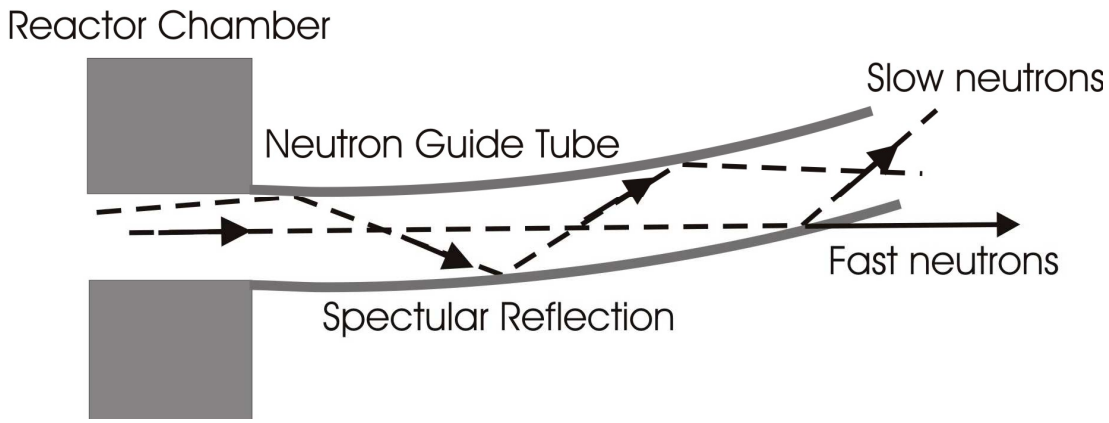

Figure 3.3: The reactor guide tube that transports the neutrons to the moderator [38].

The average kinetic energy of the exit neutrons is approximately 2.0 MeV [67]. This energy regime is still too large for condensed matter research, which requires neutron energies of the order of 10^{-2} eV. The exit neutron's kinetic energy is reduced using a process known as neutron moderation. The process is achieved by immersing the hot neutrons in a medium of light atoms such as liquid hydrogen (H) or deuterium (D_2O). Through a series of inelastic collisions via the medium, the neutrons are brought into thermal equilibrium with the moderator. At thermal equilibrium the neutrons have an average kinetic energy of 3/2kT where T is the moderator temperature. The neutron energy distribution in thermal equilibrium is expressed by the Maxwell-Boltzmann distribution, $p(E) \propto E^{3/2} \exp(-E_k/kT)$ where $E_k = 1/2mv^2$ is the neutron's kinetic energy. In Figure 3.4 the thermal distributions are plotted for the temperature range of 10-1000 K. For the light water moderator with a temperature of 300-350 K, the energy spectrum falls within the range 0.005-0.20 eV [66]. This energy regime gives the neutron beam an adequate wavelength to investigate most condensed matter structures.

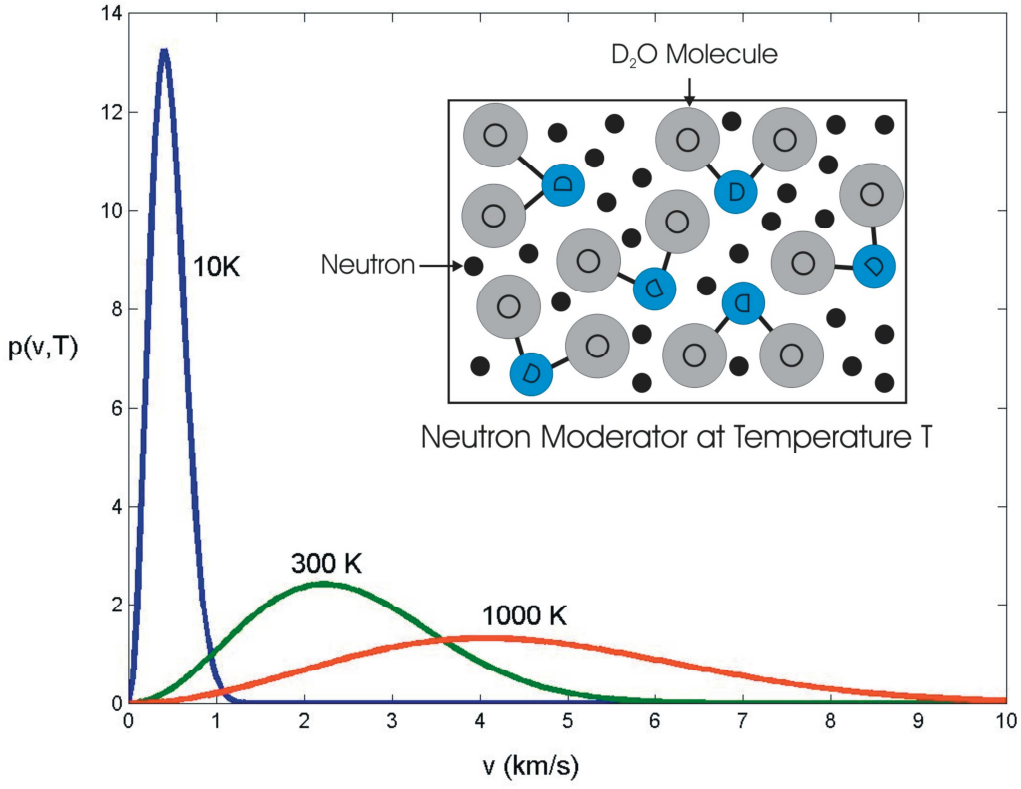

Figure 3.4: The Maxwell-Boltzmann distribution for thermal neutron velocities. The figure inset shows the thermalisation of neutrons within the D_2O moderator.

The SANS experiment requires a monochromatic wavelength with a narrow wavelength spread of about 9-10%. This is achieved by collimating the neutron beam into a mechanical monochromator known as the Dornier velocity selector [68]. The monochromator is positioned between the exit guide tube and the SANS polariser as shown in Figure 3.2. The selector uses the time of flight method to monochromatise the neutron beam. An array of slits encompasses the surface area of a rotating cylindrical drum. These slits are commonly made out of aluminium alloy covered in a 1-2 mm sheet of highly absorbing Cd metal. Each slit follows a helical trajectory along the length of the cylinder. Due to these skewed slits, a stationary velocity selector will prevent the neutron beam from travelling the entire length of the drum thereby chopping off the beam, see Figure 3.5(a). When the velocity selector is rotating, any neutrons that exit the selector must traverse the slits in time $\Delta t=t_2-t_0$, see Figure 3.5(b). The neutron velocity depends on the drum's rotation frequency and slit dimensions. The neutron's average wavelength is calculated by using the DeBroglie relation $\lambda=\hbar/(m_n v'_{ave})$.

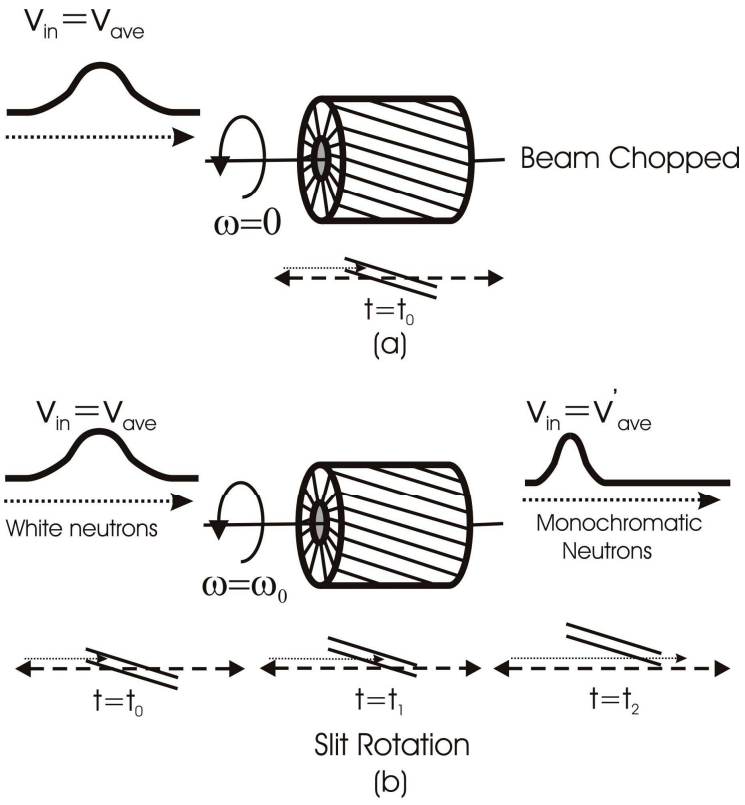

Figure 3.5: The schematic of the Dornier velocity selector. In setup (a) the incident neutron beam, with an average velocity $V_{in}=V_{ave}$ is chopped by the stationary velocity selector. In setup (b) the incident neutrons pass through the rotating selector with velocity $V_{out}=V'_{ave}$.

The monochromatic neutrons that exit the velocity selector pass through the beam attenuator, see Figure 3.2. This disc shaped device is mounted with a series of cadmium plates of varying thickness. By rotating a different attenuator into the path of the neutron beam one can control the intensity of the incident beam. The attenuator is used to protect the detector's cathode-anode vessels from direct beam measurements such as sample alignment and transmission. If for example there is no beam stop or attenuator then the incident neutron beam will burn out the detector's cathode wires.

The incident neutron beam exists in an unpolarised spin state where the spin wave function expresses an equal probability of the spin up |+> and spin down |-> state. The neutron beam is polarised using a magnetic multi-layer which screens out the + or – spin state. The multi-layer is constructed from a series of ferromagnetic/non-magnetic thin films for example Fe/Si [66]. As the neutron beam penetrates the multi-layer, the ferromagnetic layer causes the total reflection of one spin state and the transmission of its opposite state. In Figure 3.6 the neutron beam's |-> states are transmitted through the mirror while the |+> states are totally reflected. Note the polarised spin states are susceptible to depolarisation fields such as the earth's magnetic field. Shielding the guide with magnetised iron plates preserves the neutron polarisation. The plates are magnetised by a permanent magnetic of field strength 10-20 Oe.

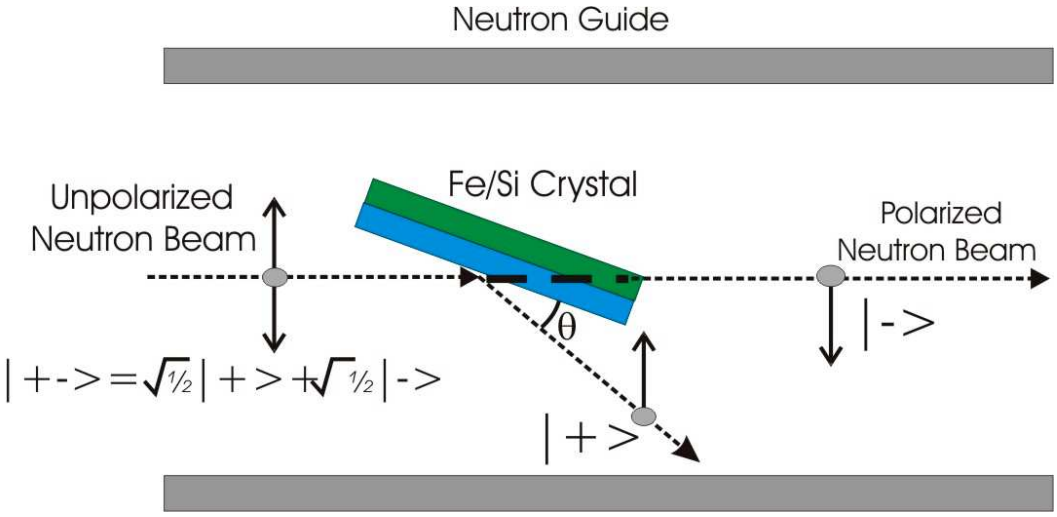

Figure 3.6: The polarisation of the incident neutron beam through total reflection from the Fe/Si multi-layer.

The polarised neutron beam is focused on the target by a series of guide tubes and collimators [63,64]. Initially the neutrons are propagating through an incident guide tube G_0. At this position the neutrons encounter the collimator tube. This point defines the source of the neutron beam. By using a combination of slits and guide tubes, the beam spot is focused on the target. Figure 3.7 shows the cross-section of the collimator instrument. The guide G_i and collimator C_i tubes are sectioned into a series of rotating units. The collimation distance is varied by rotating the guide or collimator in or out of the path of the neutron beam.

The polarised neutron beam is flipped |-> → |+> by applying magnetic torque to spin state. The applied magnetic field is generated by an electromagnet known as the spin flipper, which is placed before the sample stage. The sample is mounted on the target plate. For magnetic SANS measurements, the sample is immersed in an applied magnetic field. The electromagnet is used to saturate the sample for fields of the order of a Tesla. The cryomagnet is used for fields of the order of 2-11 T.

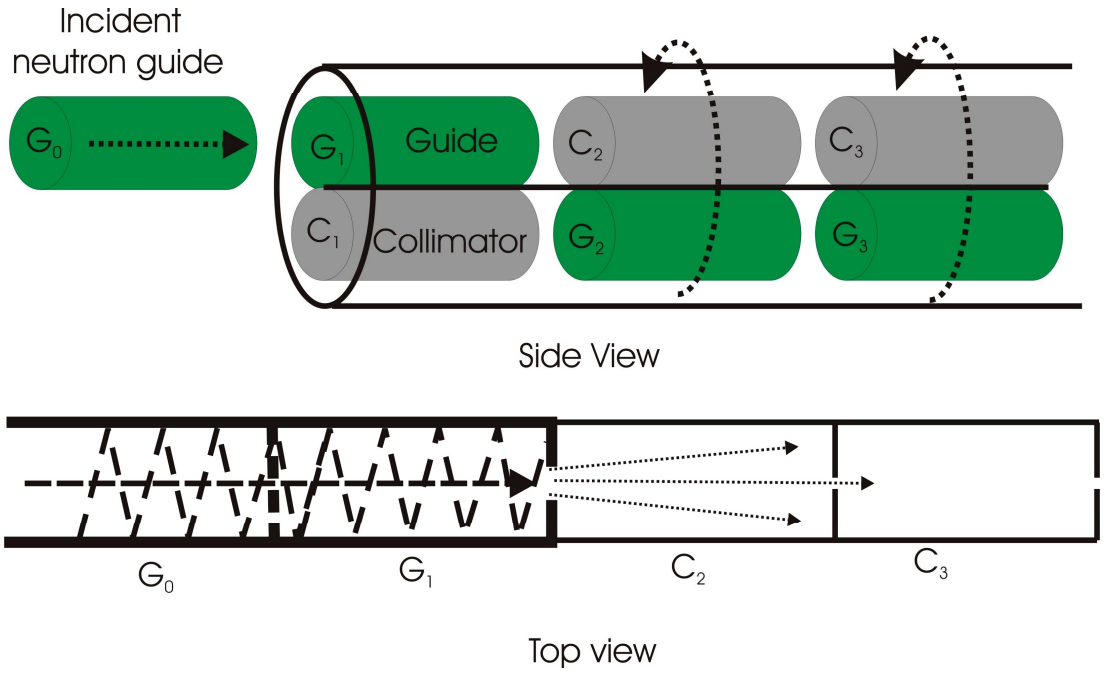

Figure 3.7: The side and top view of the SANS collimator. The guide section G_0 remains fixed. To change the collimation length the guide G_i and collimation C_i sections for i=1,2,3 rotate in and out of the neutron beam.

The SANS instrument is equipped with a two-dimensional position sensitive detector, see Figure 3.8. The detector unit is encased within a vacuum chamber to prevent microscopic particles from changing the beam's scattering trajectory. This will effectively limit the detector noise. The electronics are constructed from an array of cathode-anode reaction chambers each filled with gaseous helium [63]. The scattered neutrons enter the reaction chamber and are sequentially captured by the ^{3}He atoms. This nuclear reaction is expressed by $n+{}^3He \rightarrow {}^3H+{}^1H+e^-$ where the reaction electron has an average energy of 0.70 MeV. The reaction electrons drift to the anode producing a charged pulse. The signal is amplified by applying a voltage to the reaction elections. The high-energy electrons ionise the ^{3}He atoms producing an avalanche of new reaction electrons. The detector electronics converts the voltage spikes to an array of digital pixels, which forms the scattering plane. The sample's scattering q-range is measured by translating the detector along a horizontal or vertical track. For example the D11 SANS machine at the ILL can extend to a maximum horizontal distance of 40.0 m.

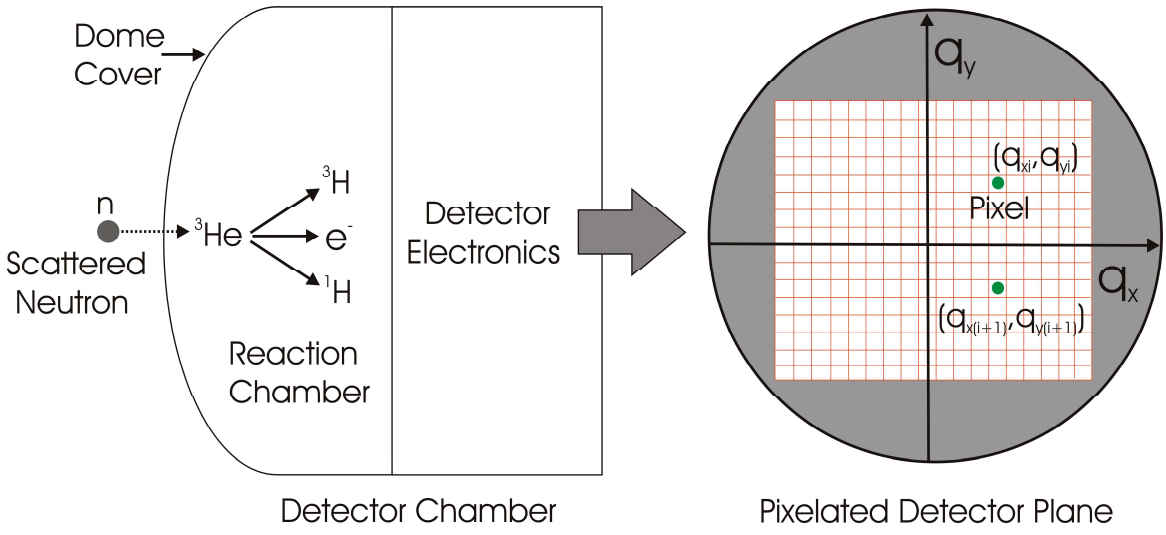

Figure 3.8: The schematic of ^{3}He position sensitive detector. The detector consists of a reaction chamber that contains the ^{3}He atoms and the detector electronics. The scattering intensity is converted to a pixelated map of q space.

3.1.2 SANS Geometry

The scattering geometry for the conventional SANS instrument is shown in Figure 3.9. The monochromatic neutron beam is defined by the incident wave vector $\mathbf{k}_i$ where the magnitude is $|\mathbf{k}_i|=2\pi/\lambda$. At point S the neutron beam of incident angle θ scatters off a lattice plane defined by the its spacing d. Elastic neutron scattering occurs when the Bragg condition, $2d_j\sin\theta_j=n\lambda$, is satisfied at the jth lattice plane. The coherent scattering wave vector is defined by $\mathbf{k}_s$ where $|\mathbf{k}_s|=2\pi/\lambda$. The scattering intensity is measured within a detector plane positioned at point O. The wave vector $\mathbf{k}_s$ is detected at the position OP located a distance D_2 from the detector's centre. The scattering intensity is a function of the momentum transfer $|\mathbf{q}|=|\mathbf{k}_s-\mathbf{k}_i|=4\pi/\lambda\sin\theta$ where θ is the neutron's incident angle. The scattering angle is expressed by $2\theta\approx D_2/D_1$, which is valid for small angles. By changing the distance D_1 or D_2 one can vary the range of the momentum transfer variable $|\mathbf{q}|$.

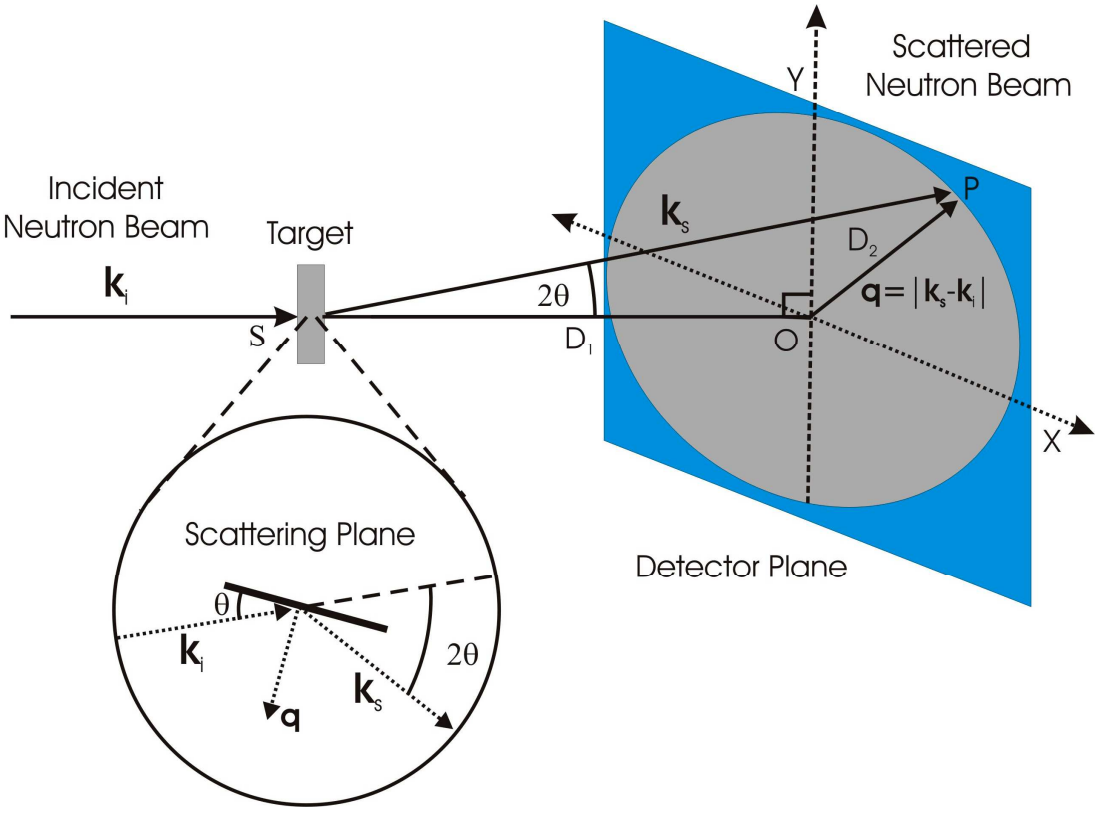

Figure 3.9: The scattering geometry for the SANS target and two-dimensional detector. The circular inset depicts the neutron scattering event within the Bragg plane.

3.2 Magnetometry

The ferromagnetic metal such as iron has a zero magnetisation at an applied magnetic field of zero. This magnetic state is attributed to flux closure at the magnetic domain boundaries. The nature of the domain structure is determined by the relative strengths of dipolar, exchange and anisotropy energies. The experimental technique of magnetometry is used to investigate the domain's hysteretic response to an external magnetic field. For example the area of the hysteresis loop characterises the sample's magnetic phase for example paramagnet or ferromagnet. The magnetometer is an instrument that measures the sample's bulk magnetic moment as a function of applied magnetic field and temperature. In this thesis various types of magnetometers were used to study the in-plane and out of plane magnetism of magnetic recording media. This section reviews the physics and operation of the magnetometer.

3.2.1 SQUID

The Superconducting QUantum Interference Device also known as the SQUID is a magnetometer that utilises a superconducting loop to measure the sample's magnetic flux. The SQUID device is essentially a closed circuit loop, which is formed by connecting two Josephson Junctions in parallel, see Figure 3.10 [69]. When an external flux is threaded through the loop, the voltage output is periodic in the applied flux with a period of one flux quantum Φ_0. As a result, the SQUID instrument has unparalleled sensitivity where the field threshold is of the order of 10^{-14} T [70]. The flux measurement is used to extract the magnetic quantities of magnetic moment, magnetic field gradient, current eddies and magnetic susceptibility. This makes the SQUID an ideal probe for measuring the flux from inorganic to biological materials.

The various components of the SQUID instrument are shown in Figure 3.11. The SQUID circuit is submerged within a cryostat containing liquid helium (bpt.4.2 K). The cryostat regulates the temperature of the SQUID circuit, superconducting coils and sample chamber. The superconducting magnet generates an external field typically in the range of $0<H<5.0$T. The pickup coils measures the magnetic flux generated by the sample. The sample is placed at the centre of the pickup coils. The sample flux is measured by translating the sample insert through the entire length of the pickup coils.

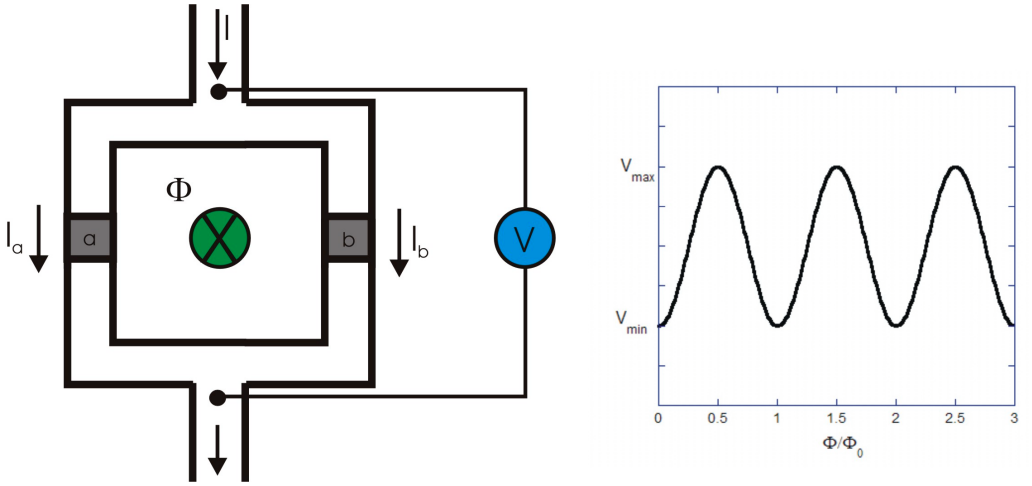

Figure 3.10: The SQUID junction threaded with an external flux. The voltage across the SQUID osciilates as a function of external flux.

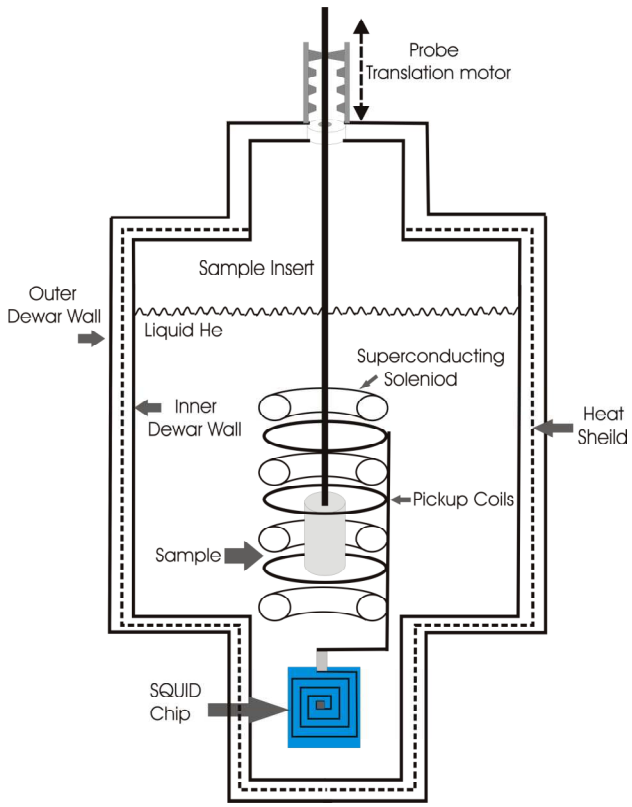

Figure 3.11: A simplified schematic of the SQUID chip, cryomagnet and sample mount.

3.2.2 VSM and MOKE

The instrument known as the Vibrating Sample Magnetometer (VSM) measures the sample's magnetic moment when it is vibrated perpendicular to a uniform magnetic field [71,72]. Figure 3.12(a) shows the typical setup for the VSM instrument. The sample is inserted into a drinking straw and positioned at the centre of the detection coils. The electromagnet immerses the sample within a uniform magnetic field, which is applied perpendicular to the drinking straw. The calibration sample is a permanent magnet and is positioned between reference coils located near the top of the sample insert. The measurements involve vertically vibrating the sample at a frequency f through the detection coils. The change in magnetic flux induces a voltage within the detection coils. The voltage output is calibrated with a second voltage signal induced at the reference coils. The VSM has a sensitivity of 10^{-5}-10^{-6} emu, which allows the measurement of weakly magnetic materials and small changes in the magnetic moment.

Another type of magnetometer is based on the Magneto-Optical Kerr Effect (MOKE) [73]. This characterisation technique utilises the properties of polarised light to probe the sample's magnetisation pattern. The simplified schematic of the MOKE instrument is shown in Figure 3.12(b). In this diagram we will neglect any discussion on the instrument components and only consider the electromagnetic interaction at the sample surface. The typical MOKE experiment is shown in Figure 3.13(a). Though the application of a magnetic field, the experiment can measure the magnetisation in the longitudinal, polar and transverse geometries. The incident light beam is represented by an electromagnetic plane wave where the vector $\mathbf{E}_P$ is linearly polarised within the plane of incidence. The linearly polarised wave is a combination of right-handed and left-handed circular polarised light. Upon reflection the electromagnetic wave becomes elliptically polarised defined by the vectors $\mathbf{E}'_P$ and $\mathbf{E}'_S$. The Kerr effect is observed when the reflected wave is slightly rotated with respect to the plane of incidence. In Figure 3.13(b) the reflected EM wave is measured within the S′-P′ plane where $\pm\theta_P$ defines the instrument's analyser angle. These measurements are used to extract the Kerr rotation θ_k and the associated Kerr ellipticity ε_k. The magnitude and sign of these parameters are proportional to the sample's magnetisation. The Kerr effect originates from the spin-orbit interaction. In short the sample's field induced spin component couples to the orbital part influenced by the circular polarised light [31].

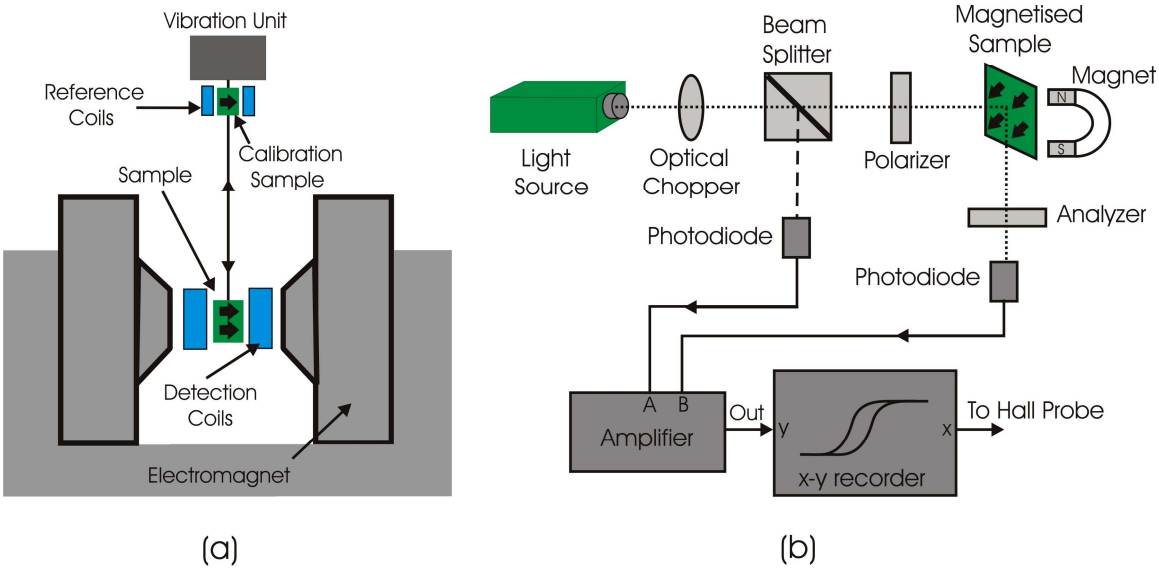

Figure 3.12: The simplified schematics of the (a) VSM and (b) MOKE instruments.

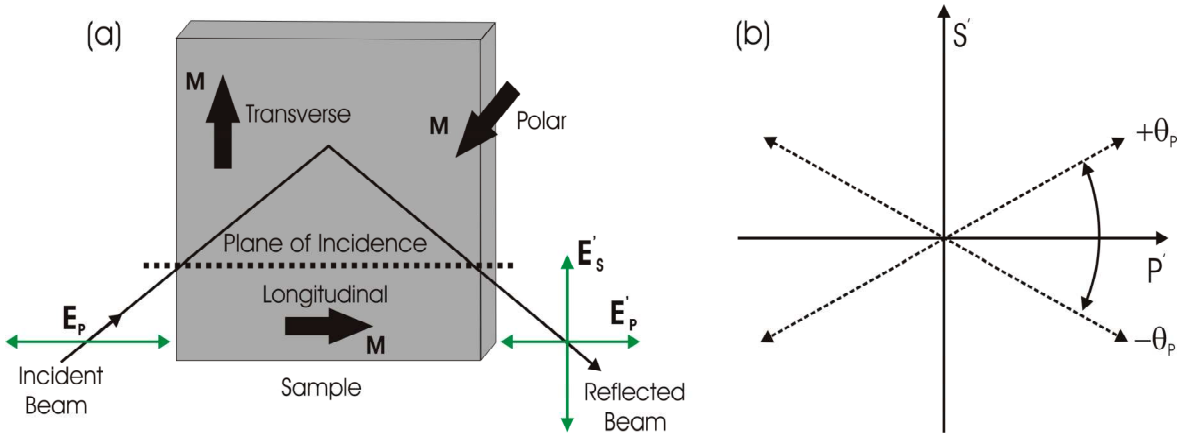

Figure 3.13: The diagram (a) shows the MOKE reflection for the longitudinal, polar and transverse magnetisation. The Kerr rotation is observed in the (b) S′-P′ plane where $\pm\theta_P$ defines the rotation angle of the analyser with respect to the plane of incidence [75].

Chapter 4

Longitudinal Magnetic Recording Media

4.1 Introduction

Longitudinal Magnetic Recording Media (LMRM) was once the mainstay of the disk drive industry. The modern day demands for information storage has rapidly increased the LMRM's storage density. Conventionally computer data is stored on a ferromagnetic recording layer of longitudinal bits where the bit is an aggregate of exchanged de-coupled grains. Research into the LMRM has focused on increasing the recording layer's areal density by decreasing the magnetic grain size. The fabrication of ever-smaller magnetic recording grains has become a complicated process due to thermal instabilities and inter-granular exchange coupling.

The problems associated with fabricating a high-density recording medium are understood by modelling the sample's grain size distribution function. Traditionally the size distribution for nucleated grain growth is represented by the lognormal function. In Figure 4.1(a) the size distribution function is plotted as a function of the grain diameter D. The lognormal function is weighted towards large grain sizes with a standard deviation fraction of the order of $\delta D/D=0.6$. The bit is composed of oversized recording grains, which increases the likelihood of inter-granular exchange coupling. Excessive exchange coupling leads to decreases in the sample's signal to noise ratio (SNR). The bit's exchange coupling is reduced by modelling the sample with a smaller grain size and deviation fraction, see Figure 4.1(b). The ideal magnetic recording media is illustrated in Figure 4.1(c) where the ensemble is modelled by a narrow grain size distribution. In this situation the recording grains will behave independently thus improving on the SNR. However any further reductions in the deviation fraction may result in thermally unstable grains. This magnetic state can lead to the loss of recorded information over long periods of time.

The performance of the LMRM sample was highly dependent on the grain size and size distribution function. The accurate characterisation of the magnetic grain size was essential for understanding the thermal and magnetic properties of the recording bit. In this chapter, the physical and magnetic structure of the LMRM sample was studied at the local length scale of the order of 1-10 nm. The first section reviews the LMRM sample's composition and fabrication. The next section characterises the sample's bulk magnetisation by using SQUID magnetometry. Finally the recording layer's granular structure was measured by using small-angle neutron scattering (SANS).

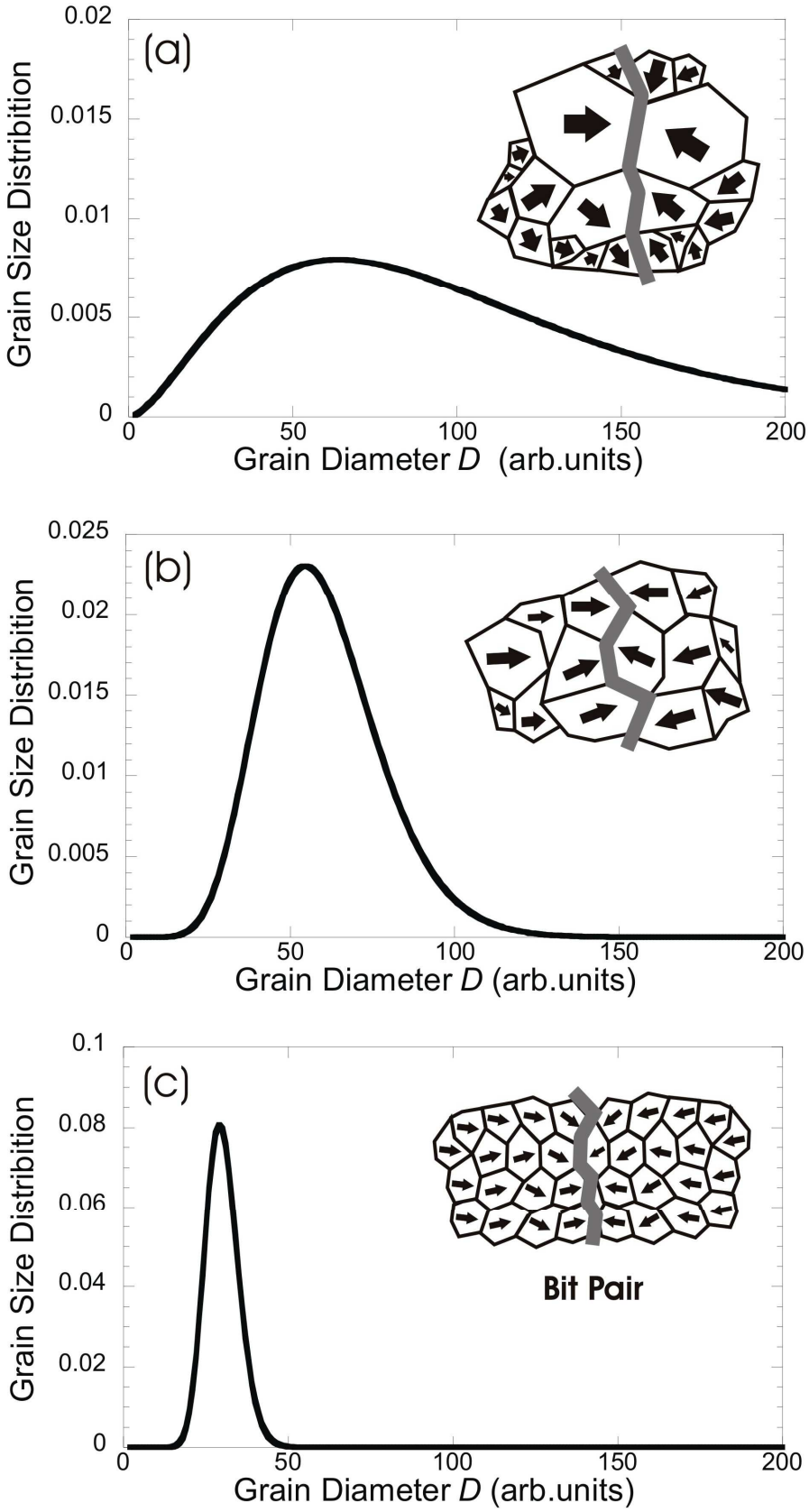

Figure 4.1: The log-normal distribution for an ensemble of recording grains with the standard deviation fractions of (a) 0.6, (b) 0.3 and (c) 0.1.

4.2 The Recording Media Sample

In this chapter, the LMRM samples identified as AX1646, AX341 and AX1821 were fabricated at Seagate California USA [76]. Table 4.1 lists the sample's chemical composition and physical microstructure. These samples were classified as an alloy based recording media where the recording grains were composed of the ferromagnetic alloy CoCrPt. The recording layer was grown onto a series of seed layers, underlayer and an aluminium substrate.

The composition and physical dimensions of AX1646 is shown in Figure 4.2. The underlayer, seed layers and recording layer were sputtered onto an aluminium substrate with a thickness of 0.2 mm. The NiP underlayer of thickness 10,000 Å was sputtered upon the Al substrate. The alloy based materials NiAl and CrMo form the sample seed layers each with an approximate thickness of 100 Å. The recording layer was composed of the cobalt-based alloy CoCrPtB with a thickness of 150 Å.

The recording layer was coated with a 50 Å layer of carbon. This layer protects the recording grains from physical abrasions and oxidation. TEM measurements showed that the recording grains form an array of irregular shaped objects known as the Voronoi structure. The average grain size was 100.0 Å with a grain size distribution of 30% [76]. The grains were segregated by a Cr rich grain boundary of thickness 10.0 Å. The element boron improved the grain segregation by driving a high fraction of Cr atoms to the grain boundaries. The element Pt was distributed randomly throughout the recording layer, which increases the grain's anisotropy energy.

The composition and dimensions of AX341 were similar to the AX1646 sample. The recording layer was composed of the ferromagnetic alloy CoCrPtTa with an approximate thickness of 240 Å. It will be later illustrated that this sample forms a bi-crystal structure whereby adjacent grains, via exchange coupling, cluster into larger units. The average grain size was of the order 100-200 Å with a grain size distribution of 120%. The element Cr reduces the exchange coupling between recording grains. The element Ta acts as a catalyst to drive the Cr atoms to the grain boundary. The sample AX1821 was fabricated with a single layer of NiP of thickness 10,000 Å, which was sputtered upon the Al substrate. The sample AX1821 was used as a background measurement for the up-coming SQUID experiments.

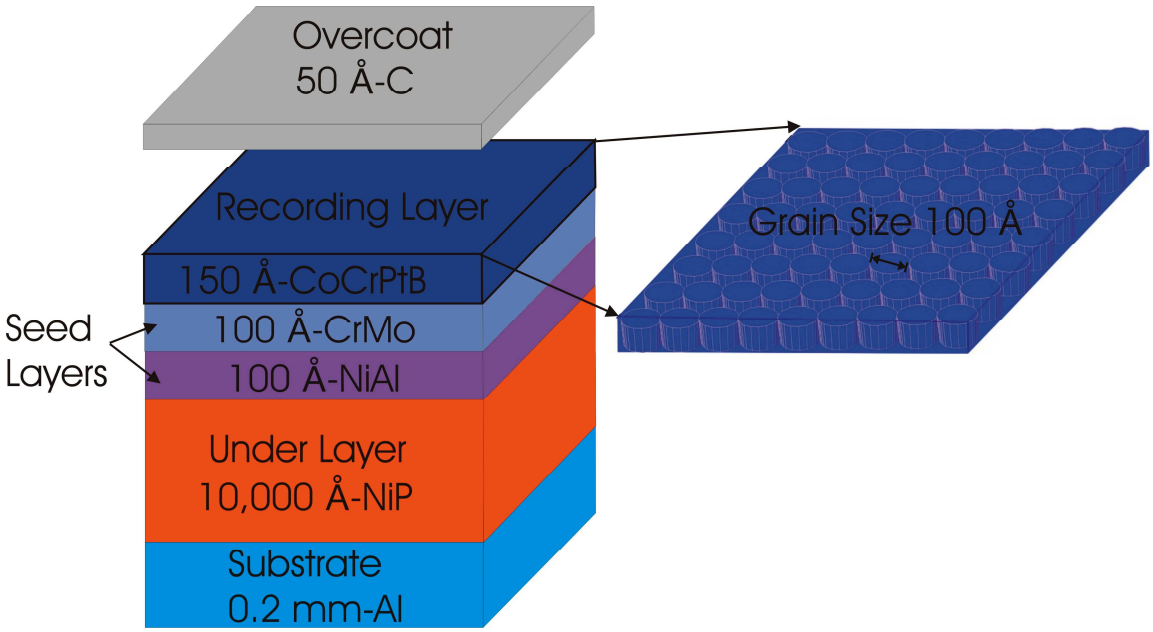

Figure 4.2: The composition and dimensions of the CoCrPtB LMRM sample.

Sample	***Composition***	***Microstructure***
AX1821	NiP/Al	Amorphous based alloy with no seed layers and recording layer.
AX1646	CoCrPtB/CrMo/NiAl/NiP/Al	Single isotropic recording grains with a grain size of 100.0 Å.
AX341	CoCrPtTa/CrMo/NiAl/NiP/Al	Bi-crystal recording grains with a grain size of 100-200 Å.

Table 4.1: The chemical composition and microstructure of the LMRM samples.

4.2.1 Sample Fabrication

The conventional LMRM cross-section is shown in Figure 4.3. The sample's multiple layers were fabricated by using DC magnetron sputtering. The fabrication process occurs at temperatures of 100-220 K with pressures between 5-15 mTorr [77]. The deposition rate was of the order of 10-15 nm/min [78]. The sample substrate provides the skeletal structure for the underlayer, seed layers and recording layer. The substrate was fabricated from aluminium. In some cases the recording media was grown onto a glass substrate, which provides a smooth surface for uniform sputtering growth. The underlayer was composed of the amorphous material NiP. This material provides a hard and level surface for the seed and recording layers. The seed layers, composed of NiAl and CrMo, were deposited onto the NiP underlayer. The seed atoms accumulate upon the NiP layer resulting in formation of columnar grains. Figure 4.4 shows the magnetron sputtering process for Cr atoms. The recording grain's diameter is expressed by,

$$D \propto \left(\frac{\mathrm{G}}{\mathrm{I}} \right)^{\frac{2}{3}}. \tag{4.1}$$

The variable G represents the grain's growth rate. The nucleation rate, I, describes how quickly the sputtered atoms are forming into polycrystalline grains [79]. The recording layer, composed of the ferromagnetic alloy CoCrPt, was grown onto the seed layer. The magnetic grain size and size distribution was determined by the seed grain size which in turn was controlled by the sputtering growth and nucleation rate.

In equation 4.1 the increase in the nucleation rate has the effect of reducing the recording grain size. It was observed for a smooth NiP underlayer that the seed layers form large grains resulting in coalescence. To increase the seed layer's nucleation rate, the fabrication technique of surface roughness was applied to the NiP underlayer. The underlayer's surface roughness was on the scale of 5-50 Å [80]. Further reductions were achieved by sputtering Cr atoms onto the seed layer of NiAl. The NiAl seed layer has a smaller grain size than the CrMo alloy. This effect was due to stronger inter-metallic bonds between the Ni and Al atoms when compared between the Cr bonds. Additionally the NiAl material was known to provide improved crystalline texture for improved sputtering growth. These properties increased the nucleation rate thus decreasing the recording layer's average grain size.

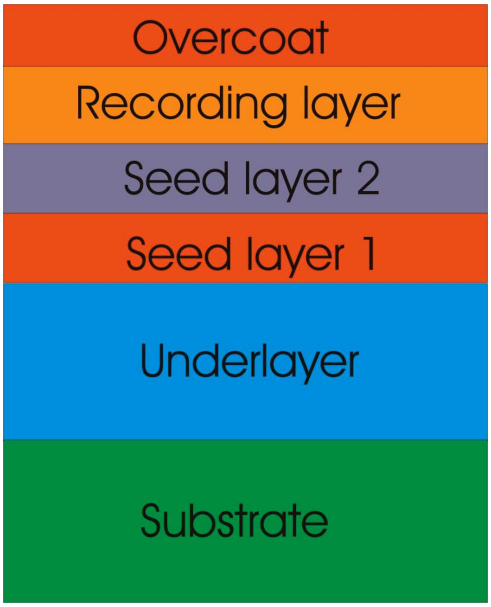

Figure 4.3: The cross-section for the conventional longitudinal magnetic recording film.

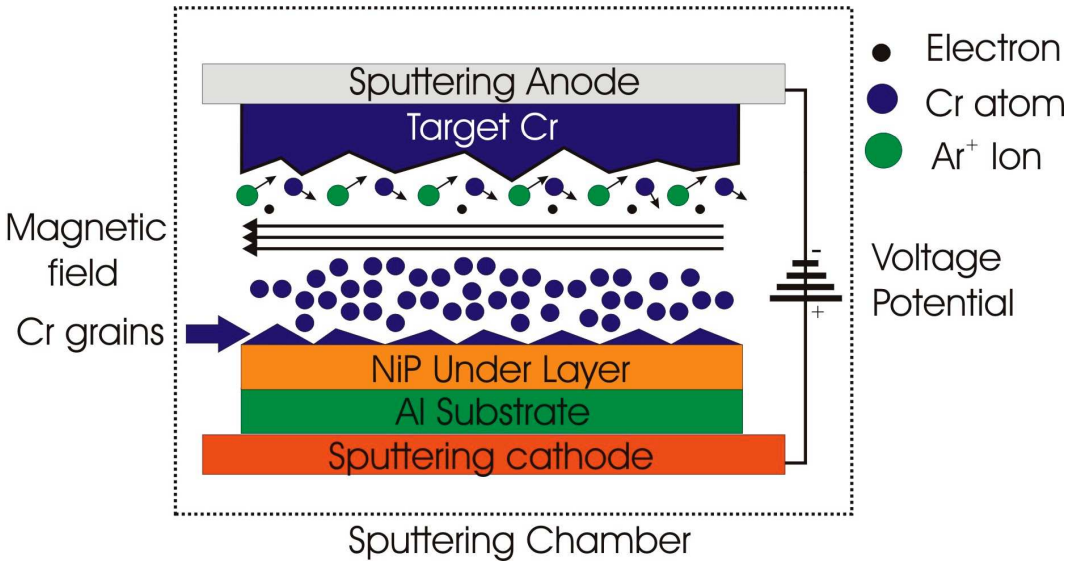

Figure 4.4: The schematic of magnetron sputtering. The chamber is filled with a plasma consisting of Ar^+ ions and electrons. The ion is accelerated by an applied voltage and collides with the target material. Collisions break off Cr atoms, which form into columnar grains upon the NiP under layer.

4.2.2 Seed Layer

The recording layer was composed from a cobalt-based thin film alloy, which exhibits the crystalline phase of hexagonal closed packed (hcp). If the recording layer was sputtered directly onto the Al substrate then the grain's c-axis would lie out of the sample plane. This crystalline property is undesirable for longitudinal magnetic recording where the c-axes must lie within the sample plane. In fact the recording layer was fabricated on a seed layer that allows one to grow the c-axes within the sample plane. The seed layer was deposited onto the NiP substrate where a certain degree of crystalline texture will form at the seed layer surface. For LMRM sample, the recording layer was grown on the bodied centred cubic (bcc) CrMo seed layer. The bcc textures of (110), (112) and (200) arrange their c-axes parallel to the sample plane. The cobalt textures of (100), (101) and (110) provide the closest lattice match to their respective seed layers. The possible texture interfaces were Co(100)/Cr(110), Co(110)/Cr(200) and Co(100)/Cr(112) [81]. Figure 4.5 depicts lattice matching for the recording/seed layer interface. The c-axes of the interfaces Co(110)/Cr(200) and Co(100)/Cr(112) were randomly oriented in the plane, which was desirable for longitudinal recording.

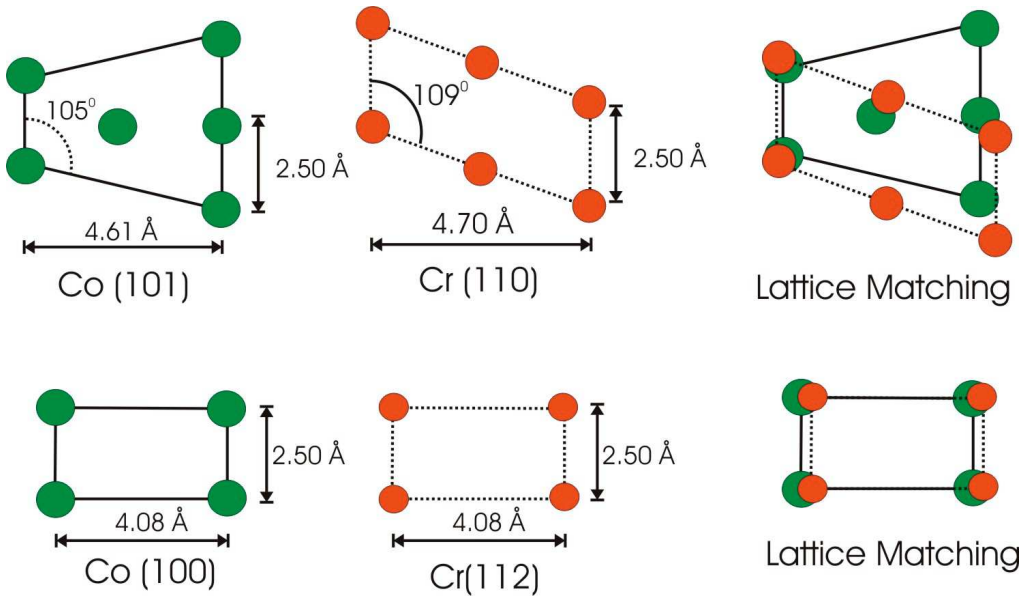

Figure 4.5: The crystal lattice matching for Co(101)/C(110) and Co(100)/Cr(112).

4.2.3 Recording Layer

The conventional LMRM recording layer was formed from the crystalline texture interface of Co(100)/Cr(112). The recording grains were composed of the ferromagnetic CoCrPt-X based alloy where X is the non-magnetic doping atom. Figure 4.6(a) illustrates a section of the recording layer approximately 1000.0 Å across. The recording grains form the Voronoi structure [82] where the grain size distribution was represented by a lognormal or gamma-Shultz distribution function. The black cell represents the grain's core region, which was highly enriched with cobalt. The cores were segregated from its neighbours by the grain boundary shown in white. The single recording grain of the order of 100.0 Å is shown in Figure 4.6(b). The grain's in-plane c-axis defines the easy axis of magnetisation. In Figure 4.6(c) the grain's crystalline lattice structure is shown at the length scale of 2.5 Å. The Co and Cr atoms form the hcp structure where the c-axis lies parallel to the (112) plane. The remaining fraction of Pt atoms was randomly distributed throughout lattice structure.

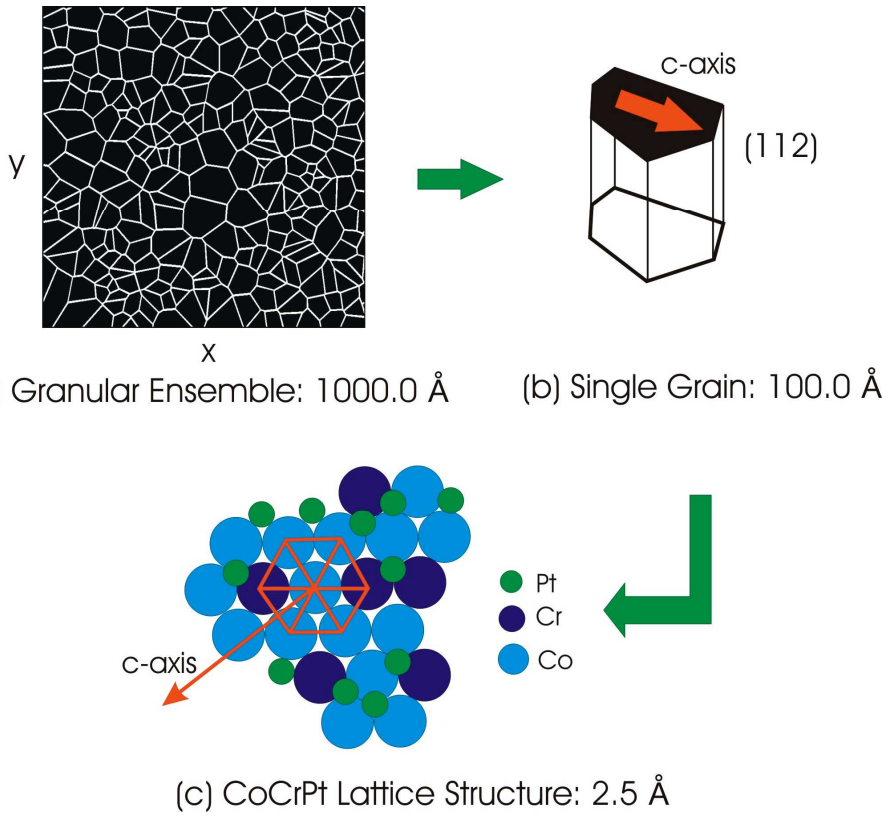

Figure 4.6: The CoCrPt longitudinal recording layer's (a) granular ensemble, (b) single grain and the (c) crystalline lattice.

The recording layer of AX341 was fabricated using the crystalline texture interface of Co(110)/Cr(200). This lattice match results in the formation of bi-crystal recording grains. The formation of bi-crystals comes about by the following process. When the recording layer was deposited onto the lattice plane Cr(200), an equal fraction of Co crystallites orient their c-axes parallel and anti-parallel to the respective lattice planes of Cr(110) and Cr($1\bar{1}0$) [22]. Due to these lattice formations, adjacent recording grains arrange their c-axes in orthogonal moment pairs. Figure 4.7 illustrates the magnetic structure of the bi-crystal recording layer.

The advantage of bi-crystal media was that they refine the grain size and possibly increase the recording system's SNR. The drawbacks were the formation of granular clusters, which is linked to strong exchange forces between bi-crystals. In previous compositional studies the bi-crystal grain boundary has less Cr-segregation than the conventional recording grain [22]. In this case the bi-crystal grain boundary cannot provide an effective non-magnetic barrier between the neighbouring grains. When the bi-crystal grains were exchanged coupled, there was a marked reduction in the grain's magneto-crystalline anisotropy energy. It is shown later that a reduction in the anisotropy energy increases the grain's likelihood of thermal activation.

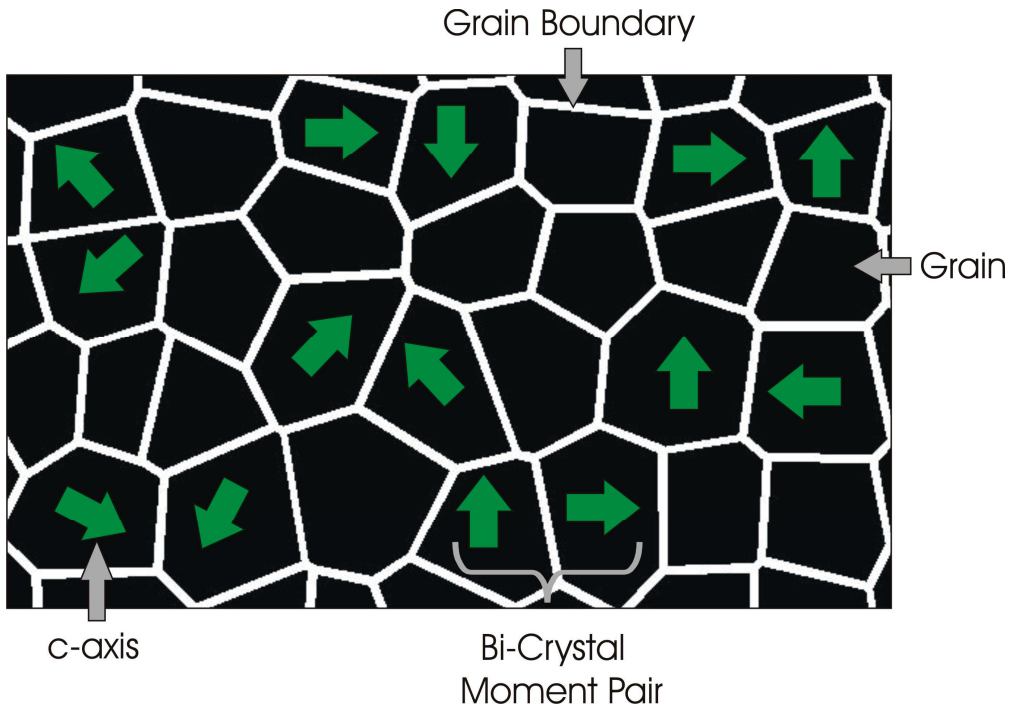

Figure 4.7: The schematic of a bi-crystal longitudinal recording layer. The bi-crystal grains form orthogonal moment pairs, which are coupled via exchange forces.

A single recording grain was composed of ferromagnetic core and a weakly magnetic grain boundary. The grain boundary or shell component was fabricated by doping the Co atoms with the non-ferromagnetic Cr atom. The magnetisation of the core or shell was dependent on the percentage of Cr within each region. The increase of Cr atoms will displace the cobalt atoms thereby giving the magnetic alloy a reduced moment density. Figure 4.8 plots the saturation magnetisation of the CoCrPt alloy as a function of Cr percentage. At 12-15% Cr the material is highly ferromagnetic while at 25% Cr the material is close to a soft ferromagnetic state [83].

The grain's shell component was mainly composed Cr, which provides a physical barrier against inter-granular exchange coupling. Fabrication conditions such as high substrate temperatures and low sputtering pressures drive the Cr atoms to the grain boundary thus forming the shell component. For example the fabrication of the alloy $Co_{81}Cr_{15}Ta_4$ consists of a Cr rich grain boundary with a thickness of 1.0 nm [83]. The atomic percentages within the core and shell components are ≈15% and ≈25% respectively. The high Cr percentage at the grain boundary leaves the shell component non-magnetic or possibility ferromagnetically soft. This type of chemical segregation is known as vacancy exchange diffusion. The diffusion process was improved by doping the recording grains with the elements Ta or B.

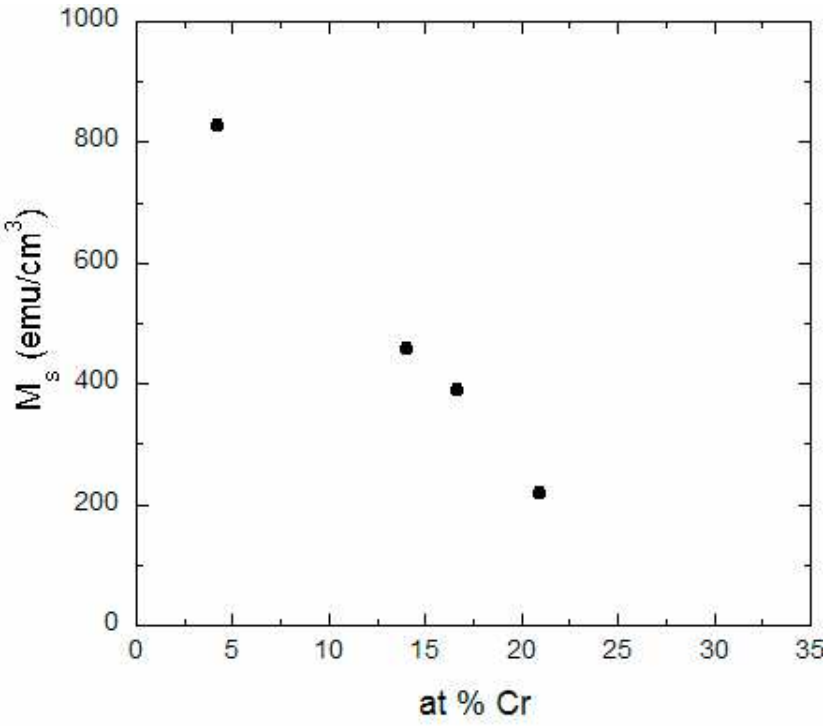

Figure 4.8: The saturation magnetisation of the CoCrPt alloy as a function of the atomic percentage of Cr [83].

The thermal activation of magnetic recording media depends on the recording grain's magneto-crystalline anisotropy and thermal energies. The condition for a thermally stable grain is defined by the energy ratio,

$$\left(\frac{E_{aniso}}{E_{thermal}}\right) = \frac{K_U V}{k_B T} >> 1, \qquad (4.2)$$

where E_{aniso} and $E_{Thermal}$ are the anisotropy and thermal energies respectively. The grain's anisotropy energy is defined as the product of the anisotropy constant K_U (J/m^3) and the magnetic volume V. The increase in storage density results in a decrease in the grain volume. This reduces the size of the anisotropy energy thereby increasing the likelihood of thermal activation. The energy ratio was maintained by increasing the magnitude of the anisotropy constant, K_U. This was achieved by alloying the recording grain with the element Pt. The anisotropy field of the alloy CoCrPtB was found to increase rapidly as one increases the atomic percentage of Pt, see Figure 4.9. The variation of the magneto-crystalline anisotropy field with Pt concentration possibility results from the formation of the fcc crystalline phase [84].

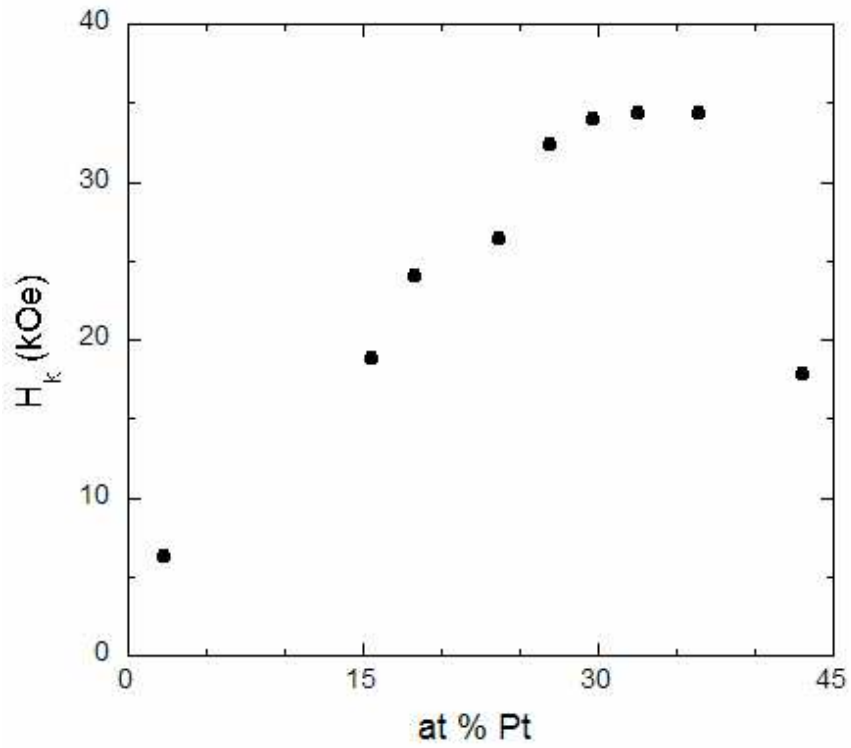

Figure 4.9: The magneto-crystalline anisotropy field H_K of the compound CoCrPtB as a function of the atomic percentage of Pt [84].

4.3 Bulk Magnetisation

In this section the bulk magnetisation of the LMRM sample was investigated using the characterisation technique of SQUID magnetometry [85]. The magnetisation measurements extracted the recording layer's in-plane hysteresis loop as a function of applied field and temperature. The shape of the hysteresis loop was determined by the recording layer's magnetic properties such as saturation magnetisation M_s, remanent magnetisation M_r and coercive field H_c. The saturation magnetisation measures the CoCrPt recording grain's average moment density. The magnitude of M_s gauges the grain's ferromagnetic hardness with respect to the bulk value of cobalt. The remanent field measures the grain's magnetisation at zero field. In certain cases the magnitude of the remanent field will give information on the demagnetisation and anisotropy fields. The coercive field defines the state where the ensemble undergoes magnetisation reversal. The size of H_c depends on the grain's anisotropy, demagnetisation and thermal activation fields. These hysteresis measurements in combination with SANS studies were later used to characterise the recording grain's magnetic diffraction pattern.

4.3.1 Measurements

The SQUID magnetometer was calibrated using a highly pure palladium sample with a ferromagnetic purity of less than 30 ppm [85]. This property insures that the calibration measurement was not distorted by any ferromagnetic contributions. The Pd moment was measured for the in-plane field of 1.0 T<H<5.0 T at room temperature. For this field range, the total moment is dominated by the paramagnetic contribution. The Pd sample shows a paramagnetic moment of the order of 10^{-2} emu at the field of 5.0 T. The in-plane magnetisation of the LMRM samples AX1646, AX341 and AX1821 were characterised using the SQUID magnetometer. The sample's chemical and physical microstructure are listed table 4.1. The sample disc of diameter 0.6 cm was attached to drinking straw and lowered into the SQUID cryostat. The sample plane lied parallel to the longitudinal axis of the superconducting solenoid where the applied magnetic field was positioned in-plane to the sample surface. The total moment was measured for the field range of –5.0 T<H<5.0 T at the temperature range of 5 K-300 K.

4.3.2 Results and Discussion-AX1821

The hysteresis measurements of AX1821 are show in Figures 4.10 and 4.11 for the respective temperatures of 5 K and 300 K. The measured total moment of AX1821 was a superposition of magnetic contributions from the NiP layer and Al substrate. At either temperature the total moment traces out a thin hysteresis loop where the coercive field and remanent moment were near zero, see the inset of Figure 4.10. The magnetic hysteresis loop originates from the NiP underlayer, which was characteristic of a soft ferromagnet. At high field, the total moment increases linearly as a function of applied field. This magnetic response was characteristic of paramagnetism, which originates from the Al substrate and possibly the NiP layer. Furthermore it was observed that the paramagnetic moment was independent of temperature. The paramagnetic contribution from the Al substrate was due to the phenomenon of Pauli paramagnetism. It was assumed the Pauli moment is independent of the measured temperature range. This is a reasonable assumption for the first order approximation of Pauli paramagnetism.

The magnetic moment from the NiP layer was extracted by correcting for the Pauli paramagnetic contribution. The Pauli moment as a function of applied field H is given by, $\mu_{Al}=\chi_{Al}V_{sub}H$ where $\chi_{Al}=1.67\times10^{-6}$ emuOe^{-1}cm^{-3} [34] is the Pauli susceptibility of Al and V_{sub} is the volume of the substrate. The volume is defined by $V_{sub}=\pi R^2_{disc}L$ where R_{disc} and L are the radius and thickness of the sample disc respectively. The disc radius was 0.3 cm with a substrate thickness of 0.02 cm. These calculations were used as the initial fit parameters to model the paramagnetic moment. In Figure 4.10 the fit equation was used to subtract off the Pauli paramagnetic contribution.

The inset shows the magnetic hysteresis loop at 5 K to be slightly wider than the 300 K measurement. This temperature variation in coercive field was understood in terms of the energy barrier argument. At 300 K the domains rest in a micromagnetically stable state where the energy barrier prevents the moments from magnetisation reversal. The magnitude of the energy barrier depends on the domain's Zeeman, anisotropy, demagnetisation and thermal energies. The applied Zeeman field reduces the height of the energy barrier thereby increasing the probability of the moment reversal. When the temperature was decreased, the thermal switching field was reduced thus increasing the height of the energy barrier. This has the effect of increasing the magnitude of the coercive field.

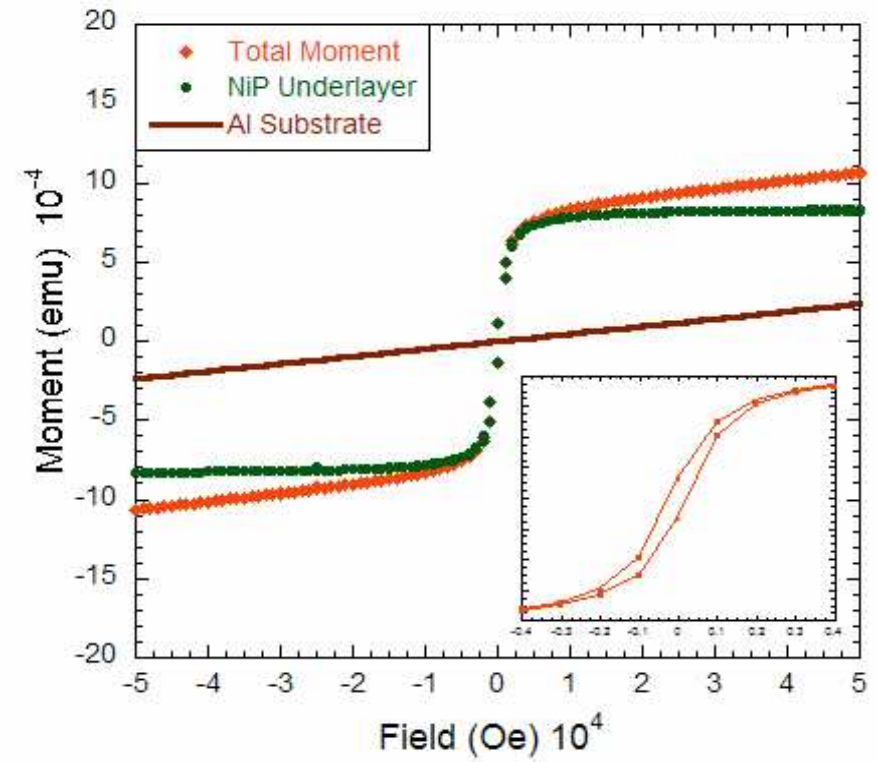

Figure 4.10: The AX1821 in-plane magnetic hysteresis at the temperature of 5 K.

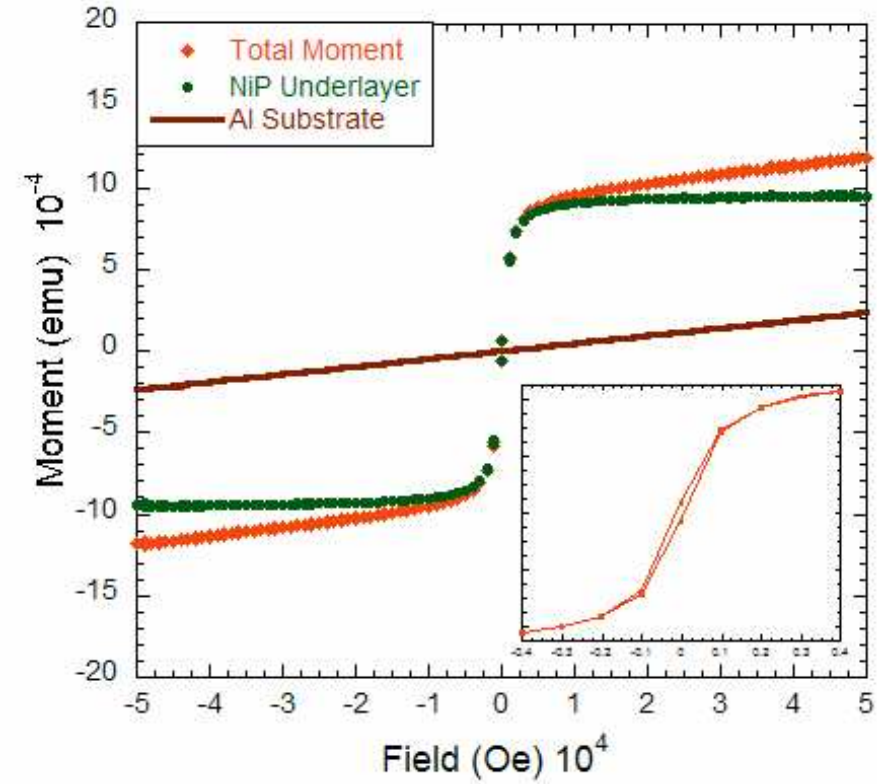

Figure 4.11: The AX1821 in-plane magnetic hysteresis at the temperature of 300 K.

The corrected NiP hysteresis loop appears to show no significant paramagnetic moment at the temperatures of 5 K and 300 K. This shows the NiP layer to exhibit only the ferromagnetic phase. The magnetic moment density of NiP (magnetisation) was extracted by normalising the moment to the layer's volume. The layer thickness of was of the order of 10,000 Å. Figures 4.12(a) and 4.12(b) show the magnetisation plots for the temperatures of 5 K and 300 K respectively. The saturation magnetisation at either temperature was very small when compared to the bulk magnetisation of nickel of magnitude M_s=500 emu/cm^3 [31]. This clearly shows that the NiP layer was a soft ferromagnetic material. The loop squarness of S<<1 was further evidence that this sample was magnetically soft.

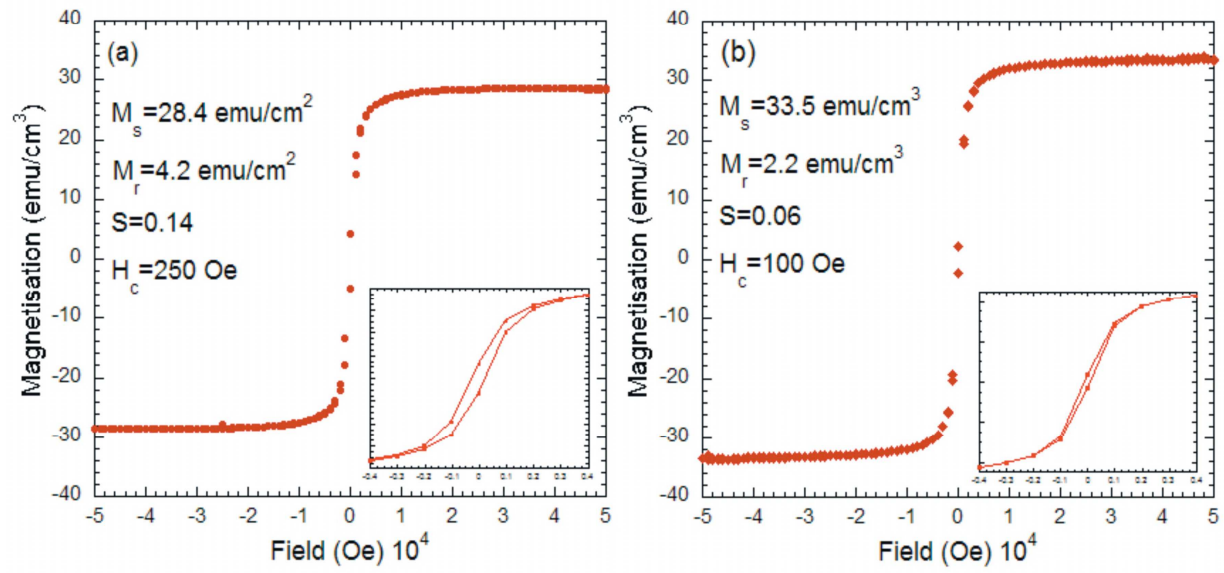

Figure 4.12: The AX1821 magnetisation at the temperatures of (a) 5 K and (b) 300 K.

4.3.3 Results and Discussion-AX1646

The hysteresis measurements of AX1646 at 5 K and 300 K are shown in Figures 4.13 and 4.14. The total magnetic moment was composed of a superposition of hard and soft ferromagnetic components. The hard ferromagnetic loop originates from the recording layer while the soft magnetic component arises from the NiP underlayer. The ferromagnetic moment was superimposed on a paramagnetic background that mainly originates from the aluminium substrate. The total moment from the recording layer was extracted by subtracting off the aluminium and NiP background.

The hysteresis measurements performed on the sample AX1821 represent a possible background subtraction for AX1646. In this case the total moment of AX1821 was much larger than the background component of AX1646 making it unsuitable for a background subtraction. The alternative was to measure the background moment from the AX1646 sample with its recording layer etched away. This required the removal of the sample's carbon overcoat (50 Å), seed layers (200 Å) and recording layer (150 Å) leaving the NiP and aluminium substrate. The net thickness of these over-layers was not less than 400 Å therefore it was essential to develop an accurate method to etch down to the NiP underlayer. The first experiment tried was to remove the over-layers by using an ion beam etch. Through the use of an applied potential, a beam of Ar ions was impacted onto the sample surface. The beam exposure time ranged from 3-30 min. Hysteresis measurements determined that the ion beam etch failed to fully remove the magnetic recording layer. It may be possible that the carbon layer was quite resistant to the etching process resulting in a partial removal of the over-layers.

Another etching experiment was to remove the over-layers by finely sanding the sample surface with emery paper. This removal technique proved efficient in removing material from the sample surface. The disadvantage of this process was the inability to accurately measure the amount of material sanded off the sample surface. The magnetic hysteresis loop of the etched sample was measured at the temperature of 5 K. Note for the background measurements the total moment did not vary significantly over the temperature range of 5-300 K, see also AX1821 measurements. Hence the background measurement at 5 K was used to correct the hysteresis for the measured temperature range. In Figures 4.13 and 4.14 the background measurements are plotted alongside the total and recording layer moments at 5 K and 300 K.

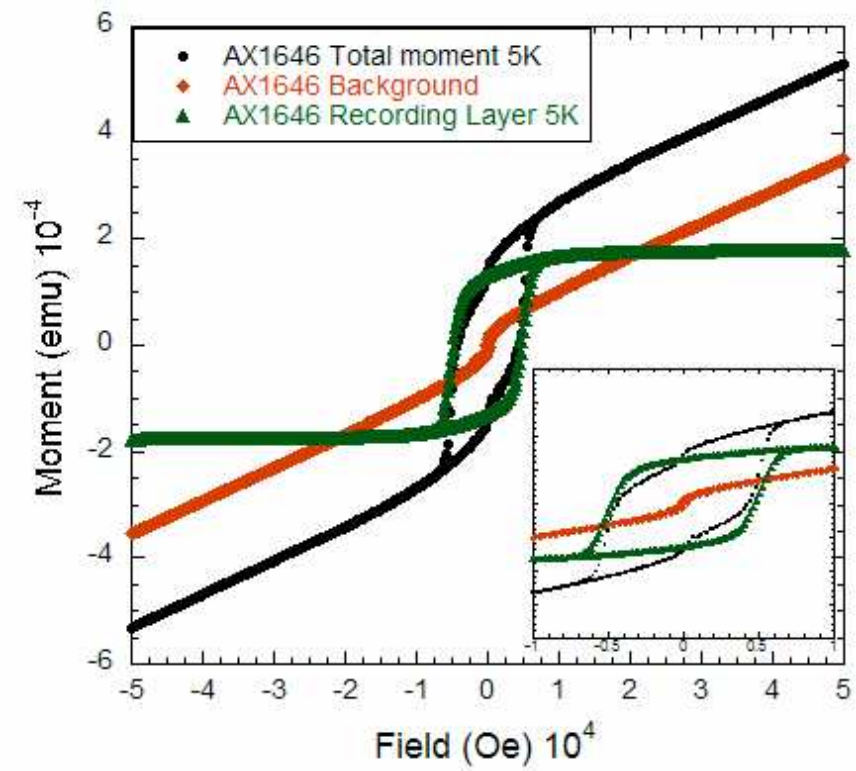

Figure 4.13: The AX1646 in-plane magnetic hysteresis measurements of the total moment, background and recording layer at the temperature of 5 K.

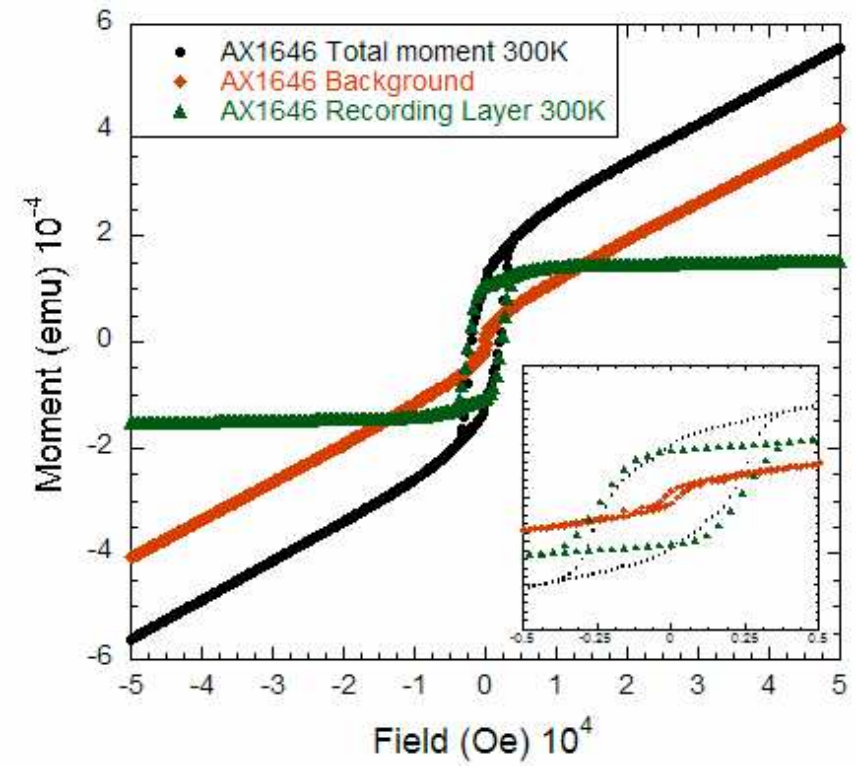

Figure 4.14: The AX1646 in-plane magnetic hysteresis measurements of the total moment, background and recording layer components at the temperature of 300 K.

The magnetisation was obtained by normalising the ferromagnetic moment to the volume of the recording layer. The recording layer's thickness was approximately 150 Å. The magnetisation loops at 5 K and 300 K are shown in Figure 4.15. At the temperature of 5 K the saturation magnetisation was M_s=424 emu/cm^3. According to the current literature, the saturation magnetisation was comparable for a cobalt-enriched recording grain [86]. The width of the magnetisation loop, defined by the coercive field, was of the order of H_c=4700 Oe. The small H_c of AX1821 indicates that the NiP layer possesses no significant in-plane crystalline anisotropy. However AX1646 gives a much larger value of H_c indicating that the recording grain exhibits a strong in-plane magneto-crystalline anisotropy field.

At the temperature of 300 K, the recording layer's saturation magnetisation was M_s=362 emu/cm^3. This result was moderately smaller than the values quoted in the literature at M_s~450 emu/cm^3 [86]. The Co/Cr percentage within the recording grain was extracted by using the magnetisation plot of Figure 4.8. At the magnetisation of M_s=362 emu/cm^3, the cobalt-chromium percentage was approximately 82% and 18% respectively. The coercive field at room temperature was H_c=2560 Oe. It is shown in the following section that the decrease in coercive field was attributed to changes in anisotropy and thermal activation energies as a function of temperature.

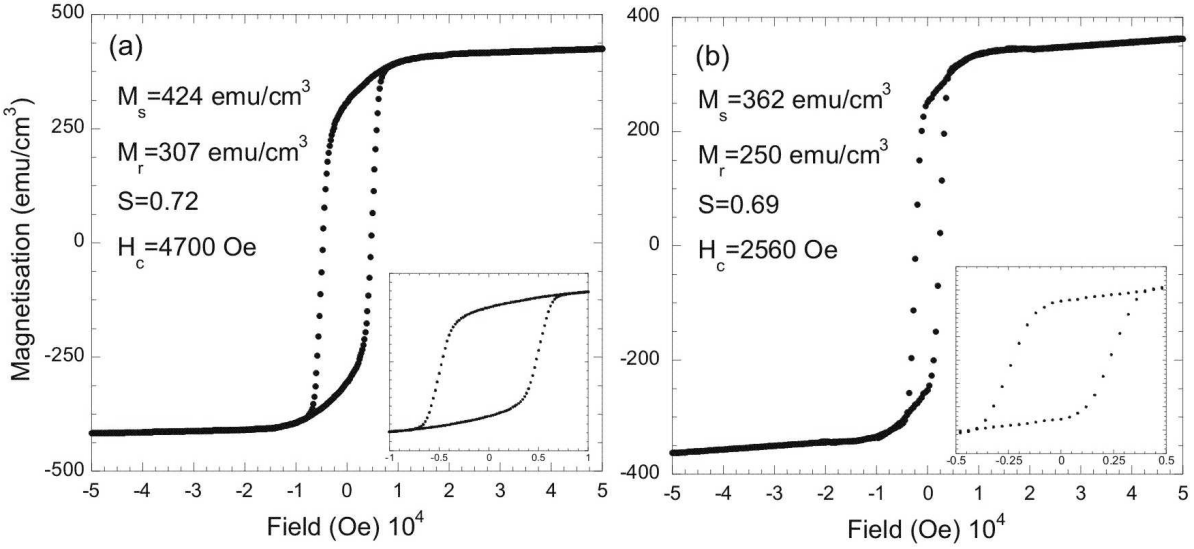

Figure 4.15: The AX1646 magnetisation at the temperatures of (a) 5 K and (b) 300 K.

4.3.4 Results and Discussion-AX341

The hysteresis measurements of AX341 were performed at the temperatures of 5 K and 300 K, see Figure 4.16. In a similar fashion the ferromagnetic hysteresis loop from the recording layer was extracted by subtracting off the NiP and Al background. Due to time constrains it was not possible to prepare a background sample for AX341. The underlayer and substrate background was approximated using the etched sample of AX1646 at 5 K. The background measurement proved to have a much smaller moment than the total moment of AX341. In this case the background moment was scaled appropriately to subtract off any paramagnetic contributions.

The total moment was normalised to the volume of the recording layer. For the sample AX341 the recording layer has a thickness of 240.0 Å. The magnetisation loops at 5.0 K and 300 K are plotted in Figure 4.17. At 5 K the saturation magnetisation was of the order of M_s=633 emu/cm^3. This indicates that the recording grain of AX341 was slightly more ferromagnetic than AX1646. This can only occur if the percentage of cobalt was larger within the AX341 grain. The coercive field of H_c=2750 Oe was much smaller than the value obtained for AX1646. Due to the sample's larger saturation magnetisation, the recording grain's demagnetisation field shifts the coercive field to smaller values. The reduction in the coercive field could also be due to AX341 smaller in-plane magneto-crystalline anisotropy field.

At the temperature of 300 K the saturation magnetisation reduces to the value M_s=576 emu/cm^3. The saturation value was again lower than the quoted measurement of the order of 650 emu/cm^3 [86]. However, this discrepancy may be due to a slightly miscalibrated background measurement. By using the M_s plot in Figure 4.8, the cobalt-chromium percentage within the recording grain was approximately 88% and 12% respectively. According to these results the recording grain has a smaller percentage of chromium with respect to AX1646 recording grain. The low faction of Cr within the AX341 sample results in less Cr segregating to the grain boundary. This was a characteristic of the bi-crystal media where the recording grain becomes more prone to inter-granular exchange coupling.

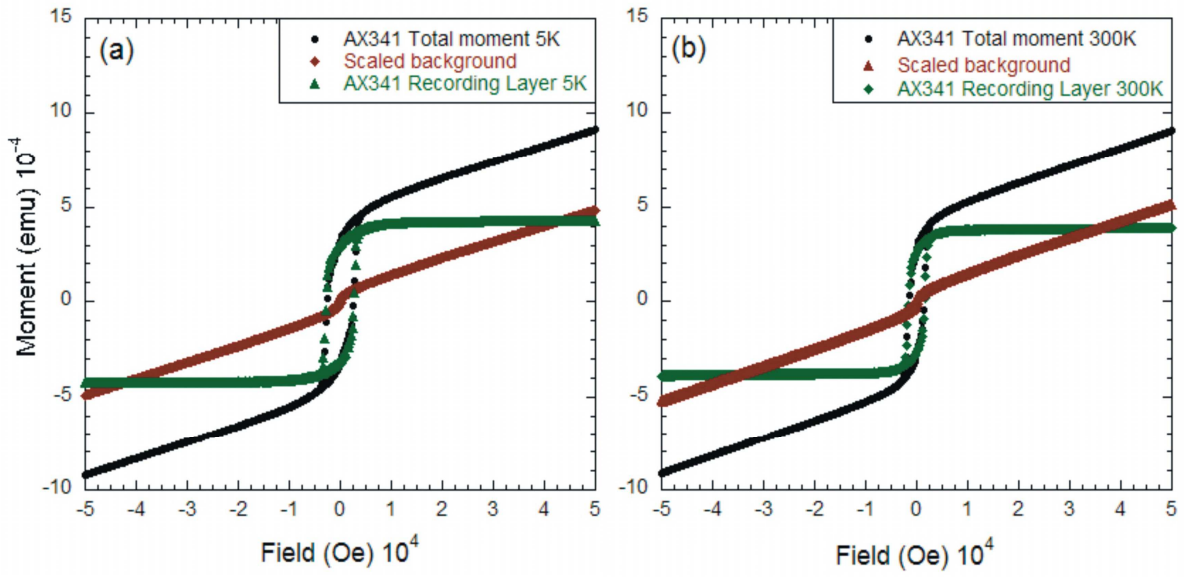

Figure 4.16:The AX341 in-plane magnetic hysteresis measurements of the total moment, background and recording layer at the temperatures of (a) 5 K and (b) 300 K.

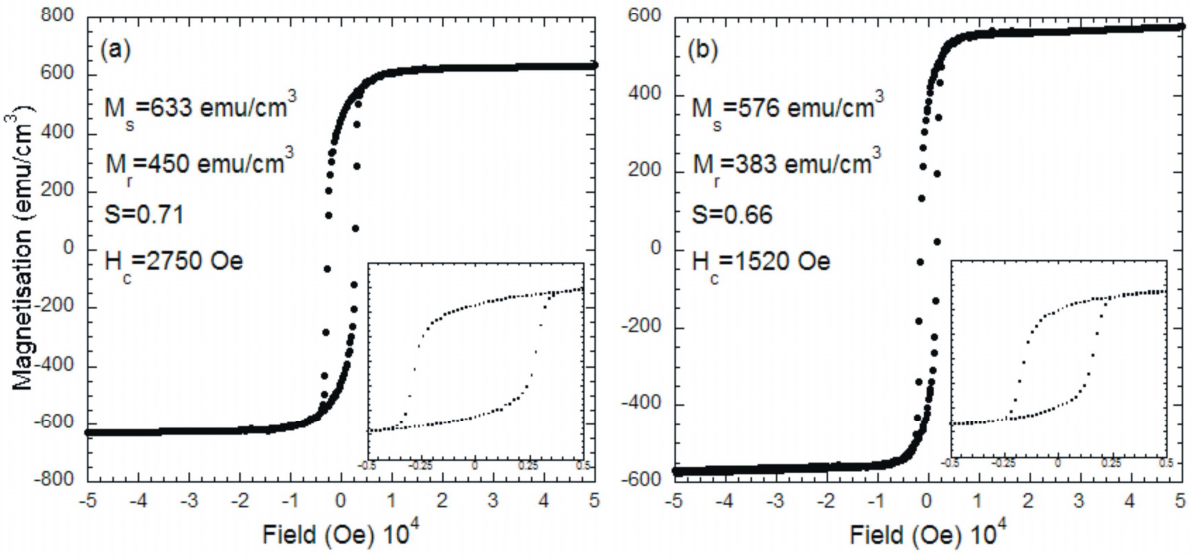

Figure 4.17: The AX341 magnetisation at the temperatures of (a) 5 K and (b) 300 K.

The magnetic stability of the recording grain was determined by the anisotropy to thermal energy ratio, see equation 4.2. The recording grain was considered stable when the energy barrier was much greater than the thermal energy. For longitudinal grains, the energy ratio of 60.0 is most commonly quoted. The magnitude of the energy barrier was dependent on the anisotropy density K_u and the average volume of the recording grain. These physical properties were characterised and compared for the samples AX1646 and AX341. In Figure 4.18 the saturation magnetisation is plotted for the temperature range of 5-300 K. The difference between the sample's saturation values was attributed to AX341 having a larger fraction of cobalt within the recording grain. The least squares fit was performed on each data set. The small variation of M_s over the temperature range was characteristic for a ferromagnetic alloy at $T<<T_c$.

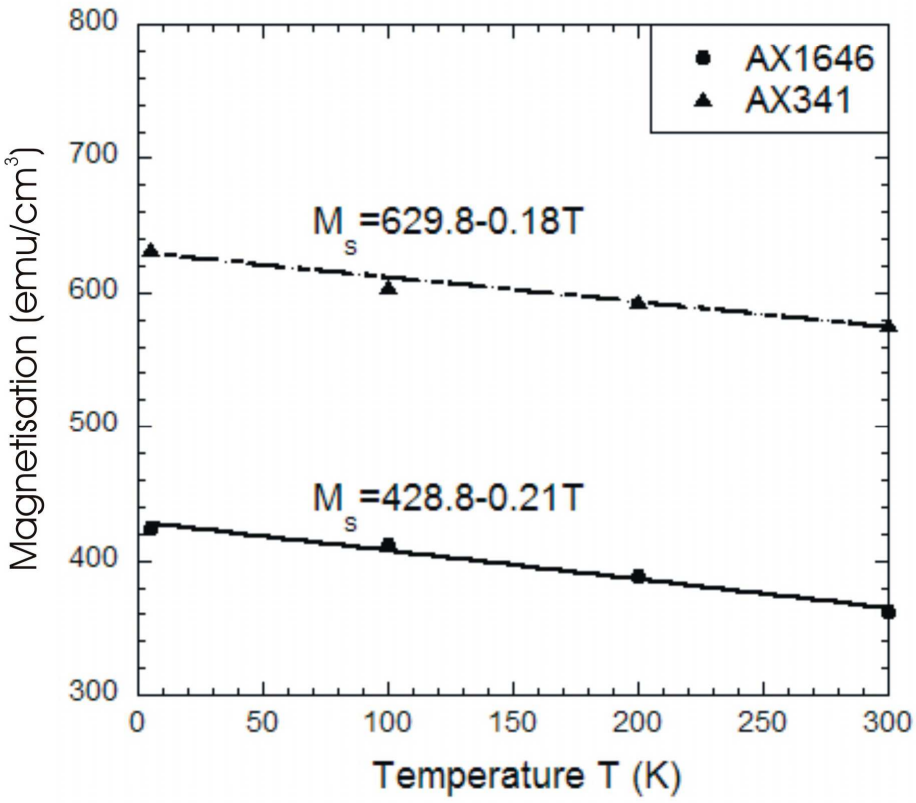

Figure 4.18: The saturation magnetisation of the LMRM samples AX1646 and AX341 plotted as a function of temperature.

The coercive field as a function of temperature is plotted in Figure 4.19. The coercive slope reveals information on the grain's magneto-crystalline anisotropy energy. The coercive field was approximated by the following equation $H_c=H_0(1-k_BT/E_a)$ where H_0 is the zero temperature coercive field and $E_a=K_UV$ is the recording grain's crystalline anisotropy energy [87]. The coercive field slope of AX1646 was twice that of AX341, which shows that the anisotropy energy was larger for the sample AX341. The large energy barrier of AX341 was attributed to the large magnetic volume of the recording grain rather than the anisotropy energy density. For example the AX341 sample has an inherently smaller anisotropy density due the recording grain's bi-crystal structure. This occurs when exchange coupled grains form a new c-axis that effectively reduces the anisotropy constant. This fact leads one to assume that the in-plane anisotropy field was smaller than AX1646. However the grain size of AX341 was approximately twice that of AX1646. This results in an overall increase in AX341 anisotropy energy and hence energy barrier.

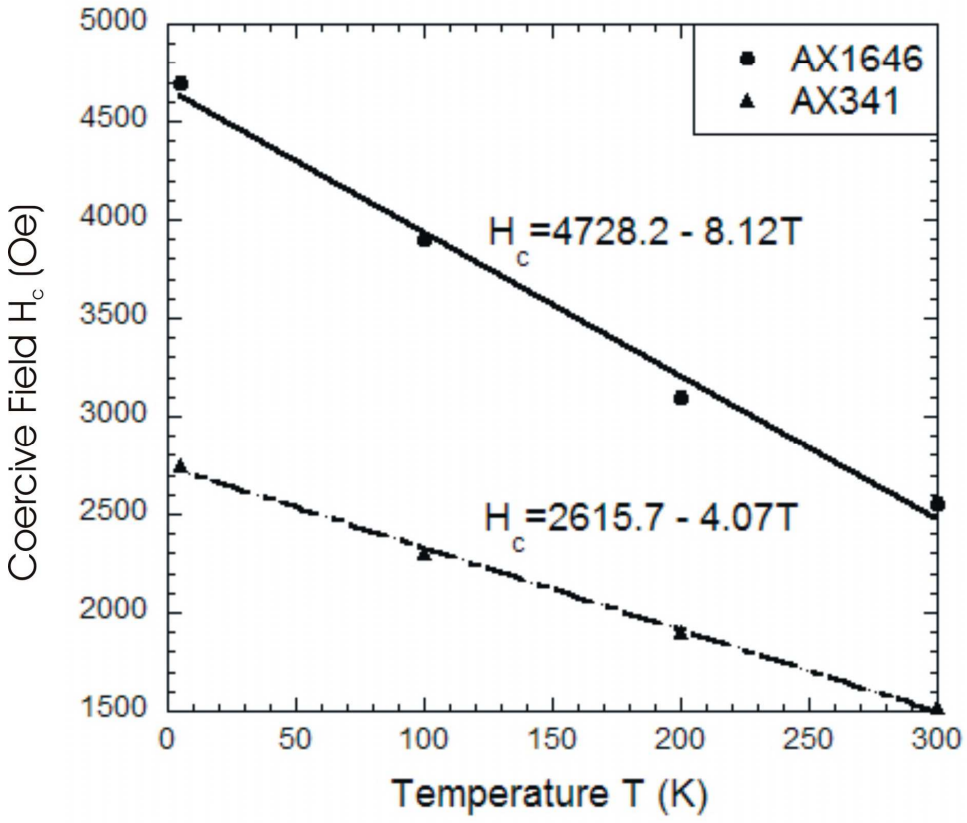

Figure 4.19: The coercive field of AX1646 and AX341as a function of temperature.

Summary 4.3.5

The in-plane hysteresis loop of the LMRM sample was measured using the SQUID magnetometer. The magnetisation measurements were performed at the applied in-plane field range of –5.0 T<H<5.0 T over the temperature of 5-300 K. The magnetic recording medium and underlayer were characterised by the saturation magnetisation, remanent magnetisation and coercive field. These magnetic properties were used to better understand how the grain's energy barrier was influenced by the demagnetisation, magneto-crystalline anisotropy and thermal fields.

The background sample AX1821, composed of the ferromagnetic alloy NiP, exhibited magnetic hysteresis at 5 K and 300 K. The measured magnetic moment was a superposition of paramagnetic and soft ferromagnetic components. The paramagnetic contribution known as Pauli paramagnetism, emanated from the sample's aluminium substrate. The soft ferromagnetic moment originated from the NiP layer. The magnetic hysteresis loop was characterised by a small saturation magnetisation and a coercive field of less than a few hundred Oersteds.

The magnetisation measurement of the sample AX1646 showed magnetic hysteresis over the measured temperature range of 5 K-300 K. The hysteresis loop at 5 K exhibited three magnetic phases: soft ferromagnetism, Pauli paramagnetism and hard ferromagnetism. The soft-ferromagnetic and paramagnetic contributions emanated from the sample's NiP underlayer and Al substrate respectively. The hard-ferromagnet originated from recording grains composed of the cobalt-based alloy CoCrPtB. The etched sample of AX1646 was used to subtract off any background components from the soft underlayer. The recording layer exhibited a large saturation magnetisation and coercive field. These magnetic properties were characteristic of a cobalt enriched recording grain with a large in-plane magneto-crystalline anisotropy field.

The third set of magnetisation measurements was performed on the sample AX341 composed of the bi-crystal grain CoCrPtTa. The recording layer was found to have a larger saturation magnetisation than AX1646. As a consequence the percentage of cobalt within the recording grain was greater for AX341 sample. The larger fraction of Co within the recording grain led to an increase in the saturation magnetisation and a reduction in the coercive field. Further analysis showed that AX341 exhibited a larger energy barrier than AX1646 making it less prone to thermal activation during the read/write process.

4.4 Unpolarsied SANS

In the previous section the in-plane magnetisation of longitudinal magnetic recording media (LMRM) was measured by the characterisation technique of magnetometry. Magnetic hysteresis measurements showed that the total moment was a superposition of magnetic contributions from the recording layer, underlayer and substrate. The recording layer was composed of the cobalt-based alloy CoCrPt. The layer's magnetic response was characteristic of a hard-ferromagnet. The magnetisation was calculated by normalising the total ferromagnetic moment to the recording layer's volume. The magnetisation was interpreted as the recording grain's moment density averaged over the granular ensemble. Since the recording layer's magnetisation was a bulk measurement one cannot expect to extract reliable information regarding the grain's local magnetism of the order of 1.0-10.0 nm. The characterisation technique known as small angle neutron scattering (SANS) has the ability to measure the recording grain's magnetic structure on the sub-granular length scale. In the following section, the local magnetism of the LMRM samples AX1821, AX1646 and AX341 was investigated by using the characterisation technique of unpolarised SANS.

4.4.1 Scattering Model

The unpolarised SANS experiment measured the sample's diffraction pattern within a two-dimensional scattering plane oriented normal to the incident neutron beam, see section 3.1.2 SANS Geometry. In general the total scattering intensity from the LMRM recording layer was composed of nuclear and magnetic scattering components from a single grain. The interference scattering of neighbouring grains modulates the scattering intensity from the single grain. The scattering physics of the single grain was analogous to single slit diffraction in optics where the slit dimensions correspond to the grain's local length scale. The scattering intensity was described using the expression $I(q) \propto F^2(q)$ where F(q) is the form factor function [51]. The form factor expresses the grain's scattering density in reciprocal q-space. The Fourier transform of the form factor extracts information on the recording grain's scattering potential. The potential in real space characterises the target's physical or magnetic properties such as grain size, size distribution and probability of the scattering event.

The scattering intensity from an ensemble of recording grains is analogous to the interference pattern from a diffraction grating. In this case the grating type corresponds to the grain's spatial order where the slit dimensions define the inter-granular spacing. The scattering intensity will exhibit constructive and destructive interference between neighbouring grains. The scattering intensity was described by the modulated function, $I(q) \propto F(q)^2 S(q)$. The function S(q) is known as the structure factor, which models the interference scattering for an ensemble of grains [61]. The peak positions in reciprocal space correspond to density correlations in real space. The total correlation function h(r) relates these spatial correlations to the pair separation distance.

The above scattering expression assumes that the form factor and structure factor have a zero grain size distribution. In this case the grain size distribution was represented by a delta function. This was known as the monodispersed scattering model. In reality no grain ensemble is truly monodispersed and one must average the scattering intensity over a finite size distribution. The term polydispersed describes an ensemble scattering objects with a finite size distribution [52]. The scattering intensity for a polydispersed system of grains was approximated by

$$I(q)=N[\langle F^2(q)\rangle - \langle F(q)\rangle^2] + N\langle F(q)\rangle^2 \langle S(q)\rangle \quad (\text{counts s}^{-1}\ \text{srad}^{-1}), \qquad (4.3)$$

where N is the normalisation constant and $\langle\ \rangle$ represents the average over the grain size distribution. The details of the derivation were expressed in Chapter 2 section 2.5.1. Equation 4.3 was only valid for moderately sized distribution widths. If for example the granular distribution width was greater than 30% then the structure factor reduces to unity hence equation 4.3 simplifies to the following $I(q)=N\langle F^2(q)\rangle$.

The scattering model for the LMRM grain was determined by obtaining analytic expressions for the form factor and structure factor. To derive the form factor, one must search for a mathematical function (with a solvable Fourier transform) that describes the grain's shape and size. The analysis can be simplified by having prior knowledge on the grain's physical microstructure. Figure 4.20 shows TEM measurements [88] for the conventional LMRM sample at the granular resolution of 10.0 nm. The in-plane image shows a closed packed ensemble of irregular shaped grains with a finite grain size distribution. The grains were arranged in a cellular type pattern known as the Voronoi construction [82]. It would be mathematically difficult to determine an analytic form factor based on the Voronoi cell.

The shape and size of the Voronoi grid was modelled by replacing the irregular shaped cells with cylindrical objects. The form factor expression was reduced to the Fourier transform of a cylindrical object with a finite length. To account for the grain's irregular shaped cells, the form factor function was averaged over the gamma-Shultz size distribution function,

$$g(r)=b^{-1}\Gamma^{-1}(c)(r/b)^{c-1}\exp(-r/b), \qquad (4.4)$$

where $r_{mean}=bc$ and $\sigma^2_{mean}=b^2c$ represent the ensemble's mean radius and variance respectively [50]. The symbol $\Gamma(c)$ defines the gamma function. At a large variance the distribution function becomes broad and asymmetric. This type of distribution function was ideal for modelling recording grains that have formed through the process of nucleation. During the sample fabrication, the recording grains cannot be smaller than the critical nucleus size (smallest possible grain size). Hence the grain size distribution function will be truncated on the left-hand side. This property gives the distribution function its characteristic asymmetric shape.

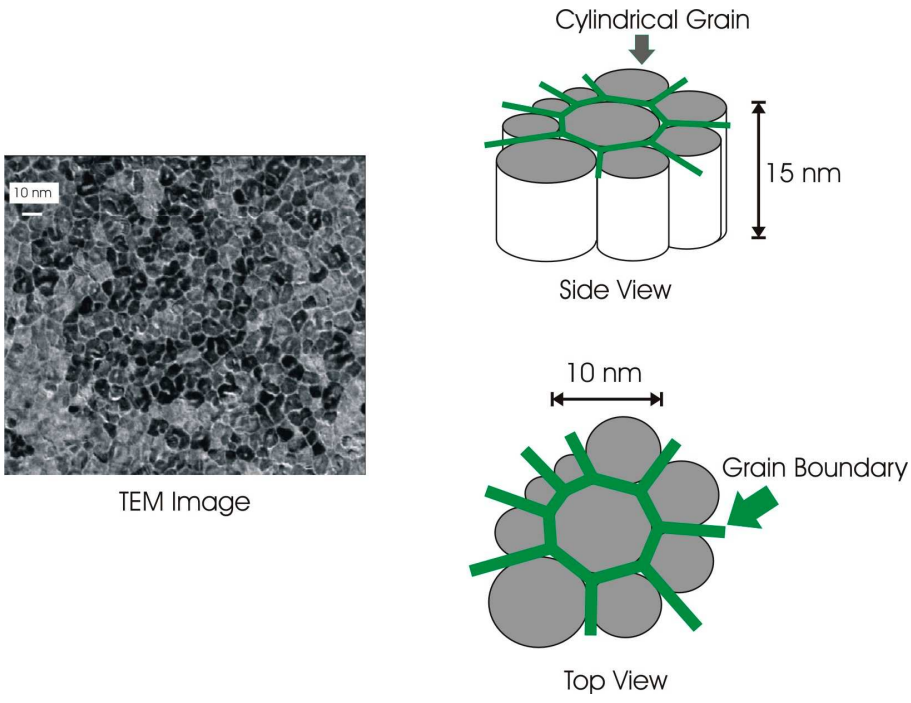

Figure 4.20: The TEM image of the conventional LMRM film [88]. The granular structure is modelled using cylindrical objects embedded in the grain boundary matrix.

The proposed scattering model assumes that the granular form factor was a rigid cylindrical object. This was a good approximation for nuclear and x-ray diffraction since the scattering potential most likely matches the shape and boundary conditions set out by the physical grain. The scattering model for the ferromagnetic grain was slightly more complicated due to the weakly magnetic grain boundary, which acts to 'soften' the magnetic scattering potential. Magnetic softening results from surface effects such as dipolar and exchange fields. The SANS scattering geometry for the softening effect is demonstrated in Figure 4.21. The recording grain starts out as a cylindrical object S_1 with no weakly magnetic grain boundary. The neutron beam scatters off multiple slices, which makes up the cylindrical object. The scattering potential as a function of radius was defined using the top-hat function. In object S_2 the grain boundary was introduced resulting in the recording grain's magnetic softening. This effect was represented by the multiple step scattering potential. Further magnetic softening leads to a near spherical object S_3 where the scattering potential approaches a continuous limit. The magnetic SANS measurements performed on the LMRM samples found that the recording grain's magnetic structure was correctly modelled using the spherical core-shell form factor.

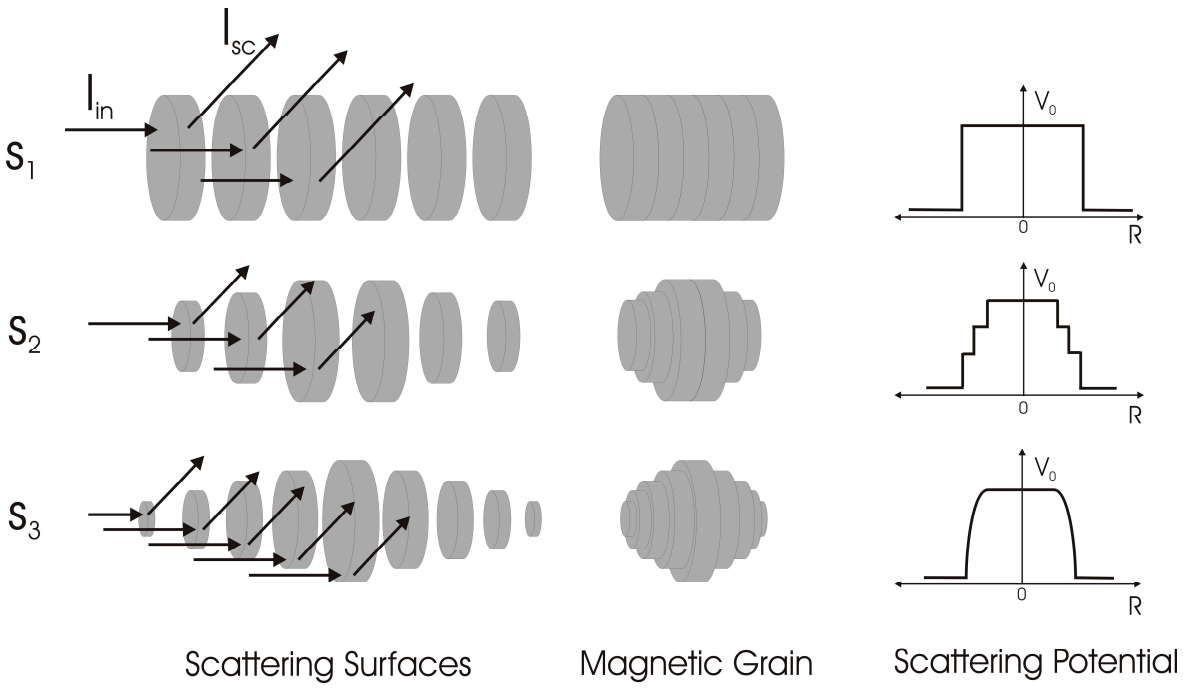

Figure 4.21: The magnetic recording grain is represented as a series of scattering surfaces. The effect of magnetic softening occurs at the grain's surface where $S_1 \rightarrow S_3$ represents the transition from cylindrical to spherical grain. The scattering potential V_0 is plotted as a function of the grain's radius R.

The magnetic recording grain was partitioned into a spherical core-shell structure as shown in Figure 4.22. The Fourier Transform of the spherical core-shell grain is expressed by

$$F_M(q) = \Delta\eta_c^M \left(\frac{4\pi R_c^3}{3}\right) f(q, R_c) + \Delta\eta_s^M \left[\left(\frac{4\pi R_s^3}{3}\right) f(q, R_s) - \left(\frac{4\pi R_c^3}{3}\right) f(q, R_c)\right], \quad (4.5)$$

where $f(q,R)=(qR)^{-3}[\sin(qR)-qR\cos(qR)]$ represents the shape function for a solid spherical object, see section 2.5.1 The first term represents the core form factor where R_c defines the core radius. The terms grouped within the square brackets express the outer shell form factor where R_s defines the radius of the shell. The coefficient's $\Delta\eta_c^M$ and $\Delta\eta_s^M$ define the magnetic scattering contrast for the core and shell components respectively. The contrast parameters are proportional to the magnetisation of the core and shell components. The core contrast was decomposed into its x and y components where $\Delta\eta_{cx}=\Delta\eta_c^M\cos(\varphi_c)$ and $\Delta\eta_{cy}=\Delta\eta_c^M\sin(\varphi_c)$. Similarly the shell components were expressed by $\Delta\eta_{sx}=\Delta\eta_s^M\cos(\varphi_s)$ and $\Delta\eta_{sy}=\Delta\eta_s^M\sin(\varphi_s)$. The angle's φ_c and φ_s define the direction of the core and shell magnetisation.

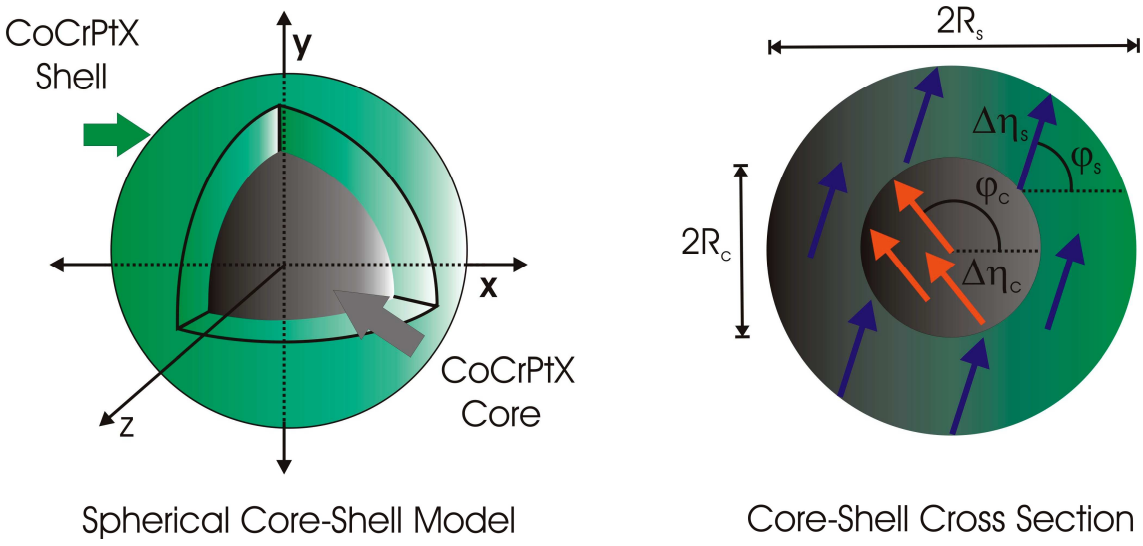

Figure 4.22: The proposed spherical core-shell structure for the longitudinal recording grain composed of the cobalt-based alloy CoCrPtX. The cross-section image shows the local micromagnetics within the grain's core and shell components.

4.4.2 Instrumentation

The LMRM samples AX1821, AX1646 and AX341 were characterised using the D11 instrument at the ILL, Grenoble France [63]. The overview of the D11 SANS instrument is depicted in Figure 4.23(a). The D11 instrument parameters are listed in Table 4.2. Measurements for the sample AX341 were performed on the D22 SANS instrument [64]. The initial task of the SANS experiment was to mount the LMRM sample at the target region, see Figure 4.23(b). The media sample was fabricated into the shape of a disc with a diameter of 1.72 cm and an approximate thickness of 0.02 cm. It was observed that the neutron scattering from a single sample was much smaller than the background scattering from instrument components such as the cryostat. The magnetic scattering statistics of the recording layer were improved by assembling the target sample into a stack of 26 identical sample discs. The LMRM samples were shuffled to ensure that the zero field magnetic diffraction pattern was isotropic within the scattering plane. This scattering property was further explained in the following section on measurements

SANS SPECIFICATIONS	***DETAILS***
Neutron Guide	Cold Neutron Guide H15
Monochromator	Helical Slot Velocity Selector
Wavelength	$0.45\ nm < \lambda < 4.0\ nm$
Resolution	$100\times\Delta\lambda/\lambda=9\%$
Incident Neutron Flux 10x10 mm^2 sample	$3.20\times10^{7}\ n\ cm^{-2}s^{-1}$
q-Range	$5.0\times10^{-3}\ nm^{-1} < q < 4.40\ nm^{-1}$
Detector	2D ^{3}He 64×64 elements of 10×10 mm^2
Collimation	1.5-40.5 m
Sample-Detector Distance	1.1-36.7 m continuously

Table 4.2: The instrument parameters for the D11 SANS machine [63].

(a)

(b)

(c)

Figure 4.23: Snapshots of the D11 SANS instrument. The first image (a) shows an overview of the SANS tube which houses the ^{3}He position sensitive detector. The tube extends to the far end of the instrument hall with a maximum sample-detector distance of 36.7 m. The second image (b) depicts the SANS sample target while the following image shows the (c) cryostat fixed to the table mount.

The sample stack shown in Figure 4.24 was encased in an aluminium foil and secured to the aluminium sample holder. The sample holder was lined with cadmium strips, which reduced the nuclear background scattering from the instrument components. In this SANS experiment the sample AX1821 was magnetised using an electromagnet. The electromagnet reaches a maximum magnetic field of 1.3 T, which was adequate to saturate the NiP sample. The samples AX1646 and AX341 saturate at the in-plane field of 2.0 T. Hence these samples were magnetised using the cryomagnet. The samples were inserted into their respective magnet and bolted onto the table mount, see Figure 4.23(c). The Dornier velocity selector channelled the incident neutron beam with an average wavelength of λ=4.5 Å. The SANS instrument was aligned by centring the sample on the collimated beam spot.

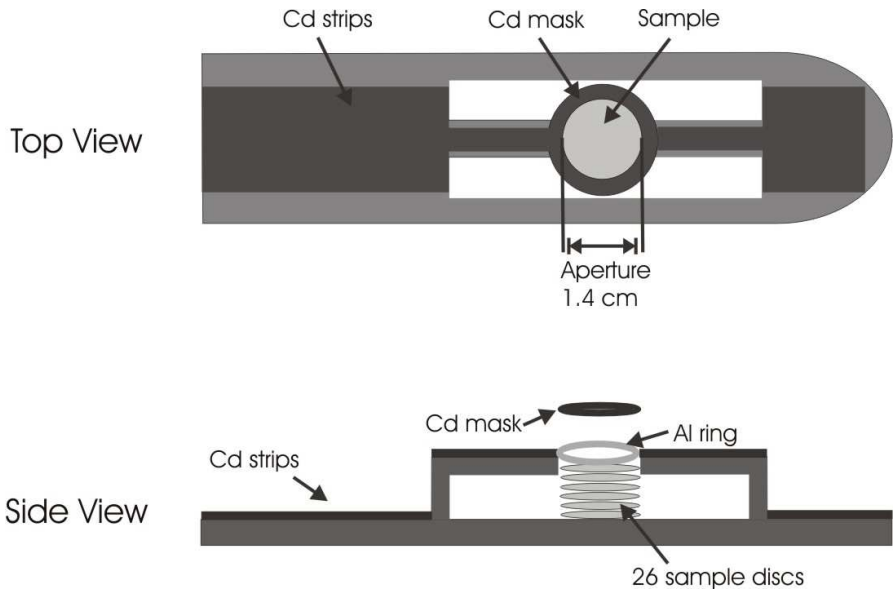

Figure 4.24: The schematic of the aluminium sample holder. The 26 samples are fastened to an aluminium ring located at the centre of the holder. The Cd mask is fabricated with a 1.4 cm aperture that allows the incident beam to illuminate the sample.

4.4.3 Measurements

The SANS measurements were performed at the sample-detector distances of 1.5, 5.0, 8.0, 12.0 and 20.5 m. The neutron beam has a neutron wavelength of 4.5 Å. The momentum transfer argument spans the q-range of 6.26×10^{-3} Å^{-1}<|**q**|<0.27 Å^{-1}. This scattering q-range was adequate to measure the recording layer's sub-granular structure of the order of 10-100 Å. The measurements consisted of three separate parts (a) zero field sample transmission intensity I_T, (b) zero field background scattering $I_B(q)$ and (c) magnetic field foreground scattering $I_F(q)$. The foreground and background scattering measurements at different sample-detector distances were matched up by calculating the solid angle correction.

The transmission measurement I_T was used to determine the q=0 position on the detector and to extract the instrument's incident flux. In Figure 4.25, the transmission intensity is measured as a function of q at the collimator distance of 1.5 m. The I_T measurement was performed with the appropriate attenuator, which protects the detector from the full intensity of the incident beam. The inset defines the q=0 position of the straight through beam. The flux on the sample was expressed by $\Phi=AI_T/S$, where S is the sample area exposed to the incident beam and A is the beam attenuation. The A-attenuator depends on the collimation and sample-detector distance. The S-area was determined using a Cd mask with an aperture diameter of 1.4 cm. The incident flux as a function of collimation distance is plotted in Figure 4.26. The plot shows the effective flux was modified for a change in collimation distance. These calculations were used to correct the corresponding flux change at each scattering measurement. The flux was also used to normalise the scattering intensity to cross-section units of cm^2.

The background scattering was composed of nuclear scattering and isotropic magnetic scattering from the sample and instrument components. The background measurement was used to subtract the nuclear scattering intensity from the foreground measurements. The total background scattering was expressed by the following $I_B(q)=I'_N(q)+\{I_N(q)+I_M^{iso}(q)\}$. The first term represents the nuclear scattering from the instrument such as the magnet and sample holder. The curly bracket term represents the isotropic nuclear and magnetic scattering from the sample stack. In this experiment, the nuclear scattering from the instrument dominates the background measurement where $I'_N(q)>>\{I_N(q)+I_M^{iso}(q)\}$. The nuclear scattering intensity $I_N(q)$ was a superposition of the Al substrate, soft underlayer and recording layer multiplied by 26 sample layers.

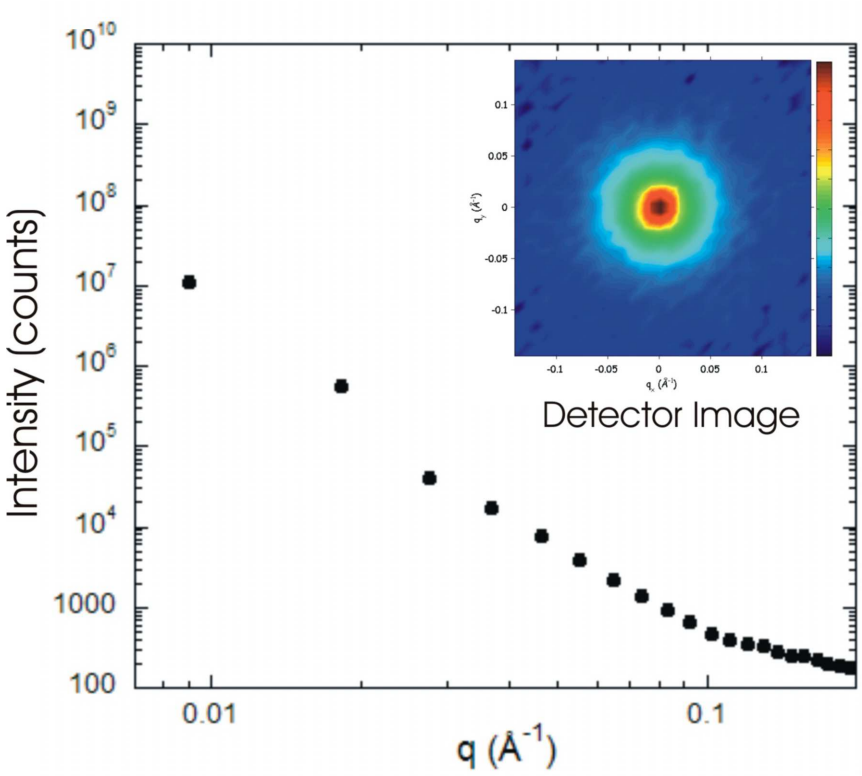

Figure 4.25: The transmission measurement at the detector distance of 1.5 m.

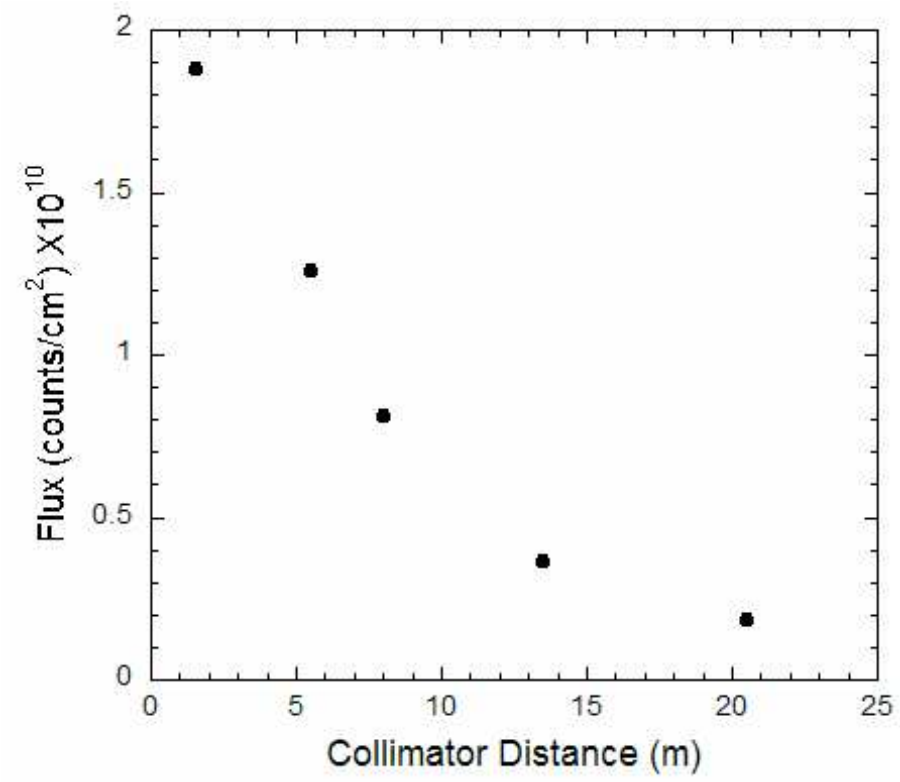

Figure 4.26: The incident neutron beam flux as a function of collimator distance.

The magnetic scattering component $I_M^{iso}(q)$ at zero field was the superposition of scattering intensities from 26 recording layers. The isotropic magnetic scattering was achieved by shuffling the stack of 26 discs which effectively randomises the in-plane magnetisation. This ensures that the background subtraction contains no anisotropic magnetic components that can distort the foreground measurements. The method for randomising the stacks in-plane magnetisation was understood in terms of the following argument. The recording layer consists of an ensemble of granular moments that exhibit a strong in-plane magneto-crystalline anisotropy. At zero field the moment ensemble forms the remanent state whereby the average magnetisation <M> lies along a preferred in-plane direction. The magnetic diffraction pattern was anisotropic within the scattering plane. When the discs were shuffled and combined into the sample stack the average magnetisation of each disc points in a random direction. The superposition of 26 magnetisation pattern results in a demagnetised sample and hence an isotropic magnetic scattering pattern. Figure 4.27 illustrates a series of recording layers alongside their simulated diffraction patterns.

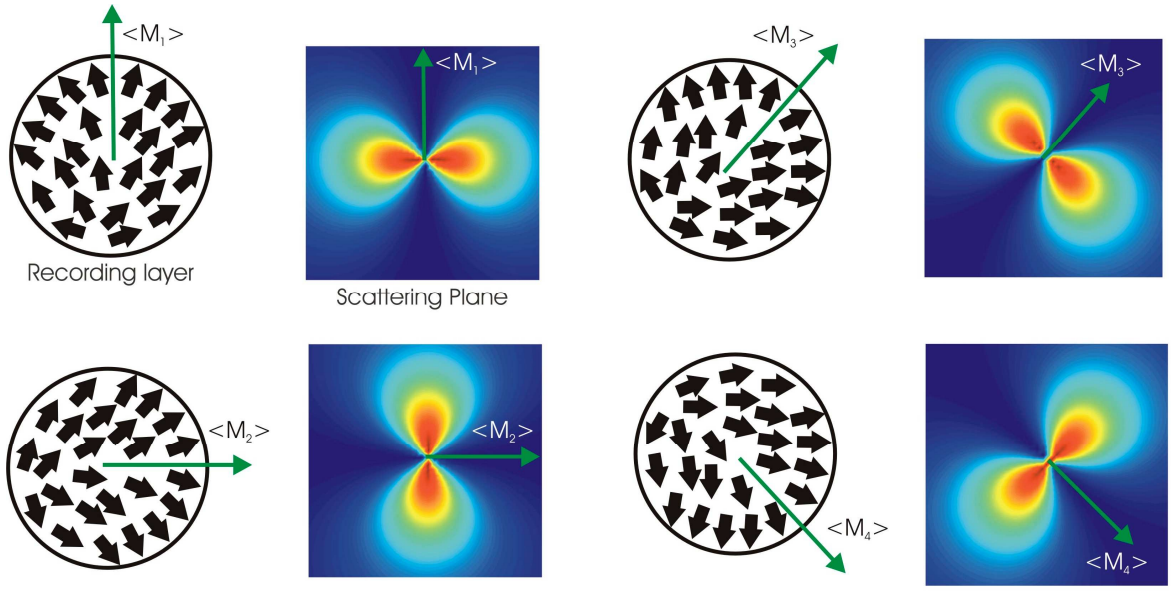

Figure 4.27: The magnetisation map within the recording layer where <M> defines the sample's remanent magnetisation. The anisotropic magnetic diffraction plot is illustrated for each remanent state.

The foreground measurement $I_F(q)$ was composed of nuclear scattering and magnetic scattering components from the instrument and sample respectively. The foreground scattering at an applied magnetic field was expressed by the following $I_F(q)=I'_N+\{I_N(q)+I_M^{aniso}(q)\}$. The nuclear scattering components remain unchanged for the foreground measurement. The term $I_M^{aniso}(q)$ represents the anisotropic magnetic scattering from the sample stack where the granular moments within all 26 recording layers align along the field direction. The magnetic scattering intensity was expressed by $I_M^{aniso}(q)=I_M(q)\sin^2\alpha$ where α defines the azimuthal angle between the scattering and magnetisation unit vectors **q** and **m** respectively. The foreground measurements were performed within the applied in-plane field range of $0.45\,T<H<2.20\,T$ at the quoted sample-detector distances.

For the purposes of illustration, the background and foreground diffraction patterns were modelled within the two-dimensional scattering plane. The nuclear and magnetic scattering components were modelled by the simplified function $I(q)=Aq^{-4}+B$ known as the Porod scattering function [28]. The left plot of Figure 4.28 shows an isotropic diffraction pattern at zero field where the magnetisation vectors were randomised in-plane. In the right plot, the in-plane magnetic field was applied along the q_x axis. The diffraction pattern exhibits magnetic scattering lobes along the q_y-axis.

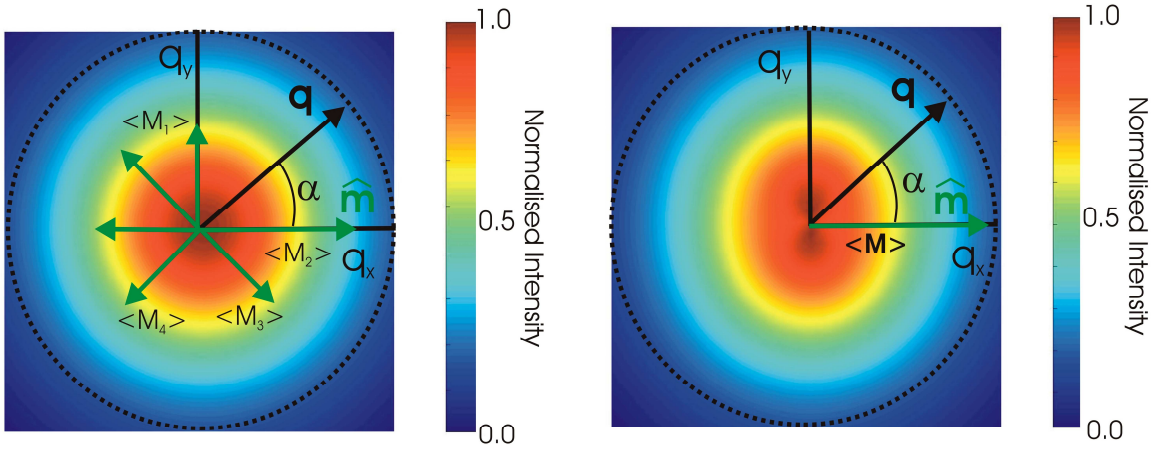

$I_B(q)=I_N(q)+I_M^{iso}(q)$ $I_F(q)=I_N(q)+I_M(q)\sin^2\alpha$

Figure 4.28: The modelled diffraction patterns for the isotropic background scattering $I_B(q)$ and the foreground scattering intensity $I_F(q)$ where the magnetisation unit vector **m** is defined along the q_x axis. The nuclear and magnetic components are represented by the Porod scattering intensity.

The magnetic diffraction pattern contained within the foreground simulation was extracted by subtracting off the zero field background components. The remaining scattering intensity consists of a difference between the magnetic anisotropic and isotropic components. The left-plot of Figure 4.29 shows the modelled difference pattern where $\Delta I_M = I_M^{aniso}(q) - I_M^{iso}(q)$. The diffraction plot shows a strong positive (red) anisotropic scattering within the two-dimensional scattering plane. Due to the moment orientation factor, $\sin^2\alpha$, the magnetic scattering component vanishes along the q_x axis. The anisotropic scattering was superimposed on the isotropic magnetic diffraction pattern contoured in dark blue. The right difference plot of Figure 4.29 shows the three-dimensional pattern for isotropic and anisotropic scattering components. The scattering lobes were superimposed on the magnetic isotropic component, which falls below zero.

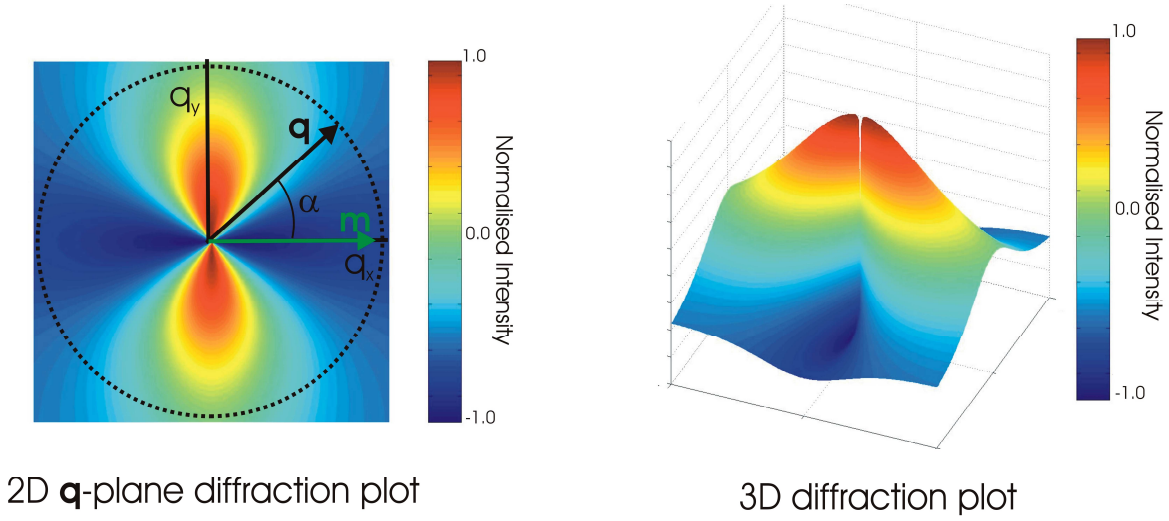

Figure 4.29: The simulated 2D and 3D magnetic difference plots resulting from the superposition of anisotropic and isotropic scattering components.

The magnetic difference plot was composed of the anisotropic magnetic scattering component, which was superimposed on the isotropic magnetic scattering background. The amplitude was defined as the magnetic scattering intensity at an applied in-plane field. The offset was defined as the magnetic scattering intensity at zero field. These scattering components were extracted from the difference plot by using the GRASP fitting program ANCOS^2 [89]. The program fits the scattering function $I_{ANCOS}{}^2=I_a+I_b\cos^2(\theta+\delta_c)$ to the difference plot defined within an annulus of radius q_i and width Δq_i. The intensity terms I_a and I_b represent the offset and amplitude respectively. The moment orientation function was described by the cosine squared function where θ defines the polar angle. The angular parameter δ_c defines the phase shift of the moment orientation factor. Spatially this represents a change in direction for the in-plane average magnetisation. The ANCOS^2 program outputs three sets of data; (a) amplitude $I_b(q)$, (b) offset $I_a(q)$ and (c) phase shift δ_c. Figure 4.30 illustrates the ANCOS^2 program using the simulated difference plot.

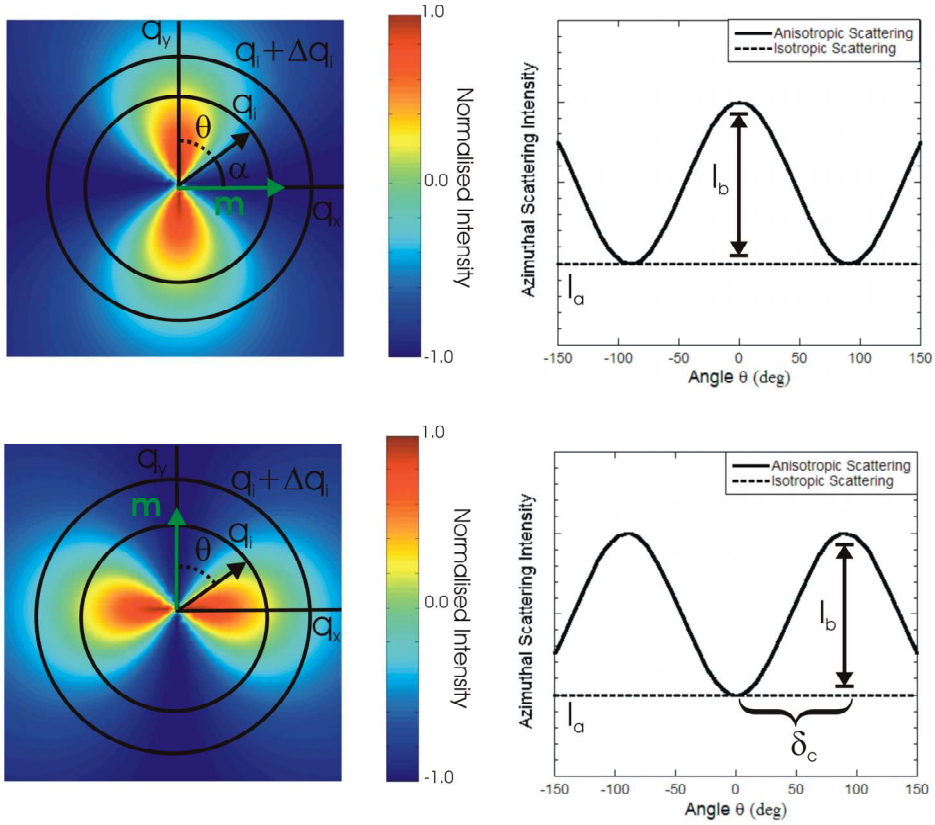

Figure 4.30: The simulated difference plot for an in-plane moment along the q_x and q_y axes. The ANCOS^2 function fits the difference plot over an annular ring of radius q_i and width Δq_i. The amplitude I_b, offset I_a and phase shift δ_c are defined on the azimuthal scattering intensity plot.

4.4.4 Results and Discussion-AX1821

The SANS diffraction pattern of AX1821 was measured at the in-plane field of 1.0 T. Due to the samples soft ferromagnetic nature, the applied field was adequate to saturate the moments, refer back to section 4.3.2 for the hysteresis measurements of AX1821. The background measurements were performed in the zero field state where the moments were randomly oriented within the sample plane. The measured scattering intensity was converted to the differential scattering cross-section by the direct beam correction, $d\sigma/d\Omega=I(q)/\Phi_{inc}$ where I(q) is the foreground or background scattering intensity and Φ_{inc} is the incident flux on the sample. Figure 4.31 shows the foreground and background scattering measurements at the sample-detector distance of 1.5 m. This distance corresponds to the q range of 0.04 $Å^{-1}$<q<0.30 $Å^{-1}$. Below the diffraction plot was a schematic of the magnetic scattering geometry, note the image represents the stack of 26 samples. The grey arrow depicts the direction of the incident neutron beam. The zero field background was subtracted from the foreground scattering at 1.0 T resulting in the magnetic difference plot.

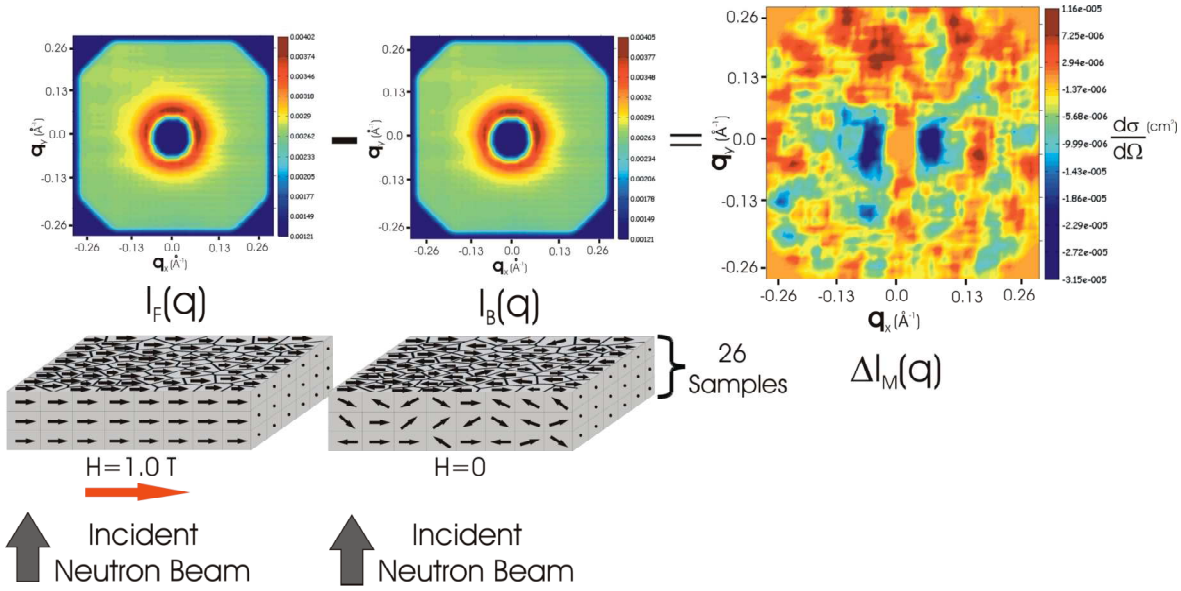

Figure 4.31: The AX1821 1.0 T foreground $I_F(q)$ and background $I_B(q)$ measurements at the sample-detector distance of 1.50 m. The subtraction results in the magnetic difference expressed in cross-section units.

The difference plot defined by ΔI_M shows an anisotropic diffraction pattern about the two-dimensional scattering plane. This was characteristic of a system of magnetic domains aligned along the field direction. The GRASP program extracts the azimuthal scattering data as a function of $\theta=90^0-\alpha$, see Figure 4.32. The azimuthal data exhibits the $\sin^2\alpha$ dependence where α is the angle between the **q** and **m** vectors. The difference plot was fitted using the scattering function $\Delta I_M(q)=I_a+I_b\cos^2(\theta+\delta_c)$ where I_a and I_b represent the magnetic scattering intensities at zero and 1.0T respectively.

Figure 4.33 compares the foreground and anisotropic magnetic scattering intensities at the in-plane field of 1.0 T. The foreground scattering was on average a factor of 10 larger than the anisotropic component. This shows that the foreground component was dominated by the nuclear background scattering. The majority of the background scattering originates from the electromagnet used to magnetise the sample. The magnetic scattering intensity exhibits Porod Scattering which was characteristic of a magnetically amorphous material. The anisotropic scattering intensity was modelled using the Porod function $I_M^U(q)=A/q^n+B$ where A, B and n are the fitting parameters. Figure 4.34 plots the anisotropic magnetic scattering data and fit on a log-log scale.

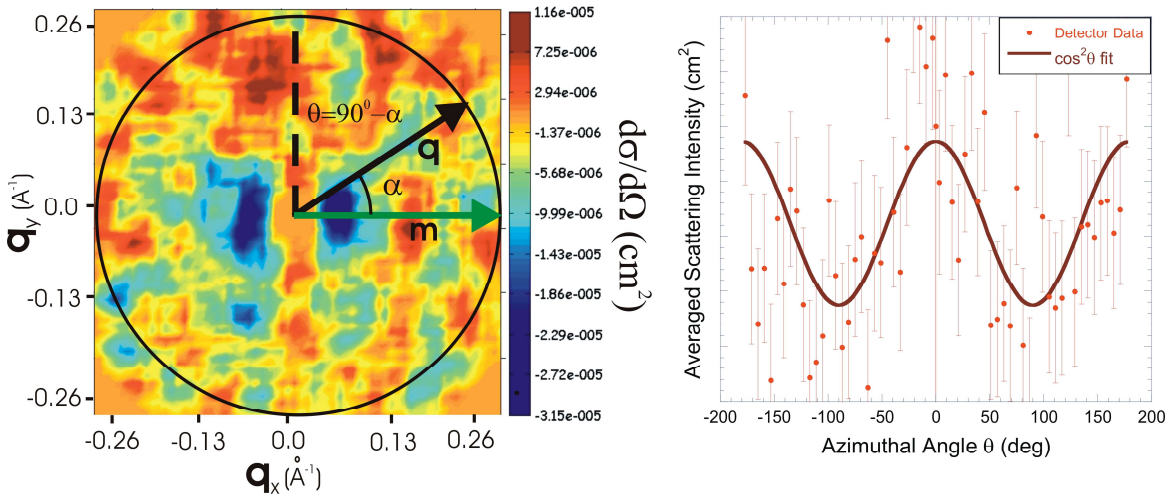

Figure 4.32: The AX1821 1.0 T magnetic difference plot measured at the sample-detector distance of 1.5 m. The azimuthal scattering intensity is calculated over the q range 0.04 Å^{-1} <$q_{1.5m}$<0.30 Å^{-1}. The orientation dependence is expressed by $\sin^2\alpha$. The azimuthal scattering intensity is fitted by the function $I_a+I_b\cos^2(\theta+\delta_c)$ where $\theta=90^0-\alpha$.

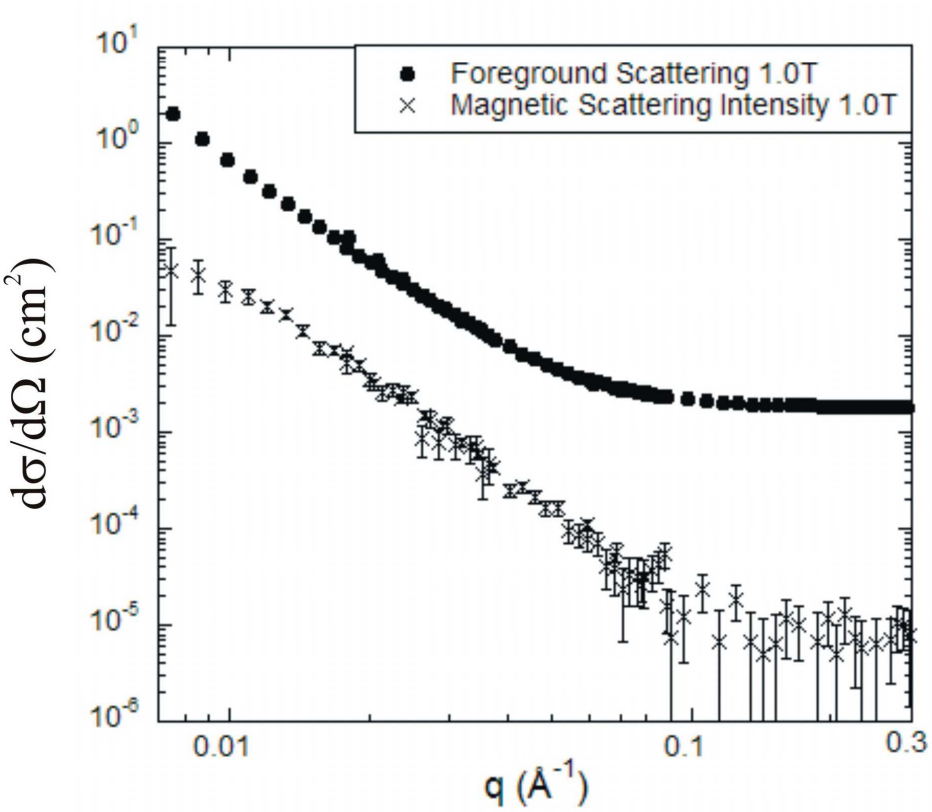

Figure 4.33: The AX1821 1.0 T foreground measurement and the anisotropic magnetic scattering intensity.

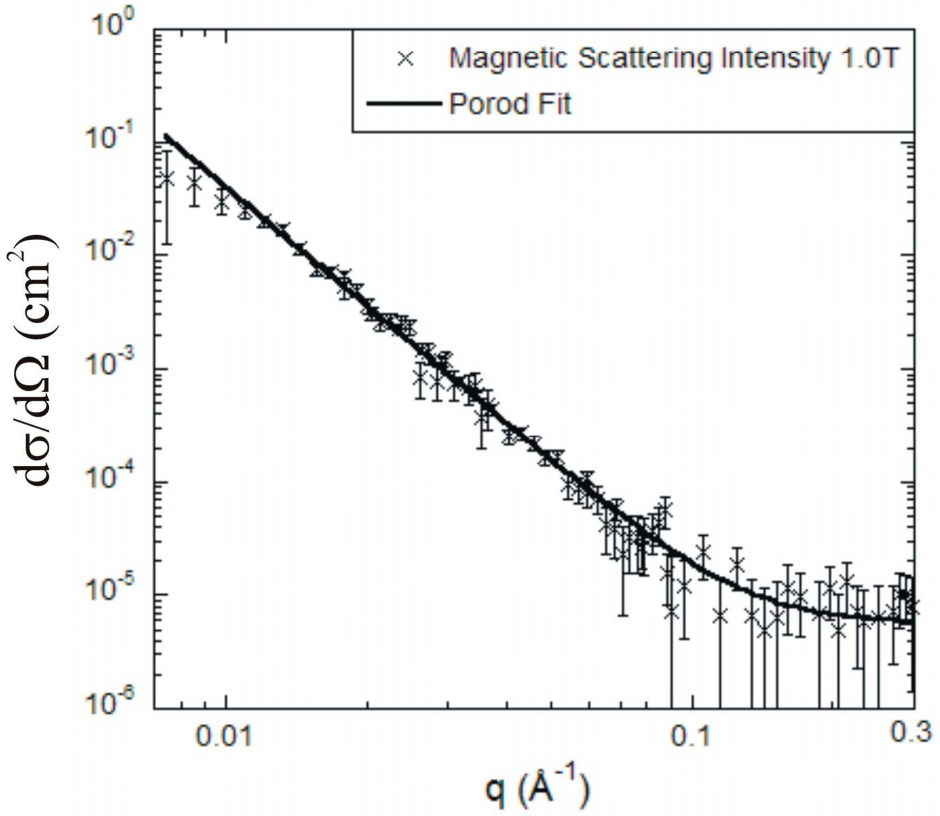

Figure 4.34: The AX1821 1.0 T anisotropic magnetic scattering intensity fitted to the Porod scattering function $I_M^{aniso}(q)=Aq^{-4}+B$.

The SANS diffraction pattern of AX1821 was also measured at the remanent state. The two-dimensional magnetic difference plot at the sample-detector distance of 5.0 m is shown in Figure 4.35. The anisotropic magnetic scattering was quite noisy within the scattering plane. The azimuthal scattering data shows a less than ideal $\sin^2\alpha$ dependence. It would appear that the magnetic scattering signal was too weak to measure any definite anisotropy within the scattering plane. The magnetic scattering intensity shows Porod type scattering behaviour, see Figure 4.36. The Porod fit remains questionable due to the sample's noisy scattering statistics. The severity of the poor scattering statistics was demonstrated by plotting the $ANCOS^2$ phase as a function q, see Figure 4.37. The $ANCOS^2$ fit shows multiple phase shifts. The scattering data appears to exhibit no preferred moment orientation factor over the measured q range. The poor scattering statistics were attributed to the reduced magnetic scattering contrast at remanence. By referring back to the AX1821 hysteresis measurement at 300 K, the remanent magnetisation was approximately sixteen times the size of its saturation value. As a result the magnetic contrast, which is proportional to the sample's magnetisation, was reduced by a similar magnitude.

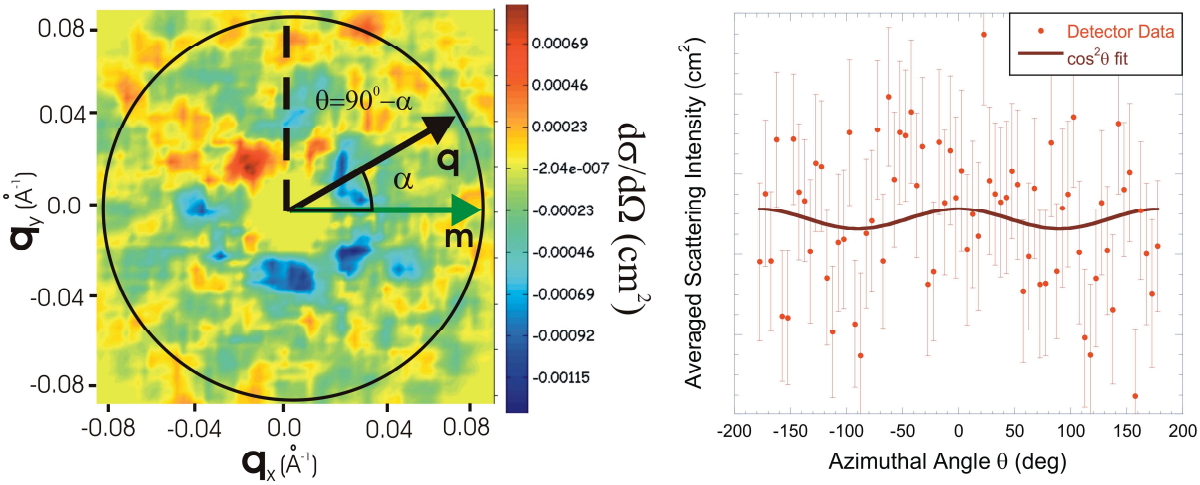

Figure 4.35: The AX1821 remanent magnetic difference plot measured at the sample-detector distance of 5.0 m. The azimuthal scattering intensity is calculated over the q range 0.02 Å^{-1}<$q_{5.0m}$<0.09 Å^{-1}.

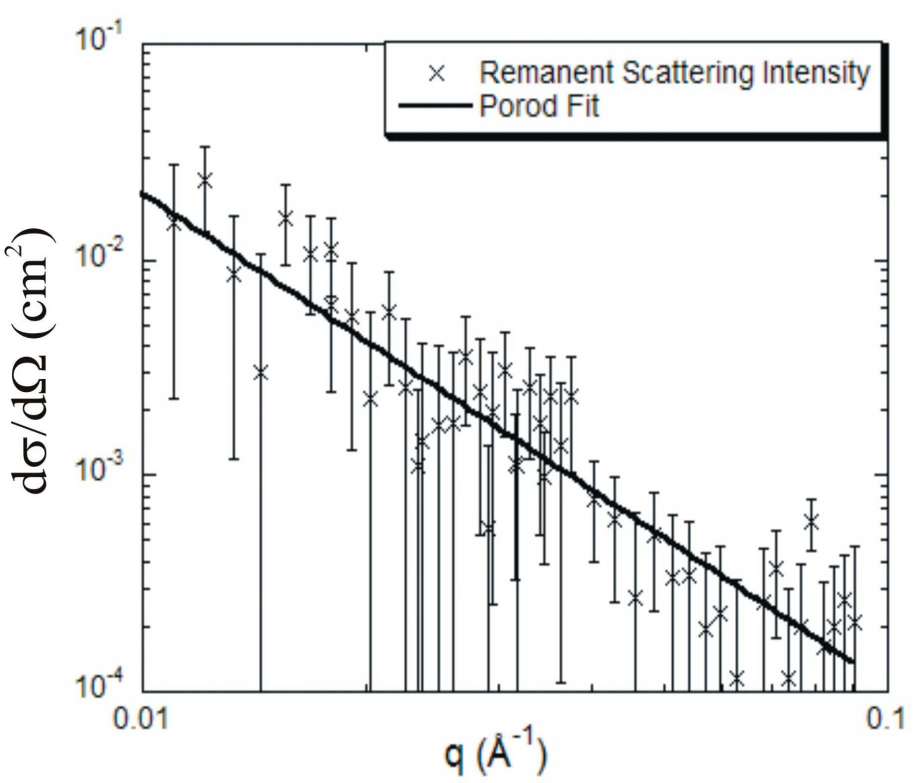

Figure 4.36: The AX1821 magnetic scattering intensity at remanence fitted to the Porod scattering function $I_M^{aniso}(q)=Aq^{-4}+B$.

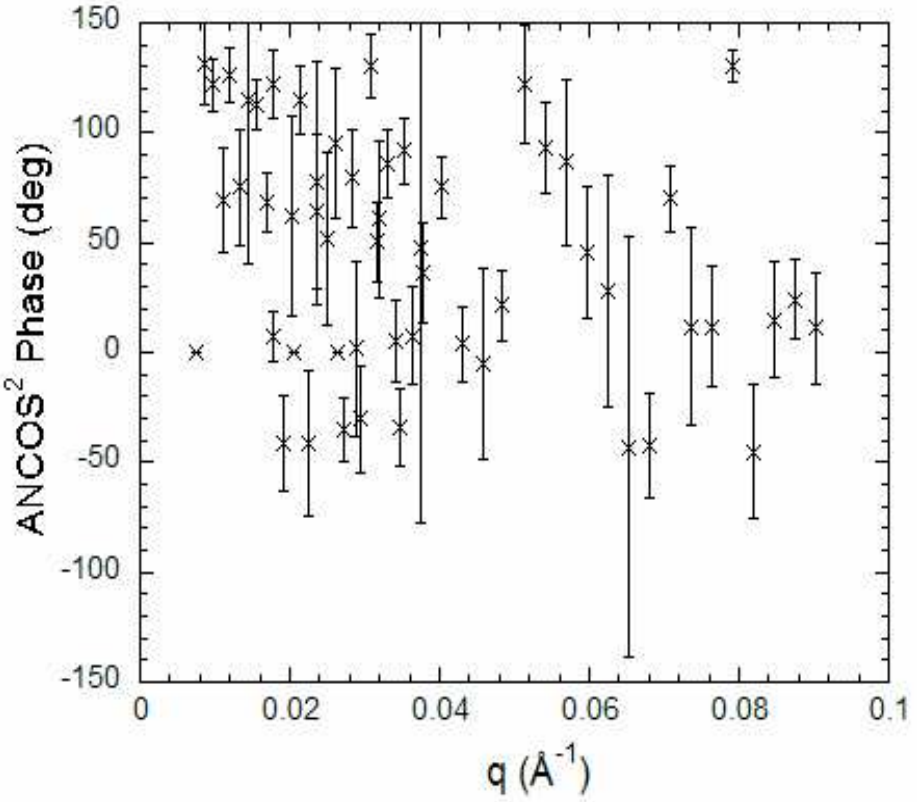

Figure 4.37: The AX1821 $ANCOS^2$ phase at remanence. The zero phase refers to a moment orientation along the q_x axis while for the $\pi/2$ phase the moments are aligned along the q_y-axis.

4.4.5 Results and Discussion-AX1646

The SANS diffraction pattern for AX1646 was measured at the applied in-plane field of 2.2 T. The hysteresis measurements of AX1646 showed the recording layer was fully saturated at the in-plane field of 2.2 T. Figure 4.38 shows the SANS foreground and background diffraction patterns at the sample-detector distance of 1.50 m. This distance corresponds to the q range of 0.04 $Å^{-1}$<q<0.27 $Å^{-1}$. The magnetic scattering geometry was shown for the stack of 26 samples. For the foreground measurement, the magnetic moments within the soft underlayer (grey) and recording layer (green) were saturated in-plane. The background scattering measurements show the recording layer's in-plane moments aligned along their easy axis. The dark-grey arrows represent the direction of the incident beam with respect to the applied magnetic field. The scattering measurements were normalised to the incident flux calculation. The difference plot exhibits strong scattering anisotropy about the detector plane. The contour plot shows the preferred magnetic scattering as red coloured lobes. Due to the moment orientation factor, the anisotropic magnetic scattering drops off along the x-axis. The blue region represents the offset of the zero field magnetic scattering intensity.

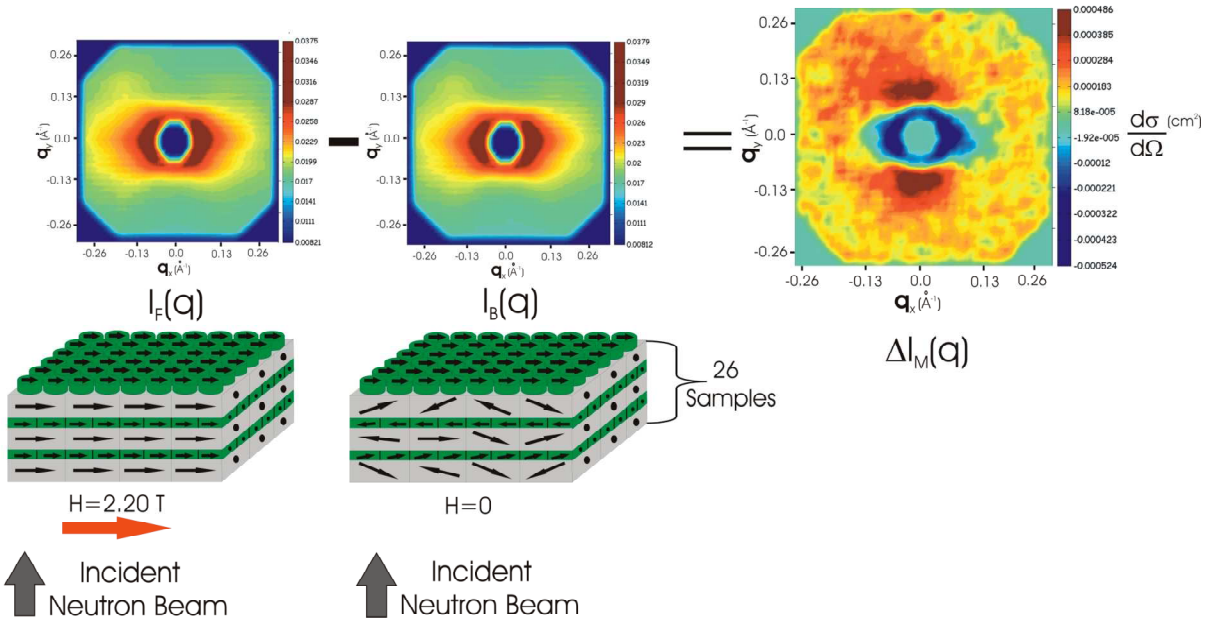

Figure 4.38: The AX1646 2.2 T foreground and background scattering measurements at the sample-detector distance of 1.50 m. The background subtraction gives the magnetic difference plot.

The azimuthal scattering intensities were shown for the detector distances of measurements of 1.5 m and 20 m, see Figure 4.39. The black annulus defines the respective measurements of 0.04 $Å^{-1}$<$q_{1.5m}$<0.30 $Å^{-1}$ and 0.01 $Å^{-1}$<q_{20m}<0.02 $Å^{-1}$. The magnetic scattering was fitted using the function $I(q)=I_a+I_b\cos^2(\theta+\delta_c)$. In Figure 4.39(a) the cosine^2 function closely fits the magnetic intensity within the scattering plane. The scattering function does not change phase where $\delta_c=0$. This indicates that the in-plane magnetisation was fully aligned along the q_x-axis. In Figure 4.39(b), the larger detector distance shows no phase change in the cosine^2 function. There was a uniform saturation of moments throughout the underlayer and recording layer. Note for this low q-range the scattering anisotropy mainly originates from the NiP soft underlayer.

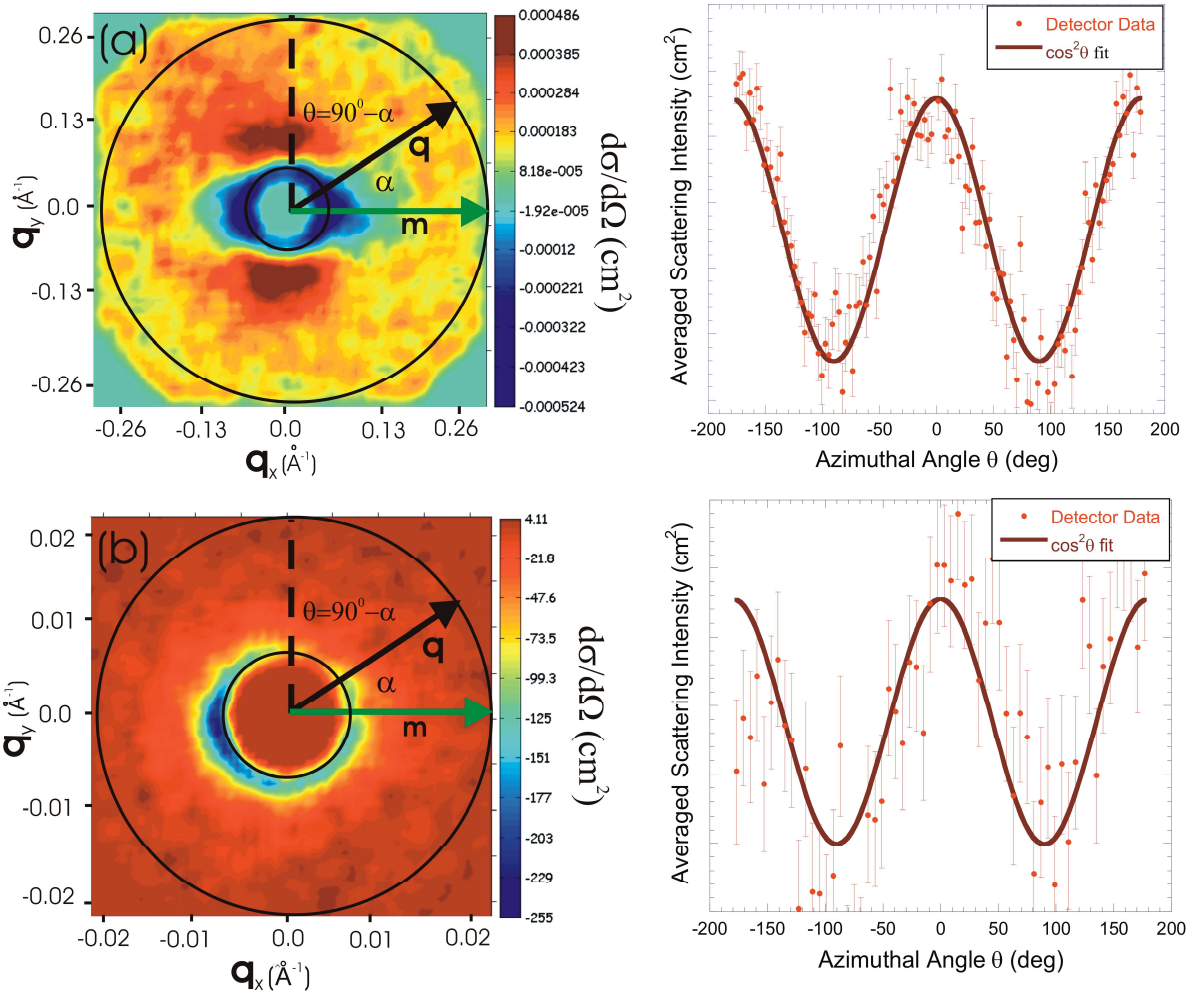

Figure 4.39: The AX1646 2.2 T magnetic difference plot measured at the sample-detector distance of (a) 1.5 m and (b) 20.0 m. The azimuthal intensity was calculated over the respective q ranges of 0.04 $Å^{-1}$<$q_{1.5m}$<0.30 $Å^{-1}$ and 0.01 $Å^{-1}$<q_{20m}<0.02 $Å^{-1}$.

The foreground and anisotropic scattering components were plotted on log-log scale, see Figure 4.40. The foreground scattering was on average 100 times larger than the magnetic scattering intensity. This intensity difference was due to the dominance of the nuclear background scattering, which originates mainly from the cryostat window. Note the foreground scattering of AX1646 was greater than the AX1821 experiment. It appears that the nuclear scattering background from the cryostat was approximately ten times larger than the electromagnet background. The magnetic anisotropic scattering was a superposition of the recording layer and underlayer scattering components. At low q the magnetic scattering intensity was characteristic of Porod scattering. The NiP underlayer dominates the magnetic scattering where the amorphous grains form a random size distribution of domain clusters. At $q>0.04\,Å^{-1}$ the magnetic scattering intensity deviates from Porod scattering behaviour. There was an immediate increase in the scattering intensity at $q=0.1\,Å^{-1}$ and $q=0.25\,Å^{-1}$. These magnetic features originate from the samples recording layer that contain structural information on the grain size and grain size distribution.

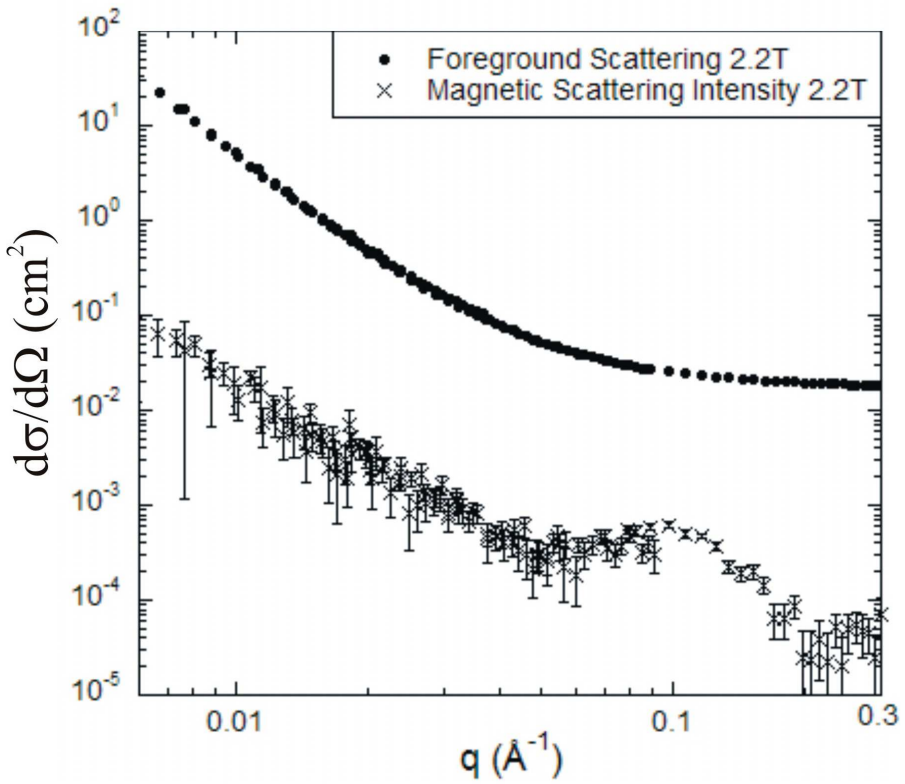

Figure 4.40: The AX1646 2.2 T foreground measurement and anisotropic magnetic scattering intensity.

The anisotropic magnetic scattering intensity was expressed by the following, $I_M^{aniso}(q)=I_M^R(q)+I_M^U(q)$ where the terms $I_M^R(q)$ and $I_M^U(q)$ represent the scattering intensity from the recording layer and soft underlayer respectively. The recording layer scattering intensity was modelled using equation 4.3. The grain size distribution was represented by the gamma-Shultz function, equation 4.4. The sub-granular structure in q-space was modelled by the spherical core-shell form factor, see equation 4.5. To test the validly of the core-shell form factor, the scattering data was also fitted with the solid sphere model. The interference scattering was described by the structure factor S(q) which was calculated using the Percus-Yevick method. The magnetic scattering from the NiP underlayer was expressed by the Porod relation $I_M^U(q)=Aq^{-n}+B$. The magnetic scattering data was fitted using the Nonlinear Least Squares Method (NLS) [90].

The magnetic scattering intensity at the in-plane field of 2.2 T was fitted with the solid sphere form factor. Figure 4.41 shows a series of fits for the granular diameters of 20.0 Å, 30.0 Å and 106 Å with a grain size distribution of 30%. The solid sphere model at 20.0 Å shows the closest fit to the scattering data. At $q<0.04$ Å^{-1} the magnetic scattering data was easily modelled using the Porod function. For the q-range $q>0.04$ Å^{-1} the form factor partially fits the scattering structure though fails to predict the intensity peak at $q=0.10$ Å^{-1}. As the diameter was increased, the tail of the form factor intensity was absorbed into the Porod scattering term where the scattering intensity takes the form, $I_M^{aniso}(q)\propto q^{-4}$. These fit results provide evidence that the recording grain were not entirely single phased magnetic particle.

The recording grain's multi-phased magnetic structure was modelled using the spherical core-shell model. Figure 4.42 shows the NLS fit to the magnetic scattering intensity at the in-plane field of 2.2 T. The model shows reasonable agreement with the scattering data where the closeness of fit $\chi^2=1.33$. Table 4.3 shows the NLS fit parameters. The magnetic scattering was devoid of any interference scattering between magnetic grains. This scattering characteristic occurs for highly amorphous magnetic grains where the size distribution, about 26%, damps out any interference effects from neighbouring grains. As a consequence the Percus-Yevick structure factor reduces to unity where $S(q)\approx 1.0$. The scattering intensity expression, equation 4.3, simplifies to the following relation, $I_M^{aniso}(q)=N\langle F^2(q)\rangle$.

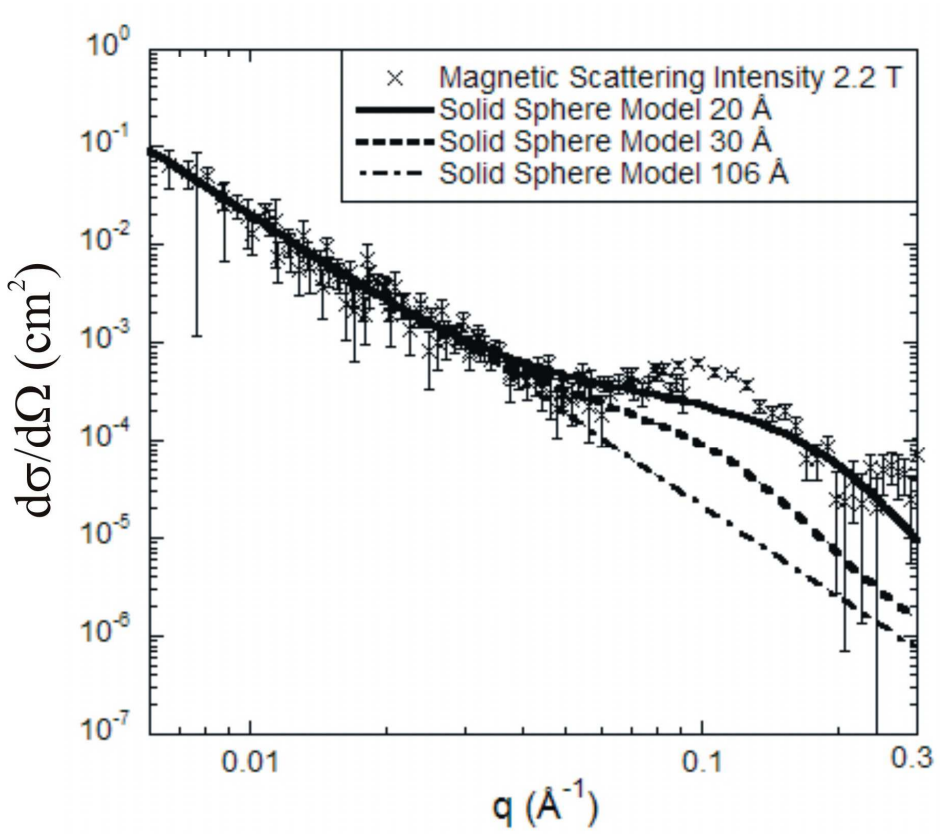

Figure 4.41: The AX1646 2.2 T anisotropic magnetic scattering intensity fitted to the solid sphere model of diameter 20 Å, 30 Å and 106 Å.

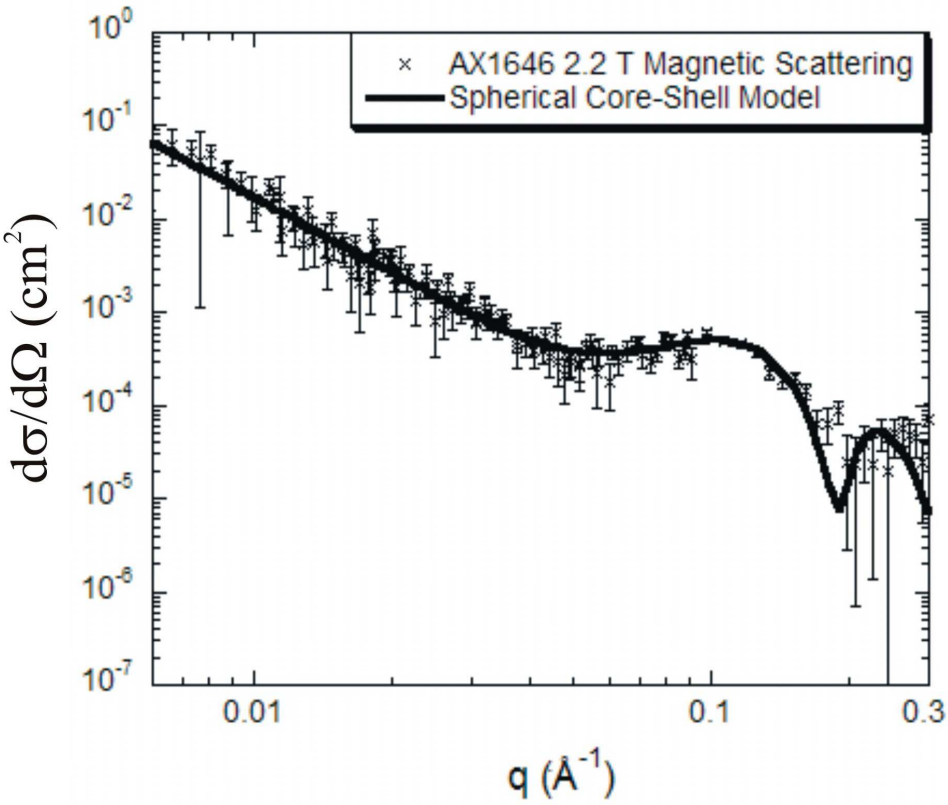

Figure 4.42: The AX1646 2.2 T anisotropic magnetic scattering intensity fitted to the spherical core-shell model.

The spherical core-shell form factor $F_M(q)$ provides information on the recording grain's ferromagnetic sub-granular structure. The average core and shell diameter were 60.0 ± 1.00 Å and 112.0 ± 1.50 Å respectively. The grain ensemble was polydisperse with a grain size distribution of 26%. These results moderately agree with the physical grain size of the order of 120.0 Å with a grain size distribution of 33% [76]. The difference between the physical and magnetic grain size defines the weakly magnetic region of the outer shell known as the grain boundary. For example the thickness of this grain boundary was approximately t=|120-112|=8.0 Å. This thickness is typical for a Cr-enriched grain boundary of order 6-12%.

The form factor scaling constants provided the grains core and shell magnetic contrast components. The core component was expressed by $\Delta\eta_c^M=\eta_c-\eta_s$ where η_c and η_s represent magnetic scattering length density of the core and shell components. The magnetic scattering length density was proportional to the core or shell magnetisation at q=0. The grain's shell contrast takes the form $\Delta\eta_s^M=\eta_s-\langle M\rangle$ where $\langle M\rangle$ is the volume averaged magnetisation of the recording grain. The average magnetisation of the core and shell components was expressed by the following expression $\langle M\rangle=v_cM_c+v_sM_s$ where $v_c=V_c/V_t$ and $v_s=Vs/V_t$ represent the core and shell volume fractions respectively. The core and shell contrast components were expressed by $\Delta\eta_c^M=(3.11\pm0.1)\times10^{-6}$ Å^{-2} and $\Delta\eta_s^M=(-6.58\pm0.20)\times10^{-7}$ Å^{-2} respectively. The contrast ratio of $|\Delta\eta_c/\Delta\eta_s|\approx5.0$ shows that the core component dominates the magnetic scattering density. This result possibly indicates that the granular core was more ferromagnetic than the shell component. In Figure 4.43 the magnetic scattering contrast is plotted as a function of granular radius.

Another interesting feature of the spherical core-shell model was the negative shell contrast. There were two explanations on why the shell component exhibited a negative shell contrast. The first hypothesises that the negative shell contrast represents a magnetisation shift below the average value $\langle M\rangle$. The other explanation relates to the onset of an ANCOS^2 phase shift, which was represented by the smoothed out scattering node at q=0.05 Å^{-1}. The negative contrast value was required to fit the scattering node forming at the quoted q–position. In the following low field SANS studies, it is shown that the scattering node pinpoints a $\pi/2$ phase shift in the azimuthal scattering intensity.

The magnetic contrast difference between the core and shell components was explained in terms of the grain's alloy composition. Consider the recording grain composed of the alloy $Co_{82}Cr_{18}Pt_6B_6$. The Pt was uniformly distributed throughout the grain while the B atoms segregated to the grain boundary. The Cr atoms mainly segregate to the grain boundary leaving only a small percentage within the granular core. This results in an enriched ferromagnetic core with a magnetically depleted shell. The formation of these distinct ferromagnetic phases leads to the variation in the core and shell contrast components.

The in-plane hysteresis of AX1646 found that the recording grain's average magnetisation at room temperature was M_s=362 emu/cm^3. It was known from the scattering model that the magnetic core contrast was five times larger than its shell counterpart. By utilising the average magnetisation formula, the core and shell values were 1120 emu/cm^3 and 224 emu/cm^3 respectively. Note the bulk value for pure Co is approximately 1400 emu/cm^3. The magnetisation of the core was characteristic of hard ferromagnet with a high percentage of cobalt. The shell component was much smaller than the bulk value, which was due to a Cr enriched grain boundary. Calculations show that the shell magnetisation corresponds to the Cr atomic percentage of 25%. It was unclear if the outer shell was a soft ferromagnet or behaves as a paramagnet.

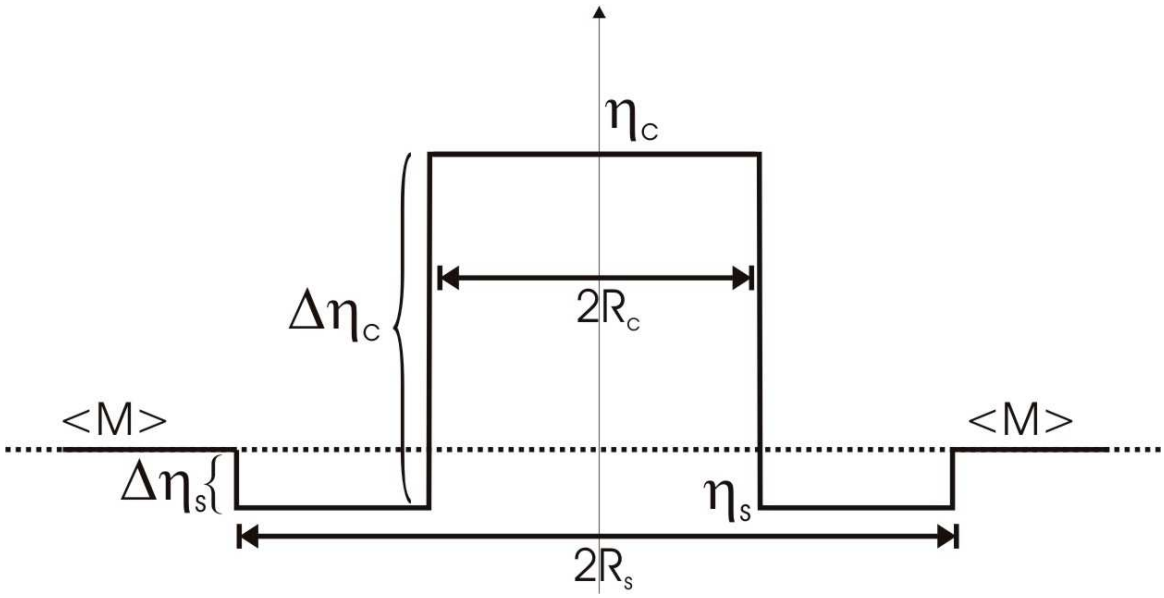

Figure 4.43: The magnetic scattering contrast profile of the AX1646 recording grain.

Scattering Function	***Description***	***Parameter***	***NLS Switch***	***Value***
F(q)	Magnetic Core Contrast	$\Delta\eta_c$	*Free*	$(3.11 \pm 0.1)\times10^{-6}$ Å^{-2}
	Magnetic Shell Contrast	$\Delta\eta_s$	*Free*	$(-6.58 \pm 0.20)\times10^{-7}$ Å^{-2}
	Core Radius	R_c	*Free*	30.0 ± 0.70 Å
	Shell Radius	R_s	*Free*	56.0 ± 1.10 Å
	γ-Distribution Width	σ	*Fixed*	15.0 Å
I_{Porod} (q)	Porod exponent	n	*Fixed*	2.60
	Scale factor	A	*Fixed*	1.3×10^{-4}
	Background Factor	B	*Fixed*	1.3×10^{-5}
	Closeness of Fit	χ^2	---	1.33

Table 4.3: The AX1646 2.2 T fit parameters for the form factor F(q) and Porod $I_{Porod}(q)$ scattering functions. The third column shows which parameter was varied (*Free*) or held constant (*Fixed)* during the NLS fitting routine.

The SANS foreground diffraction pattern for AX1646 was measured at the in-plane magnetic field of 1.45 T. Figure 4.44(a) shows the difference plot for the detector distance of 1.5 m. By using the momentum transfer argument, the measured q range corresponds to $0.04\,\text{Å}^{-1}<q_{1.5m}<0.30\,\text{Å}^{-1}$. Within the black annulus, the plot exhibits strong anisotropic magnetic scattering where $I_M^{aniso}(q_y)>I_M^{aniso}(q_x)$. The cosine^2 fit closely fits the azimuthal scattering intensity which was characteristic of the moment orientation factor $\sin^2\alpha$. The foreground scattering performed at the sample-detector distance of 5.0 m is shown in Figure 4.44(b). Calculations show the measured q-range of $0.02\,\text{Å}^{-1}<q_{5.0m}<0.09\,\text{Å}^{-1}$. In these measurement the maximum magnetic scattering intensity undergoes a shift from $q_y \rightarrow q_x$ where $I_M^{aniso}(q_y)<I_M^{aniso}(q_x)$. This phenomenon was observed in the azimuthal scattering intensity where the cosine^2 function undergoes a phase shift of $\pi/2$. At the sample-detector distance of 12.0 m the maximum magnetic scattering intensity shifts back to the q_y axis for the q range $0.0045\,\text{Å}^{-1}<q_{12m}<0.02\,\text{Å}^{-1}$. Note as the detector moves further out, the magnetic scattering statistics gradually decrease. This effect was attributed to the noisy scattering signal near the beam stop.

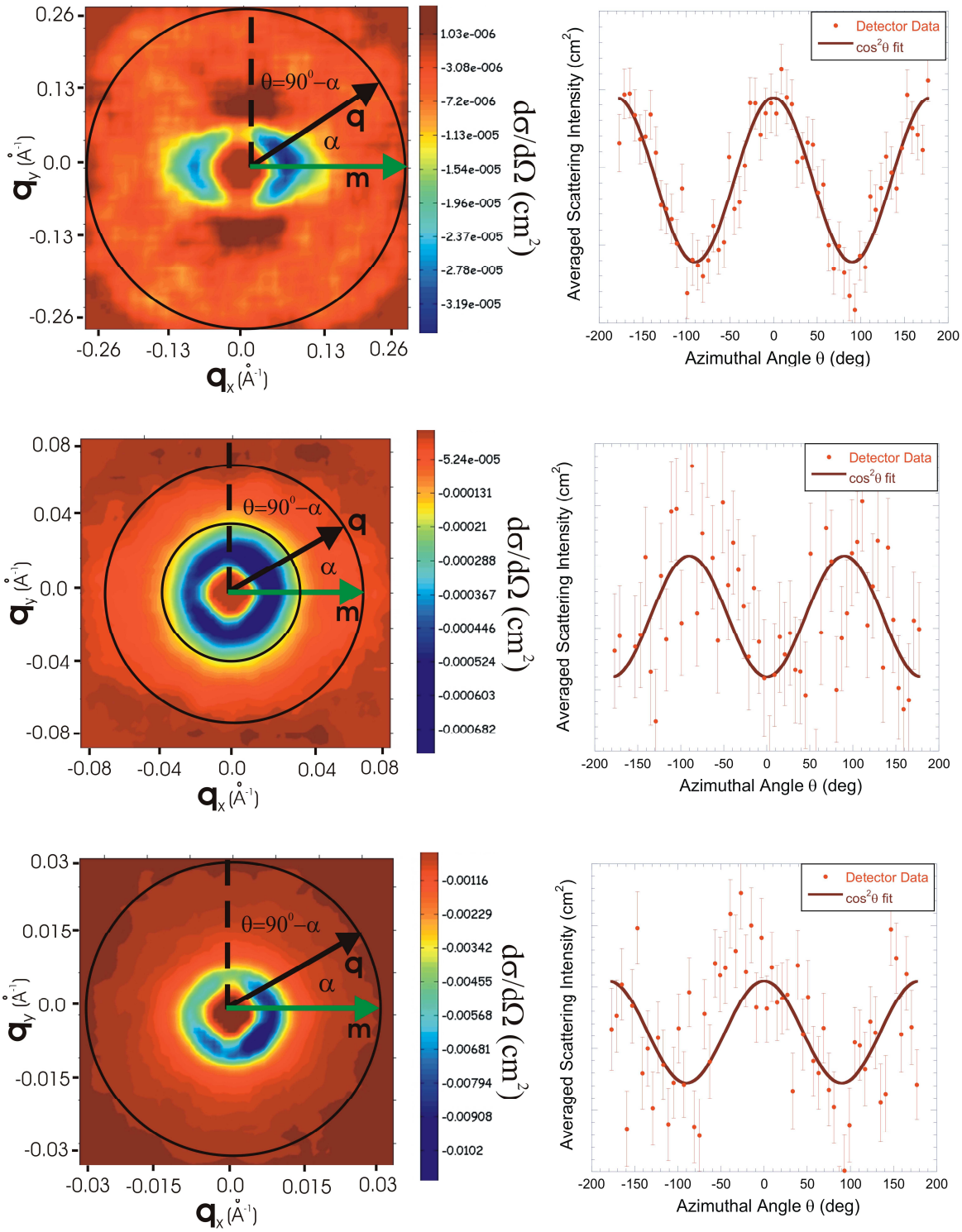

Figure 4.44: The AX1646 1.45 T magnetic difference plot and azimuthal scattering intensities for the q range (a) 0.04 Å^{-1}<$q_{1.5m}$<0.30 Å^{-1}, (b) 0.02 Å^{-1}<$q_{5.0m}$<0.09 Å^{-1} and (c) 0.0045 Å^{-1}<q_{12m}<0.02 Å^{-1}.

The difference plots were fitted using the cosine^2 function where its phase varies as a function of q. This phenomenon results from the variation between the magnetic scattering contrast components $\Delta\eta_y^M$ and $\Delta\eta_x^M$. In this situation the magnetic scattering intensity was modelled by a two-dimensional function which accounts for the scattering variation along the q_y and q_x axes. The magnetic scattering intensity was expressed by the following equation $I_M^{aniso}(q)=\{I_M^R(q_y)-I_M^R(q_x)\}+I_M^U(q)$ where the intensity terms $I_M^R(q)$ and $I_M^U(q)$ represent the magnetic scattering from the recording layer and soft underlayer respectively.

The program ANCOS^2 fits the magnetic difference plot by using the function $\Delta I_M(q)=I_a+I_b\cos^2(\theta+\delta_c)$. This equation outputs the magnetic scattering intensity I_b and cosine^2 phase shift δ_c as a function of q. Figure 4.45 plots the ANCOS^2 phase for the measured q range of $0.0045\,\text{Å}^{-1}<q<0.30\,\text{Å}^{-1}$. The noisy regions on the phase plot were due to poor fitting results of the ANCOS^2 scattering function. This undoubtedly was caused by low scattering statistics at the detector's edge. The data exhibited multiple phase shifts at $\delta_c=0$ and $\delta_c=\pi/2$ which correspond to the maximum magnetic scattering about the q_y and q_x directions respectively. According Figure 4.45 the phase steps occurred for the following co-ordinates,

$$\delta_c=\begin{cases}0 & ,0.00450\text{Å}^{-1}<q_1<0.020\ \text{Å}^{-1}\\ \pi/2 & ,0.020\,\text{Å}^{-1}<q_2<0.0570\,\text{Å}^{-1}\\ 0 & ,0.0570\,\text{Å}^{-1}<q_3<0.180\ \text{Å}^{-1}\\ \pi/2 & ,0.180\,\text{Å}^{-1}<q_4<0.30\,\text{Å}^{-1}\end{cases} \tag{4.6}$$

In Figure 4.46 the magnetic scattering intensity at the respective phase co-ordinates is plotted onto a log-log scale. The scattering intensity exhibits phase shifts at the q-nodes of q=0.02 Å^{-1}, 0.057 Å^{-1} and 0.18 Å^{-1}. The maximum scattering intensity results from the superposition of the recording layer and soft underlayer scattering components. The magnetic scattering intensity was modelled using the spherical core-shell form factor and Porod scattering functions as derived section 4.4.1. The scattering intensity and cosine phase were combined onto a linear plot that expresses the magnitude and direction of the preferred magnetic scattering. The scattering intensity was assigned a positive value when the cosine^2 phase was zero while a negative value corresponded to the phase shift of $\pi/2$. These scattering conditions were expressed by the functions, $I_M(q,\delta=0)=\{I_M^R(q_y)-I_M^R(q_x)\}+I_M^U(q)>0$ and $I_M(q,\delta=\pi/2)=\{I_M^R(q_y)-I_M^R(q_x)\}+I_M^U(q)<0$.

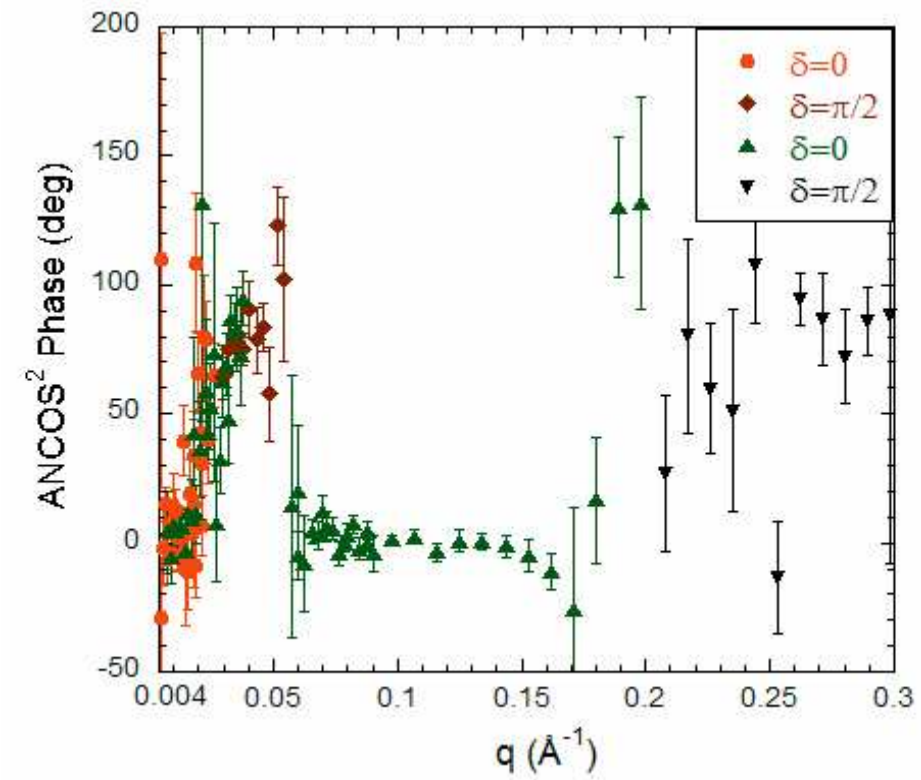

Figure 4.45: The AX1646 ANCOS^2 phase at the applied in-plane fields of 1.45 T. The zero phase refers to a moment orientation along the q_x axis while for the $\pi/2$ phase the moments are aligned along the q_y-axis.

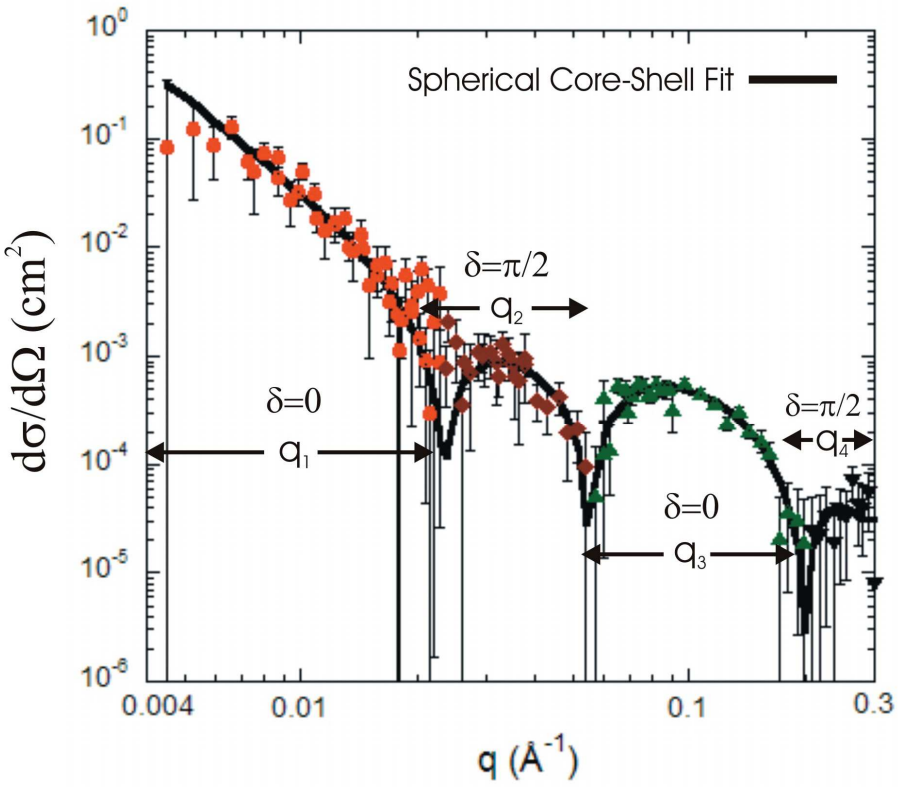

Figure 4.46: The AX1646 1.45 T magnetic scattering intensity for the ANCOS^2 phase steps of q_1, q_2, q_3 and q_4.

The magnetic scattering intensity is plotted on a linear scale as shown in Figure 4.47. The sample's total magnetic scattering was modelled using the expression $I_M(q)=N_y<F^2(q_y)>-N_x<F^2(q_x)>+I_{Porod}(q)$. The functions $F(q_y)$ and $F(q_x)$ represent the spherical core-shell form factors in q_y and q_x space and $I_{Porod}(q)$ represents the magnetic scattering from the soft underlayer. Table 4.4 lists the NLS fit parameters for the form factor and Porod functions. The scattering model bears good agreement with the data with a closeness of fit $\chi^2=1.43$. The intensity shows no signs of interference scattering, which was characteristic of an amorphous ensemble of magnetic grains. The absence of interference scattering was due to the recording layer's large grain size distribution. The ensemble of irregular shaped grains was characterised with by a gamma-Shultz size distribution of order 30%. This introduces spatial disorder to the grains thus dampening out any interference effects. Hence the Percus-Yevick structure factor reduces to unity.

The sample's magnetic scattering behaviour was best understood by plotting the individual form factor and background intensities, see Figure 4.48. The majority of magnetic scattering within the q_1 range originates from the sample's NiP underlayer expressed by the inequality $I_{Porod}(q)>\{F^2(q_y)-F^2(q_x)\}$. As was the case with the saturated measurement, the underlayer component was modelled using the Porod scattering function. Within the q_2 range the magnetic scattering becomes negative showing a cosine^2 phase shift of $\pi/2$. The total magnetic scattering was dominated by the form factor along the q_x-axis where $F^2(q_x)>\{F^2(q_y)+I_{Porod}\}$. For the q_3 range the magnetic scattering shifts back to zero phase indicating that granular moments have aligned along the q_x-axis.

The multiple phase shifts within the recording layer can be explained in terms of a magnetic contrast variation between the form factors $F_M(q_y)$ and $F_M(q_x)$. At low q the form factor intensity along the q_x-axis takes the form $F(q_x)^2>F(q_y)^2$. This condition shows that the contrast variation along the q_y-axis was greater than the x-component. The form factor intensities cross over at $q=0.05$ Å^{-1} where $F(q_x)^2<F(q_y)^2$. This indicates that the contrast variation was now larger along the q_y-axis. The contrast variation was attributed to the grain's in-plane magnetic anisotropy. Within the granular core, there exists a magneto-crystalline anisotropy field, which determines the moment's easy axis of magnetisation. The contrast variation occurs at low fields where the magnetisation no longer lies along the applied field direction. This hypothesis was tested in Chapter 7 by performing micromagnetic simulations for an ensemble of magnetic recording grains.

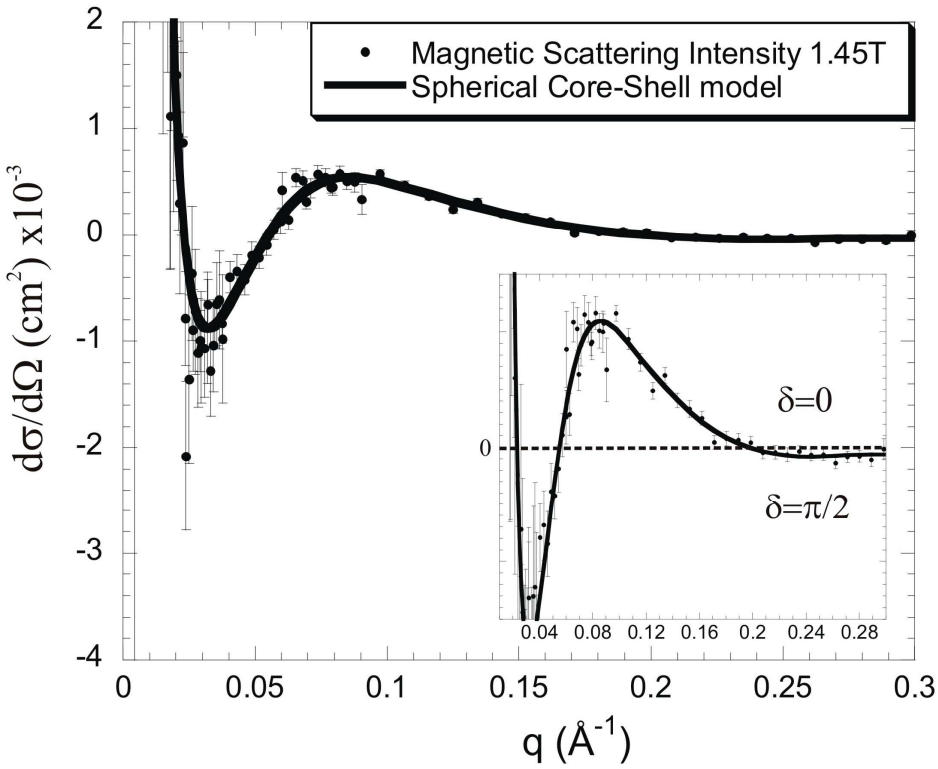

Figure 4.47: The AX1646 1.45 T magnetic anisotropic scattering intensity fitted to the spherical core-shell model. The inset shows $I_M>0;\delta_c=0$ and $I_M<0$; $\delta_c=\pi/2$.

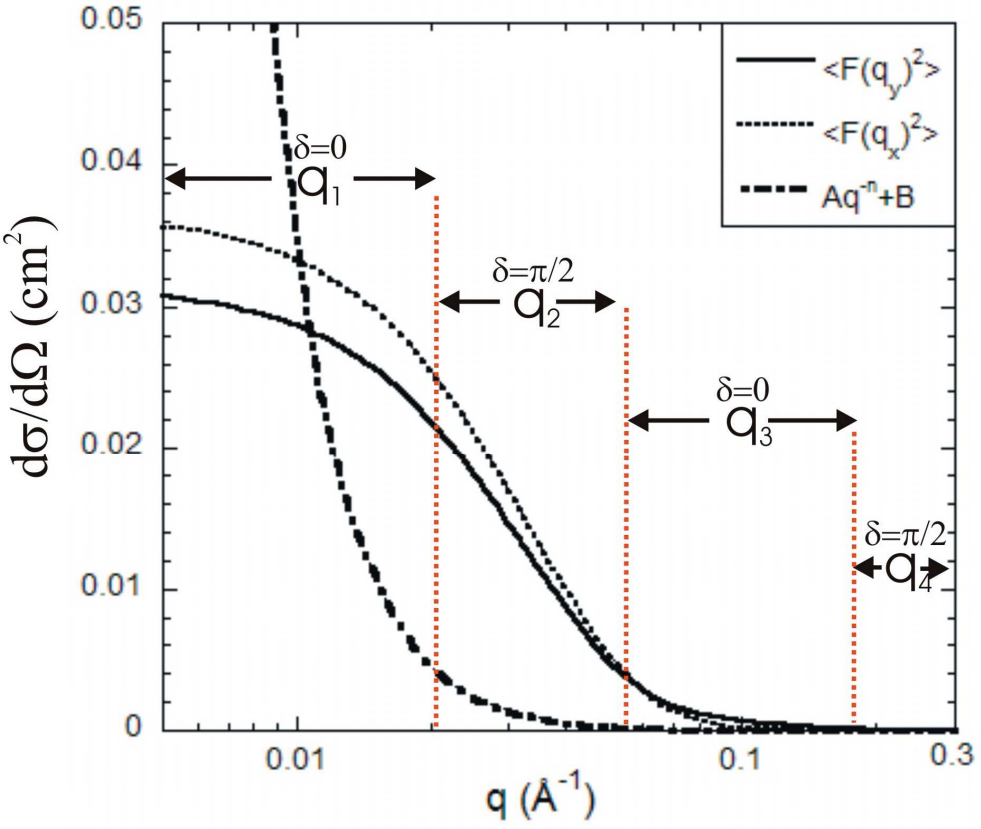

Figure 4.48: The AX1646 1.45 T form factor and Porod scattering intensities for the ANCOS^2 phase steps of q_1, q_2, q_3 and q_4.

The recording grain's magnetic structure within the x-y plane was determined from the form factors $F_M(q_y)$ and $F_M(q_x)$. The form factor along the q_y-axis shows a core and shell diameter of 29.4 ± 1.0 Å and 93.8 ± 2.5 Å respectively. The form factor along the q_x-axis gives the core and shell diameter of 57.6 ± 4.0 Å and 101.0 ± 3.5 Å respectively. The grain size distribution was approximately 33%. The magnetic length scales were consistent with the physical grain size of the order of 100 Å. The magnetic contrast ratio was slightly smaller than the saturated case where $|\Delta\eta_c/\Delta\eta_s|\approx 20.0$. The grain's core and shell angles were $\varphi_c=14.7^0$ and $\varphi_s=10.5^0$ respectively. The following result of $\varphi_c>\varphi_s$ suggests that the grain's magneto-crystalline anisotropy field was largest in the core component. This provides further evidence that the core was magnetically harder than its shell component. Figure 4.49 shows the micromagnetic map for the in-plane fields of 0.45 T, 1.38 T, 1.45 T and 2.2 T.

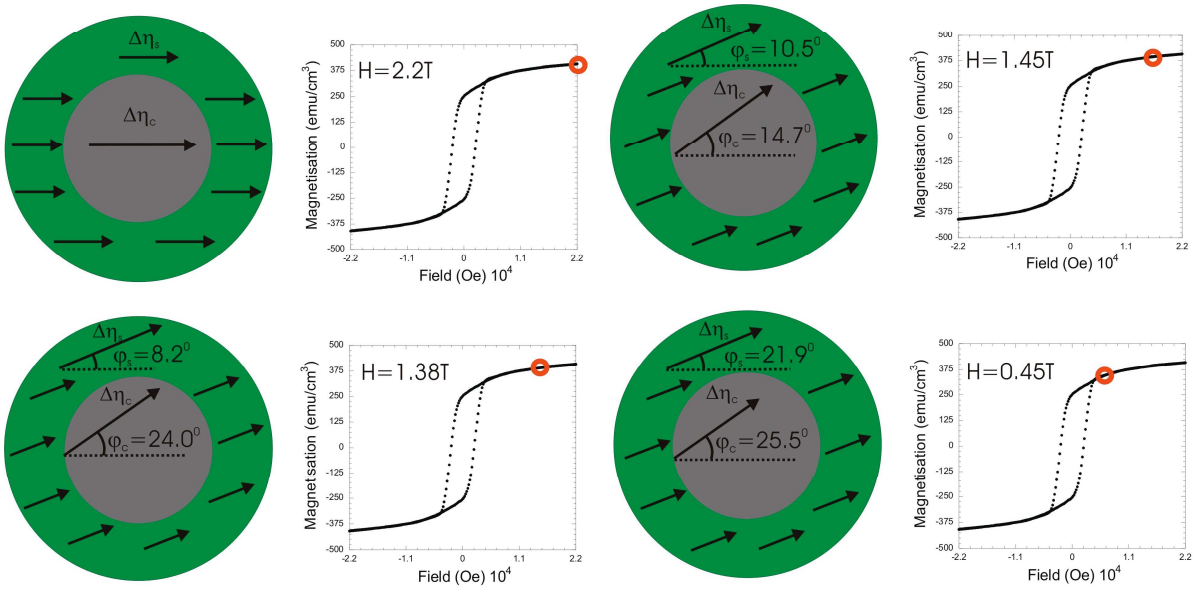

Figure 4.49: The micromagnetic diagram of the AX1646 recording grain for the in-plane field of 0.45T, 1.38T, 1.45T and 2.0T. The in-plane magnetic hysteresis loop shows the total moment for each SANS measurement.

Scattering Function	***Description***	***Parameter***	***NLS Switch***	***Value***
F(q)	Magnetic Core Contrast	$\Delta\eta_c$	*Free*	$(2.13 \pm 0.1)\times10^{-6}$ Å^{-2}
	Core Moment Angle	φ_c	*Free*	15.4 ± 2.0^0
	Core Radius	R_{cy}	*Free*	14.7 ± 1.0 Å
	Shell Radius	R_{sy}	*Free*	46.9 ± 1.8 Å
	γ-Distribution Width	σ_y	*Fixed*	15.0 Å
	Magnetic Shell Contrast	$\Delta\eta_s$	*Free*	$(1.12 \pm 0.4)\times10^{-7}$ Å^{-2}
	Shell Moment Angle	φ_s	*Free*	$10.5 \pm 1.5^{\ 0}$
	Core Radius	R_{cx}	*Free*	28.8 ± 3.0 Å
	Shell Radius	R_{sx}	*Free*	50.7 ± 2.5 Å
	γ-Distribution Width	σ_x	*Fixed*	19.0 Å
$I_{Porod}(q)$	Porod exponent	n	*Fixed*	2.90
	Scale factor	B	*Fixed*	5.5×10^{-8}
	Background factor	A	*Fixed*	-5.6×10^{-5}
	Closeness of Fit	χ^2	---	1.01

Table 4.4: The AX1646 1.45T fit parameters for the form factor-F(q) and Porod-$I_{Porod}(q)$ scattering functions.

The SANS measurements were performed at the applied in-plane field of 0.45 T. Figure 4.50 shows the magnetic difference plot for the detector distances of (a) 1.5 m, (b) 5.0 m and (c) 12.0 m. At the detector distance of 1.5 m, the azimuthal scattering intensity was calculated within the q-range $0.073\,\text{Å}^{-1}<q<0.17\,\text{Å}^{-1}$. The cosine^2 fit clearly shows anisotropic magnetic scattering however the signal was much weaker than the corresponding measurement at 1.45 T. The poor statistics were attributed to the sample's reduced background scattering from the NiP underlayer. For the detector distance of 5.0 m, the azimuthal scattering intensity was calculated for the q range of $0.02\ \text{Å}^{-1}<q_{5.0m}<0.07\ \text{Å}^{-1}$. The cosine^2 fit shows a strong anisotropic diffraction pattern within the scattering plane. Due to the increased magnetic scattering along the q_x-axis, the cosine^2 fit exhibits a phase shift of $\delta=\pi/2$. The ANCOS^2 phase steps were observed for the following q ranges,

$$\delta_c=\begin{cases}\pi/2 & ,0.0070\text{Å}^{-1} < q_1 < 0.073\text{Å}^{-1}\\ 0 & ,0.073\text{Å}^{-1} < q_2 < 0.17\text{Å}^{-1}\\ \pi/2 & ,0.170\text{Å}^{-1} < q_3 < 0.30\,\text{Å}^{-1}\end{cases} \tag{4.7}$$

These co-ordinates were mapped onto a linear plot where the positive and negative scattering intensity represents the ANCOS^2 phase of zero and $\pi/2$ respectively.

The magnetic scattering intensity at 0.45 T was fitted to the spherical core-shell model, see Figure 4.51. The NLS fit parameters are listed in table 4.5 for the form factors and background components. As before the magnetic scattering behaviour was understood by plotting the individual form factor and background intensities as a function q, see Figure 4.52. The reduction in the applied magnetic field has increased the form factor intensities along their respective axes. This again was attributed to the increase in moment variations within the core and shell components, see micromagnetic diagram in Figure 4.49. Within the q_1 range the negative scattering intensity originates mainly from the recording layer's in-plane magnetisation along the q_y-axis where $F^2(q_x)>\{F^2(q_y)+I_{porod}(q)\}$. The Porod scattering intensity no longer dominates the magnetic scattering intensity due to a slight reduction in underlayer magnetisation. This effect was somewhat unusual since one should expect the soft underlayer to be fully saturated at 1.45 T. Within the q_2 range the scattering intensity shifts to positive values where $F^2(q_y)>\{I_{porod}(q)-F^2(q_x)\}$. This shows that the recording grain's magnetic contrast along q_x was larger than its q_y component. For the final q-range, the scattering intensity shifts back to negative values.

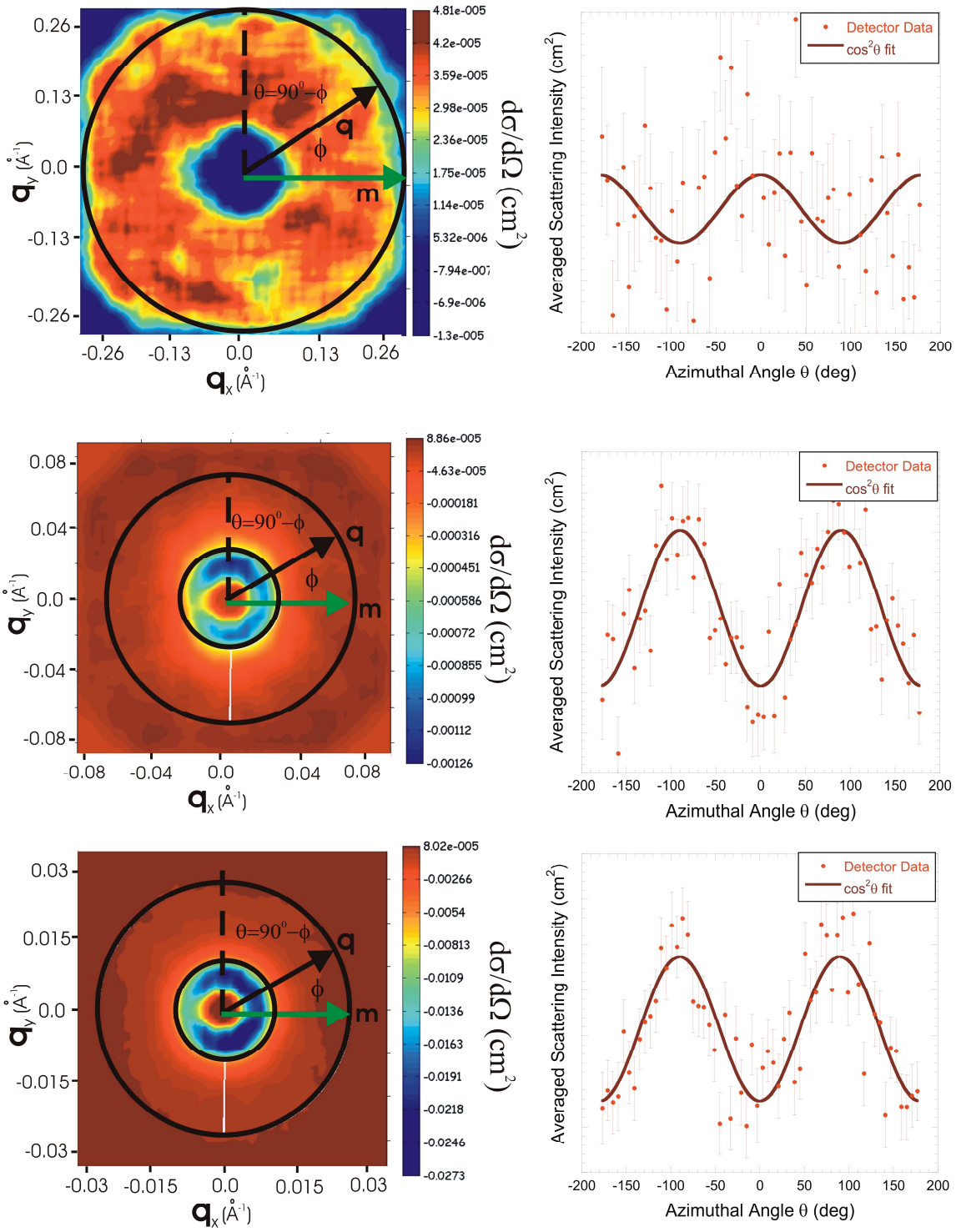

Figure 4.50: The AX1646 0.45 T magnetic difference plot and azimuthal scattering intensity for the q range (a) 0.073 $Å^{-1}$<$q_{1.5m}$<0.17 $Å^{-1}$, (b) 0.02 $Å^{-1}$<$q_{5.0m}$<0.07 $Å^{-1}$ and (c) 0.0045 $Å^{-1}$<q_{12m}<0.02 $Å^{-1}$.

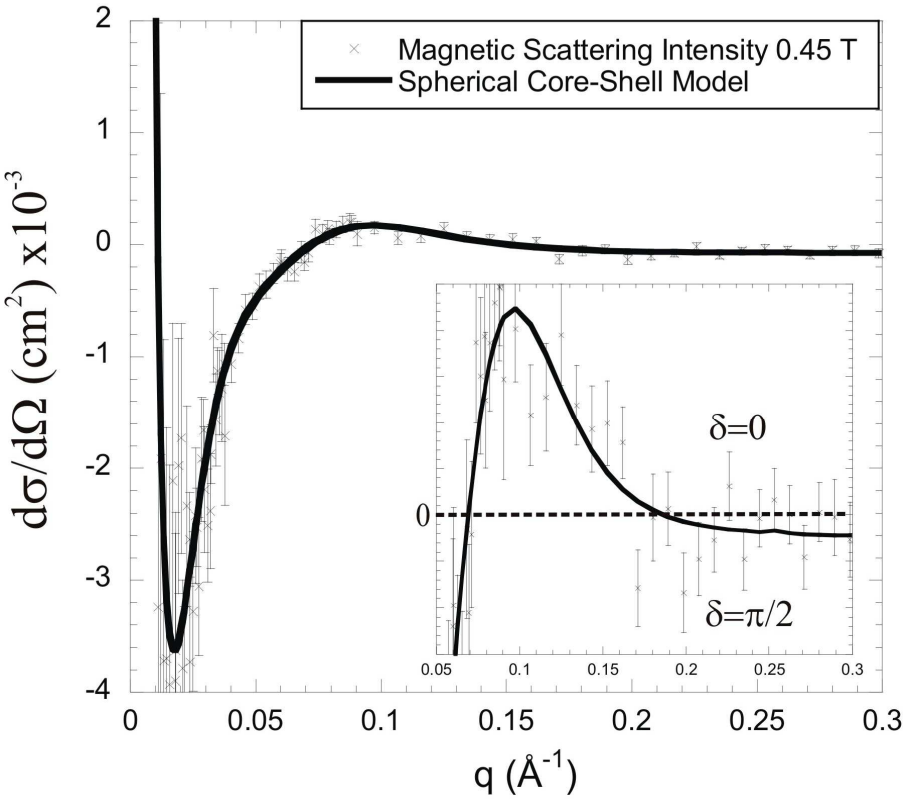

Figure 4.51: The AX1646 0.45 T magnetic scattering intensity fitted with the spherical core-shell model. The inset shows the phase at δ=0 and π/2 for the (+) and (-) scattering intensities respectively.

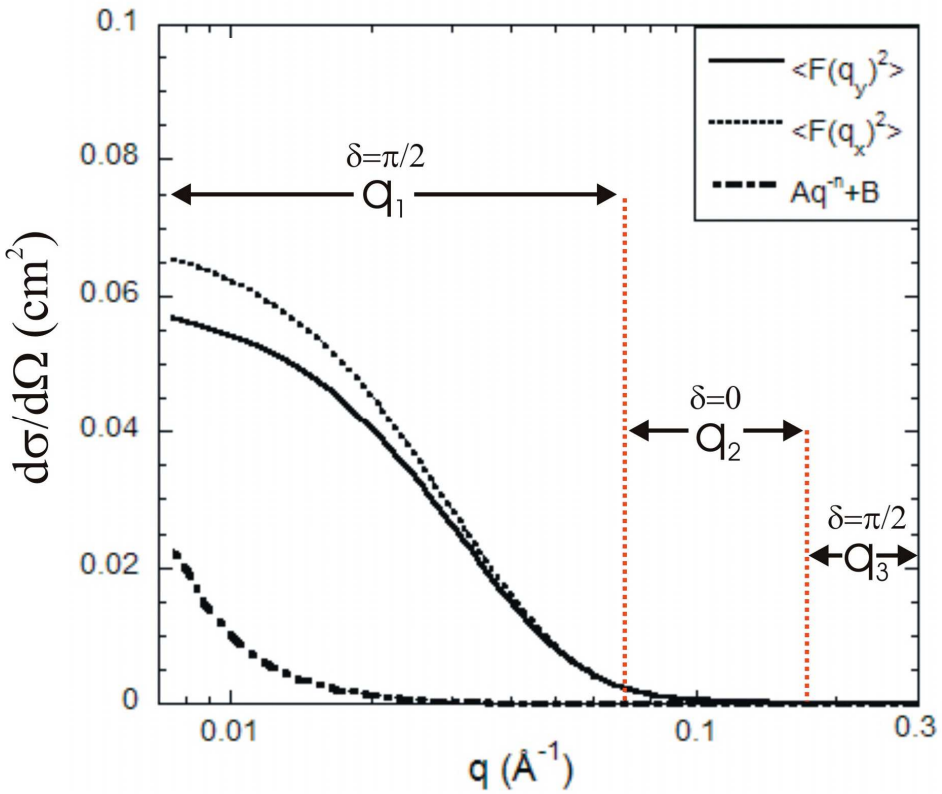

Figure 4.52: The AX1646 0.45 T form factor and Porod scattering intensities for the ANCOS^2 phase steps of q_1, q_2, and q_3

Scattering Function	***Description***	***Parameter***	***NLS Switch***	***Value***
F(q)	Magnetic Core Contrast	$\Delta\eta_c$	*Free*	$(1.47 \pm 0.3)\times10^{-6}$ Å^{-2}
	Core Moment Angle	φ_c	*Free*	26.5 ± 4.0^0
	Core Radius	R_{cy}	*Free*	18.8 ± 2.8 Å
	Shell Radius	R_{sy}	*Fixed*	50.6 ± 5.5 Å
	γ-Distribution Width	σ_y	*Fixed*	15.8 Å
	Magnetic Shell Contrast	$\Delta\eta_s$	*Free*	$(1.81 \pm 0.70)\times10^{-7}$ Å^{-2}
	Shell Moment Angle	φ_s	*Free*	21.9 ± 8.0^0
	Core Radius	R_{cx}	*Free*	30.0 ± 8.0 Å
	Shell Radius	R_{sx}	*Fixed*	56.4 ± 11.0 Å
	γ-Distribution Width	σ_x	*Fixed*	19.5 Å
$I_{Porod}(q)$	Porod exponent	n	*Fixed*	2.50
	Scale factor	A	*Fixed*	1.6×10^{-8}
	Background factor	B	*Fixed*	-7.5×10^{-5}
	Closeness of Fit	χ^2	---	1.26

Table 4.5: The AX1646 0.45T fit parameters for the form factor-F(q) and Porod-$I_{Porod}(q)$ scattering functions.

4.4.6 Results and Discussion-AX341

The D11 SANS instrument was used to investigate the sub-granular magnetic structure of AX341. The sample's diffraction pattern was extracted for the in-plane magnetic field of 2.2 T. Figure 4.53 shows the two-dimensional difference plot for the sample-detector distance of 1.5 m. This detector distance corresponds to the q range 0.04 $Å^{-1}<q_{1.5m}<0.30$ $Å^{-1}$. The foreground and background measurements were divided by the incident flux, Φ_{inc}, which normalises the scattering data to the cross-section units of cm^2. The azimuthal scattering was averaged over the entire scattering plane and fitted with the $cosine^2$ function. The diffraction data shows strong anisotropic magnetic scattering with the detector plane. This indicates that the sample's underlayer and recording layer were saturated along the applied field direction. For the sample-detector distances of 5.0 m the anisotropic scattering remains along the q_y axis showing no evidence of the $cosine^2$ phase shift.

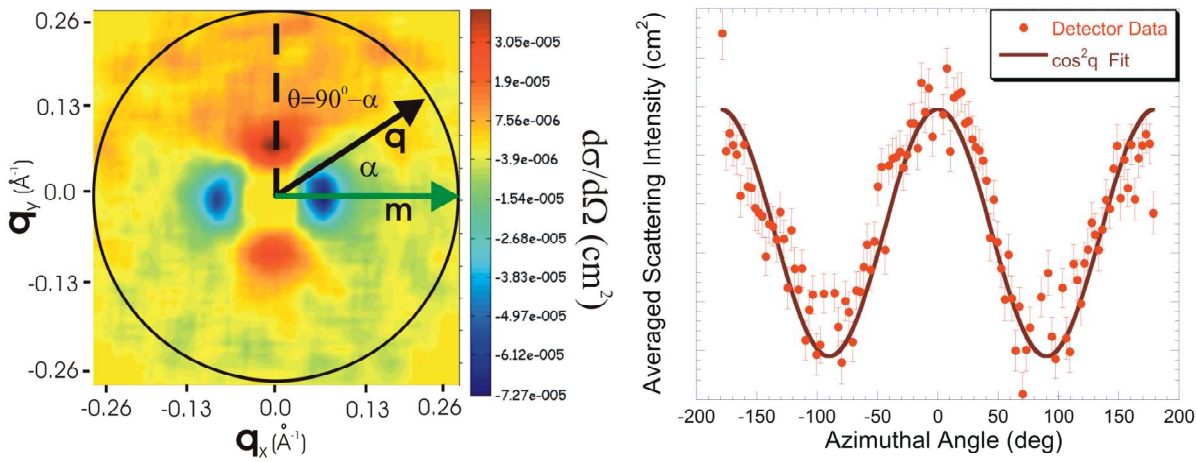

Figure 4.53: The AX341 2.2 T magnetic difference plot and azimuthal scattering intensity at the sample-detector distance 1.5 m. This corresponds to the scattering q-range of 0.04 $Å^{-1}<q_{1.5m}<0.30$ $Å^{-1}$

The ANCOS^2 function $\Delta I_M(q)=I_a+I_b\cos^2(\theta+\delta_c)$ was used to fit the difference plot where the magnetic scattering intensity was defined by $I_b(q)=I_M^{aniso}(q)=I_M(q_y)-I_M(q_x)$. As in the previous measurements, the magnetic scattering originates from the recording layer and NiP underlayer. At saturation, the moment orientation factor eliminates any magnetic scattering components along the q_x-axis where $I_M(q_x)=I_M^R(q_x)+I_M^U(q_x)\approx 0.0$. In this analysis, the magnetic recording grain was modelled using two different types of structures. The first model assumes that the magnetic grain was a solid spherical object with no weakly magnetic grain boundary. The solid sphere model was compared to the core-shell structure where the Co-enriched core was segregated by the Cr-enriched grain boundary. The interference scattering from neighbouring grains was non-existent since the ensemble has a large grain size distribution. This spatial property averages the Percus-Yevick structure factor to unity where $S(q)\rightarrow 1$. Therefore the sample's magnetic scattering intensity simplifies to the following $I_M^{aniso}(q) = N\langle F^2(q_y)\rangle + I_{Porod}(q)$.

The anisotropic magnetic scattering was fitted with the solid sphere form factor shown in Figure 4.54. The solid sphere model-A fits the magnetic scattering without using the Porod background component. The form factor only fits a slight section of the scattering intensity. The model's mismatch with the data suggests that the scattering function needs to account for the sample's NiP background component. In model-B, the addition of the Porod scattering function achieves an improved agreement with the data with a closeness of fit $\chi^2=1.13$. The form factor function extracts the average grain diameter of 38.0 ± 4.0 Å with a grain size distribution of 41%. However these results disagree significantly with TEM measurements, which show an average grain diameter of 170 Å and the grain size distribution of 120% [76].

The solid sphere model failed to correctly fit the magnetic scattering data at the saturation state. This suggests that the recording grain's magnetic structure cannot be simply modelled using a solid ferromagnetic sphere. Alternatively the recording grain was modelled using the spherical core-shell structure. The grain's core component was enriched with ferromagnetic cobalt with an atomic percentage of the order of 75%. The weakly magnetic shell was enriched with Cr and Ta atoms. According to Figure 4.8 the Cr percentage of 20-25% was adequate to render the grain boundary magnetically soft. The scattering intensity is fitted to the spherical core-shell form factor as shown in Figure 4.55. The model shows reasonable agreement with the scattering data where the closeness of fit is $\chi^2=1.11$. Table 4.6 lists the form factor and Porod fit parameters.

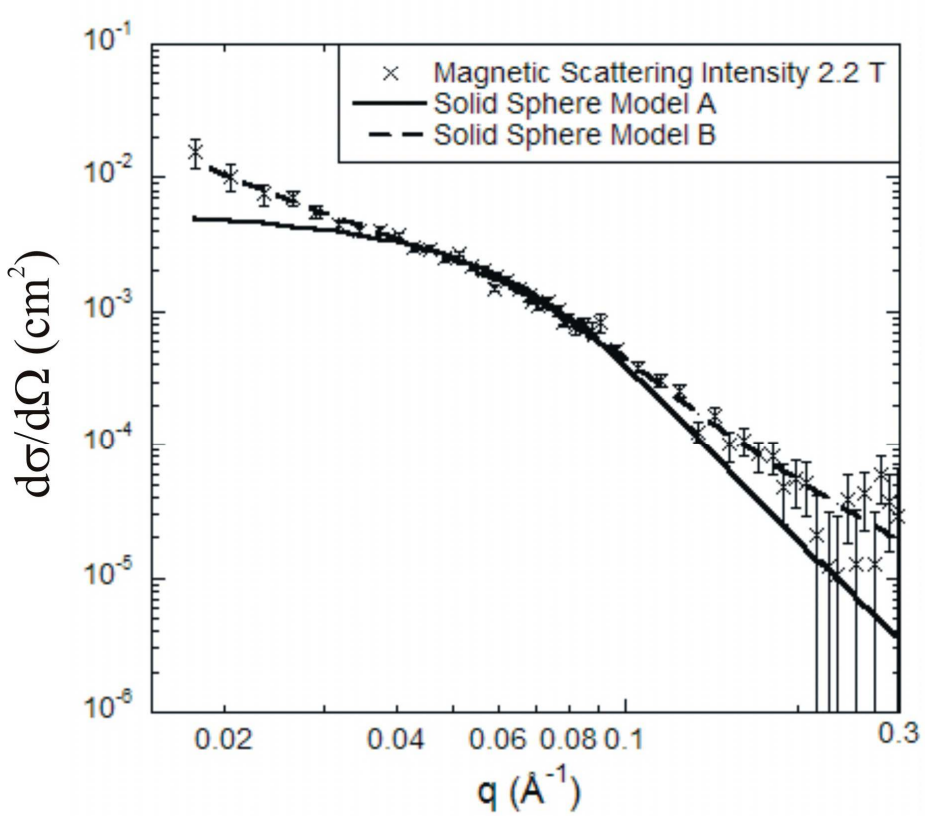

Figure 4.54: The AX341 2.2 T anisotropic magnetic scattering intensity fitted to the solid sphere model.

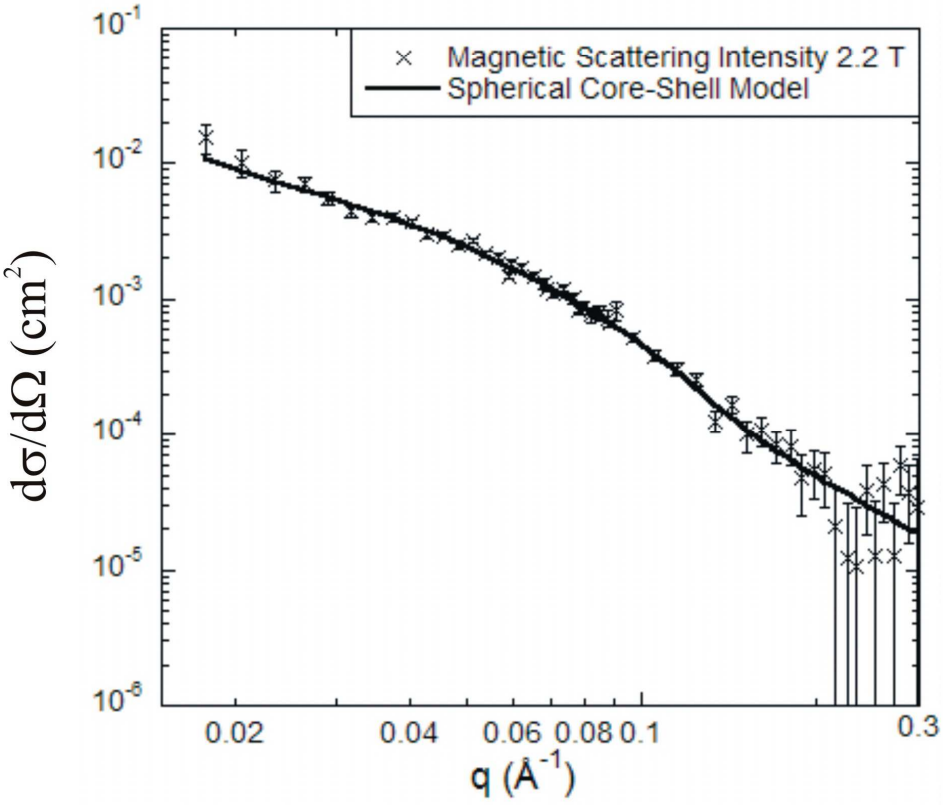

Figure 4.55: The AX341 2.2 T anisotropic magnetic scattering intensity fitted to the spherical core-shell model.

The spherical core-shell form factor defined by $F(q_y)$ extracts a core and shell diameter of 40.0 ± 1.80Å and 146.0 ± 2.2 Å respectively with a grain size distribution of 36%. The outer diameter was closer to the TEM measurements though the result falls short by 20.0 Å. This length scale may be attributed to the grain's non-magnetic region. In this situation a high percentage of Cr atoms have segregated to the outer edge of the grain boundary thus rendering this region non-magnetic. Figure 4.56 plots the magnetic scattering contrast profile as a function of the granular radius. In a similar fashion to AX1646 the granular core and shell contrast were shifted with respective to the average magnetisation. The shell's magnetic contrast of $\Delta\eta^M_s=(-2.29\pm0.7)\times10^{-7}$ Å^{-2} indicates that the grain's outer magnetisation was slightly below the average. The contrast ratio of $|\Delta\eta_c/\Delta\eta_s|\approx26.0$ shows the granular core to have a much larger magnetisation than the shell component. The contrast ratio suggests the core component was highly enriched with cobalt, which leaves the shell magnetically depleted. Further evidence for the enriched grain was obtained by comparing the core contrasts of AX1646 and AX341. The core contrast inequality of $\Delta\eta_c(AX341)>\Delta\eta_c(AX1646)$ shows that AX341 has a greater magnetisation within the core component. Hysteresis measurements confirm this result where the saturation magnetisation of AX341 was greater than AX1646.

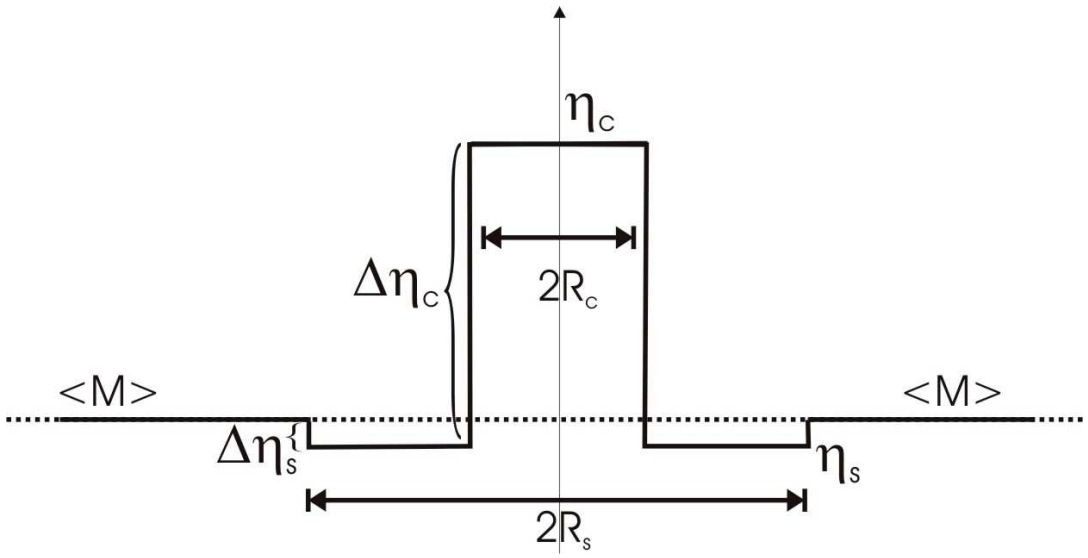

Figure 4.56: The AX341 recording grain's magnetic scattering contrast profile at the applied in-plane field of 2.2 T.

The LMRM sample AX341 was characterised using the D22 SANS instrument. The change over to this SANS instrument was meant to increase the incident beam flux to the sample thereby improving the scattering statistics. For example the maximum beam flux at the sample for D11 and D22 were 1.2×10^{8} $ncm^{-2}s^{-1}$ and 3.2×10^{7} $ncm^{-2}s^{-1}$ respectively [63,64]. The D22 beam flux was approximately 3 times larger than D11. The SANS measurements were performed for the sample-detector distances of 4.5 m and 14.0 m at the in-plane field of 0.50 T. Their respective magnetic difference plots are shown in Figure 4.57. The azimuthal scattering intensity was averaged over the scattering plane and fitted with the $\cos^2\theta$ function. At the detector distance of 4.5 m the anisotropic magnetic scattering was along the q_y-axis where $I_M^{aniso}(q_y)>I_M^{aniso}(q_x)$. Within this q-range the granular moments were saturated along the field direction. For the detector distance of 14.0 m the azimuthal scattering intensity undergoes a phase shift of $\delta=\pi/2$ where the anisotropic scattering flips from $q_y\rightarrow q_x$, $I_M^{aniso}(q_y)<I_M^{aniso}(q_x)$.

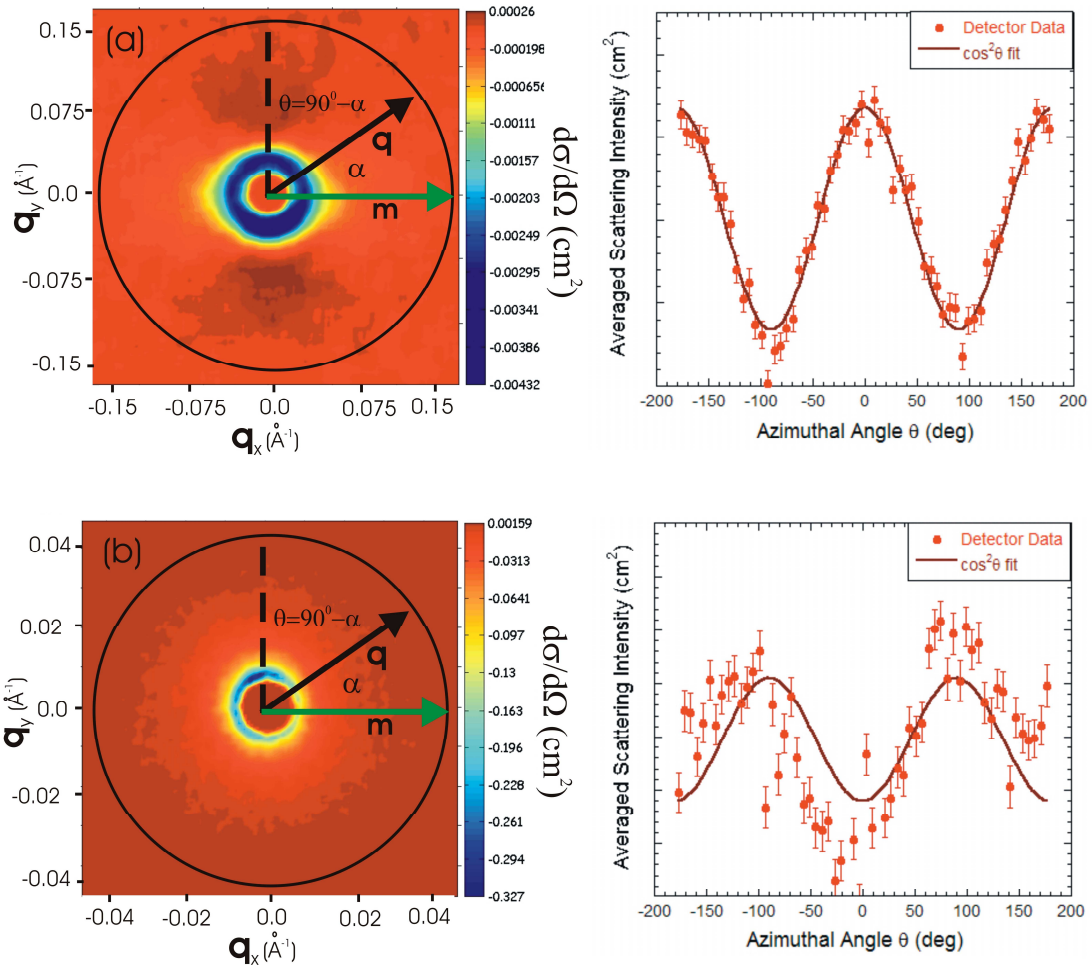

Figure 4.57: The AX341 0.5 T magnetic difference plot and azimuthal scattering intensity for the q-ranges (a) 0.02 $Å^{-1}<q_{4.5m}<0.15$ $Å^{-1}$ and (b) 0.004 $Å^{-1}<q_{14m}<0.04$ $Å^{-1}$.

The magnetic scattering data were partitioned into positive and negative values. The ANCOS[2] phase shifts occurs at q_1=0.031 Å^{-1}. This phase shift was due to the recording grain's large scattering contrast variation along the q_x-axis. The magnetic anisotropic scattering intensities $I_M^{aniso}(q_y)>I_M^{aniso}(q_x)$ and $I_M^{aniso}(q_y)<I_M^{aniso}(q_x)$ were recast onto linear plot shown in Figure 4.58. In these SANS measurements there was no magnetic interference effects as a result the scattering intensity simplifies to the following $I_M^{aniso}(q)=N_y<F^2(q_y)>-N_x<F^2(q_x)>$ where F(q) represents the spherical core-shell form factor. The NLS fit shows good agreement with the magnetic scattering intensity with a closeness of fit χ^2=1.27, see Table 4.7. The form factor and background scattering intensities were plotted in Figure 4.59. The intensity difference between the respective form factors was quite small indicating that the moment variations along the q_x and q_y axes were similar in magnitude. It may be possible that the recording layer's large demagnetisation field prevents the granular moments from aligning along the easy direction of magnetisation. This effect results in a slight contrast variation between the scattering form factors. Within the q_1 range the magnetic scattering intensity originates from the recording layer where $F^2(q_x)>\{F^2(q_y)+I_{Porod}(q)\}$. Since the D22 measurements were performed at a higher q-range than the AX1646 measurements, there was no significant magnetic background scattering from the underlayer.

The scattering form factor $F(q_y)$ gives a core and shell diameter of 55.2 ± 4.0 Å and 129.6 ± 5.6 Å respectively with a grain size distribution of 39%. These results were confirmed by the positive peak at q=0.045 Å^{-1}, which corresponds to an outer diameter of 140.0 Å. Similarly the scattering form factor $F(q_x)$ gives a core and shell diameter of 64.6 ± 2.8 Å and 172.8 ± 6.3 Å respectively with a grain size distribution of 29%. The grain's outer diameter along either scattering axis was comparable to the independent TEM measurements. The size distribution again disagrees with the TEM measurement of 120%. This discrepancy may result from the accuracy of the gamma-Shultz weighted form factor $<F^2(q)>$. The form factor was averaged with a grain size distribution of 30-40%. Within this distribution width, the averaged form factor approaches the Porod scattering function, see Griffiths [52]. Any further increase in the distribution width leaves the form factor function unchanged. The fitting routine will essentially converge to the minimum distribution width that smoothes out the scattering intensity function which in this case was of the order of 30%.

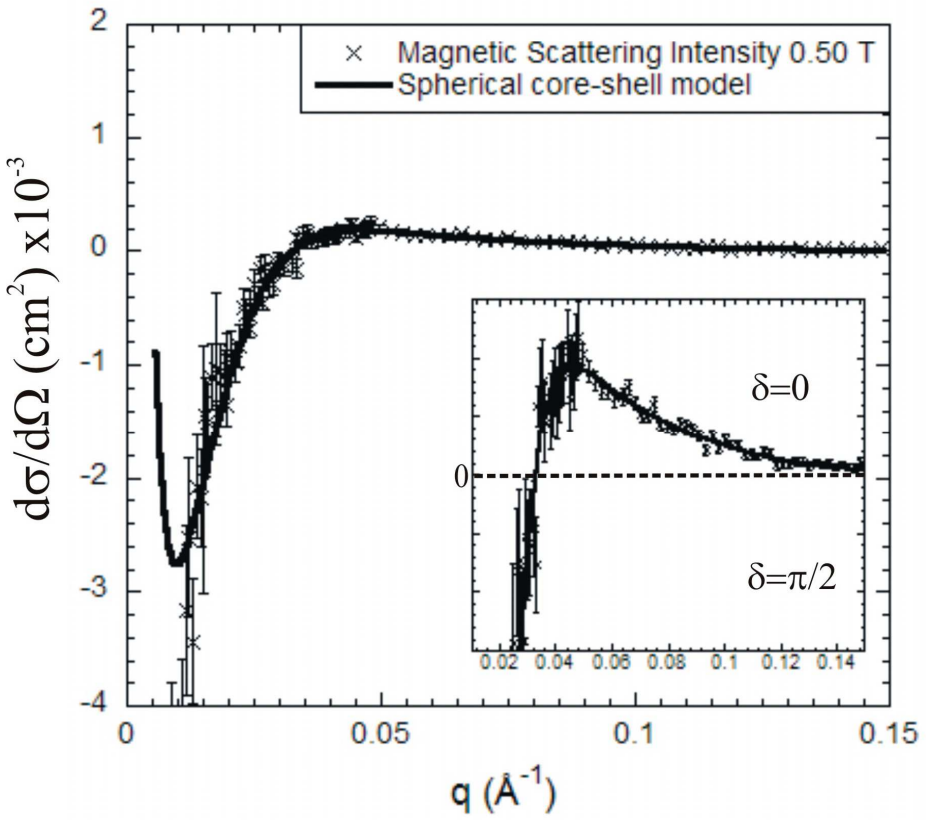

Figure 4.58: The AX341 0.50T magnetic scattering intensity fitted to the spherical core-shell model.

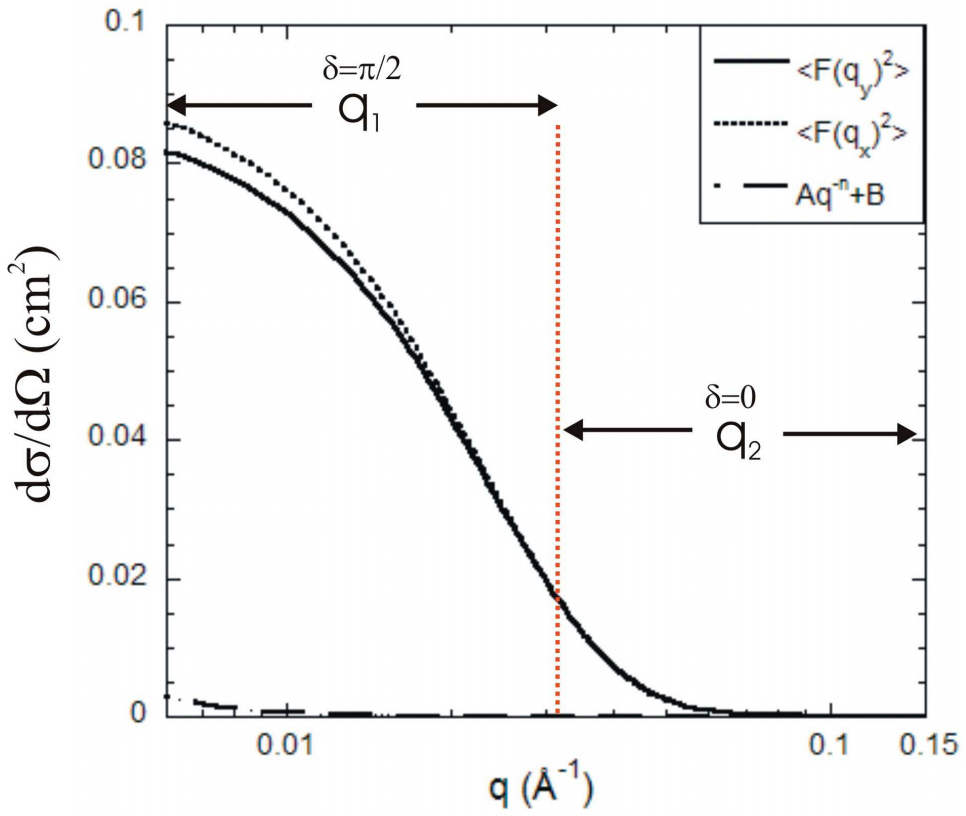

Figure 4.59: The AX341 0.50 T form factor and Porod scattering intensities for the ANCOS^2 phase steps of q_1 and q_2.

Scattering Function	***Description***	***Parameter***	***NLS Switch***	***Value***
F(q)	Magnetic Core Contrast	$\Delta\eta_c$	*Free*	$(6.02 \pm 0.2)\times10^{-6}$ Å^{-2}
	Magnetic Shell Contrast	$\Delta\eta_s$	*Free*	$(-2.29 \pm 0.7)\times10^{-7}$ Å^{-2}
	Core Radius	R_c	*Free*	20.3 ± 1.30 Å
	Shell Radius	R_s	*Free*	73.0 ± 3.5 Å
	γ-Distribution Width	σ	*Fixed*	27.0 Å
$I_{Porod}(q)$	Porod exponent	n	*Fixed*	2.40
	Scale factor	A	*Fixed*	9.3×10^{-9}
	Background factor	B	*Fixed*	-1×10^{-7}
	Closeness of Fit	χ^2	---	1.11

Table 4.6: The AX341 2.2 T fit parameters for the form factor-F(q) and Porod-$I_{Porod}(q)$ scattering functions.

Scattering Function	***Description***	***Parameter***	***NLS Switch***	***Value***
F(q)	Magnetic Core Contrast	$\Delta\eta_c$	*Free*	$(5.07 \pm 0.50)\times10^{-5}$ Å^{-2}
	Core Moment Angle	φ_c	*Free*	32.4 ± 1.4^0
	Core Radius	R_{cy}	*Free*	27.6 ± 2.80 Å
	Shell Radius	R_{sy}	*Free*	64.8 ± 4.0 Å
	γ-Distribution Width	σ_y	*Fixed*	25.0 Å
	Magnetic Shell Contrast	$\Delta\eta_s$	*Free*	$(1.68 \pm 0.70)\times10^{-6}$ Å^{-2}
	Shell Moment Angle	φ_s	*Free*	36.8 ± 3.8^0
	Core Radius	R_{cx}	*Free*	32.3 ± 2.0 Å
	Shell Radius	R_{sx}	*Free*	86.4 ± 4.5 Å
	γ-Distribution Width	σ_x	*Fixed*	25.0 Å
$I_{Porod}(q)$	Porod exponent	n	*Fixed*	3.10
	Scale factor	A	*Fixed*	-3.0×10^{-13}
	Closeness of Fit	χ^2	---	1.27

Table 4.7: The AX341 0.5 T fit parameters for the form factor-F(q) and Porod-$I_{Porod}(q)$ scattering functions

4.4.7 Summary

The LMRM sample's sub-granular magnetic structure was investigated using the characterisation technique of unpolarised SANS. The SANS experiment measured the sample's foreground diffraction pattern at an applied in-plane magnetic field for a range of detector distances. The background diffraction pattern was measured at the zero field state. The recording layer's anisotropic and isotropic magnetic scattering intensities were extracted via the zero field background subtraction.

The background sample AX1821 was composed of the soft ferromagnetic film layer of NiP. At the applied in-plane field of 1.0 T, the sample's magnetic diffraction pattern was highly anisotropic within the scattering plane. This showed that the soft ferromagnetic moments easily saturated within the sample plane. The q-dependent magnetic scattering exhibited Porod-type scattering, which resulted from the soft layer's polydisperese ensemble of domains. These measurements revealed that the NiP layer has a negligible scattering intensity within the recording layer's measured q-range.

The LMRM sample AX1646 was composed of the cobalt-based alloy CoCrPtB. The measurements were performed at the in-plane fields of 0.45 T, 1.45 T and 2.2 T. At the field of 2.2 T, the magnetic diffraction pattern was highly anisotropic about the scattering plane. The moments within the recording layer and underlayer were fully along the field direction. The magnetic scattering exhibited a cosine^2 phase shift at the fields 0.45 T and 1.45 T. This behaviour was attributed to the recording grain's magnetic contrast variation within the scattering plane. The scattering intensity from the recording layer was modelled using a spherical core-shell structure. The model showed that the recording gain was composed of a cobalt-enriched core while the grain boundary consisted of a weakly magnetic shell of Co, Cr and B atoms.

The LMRM sample AX341 was composed of the cobalt-based alloy CoCrPtTa. The SANS measurements were performed at the in-plane fields of 0.5 T and 2.2 T. At 2.2 T, the recording layer's magnetic diffraction pattern was highly anisotropic within the scattering plane. At the field of 0.5 T the diffraction pattern exhibited the cosine^2 phase shift characteristic of the recording grain's contrast variation within the scattering plane. The magnetic scattering data were fitted using the spherical core-shell model. It was found that the recording grain exhibited a Co enriched core with a Cr-depleted shell. Further contrast calculations showed that it was possible to accurately measure the relative core-shell magnetisation of the AX341 recording grain.

4.5 Polarised SANS

In the previous section the characterisation technique of unpolarised SANS was used to investigate the recording grain's local magnetic structure. The grain's magnetic scattering intensity was modelled by the spherical core-shell form factor. The magnetic nature of these core and shell components depends on the physical grain size and its chemical composition. Initially TEM and ELL-TEM measurements were used to characterise a grain's physical structure and chemical composition respectively [15,22]. These measurements were used as a guide when extracting the magnetic grain size. However it would be advantageous to develop a characterisation technique which could simultaneously measure the grain's physical and magnetic length scales. In this situation the measurement would contain no uncertainties between the physical and magnetic grain size.

The obvious characterisation technique to perform the physical and magnetic measurements was unpolarised SANS. In neutron scattering, the physical length scale was extracted by the nuclear scattering intensity. The nuclear scattering from the SANS experiment originated from the sample layers, instrument and apparatus. Only a small fraction of the nuclear scattering results from the sample underlayer while even a smaller fraction emanates from the recording layer. The task of separating the recording layer's nuclear scattering intensity was complicated by the superimposed magnetic scattering component. Regardless of the magnetic field, the magnetic scattering cannot be removed by direct a background subtraction. In short this nuclear scattering component cannot be extracted by the conventional SANS experiment due to the aforementioned reasons. However it was shown that the characterisation technique known as POLSANS has the ability to directly measure the recording layer's nuclear and magnetic scattering components.

The POLSANS technique measures the SANS diffraction pattern for an incident beam of spin polarised neutrons. The advantage of polarised neutron scattering was that it allows one to extract the sample's nuclear-magnetic interference, which was directly proportional to the grain's nuclear and magnetic scattering form factor. By using an appropriate scattering model, one can extract the recording grain's physical structure and compositional phase. In the following section, the POLSANS technique was used to investigate the local magnetic and nuclear structure of the LMRM sample AX1646.

4.5.1 Instrumentation

The sample AX1646 was characterised using the SANS1 instrument at PSI, Villigen, Switzerland [65]. Figure 4.60(a) shows a snapshot of the collimator/guide. The incident neutron beam was collimated into the target region, see second image of Figure 4.60(b). In section 3.1.1, the incident beam was polarised by using the magnetic super-mirror. The polariser was built into the system of neutron guides. The spin flipper was used to switch the neutrons between the spin up (+) and spin down (-) states. Table 4.8 lists the instrument specifications. The scattering statistics were improved by combining 26 identical sample discs into a sample pile. Similarly the diameter of each disc was 1.4 cm. The pile was wrapped in Al foil and inserted into the sample holder depicted in Figure 4.24. The samples were shuffled beforehand to ensure that the in-plane magnetisation was randomised within the scattering plane. The recording layer of AX1646 saturated at the applied in-plane field of 2.0 T. Therefore the 11 T Oxford Instruments cryomagnet was used to magnetise the sample in-plane, see Figure 4.60(c).

SANS SPECIFICATIONS	***DETAILS***
Neutron Guide	Cold Neutron Guide 1RNR16; λ>0.42 nm
Monochromator	Helical Slot Velocity Selector
Wavelength	0.45 nm < λ < 4.0 nm
Resolution	$100\times\Delta\lambda/\lambda$=10%
Incident Neutron Flux for 10x10 mm^2 sample	5.0×10^6 n $cm^{-2}s^{-1}$
q-Range	6.0×10^{-3} nm^{-1}< q < 10.5 nm^{-1}
Detector	2D ^{3}He 128×128 elements of 7.5×7.5 mm^2
Collimation	1-18 m
Sample-Detector Distance	1-20 m continuously
Lateral Displacement	0-0.5 m

Table 4.8: The instrument parameters for the SANS1 machine [65].

(a)

(b)

(c)

Figure 4.60: Snapshots of the SANS1 instrument. The first image shows the (a) neutron beam collimator/guide. The second image depicts the (b) target region where the (c) cryomagnet and sample are fixed to the table mount.

4.5.2 Measurements

The POLSANS measurements were performed for the sample-detector distances of 2.0 m and 8.0 m at the neutron wavelength of 6.0 Å. By applying the momentum transfer argument, the SANS instrument spanned the q-range of 0.007 $Å^{-1}$<q<0.25 $Å^{-1}$. The measurements consisted of three parts (a) zero field sample transmission $I_T^{\pm}$, (b) zero field background scattering $I_B^{\pm}$ (q) and the (c) applied field foreground scattering $I_F^{\pm}$(q). The solid angle correction was applied to the scattering measurements. Through polarisation analysis, the magnetic and nuclear-magnetic scattering measurements were used to extract the recording layer's nuclear scattering component. The recording layer's sub-granular physical structure was related to the nuclear scattering intensity.

The sample transmission $I_T^{\pm}$ measures the intensity of the straight through beam for the ± neutron spin states. Figure 4.61 shows the transmission measurement for an incident beam of spin up neutrons at the sample-detector distance of 2.0 m. These measurements extracted the incident flux on the sample target. The incident flux was expressed by $\Phi = AI_T^{\pm}/S$ where S is the sample area exposed to the incident neutron beam A is the beam attenuator. Again these calculations were used to correct for beam flux-collimation and to normalise the scattering intensity to the cross-section units (cm^2).

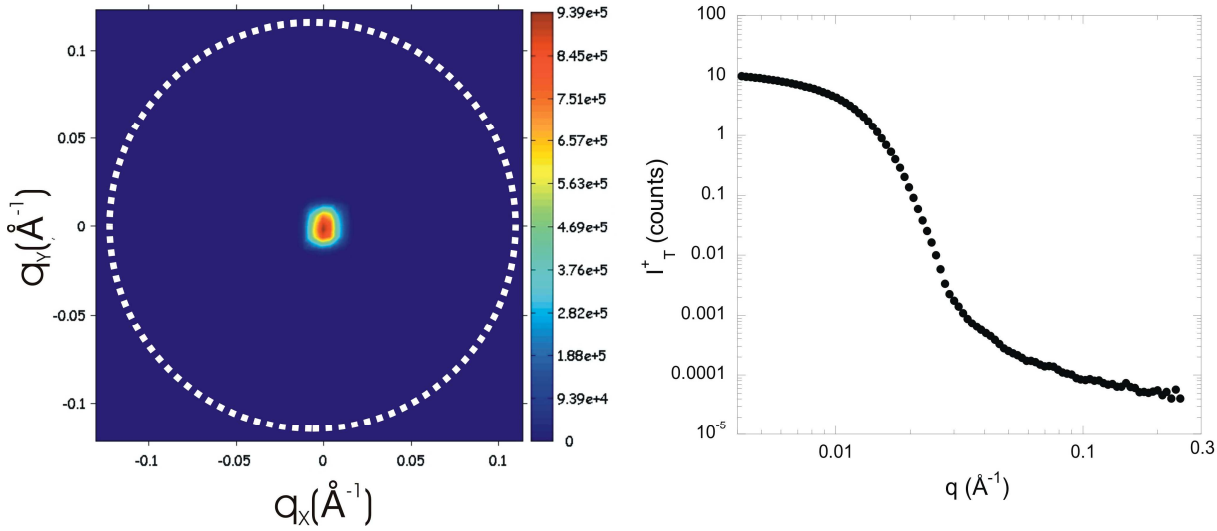

Figure 4.61: The transmission measurement for the SANS1 instrument at the detector distance of 2.0 m. The intensity plot is calculated within the dotted perimeter.

The background measurements for the ± neutron spins states were expressed by the scattering intensities $I_B^+(q)$ and $I_B^-(q)$ respectively. The unpolarised background scattering intensity was recovered by averaging the polarised background terms where $I_B(q)=\{I_B^+(q)+I_B^-(q)\}/2$. The background scattering was a superposition of nuclear and magnetic scattering components. The nuclear scattering component originates from the sample, sample holder and cryostat. The magnetic scattering component emanates from remanent state of the sample's magnetic recording layer and underlayer. The polarised background scattering was expressed by the following,

$$I_B^{\pm}(q) = \{I_N(q) + I_N'(q)\} + \{I_M(q) + I_M'(q) \pm 2\sqrt{I_N I_M}\}. \qquad (4.8)$$

The terms $I_N(q)$ and $I_M(q)$ represent the nuclear and magnetic scattering from the recording layer respectively. The nuclear background term $I_N'(q)$ defines all other scattering components not from the recording layer while $I_M'(q)$ represents the magnetic scattering from the underlayer. The term $(I_N I_M)^{1/2}$ defines the recording layer's nuclear-magnetic interference scattering. The background scattering from the instrument and non-magnetic underlayers do not exhibit magnetic scattering at the measured q-range, hence there was no nuclear-magnetic interference term.

The polarised foreground measurements for ± the spins states were expressed by the intensity terms $I_F^+(q)$ and $I_F^-(q)$. The foreground scattering intensity was expressed by the following,

$$I_F^{\pm}(q) = \{I_N(q) + I_N'(q)\} + \{I_M(q) + I_M'(q) \pm 2\sqrt{I_N I_M}\}\sin^2\alpha. \qquad (4.9)$$

The variable α defines the angle between the magnetic moment **m** and scattering **q** vectors. The ± foreground intensities within the 2D-scattering plane are illustrated in Figure 4.62. Equation 4.9 was normalised to the maximum scattering intensity either along the q_x or q_y axis. The nuclear and magnetic components were modelled using the Porod scattering function. The background terms have been neglected to emphasise the in-plane scattering anisotropy. The unpolarised foreground intensity was determined by averaging the ± foreground states where $I_F(q)=\{I_F^+(q)+I_F(q)\}/2$. The nuclear-magnetic interference term was extracted by calculating the difference between the ± foreground states where $I_F^+(q)-I_F^-(q)=4(I_N I_M)^{1/2}\sin^2\alpha$. In Figure 4.63, the left-plot illustrates the unpolarised magnetic scattering intensity while the right-plot simulates the nuclear-magnetic interference term.

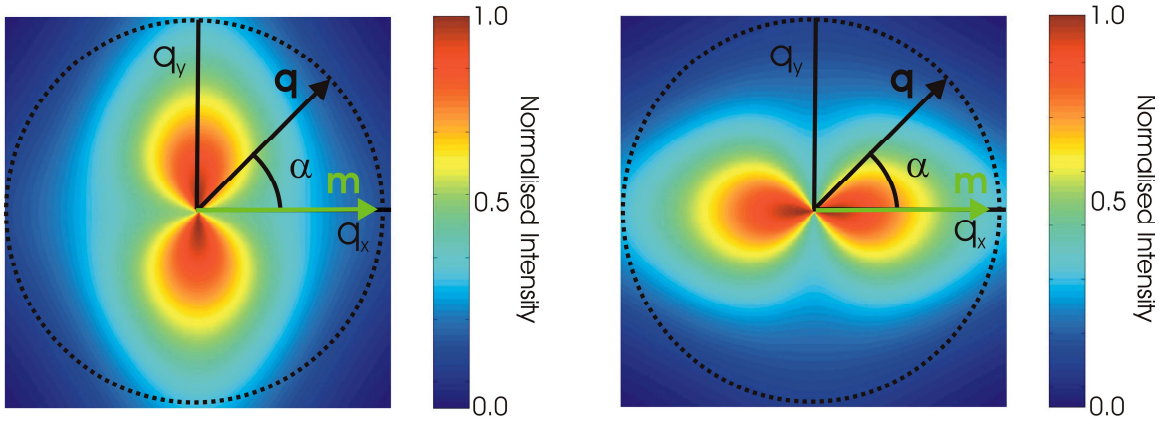

$$I_F^+(q) = I_N(q) + \{I_M(q) + 2\sqrt{I_M I_N}\}\sin^2\alpha \qquad I_F^-(q) = I_N(q) + \{I_M(q) - 2\sqrt{I_M I_N}\}\sin^2\alpha$$

Figure 4.62: The simulated foreground scattering for the polarised scattering intensities, $I_F^{\pm}(q)$. In this analysis, the recording layer's nuclear and magnetic scattering intensities are modelled using the Porod scattering function. The background scattering from the substrate and instrument has been neglected to highlight the scattering anisotropy.

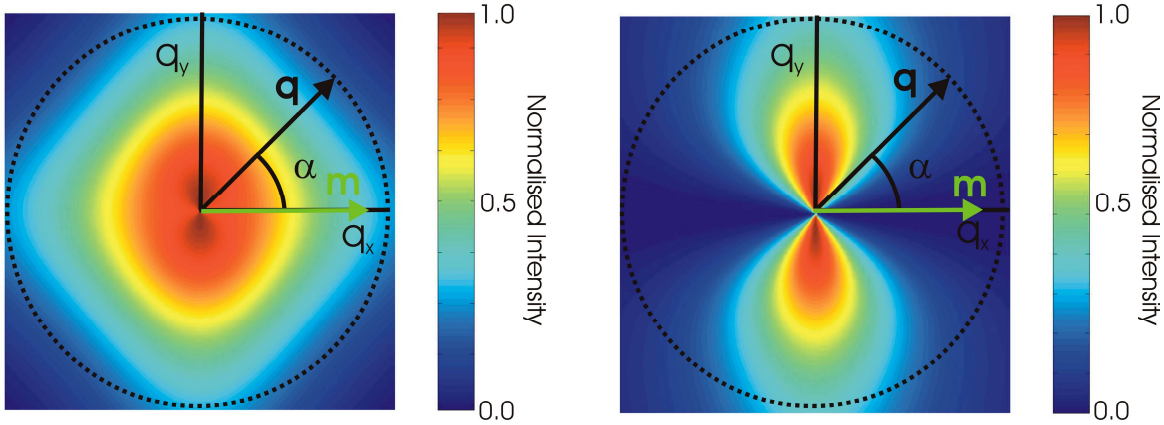

$$\frac{I_F^+(q) + I_F^-(q)}{2} = I_N(q) + I_M(q)\sin^2\alpha \qquad I_F^+(q) - I_F^-(q) = 4\sqrt{I_M I_N}\sin^2\alpha$$

Figure 4.63: The simulated unpolarsied magnetic scattering intensity and the nuclear-magnetic interference term. The background scattering from the substrate and instrument has been neglected to highlight the scattering anisotropy.

4.5.3 Results and Discussion

The first stage of the experiment was to extract the magnetic diffraction pattern from unpolarsied SANS measurements. The foreground and background diffraction pattern was measured at the sample-detector distance of 2.0 m at the in-plane field of 1.38 T. The respective polarised measurements were averaged to obtain the unpolarised diffraction patterns shown in Figure 4.64. Note the q=0 position was shifted to the right of the detector centre. This q-shift allows one to measure the scattering intensity at larger q_x values. For each diffraction pattern the magnetic scattering geometry was shown for the target sample of 26 recording layers. The grey arrow depicts the incident neutron beam. The black arrow defines the neutron beam's ± spin states. At the magnetic field of H=1.38 T, the recording layer's magnetic moments were partially saturated along the field direction. The magnetic difference plot was determined by subtracting off the nuclear scattering and zero magnetic scattering components.

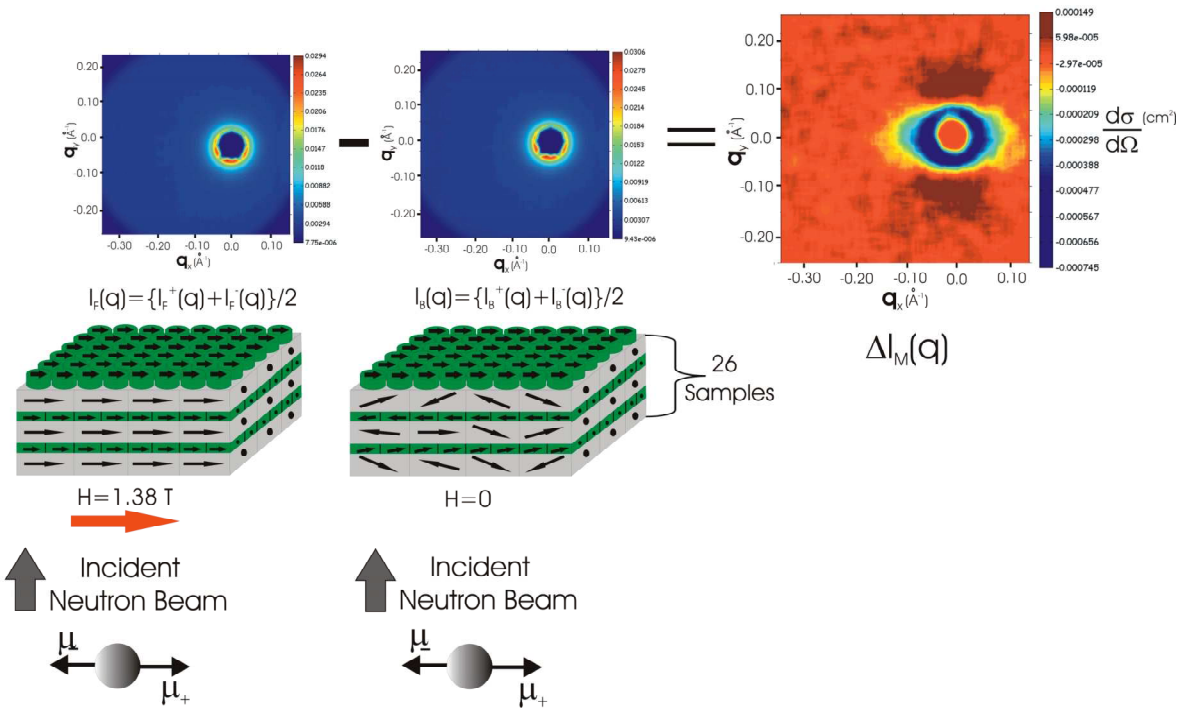

Figure 4.64: The AX1646 1.38 T unpolarised foreground and background measurements at the sample-detector distance of 2.0 m. Note in this SANS experiment the unpolarised diffraction pattern is extracted by averaging the ± foreground and background intensities. The subtraction gives the magnetic difference plot.

The azimuthal scattering intensity was extracted from the magnetic difference plot at detector distances of 2.0 m and 8.0 m. In Figure 4.65(a) the diffraction pattern was highly anisotropic within the scattering plane. This was demonstrated by the close fit of the moment orientation factor where the sample's in-plane magnetisation was fully saturated along the in-plane field direction. In Figure 4.65(b) the azimuthal scattering intensity remains anisotropic within the scattering plane although the scattering data was quite noisy at the detector's edge. The ANCOS^2 phase steps were identified by,

$$\delta_c = \begin{cases} 0 & ,0.007\text{Å}^{-1} < q_1 < 0.026\text{Å}^{-1} \\ \pi/2 & ,0.026\text{Å}^{-1} < q_2 < 0.064\text{Å}^{-1} \\ 0 & ,0.064\text{Å}^{-1} < q_3 < 0.25\,\text{Å}^{-1} \end{cases} . \qquad (4.10)$$

The magnetic scattering intensity was partitioned into its positive and negative values through the application of equation 4.10. The recording layer's magnetic scattering intensity is plotted in Figure 4.66. Within the q_1-range a large fraction of the magnetic scattering originates from the NiP underlayer. For the q_2-range the magnetic scattering was dominated by the sample's recording layer. The ANCOS^2 phase switches to $\pi/2$, which indicates that the grain's contrast variation along the q_y-axis was greater than its orthogonal component. The scattering intensity returns to zero phase for $q>0.064$ Å^{-1} where the grain's contrast variation was now greater along the q_x-axis.

The magnetic scattering intensity was modelled using the two-dimensional expression, $I(q)=N_y\langle F(q_y)^2\rangle - N_x\langle F(q_x)^2\rangle + I_{Porod}(q)$. The form factor was modelled using the spherical core-shell structure while the background term was expressed using the Porod scattering function. The NLS fitting program obtained a closeness of fit $\chi^2=1.16$. Table 4.9 lists the parameters for the form factors and Porod function. The magnetic scattering along the q_y-axis described by the form factor $F(q_y)$. The model gives a core and shell diameter of 40.0 ± 2.0 Å and 99.4 ± 3.0 Å respectively with a grain size distribution of the order of 30%. The form factor $F(q_x)$ gives a core and shell diameter of 70.6 ± 5.0 Å and 124 ± 4.0 Å respectively with a grain size distribution of 28%. The magnetic grain size and size distribution, obtained from the form factor, shows moderate agreement with respect the physical grain size of 100.0 Å with a size distribution of 30% [51]. In the latter half of the section, polarisation analysis will be used to extract the recording grain's nuclear scattering intensity. This calculation will provide a direct comparison between the magnetic and physical grain size.

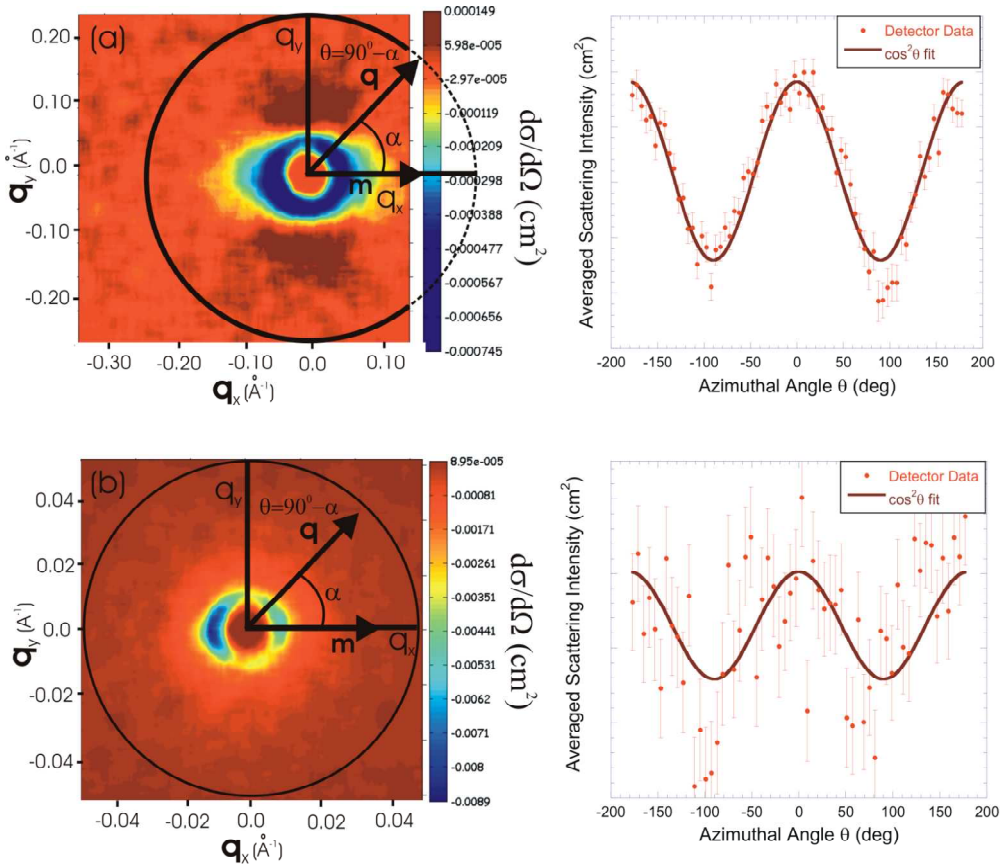

Figure 4.65:The AX1646 1.38 T magnetic difference plot at (a) 2.0 m and (b) 8.0 m for the q ranges 0.04 Å^{-1}<$q_{2.0m}$<0.25 Å^{-1}, (b) 0.008 Å^{-1}<$q_{8.0m}$<0.09 Å^{-1} respectively.

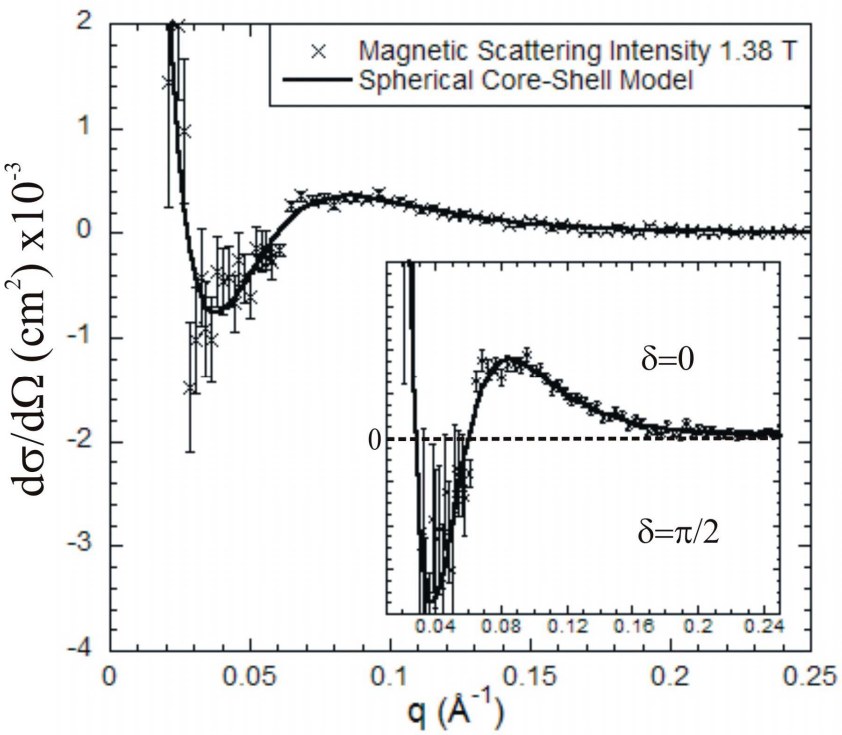

Figure 4.66: The AX1646 1.38 T anisotropic magnetic scattering intensity fitted to the spherical core-shell model. The inset shows the positive and negative intensities for the respective ANCOS^2 phase of zero and π/2.

The magnetic scattering intensity at the in-plane fields of 1.38 T (SANS1) and 1.45 T (D11) are compared in Figure 4.67. The scattering intensities at either field exhibits similar features with respect to background and form factor intensities. The significant difference between the data sets relates to the relative q-shift of the scattering nodes so defined by Δq_1 and Δq_2. The scattering node defines the $\pi/2$ phase shift for the ANCOS^2 fitting function. For the magnetic field of 1.38 T the scattering nodes were shifted towards larger q-values. This q-shift was linked to the grain's in-plane magneto-crystalline anisotropy field. As the applied magnetic field was reduced, the granular moments begin to align along their easy axis of magnetisation. At the field 1.45 T, the in-plane moment variations were smaller than that of 1.38 T. Therefore the magnetic contrast variation along the y-axis for was greater than the 1.45 T measurement where $\Delta\eta^M_y(1.38T)>\Delta\eta^M_y(1.48T)$. The third scattering node was absent from the SANS1 scattering data. It was most likely that this scattering node was shifted beyond the maximum q-range of $q>0.25$ Å^{-1}.

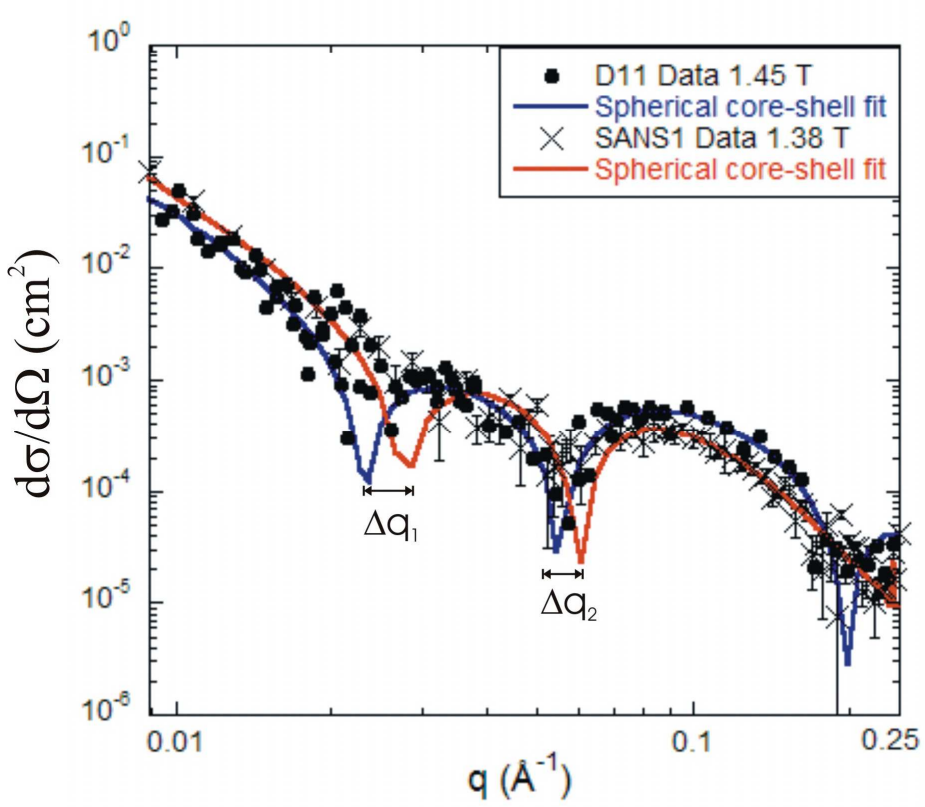

Figure 4.67: The AX1646 comparison between the SANS1 and D11 magnetic scattering intensity data at the in-plane magnetic fields of 1.38 T and 1.45 T respectively. The values Δq_1 and Δq_2 represent the q-shift of the scattering nodes.

Scattering Function	***Description***	***Parameter***	***NLS Switch***	***Value***
F(q)	Magnetic Core Contrast	$\Delta\eta_c$	*Free*	$(1.54 \pm 0.10)\times10^{-6}$ Å^{-2}
	Core Moment Angle	φ_c	*Fixed*	24.0 ± 4^0
	Core Radius	R_{cy}	*Free*	19.8 ± 1.5 Å
	Shell Radius	R_{sy}	*Fixed*	49.7 ± 3.0 Å
	γ-Distribution Width	σ_y	*Fixed*	15.0 Å
	Magnetic Shell Contrast	$\Delta\eta_s$	*Free*	$(2.01 \pm 0.50)\times10^{-7}$ Å^{-2}
	Shell Moment Angle	φ_s	*Fixed*	8.2 ± 2^0
	Core Radius	R_{cx}	*Free*	35.3 ± 3.0 Å
	Shell Radius	R_{sx}	*Fixed*	62.0 ± 4.0 Å
	γ-Distribution Width	σ_x	*Fixed*	19.0 Å
$I_{Porod}(q)$	Porod exponent	n	*Fixed*	2.9
	Scale factor	A	*Fixed*	7.6×10^{-8}
	Background	B	*Fixed*	9.5×10^{-7}
	Closeness of Fit	χ^2	---	1.16

Table 4.9: The AX1646 1.38 T fit parameters for the form factor-F(q) and Porod-$I_{Porod}(q)$ scattering functions.

The second stage of the POLSANS experiment was to calculate the intensity difference between the ± foreground scattering states. Figure 4.68 shows the nuclear-magnetic interference pattern at the sample-detector distance of 2.0 m. The azimuthal intensity was calculated over the q range of 0.05 $Å^{-1}$<q<0.25 $Å^{-1}$. The $\cos^2\theta$ fit shows a strong anisotropic diffraction pattern within the scattering plane. It was known that the scattering anisotropy stems from the moment orientation factor while the intensity results from the interference of magnetic and nuclear scattering components.

The recording grain's physical structure was determined by extracting the nuclear scattering intensity from the interference pattern. The interference intensity was expressed by, $I_{NM}(q)=4(I_N I_M)^{1/2}$ where the intensities $I_N(q)$ and $I_M(q)$ represent the recording layer's nuclear and magnetic scattering components respectively. By dividing out the magnetic scattering component, the nuclear scattering intensity was expressed by $I_N(q)=\{I^2_{NM}(q)/(I_M(q)16)\}$. The interference term $I_{NM}(q)$ and the magnetic scattering intensity $I_M(q)$ were inserted into the nuclear scattering expression. Figure 4.69 shows the magnetic, nuclear and nuclear-magnetic scattering intensities on the log-log scale.

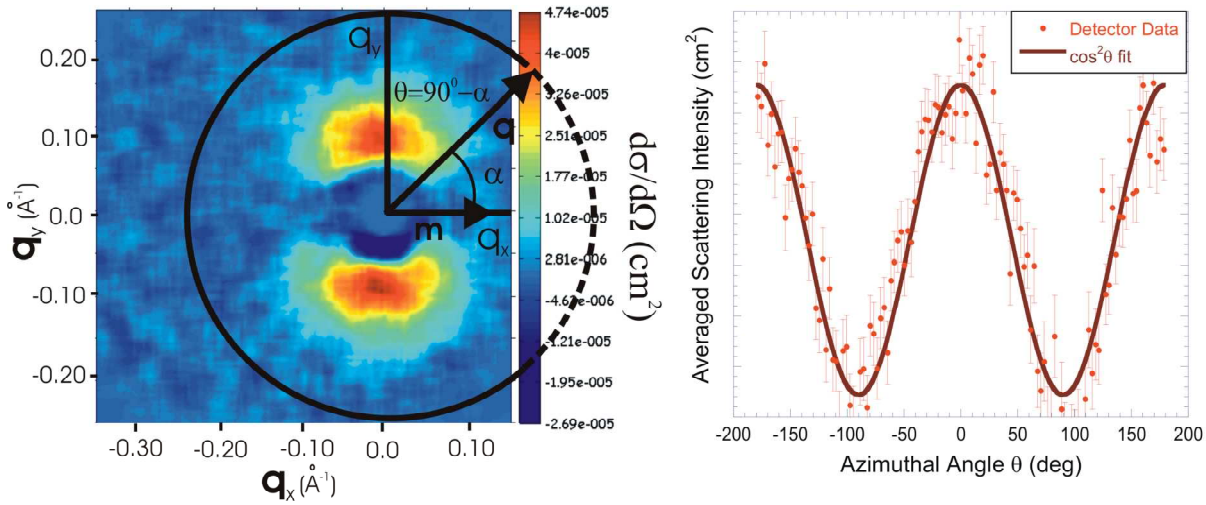

Figure 4.68: The AX1646 nuclear-magnetic interference pattern at the sample-detector distance of 2.0 m. The azimuthal scattering intensity is calculated for the nuclear-magnetic interference where the $\cos^2\theta$ function fits the scattering anisotropy.

The interference term exhibits similar scattering features when compared to the magnetic scattering intensity. The Porod-like interference scattering was observed for the q range of 0.0089 $Å^{-1}$<q<0.06 $Å^{-1}$. It would appear that this interference component originates from the sample's magnetically soft underlayer. In this case the underlayer's magnetic scattering component was interfering with its corresponding nuclear scattering intensity. Within the range of q>0.06 $Å^{-1}$ the interference term and magnetic scattering intensity exhibit matching nodes at q=0.06 $Å^{-1}$ and q=0.20 $Å^{-1}$. These nodes give the first indication that the magnetic and physical grain sizes were similar in magnitude. The nuclear scattering intensity exhibited a much weaker contrast value, however the scattering behaviour was comparable to its magnetic component. This result allows one to model the nuclear scattering with the spherical core-shell structure.

In Figure 4.70, the nuclear scattering intensity was fitted using the expression $I_N(q) \approx <F_N(q)>^2 + I_{Porod}(q)$. The scattering form factor was modelled using the spherical core-shell structure. The scattering model shows moderate agreement with a closeness of fit χ^2=3.25. The form factor extracted the core and shell diameter of 33.5±0.9 Å and 108.0±1.0 Å respectively. The outer shell was comparable to its magnetic counterpart, which confirms that the magnetic and nuclear grain size were equivalent. The grain size distribution was negligible for the scattering form factor. The TEM measurements show a physical size distribution of 30% [76]. This discrepancy was attributed to the nuclear scattering extraction procedure. When the magnetic scattering intensity was divided out from the interference term, the resulting nuclear component inherited sharper scattering features. In response the NLS routine fits these sharp scattering features by using a monodisperse averaged form factor.

The nuclear scattering core and shell contrast components were expressed by $\Delta\eta_c^N = \eta_c - \eta_s$ and $\Delta\eta_s^N = \eta_s - <\eta>$ respectively. The terms η_c, η_s, $<\eta>$ represent the grain's nuclear scattering length density for the core, shell and average component. The model extracted a core and shell contrast of $(1.43 \pm 0.10)\times10^{-8}$ $Å^{-2}$ and $(-1.05 \pm 0.04)\times10^{-9}$ $Å^{-2}$ respectively. The core contrast was about ten times the shell component as a result the core's nuclear scattering length density was greater than the outer shell structure. Another feature of the contrast components was that the shell component was slightly shifted below the average scattering density. Similar behaviour was observed for the magnetic contrast components at the saturation, however no physical explanation could be found on why the nuclear contrast resulted in a negative value.

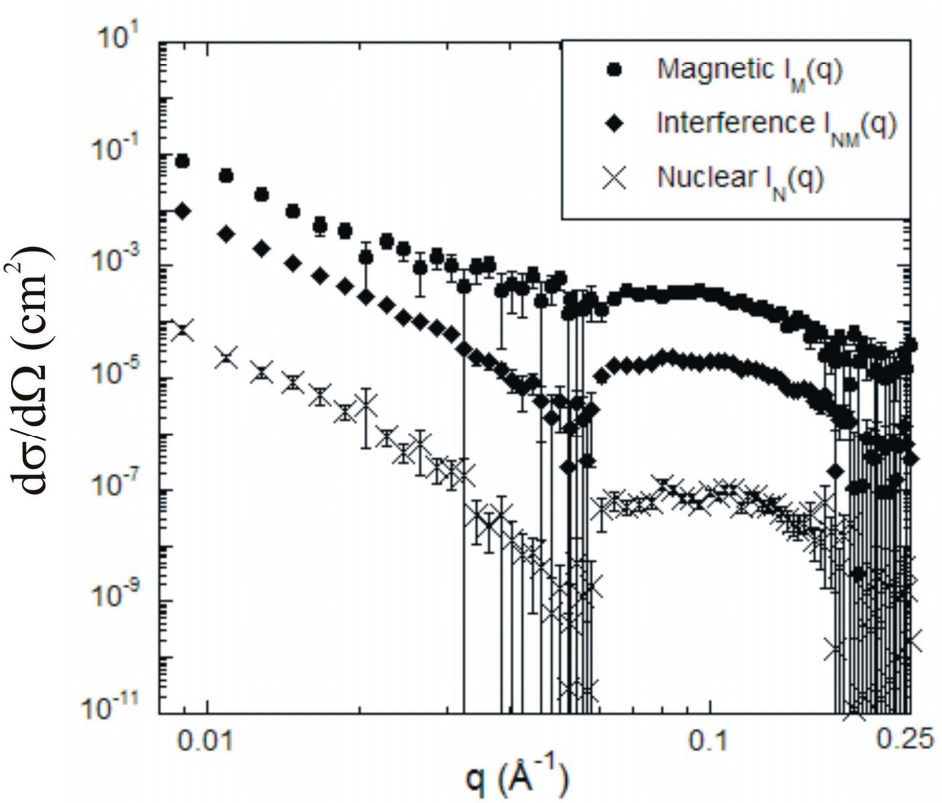

Figure 4.69: The AX1646 1.38T magnetic, nuclear-magnetic interference and nuclear scattering intensities.

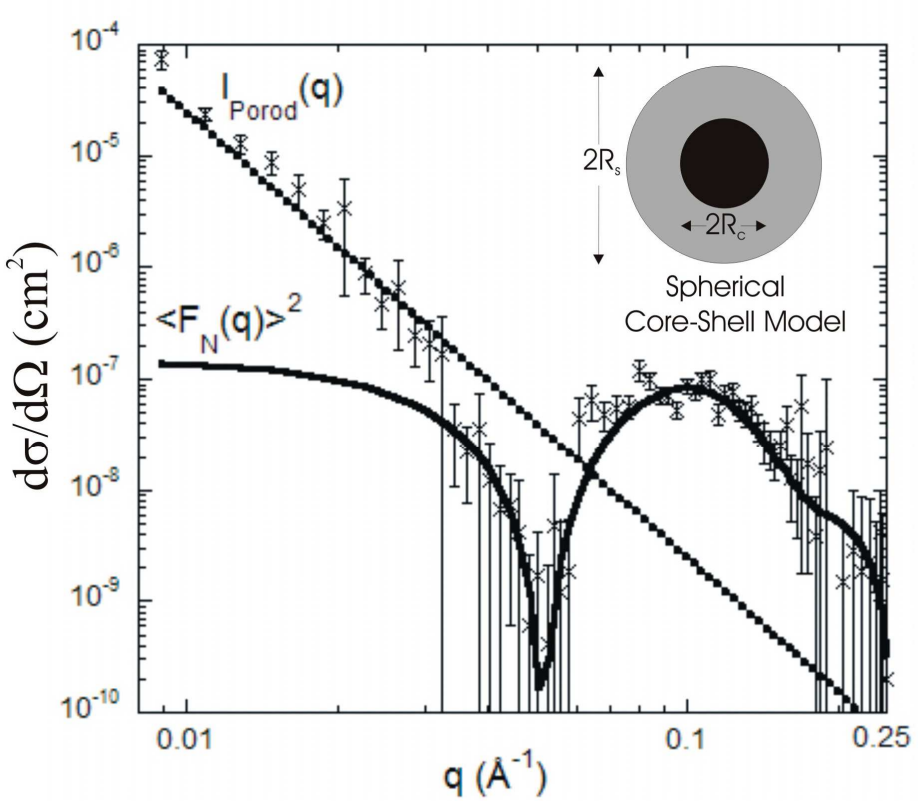

Figure 4.70: The AX1646 nuclear scattering intensity fitted to the spherical core-shell form factor and Porod scattering function.

The nuclear scattering contrast components were compared with theoretical calculations. The recording grain's composition consisted of a cobalt-enriched core ($Co_{84}Cr_{10}Pt_6$) and a chromium/boron segregated shell ($Co_{72}Cr_{18}Pt_6B_6$). Within the grain it was assumed that the majority of the boron atoms segregate to the outer shell. The density of the cobalt enriched core was approximated by the bulk value of cobalt ρ_c=8.9 g/cm^3 [34]. The shell component was slightly enriched with chromium resulting in the reduction in the alloy density. The shell density was approximated by the bulk value of chromium ρ_s=7.5 g/cm^3 [34]. The grain's nuclear scattering length density was calculated by using the formula $\eta=\Sigma_i(c_i\rho/N_A)\eta_i$ where c_i is the atomic fraction of the ith element, ρ is the compound's bulk density and η_i is the ith element's bound nuclear scattering length density [91]. The density formula was used to calculate the core and shell nuclear scattering densities of $\eta_c=2.47\times10^{-6}$ Å^{-2} and $\eta_s=2.35\times10^{-6}$ Å^{-2} respectively.

The calculated core and shell nuclear scattering contrasts were $\Delta\eta_c=1.2\times10^{-7}$ Å^{-2} and $\Delta\eta_s=-1.10\times10^{-7}$ Å^{-2} respectively. Figure 4.71 shows the grain's nuclear scattering contrast profile for the (a) SANS measurements and (b) theory calculations. The theory result shows how the grain's core and shell components were equally displaced above and below the average scattering density <η>. The experimental result gives a similar contrast profile however the shell contrast was much smaller than its core component. It was most likely that the contrast calculations have overestimated the percentage of boron and chromium within the outer shell thereby increasing the shell's nuclear scattering length density.

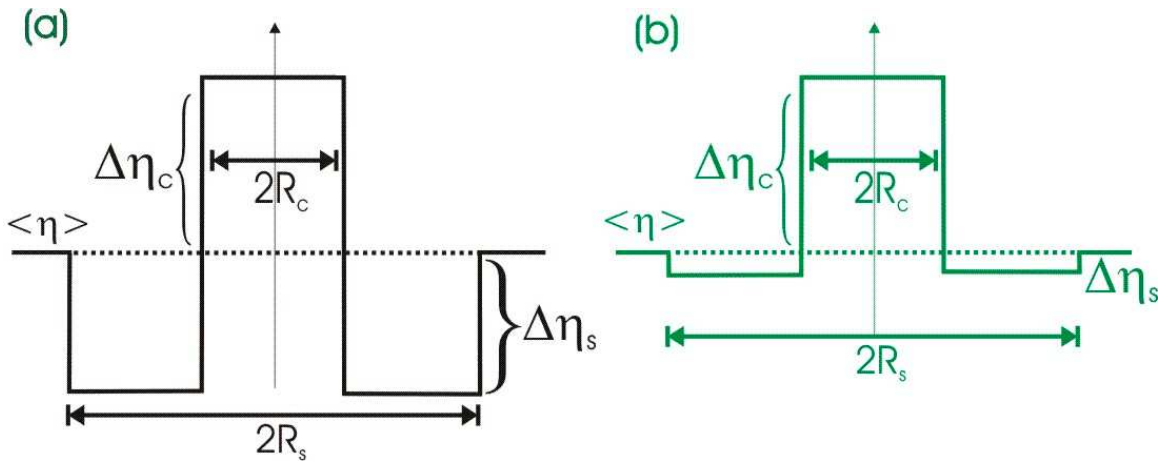

Figure 4.71: The recording grain's nuclear scattering contrast profile as a function of radius for the (a) theory calculations and (b) SANS measurements.

4.5.4 Summary

The POLSANS technique was used to characterise the recording layer's magnetic and physical structure at the sub-granular scale. The experiment measured the diffraction pattern for an incident beam of spin polarised neutrons at the applied in-plane magnetic field of 1.38 T. The anisotropic magnetic scattering was extracted from the unpolarsied foreground diffraction pattern. The nuclear-magnetic interference term was extracted by taking the difference between the polarised foreground measurements. The nuclear scattering intensity was determined by dividing the interference term by the magnetic scattering intensity at 1.38 T. The nuclear scattering component was modelled using the spherical core-shell structure. The form factor showed a large core contrast with respect to the outer shell. This was attributed to the grain's cobalt-enriched core, which has a larger scattering length density then its shell component. It was shown that the physical grain size was comparable to its magnetic counterpart. These results demonstrate that POLSANS can simultaneously extract an accurate length scale for the magnetic and physical grain size.

4.6 Conclusion

In this chapter, SANS studies in conjunction with SQUID measurements were used to investigate the magnetic and physical structure of longitudinal recording grains. The first SANS experiment used unpolarised neutron scattering to measurement the recording layer's magnetic sub-granular structure. It was successfully shown that the spherical core-shell form factor could extract the recording layer's magnetic grain size. The form factor model was proved correct by showing close agreement between the magnetic and physical grain size. The scattering model also showed that the recording grain was composed of a hard-ferromagnetic core (Co-enriched) and a weakly magnetic shell (Cr-enriched). An accurate characterisation of the grain's magnetic composition was important for determining the medium's recording properties. For example the magnetic grain size was proportional to the magneto-crystalline anisotropy energy. This property was linked to the grain's thermal activation energy, which determined the stability of the storage medium over long periods of time. The soft magnetic volume was linked to the effectiveness of the granular segregation. The well-segregated grain improves the recording media's SNR.

The second experiment used polarised SANS studies to investigate the recording layer's sub-granular length scale. It was demonstrated that the magnetic and physical grain size could be simultaneously extracted from the nuclear-magnetic interference term. These scattering measurements confirmed that the magnetic and physical grain size were of comparable magnitude. Further analysis of the nuclear scattering intensity similarly showed that the recording grain consisted of a spherical core-shell structure. Spatial information on the recording grain's physical length scale was important for characterising the grain boundary's magnetic and chemical composition.

The methodology developed from these experiments was applied to other projects that involve characterisation and simulation of nano-sized magnetic structures. The emergence of perpendicular-based recording media has resulted in further reductions in the magnetic grain size. This requires a characterisation method that can measure the recording properties at smaller sub-granular length scales. In the following chapter, SANS and POLSANS measurements were used to characterise perpendicular magnetic recording media. The SANS technique was also useful for investigating highly ordered magnetic nano-structures. In Chapter 6, SANS measurements were used to investigate the magnetic structure of self-assembled cobalt nanowires. Finally in Chapter 7 the SANS studies of longitudinal recording grains and cobalt nanowires were simulated using the micromagnetic method.

Chapter 5

Perpendicular Magnetic Recording Media

5.1 Introduction

In the last few years, the research and development of longitudinal magnetic recording media (LMRM) has focused on increasing the areal density of the recording layer. The latest longitudinal hard disk drive can achieve areal densities of the order of 100 Gbits/inch^2. Consequently the decrease in grain volume leaves the recording bits susceptible to thermal activation effects such as super-paramagnetism. For instance the reduction in grain volume decreases the energy barrier separating a pair of magnetised bits. At the threshold density, the energy barrier can no longer prevent thermal forces from switching the recording bits to alternate magnetic states. At the extreme case, thermal forces will drive the bit's magnetisation to zero. This translates into bit pattern instabilities, which in turn leads to data erasure. Due to these physical limitations, the storage capacity of LMRM is quickly approaching its maximum areal density. The next generation of recording medium known as perpendicular magnetic recording media (PMRM), is set to surpass the maximum storage density of 100 Gbits/inch^2. In the following decades it is reasonable to assume that PMRM storage device will come close to breaking the areal density mark of 1.0 Tb/inch^2.

The perpendicular recording media reads and writes information on magnetised bits aligned perpendicular to the sample plane. The recording layer is fabricated from either a super-lattice or alloy-based structure, see Figure 5.1. The super-lattice sample consists of a basic repeating structure of ferromagnetic and non-ferromagnetic thin films. Some examples of the super-lattice are Co/Pt/Co/Pt and Co/Pd/Co/Pd [93]. The recording bit is formed through generation of a large perpendicular magneto-crystalline anisotropy from the numerous interfaces. The typical energy densities are of the order of 10^8 ergs/cm^3. At these energy densities, the super-lattice has the potential to exhibit large coercivities, which are beneficial for perpendicular recording. The disadvantage of super-lattice media is the strong inter-granular exchange coupling, which leads to a large transition noise.

The alloy-based structure is fabricated from a single layered film composed of the ferromagnetic alloy such as CoCrPt. The recording bits are columnar shaped where each bit consists of 50-100 grains with a diameter of 80-100 Å. The recording grains are segregated by a grain boundary that is typically composed of a non-magnetic material such as SiO_2. The boundary thickness can vary from 10-20 Å. The following chapter focuses on the alloy-based recording media.

In previous studies of alloy-based perpendicular media, the recording bit's magnetic and physical structure were investigated using magnetic force microscopy (MFM) and transmission electron microscopy (TEM) respectively [94]. Due to the challenges of measuring small-scale structures, fewer studies have been reported on the recording bit's granular structure. Studies on the recording media's physical grain size and chemical composition were performed using the TEM and EDS measurements [95]. Further studies have examined the recording grain's crystalline properties using x-ray scattering [96]. Magnetic measurements such as MOKE and VSM have studied the recording layer's hysteresis behaviour as a function of the applied field [97,98].

With further improvements to the areal density, the perpendicular recording media becomes more prone to thermal activation and stray magnetic fields. Typically these interactions occur at a length scale of a few nanometers. To properly understand these magnetic interactions, one must develop a characterisation technique that can measure the recording grain's magnetic structure of the order of 10-100 Å. The above characterisation methods fail to extract any local information on the recording grain's magnetisation due to limitations in spatial resolution. In this chapter small angle neutron scattering (SANS) was used to investigate the local magnetism of perpendicular recording grains.

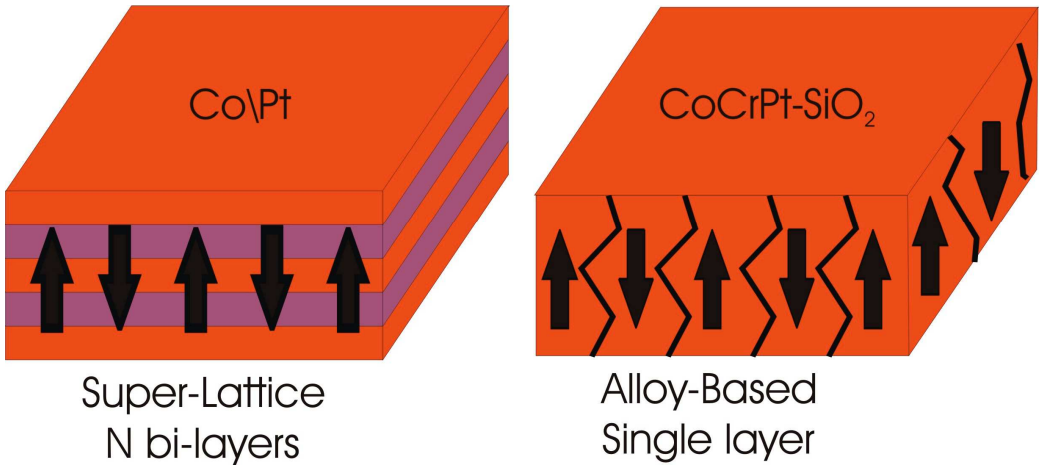

Figure 5.1: The PMRM recording layer for the super-lattice and alloy-based thin films.

5.2 The Recording Media Sample

The PMRM sample H114 was fabricated by Hitachi San Jose Research Center, San Jose, CA, USA [99]. The thin film sample was double sided which improves the magnetic scattering statistics for SANS characterisation. Figure 5.2 shows the cross-section of the PMRM sample. The sample multi-layers were grown on a glass substrate of thickness 0.6 cm. The soft magnetic underlayer (SUL) of thickness 1000 Å was deposited on the substrate. The SUL was composed of a highly permeable alloy Fe-Co. The function of the SUL was to provide the template for physical grain nucleation. In addition the SUL forms an essential component for the reading and writing of magnetic bits. A thin seed layer of Ru was deposited upon the SUL, which ensures that the c-axes of the recording grains grow orthogonal to the sample plane. The recording layer, approximate thickness of 150.0 Å, was deposited onto the seed layer. The recording grains were composed of CoCrPt-SiO_2 alloy with a grain size of 80-100 Å. A layer of carbon of thickness 50 Å was sputtered onto the recording layer. The carbon layer protects the recording layer from physical damage, electrical discharge and oxidation.

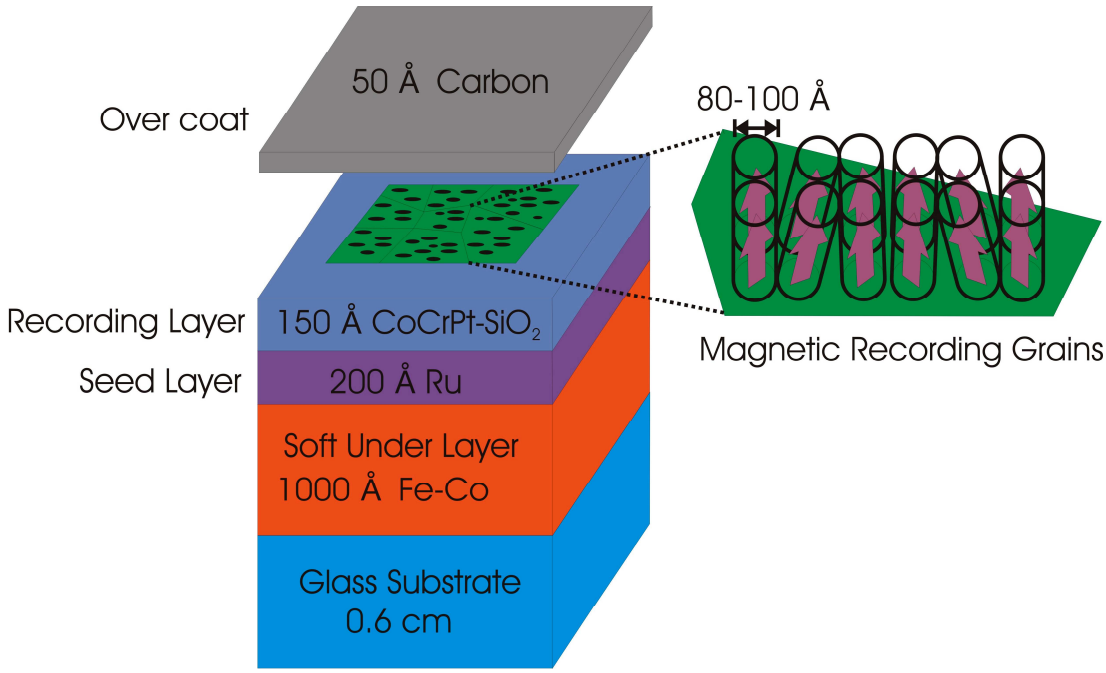

Figure 5.2: The multi-layered cross-section of the CoCrPt-SiO_2-based PMRM sample.

5.2.1 Recording Layer

The recording layer was composed of the ferromagnetic alloy CoCrPt-SiO_2. Typically the ensemble of grains forms a Voronoi type structure as shown in Figure 5.3. The grain's core region was mainly composed of cobalt with an atomic percentage of the order of 70-80%. The core was also doped with a small fraction of Cr, Pt, Si and O. Note the elements Si and O form into the non-magnetic compound SiO_2. The addition of Cr reduces the grain's saturation magnetisation thus improving the SNR during the read-write process. The addition of Pt increases the recording grain's perpendicular magneto-crystalline anisotropy field, which improves the medium's magnetic stability. The small fraction of SiO_2 only slightly reduces the grain's saturation magnetisation. The grain boundary was composed mainly of the non-magnetic compound SiO_2 with an atomic percentage of the order of 90%. The SiO_2 boundary segregates the magnetic recording grain, which reduces the inter-granular exchange coupling.

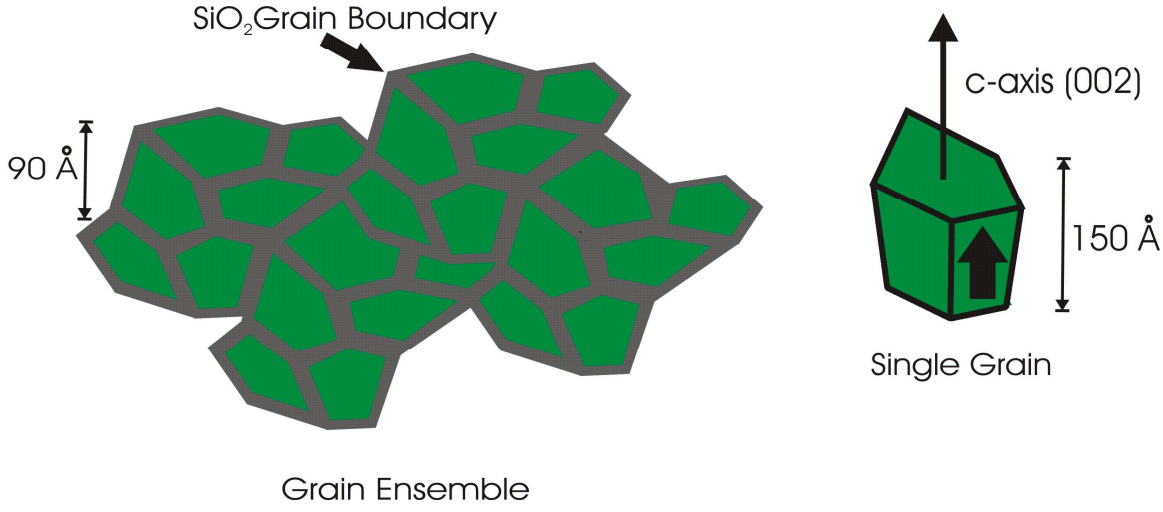

Figure 5.3: The physical microstructure of CoCrPt-SiO_2 perpendicular recording grains. The c-axis of a single grain is oriented perpendicular to the sample plane.

5.2.2 Seed Layer

The recording grain's crystalline structure was hexagonal closed packed (hcp). The c-axis lies perpendicular to the sample plane defined by the Miller index (002). The perpendicular geometry was achieved by sputtering the grains upon a Ru seed layer with a crystal texture of hcp (002). Figure 5.4 shows the PMRM sample's multi-layers and corresponding crystalline structure. The matching of textures at the recording-seed interface provides perpendicular alignment for the granular moments. The Ru layer also provides exchange de-coupling between the recording and soft under-layer. The crystal structure of CoCrPt-SiO_2/Ru was characterised using powder x-ray diffraction (XRD). Figure 5.5 shows the XRD measurements of the PMRM sample H114. The Bragg peak at $2\theta \approx 43.0^0$ originates from the recording layer's CoCrPt (002) reflection. The second peak at $2\theta \approx 93^0$ was from the CoCrPt (004) reflection. There was no Bragg reflection from the Ru seed layer due to the low incident flux of the x-ray beam. Crystallography tables show the Ru (002) reflection should occur at $2\theta \approx 42.17^0$. Figure 5.6 compares the Bragg peaks for the calculated Ru (002) and measured CoCrPt (002) reflections.

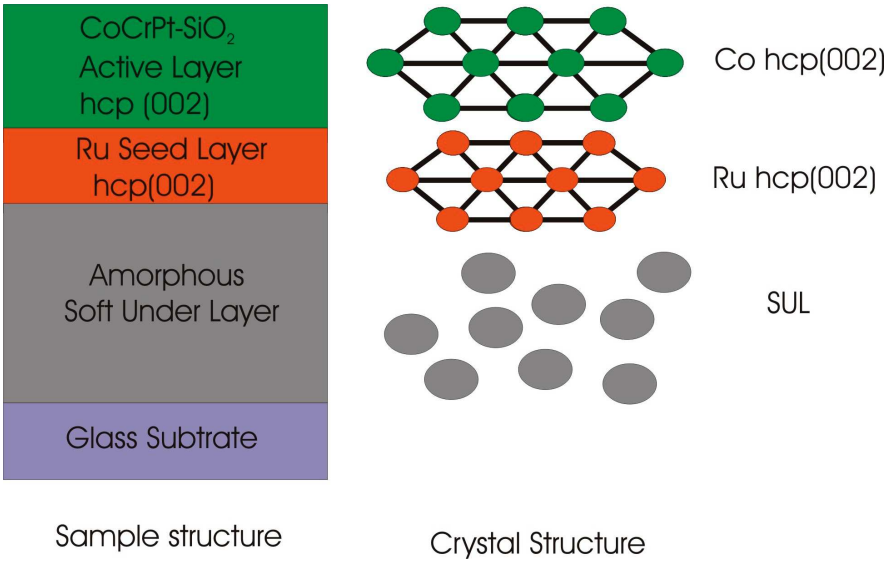

Figure 5.4: The cross-section of CoCrPt-SiO_2 perpendicular recording media showing the crystalline structure for each the respective layer [17].

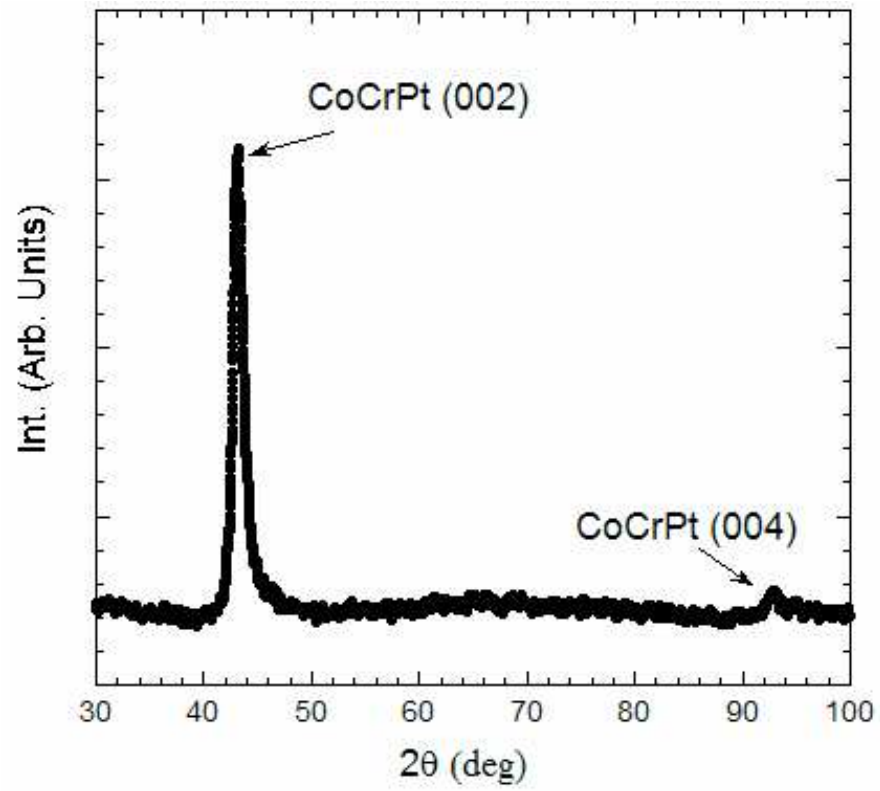

Figure 5.5: The H114 XRD measurements of the CoCrPt-SiO_2/Ru interface.

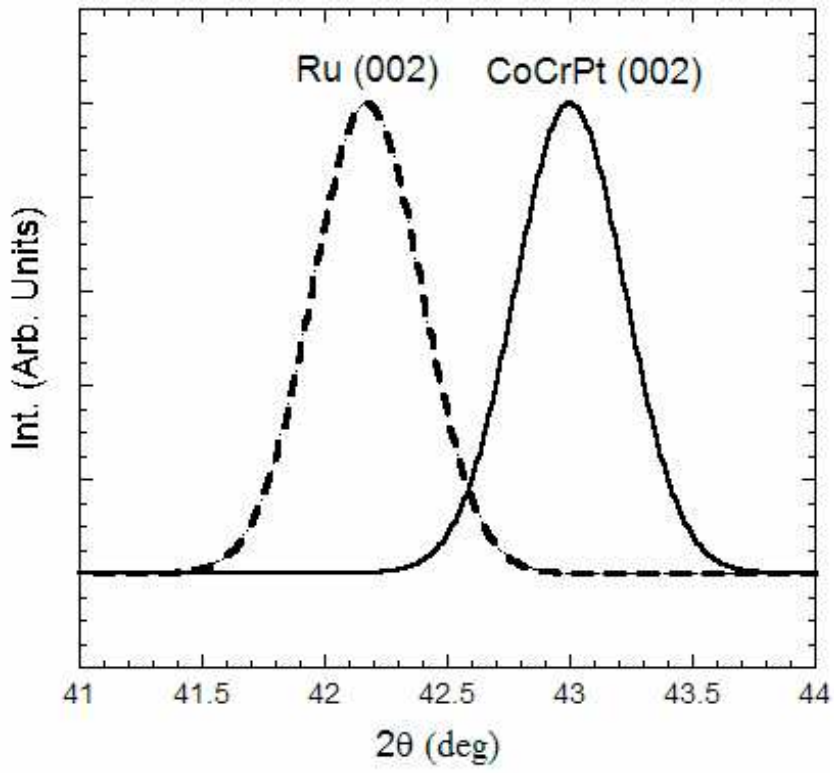

Figure 5.6: The simulated Bragg reflection of Ru(002) compared to the measured reflection of CoCrPt (002).

5.2.3 Soft Magnetic Underlayer

The sample's SUL was composed of the soft ferromagnetic alloy Co-Fe. The SUL is an essential component for the perpendicular writing process. In longitudinal recording media, magnetic data were written by using the pole-head fringe field H_F, see Figure 5.7. In perpendicular recording, the pole-head gap field H_G is used to record information. The write process is understood in terms of the image pole concept. When the pole field saturates the perpendicular media, the gap field is "funnelled" through the highly permeable SUL effectively creating an image of the single pole. The magnetic field above the SUL boundary is equal to the net sum of the fields generated by the write poles and their images. This magnetic phenomenon essentially doubles the write field amplitude and provides sharper write field gradients.

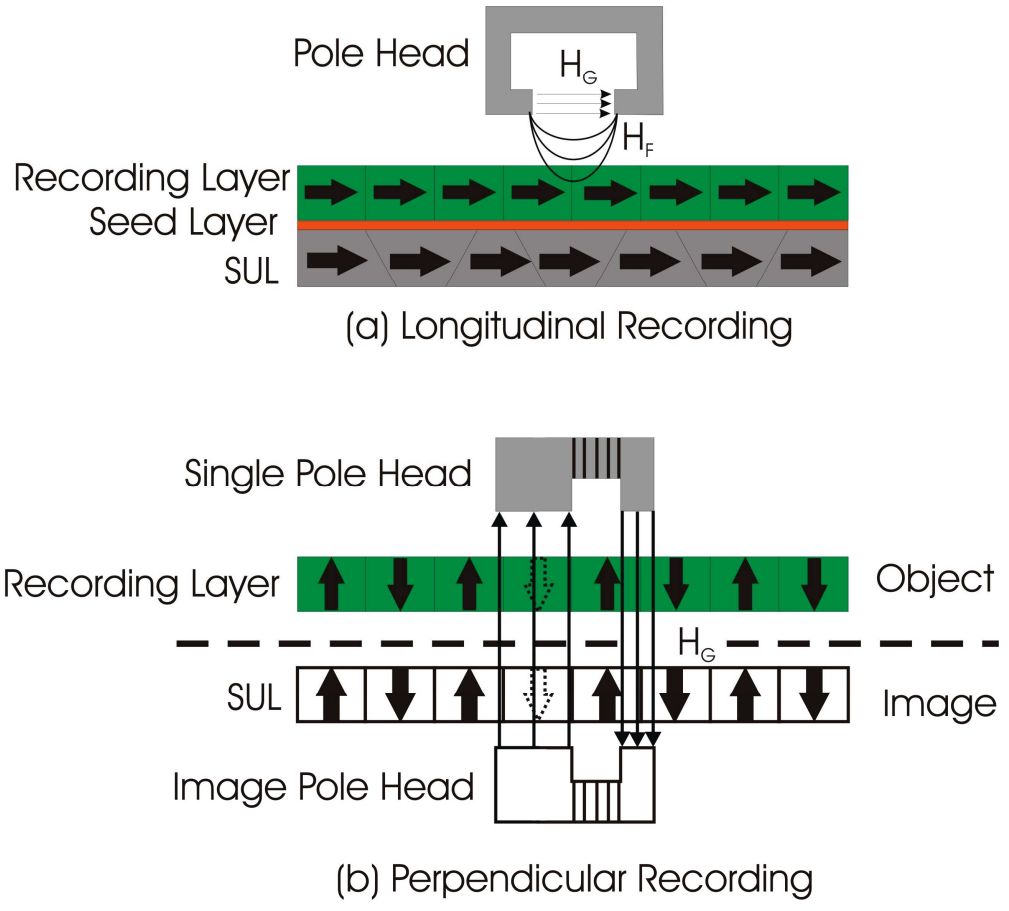

Figure 5.7: The write process for (a) longitudinal recording media using the fringe field H_F and (b) perpendicular recording media using the gap field H_G [17].

5.3 Bulk Magnetisation

The magnetisation of H114 was investigated for the out of plane and in-plane geometry as shown in Figure 5.8. The out of plane measurement was performed using the Magnetic Optical Kerr Effect (MOKE) where the applied magnetic field and moment orientation lied perpendicular to the sample plane [100]. The theory and application of MOKE was covered in section 3.2.2. The main advantage of MOKE was its ability to directly measure the magnetisation within the recording layer. Since the measurement was performed within a single layer, there was no magnetic background component from the Co-Fe underlayer. These measurements could be performed using the SQUID instrument, however the total moment would be dominated by the SUL's large magnetic moment. The in-plane measurement was carried out using the vibrating sample magnetometer (VSM) where the applied magnetic field lies parallel to the sample plane [101].

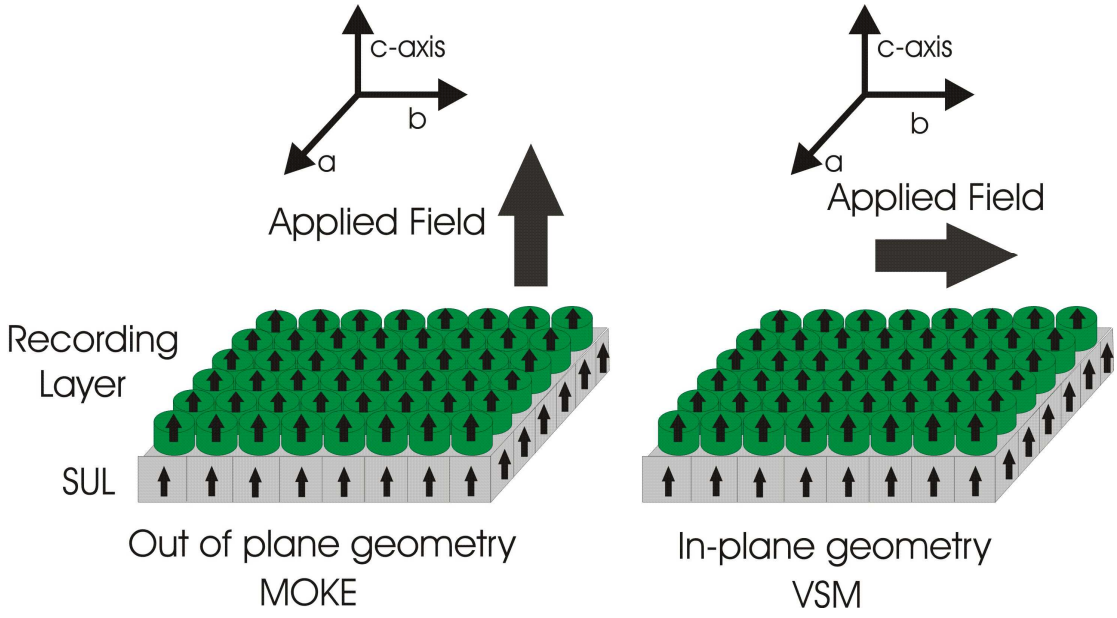

Figure 5.8: The out of plane and in-plane field geometries for the MOKE and VSM measurements respectively. In the out of plane field geometry, the perpendicular media is magnetised along the c-axis. For the in-plane geometry, the media is saturated within the a-b plane.

5.3.1 Results and Discussion

The MOKE instrument was used to measure the recording layer's out of plane hysteresis for the applied field range of -1.30 T<H<1.30T at temperature of 300 K, see Figure 5.9. In the MOKE measurement, the observed Kerr rotation was proportional to the recording layer's total moment. The total moment was normalised to the saturation value at 1.3 T (1.3×10^4 Oe) defined by the symbol μ. The remanent moment was nearly identical to the saturation value with a loop squareness of 0.98. This result shows the recording grains to have a strong out of plane magnetic anisotropy where the easy axis of magnetisation lies along the out of plane field direction. The magnetic anisotropy originates from the recording grain's magneto-crystalline field. For longitudinal based recording grains, the effective anisotropy field was smaller than the perpendicular grain. This property was attributed to the longitudinal grain's strong in-plane demagnetisation field, which reduces the strength of the magneto-crystalline field. The perpendicular grain's strong anisotropy field was beneficial for stable recording bits during the read/write process. The hysteresis loop also exhibits a large coercive field of the order of ±0.5 T. The coercive field was twice the size of the longitudinal result, which was indicative of stronger anisotropy energy

The VSM instrument was used to measure H114's in-plane moment for the applied field range of –4.0 T<H<4.0 T, see Figure 5.10. The VSM measurements were normalised to the saturation moment at the in-plane field of 4.0 T (4×10^4 Oe). The VSM measurement was a superposition of the recording layer (μ') and soft underlayer (μ'') moments where the total moment was expressed by $\mu=\mu'+\mu''$. The total moment shows no high anisotropy moment indicative of the CoCrPt recording layer. The inset in Figure 5.10 shows a hysteresis loop within the applied field range of –0.05 T<H<0.05 T. This hysteretic behaviour was characteristic of the sample's SUL, which was composed of the alloy Co-Fe. The recording layer's moment was extracted by subtracting off the SUL background. For the in-plane loop, there was no direct measurement of the SUL moment to perform the background subtraction. Alternatively the SUL background was simulated using a tangent function $\mu''(H, H_c, \mu_s, \mu_r)$ [104]. The input parameters H_c, μ_s and μ_r define the coercive field, saturation moment and remanent moment respectively.

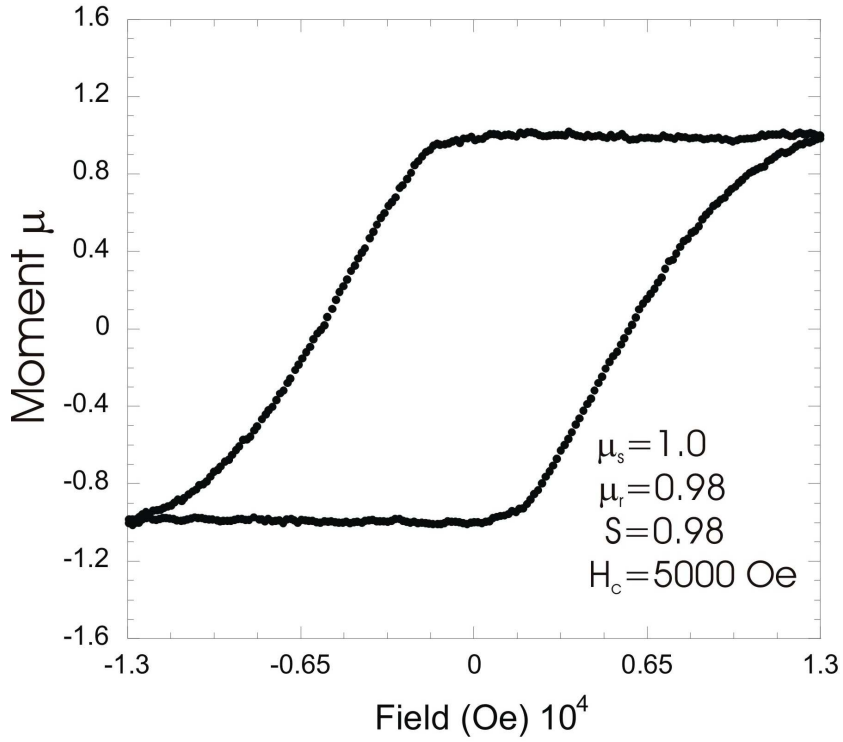

Figure 5.9: The H114 MOKE out of plane magnetic hysteresis loop for the field range of -1.30 T<H<1.30 T. The total moment was normalised to the saturation value [102].

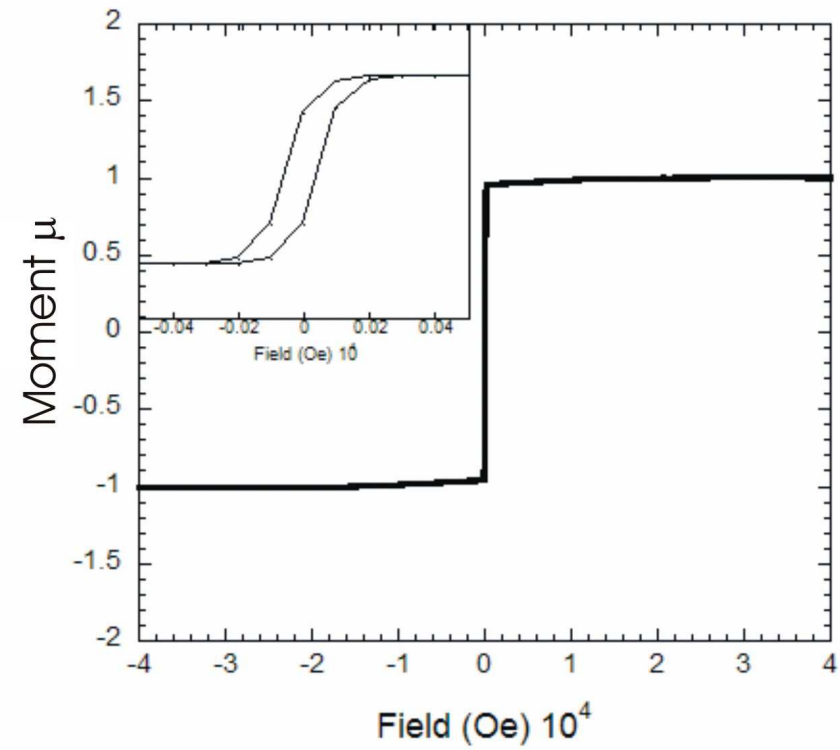

Figure 5.10: The H114 VSM in-plane magnetic hysteresis loop for the field range of -4.0 T<H<4.0 T. The total moment μ was normalised to the saturation value [103].

The input parameters of the SUL function were obtained by fitting the model to the in-plane data for the field range –0.025 T<H<0.025 T. The magnetic field limit of 0.025T defines the SUL's saturation magnetisation. Figure 5.11(a) shows the hysteresis loop of the SUL background modelled using the tangent function. According to the background fit, the SUL moment accounts for 95% of the sample's total moment. This property is a characteristic of the perpendicular medium where the large SUL moment is essential for imaging the recording layer and pole-head. The SUL's small squarness and coercive field shows that the Co-Fe underlayer exhibits a sizeable demagnetisation field.

The hysteresis loop for the recording layer was extracted by subtracting off the moment's background component so defined by the tangent function $\mu''(H,H_c,\mu_s,\mu_r)$, see Figure 5.11(b). The recording layer's saturation moment at 4.0 T contributes only a small fraction of the sample's total moment. As stated previously the SUL moment dominates the hysteresis measurement. The loop squareness was approximately 0.02. The small squareness was indicative of the recording layer's strong demagnetisation field that rotates any granular moments out of plane. The inset of Figure 5.11(b) shows a loop area of nearly zero. As a result the coercive field of 16 Oe was a small fraction of the out of plane value. Since the recording layer's easy axis of magnetisation lies out of plane, the magneto-crystalline energy plays no role in determining the magnitude of the coercive field.

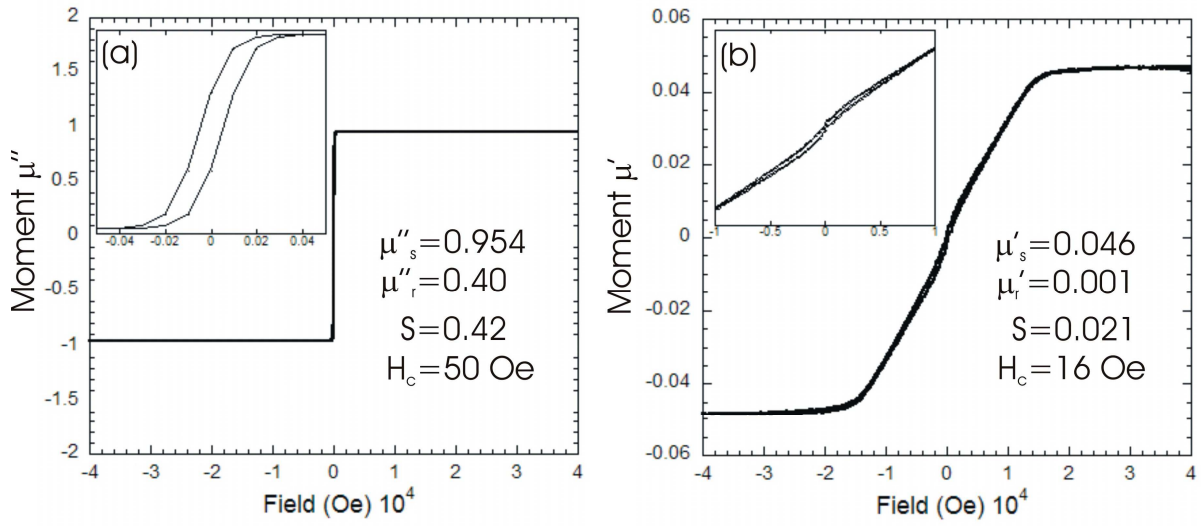

Figure 5.11: The in-plane hysteresis loop for the (a) SUL moment μ'' and (b) the recording layer moment μ'.

5.4 Unpolarised SANS

In the previous section, the characterisation technique of VSM was used to measure the in-plane hysteresis loop of perpendicular recording media. The magnetic hysteresis loop extracted information on the recording layer's bulk magnetic properties such as the saturation, remanent and coercive field. However these VSM measurements provided little information on the recording layer's sub-granular magnetisation. The characterisation technique of small angle neutron scattering (SANS) has the ability to measure the recording grain's magnetic and nuclear structure within the local length scale of 10-20 nm. In the following sections, unpolarised SANS studies were used to investigate the local magnetisation of the perpendicular recording media sample H114.

5.4.1 Scattering Model

The scattering intensity for a monodisperse ensemble of grains is described by $I(\mathbf{q}) \propto F(\mathbf{q})^2 S(\mathbf{q})$ where F(q) is the granular form factor and $S(\mathbf{q})$ is the structure factor. For elastic neutron scattering, the recording grain's physical spatial parameters such as grain size were determined by the nuclear scattering form factor. The form factor was modelled by calculating the Fourier transform of the grain's scattering potential. The geometry and density of the scattering potential was characterised using TEM and x-ray measurements respectively. It was observed in TEM measurements that the recording layer was composed of columnar grains with an approximate thickness of 15.0 nm [99].

Compositional EDS measurements showed that the CoCrPt-SiO_2 recording grain was composed of a core-shell structure [95]. The granular core was mainly composed of the cobalt-based alloy CoCrPt. The core region was highly enriched with cobalt with an atomic percentage of the order of 80%. The shell was doped with the non-magnetic compound SiO_2. The shell component effectively segregates the grain's ferromagnetic core region. The scattering potential was modelled using a cylindrical core-shell structure with finite length L and a core and shell radius of R_c^N and R_s^N respectively. The core-CoCrPt and shell-SiO_2 scattering contrasts were defined as $\Delta\eta_c^N$ and $\Delta\eta_s^N$ respectively. These respective values are proportional to the nuclear scattering length densities of the compounds CoCrPt and SiO_2. The top plot of Figure 5.12 depicts the cylindrical dimensions and nuclear contrast of the recording grain.

The grain's magnetic scattering potential was modelled using the spherical core-shell form factor expressed in equation 4.3. The magnetic grain was defined with a core and shell radius of R_c^M and R_s^M respectively. The spherical shaped object was used in place of the cylindrical model due to the apparent magnetic softening along the grain's perpendicular axis. This effect was identical to magnetic softening of recording grains explained in section 4.3. The magnetisation of the core and shell components was proportional to their respective magnetic scattering contrast $\Delta\eta_c^M$ and $\Delta\eta_s^M$. The magnitude of these contrast values was used to characterise the magnetic phase of the core and shell components. For example if $\Delta\eta_c^M > \Delta\eta_s^M$ than it is assumed that core component has a higher magnetisation than the outer shell. It was shown in the SANS measurements that shell contrast is non-magnetic, hence the magnetic recording grain was modelled using a solid sphere structure. The bottom plot of Figure 5.12 shows the solid sphere model and its magnetic scattering contrast profile.

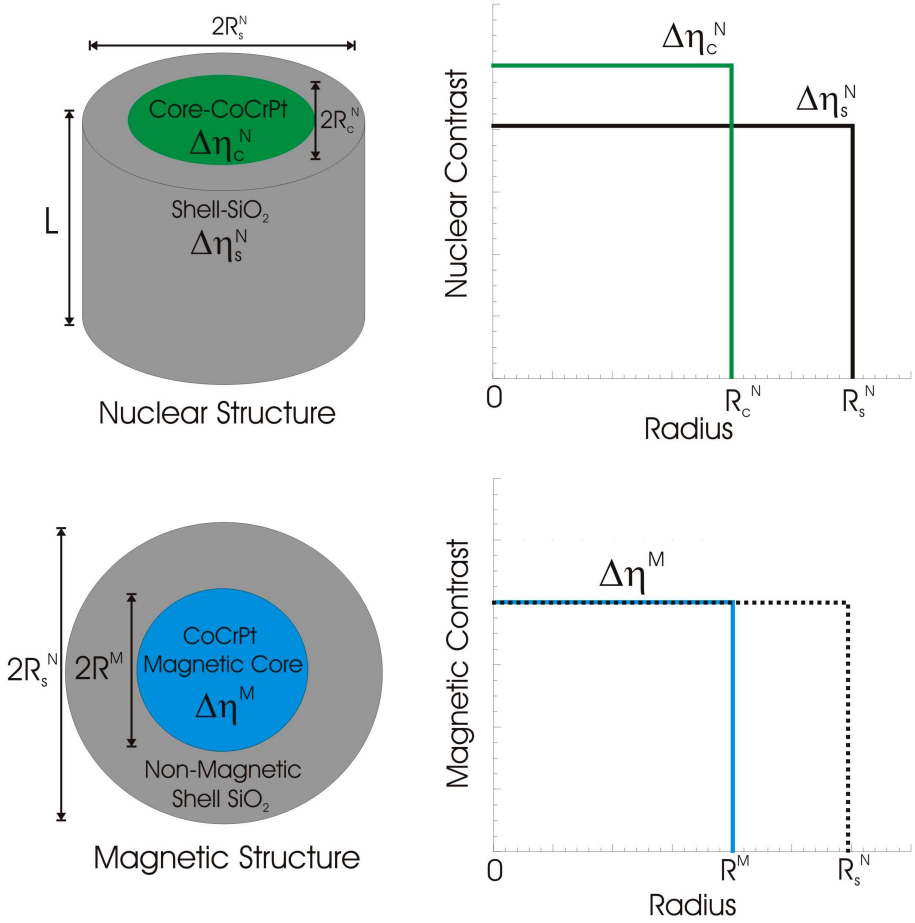

Figure 5.12: The nuclear and magnetic scattering contrast profile for the perpendicular recording grain. The nuclear grain was modelled using a solid cylinder while its magnetic counterpart is represented by a solid sphere structure.

5.4.2 Instrumentation

The PMRM sample H114 was characterised using the D11 SANS instrument at the ILL, Grenoble France [63]. The sample was cut in the shape of a 2×2 cm^2 square. The SUL and recording layer were fabricated on both sides of the glass substrate. The additional recording layer increases the magnetic volume available to the incident neutron beam thereby improving the magnetic scattering statistics relative to the cryostat's background scattering. The scattering statistics were further improved by stacking a series of 12 sample wafers, a total of 24 recording layers, into a target pile. The pile was encased in an aluminium foil covering and secured in an Al sample holder by a series of cadmium strips. A cadmium mask with an aperture diameter of 1.4 cm defines the area of the sample exposed to the incident neutron beam. To reduce neutron scattering from the aluminium sample holder a cadmium shield was fastened to the exposed area of the holder. The H114 in-plane hysteresis loop in Figure 5.11(b) shows that the sample saturates at fields greater than 1.0 T. Therefore the Oxford Instruments cryostat was used to magnetise the sample at the in-plane field of 2.0T see Figure 5.13.

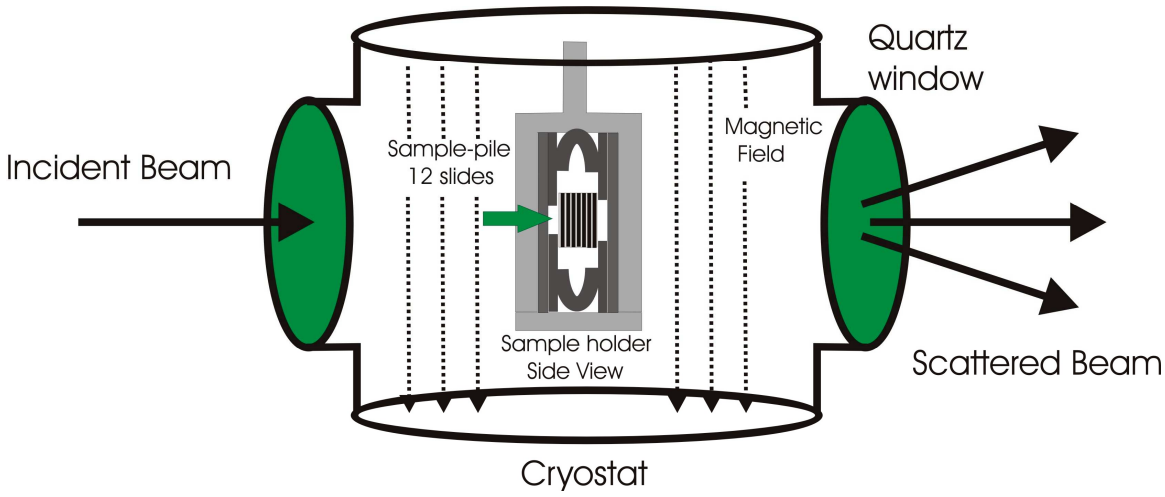

Figure 5.13: The instrument components for the D11 SANS experiment. The cryostat chamber immerses the target mount in an external magnetic field that lies parallel to the sample plane.

5.4.3 Measurements

The SANS measurements were performed at the sample-detector distances of 1.5, 4.0, 8.0 and 20.5 m. The momentum transfer argument, $|\mathbf{q}|=4\pi/\lambda\sin\theta$ shows the instrument to span the q-range of 6.26×10^{-3} Å$^{-1}<|\mathbf{q}|<0.30$ Å^{-1}. The SANS measurement consisted of three separate parts (a) zero field sample transmission I_T, (b) low in-plane field background scattering $I_B(q)$ and (c) high in-plane field foreground scattering $I_F(q)$. The scattering measurements performed at different detector distances were matched up by calculating the solid angle correction.

The sample transmission I_T measured the straight through beam intensity at q=0. The details of this measurement were outlined in section 4.4.3 on longitudinal magnetic recording media. The intensity measurement was used to calculate the incident flux on the sample, $\Phi=AI_T/S$ where S is the sample area exposed to the incident beam. The flux calculation was used to correct for flux-collimation and to normalise the scattering measurements to cross-section units of cm^2.

The zero field background measurement was prepared by first saturating the recording layer's moments out of plane. The applied field was then ramped down to a zero value. This procedure insures that the magnetic diffraction pattern at remanence was isotropic within the scattering plane. The background scattering intensity at zero field was expressed by $I_B(q,H=0)=I_N(q)+I_M(q)$ where $I_N(q)$ and $I_M(q)$ represent the nuclear and magnetic scattering components respectively. The magnetic scattering was given by $I_M(q,H=0)=I_M{}^R(q)+I_M{}^U(q)$ where $I_M{}^R(q)$ and $I_M{}^U(q)$ represent the isotropic magnetic scattering intensities from the recording layer and SUL respectively. Within the recording layer, the granular moments were oriented perpendicular to the sample plane. The magnetic scattering intensity from the recording grain was expressed by,

$$I_M{}^R(q,H=0)\propto I_0{}^R(q,H=0)[1-(\mathbf{q}\bullet\mathbf{m})^2]\approx I_0{}^R(q,H=0) \qquad (5.1)$$

where **q** and **m** form an orthogonal vector pair. Since the moments were parallel to the incident neutron beam, the magnetic diffraction pattern was isotropic within the two-dimensional scattering plane. Within the SUL the zero field moments were randomly oriented which results in isotropic magnetic scattering where $I_M{}^U(q,H=0)=I_0{}^U(q,H=0)$. For the purpose of illustration the zero field diffraction pattern was simulated in Figure 5.14(a). The nuclear, recording and SUL scattering intensities where represented by the Porod functions $I_N(q)=Aq^{-4}$, $I_0{}^R(q)=Bq^{-4}$ and $I_0{}^U(q)=Cq^{-4}$ respectively.

The background scattering intensity at the in-plane magnetic field of 250 Oe was expressed by $I_B(q,H=250Oe)=I_N(q)+I_M(q)$. The magnetic scattering from the recording layer was equal to the zero field case where $I_M^R(q,H=250Oe) \propto I_M^R(q,H=0)$. Due to the grain's strong magneto-crystalline anisotropy field the sample's magnetisation remains perpendicular to the plane. The magnetic scattering from the soft underlayer was expressed by

$$I_M^U(q,H=250Oe) \propto I_0^U(q)[1-(\mathbf{q}\cdot\mathbf{m})^2] \approx I_0^U(q,H=250Oe)\sin^2\alpha \qquad (5.2)$$

Equation 5.2 exhibits an anisotropic magnetic diffraction pattern within the scattering plane. According to the in-plane hysteresis measurements the SUL will fully saturate at the in-plane field of 250 Oe hence the magnetic moments should easily align along the field direction. Again for the purposes of illustration, the background diffraction pattern at 250 Oe was simulated within the scattering plane, see Figure 5.14(b).

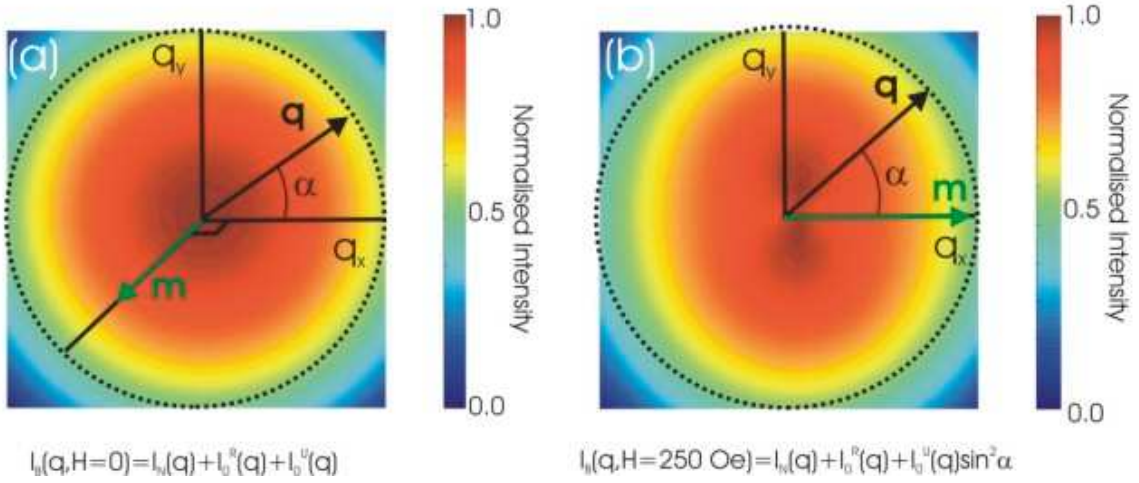

Figure 5.14: The simulated diffraction patterns for the (a) zero field and (b) background scattering components. The Porod scattering function was used to calculate the nuclear and magnetic scattering components.

The foreground scattering intensity was measured at the in-plane saturation field of 2.0 T where $I_F(q,H=2T)=I_N(q)+I_M(q)$. The magnetic scattering intensity from the recording layer was $I_M^R(q,H=2T)\propto I_0^R(q,H=2T)\sin^2\alpha$ while the magnetic scattering from the SUL was given by $I_M^U(q,H=2T)\propto I_0^U(q,H=250Oe)\sin^2\alpha$. In Figure 5.15(a) the foreground scattering was simulated for the in-plane saturation field. The magnetic scattering from the recording layer was extracted by subtracting the background scattering $I_B(q,H=250Oe)$ from the foreground component, $I_F(q,H=2T)$, where

$$\Delta I_M = I_F(q) - I_B(q) = I_0^R(q, H=2T)\sin^2\alpha - I_0^R(q, H=250\ Oe). \qquad (5.3)$$

The first term represents the magnetic scattering intensity at 2.0T while the second term gives the magnetic scattering at the in-plane field 250 Oe. Notice that by subtracting off the in-plane background at 250 Oe rather than at remanence, one has totally removed the SUL magnetic scattering component. Figure 5.15(b) shows the magnetic difference plot for the simulated scattering functions. The GRASP routine ANCOS[2] extracts the magnetic scattering intensity (term 1) and offset (term2) from the magnetic difference plot defined by equation 5.3. Details of the GRASP fit were outlined in section 4.3.4.

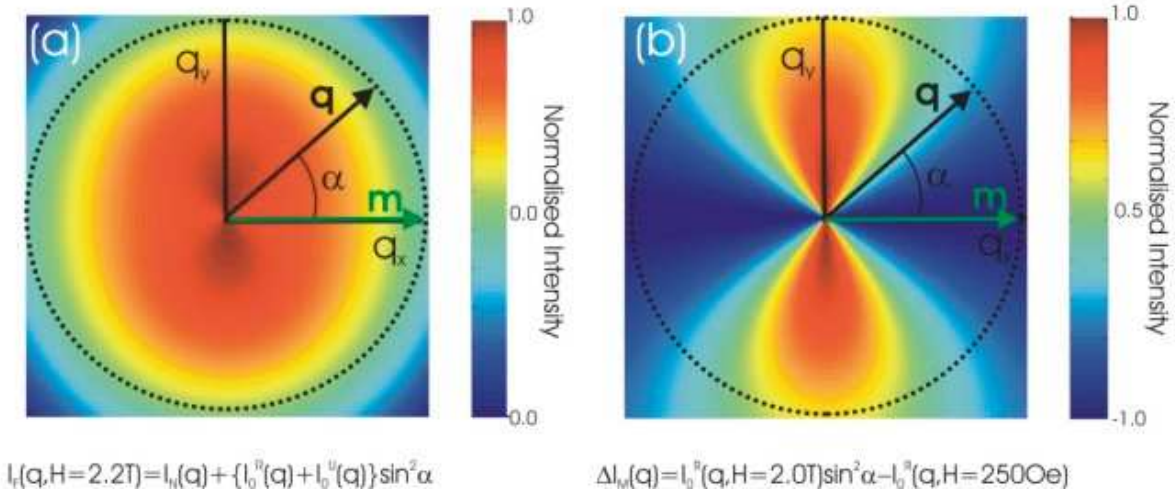

Figure 5.15: The simulated (a) foreground and (b) magnetic difference patterns at the in-plane saturation field. The relevant scattering intensities are modelled using the Porod scattering functions.

5.4.4 Results and Discussion

The background measurements were performed at the in-plane field of 250 Oe. The anisotropic magnetic scattering from the sample's underlayer was extracted by subtracting off the zero field measurement. Figure 5.16 shows the background and zero field diffraction patterns at the detector distance of 1.5 m. The scattering measurements correspond to the q range of 0.04 $Å^{-1}$<q<0.30 $Å^{-1}$. For each diffraction plot, a schematic shows the sample's magnetic scattering geometry. The green layer depicts the sample's recording layer while the grey regions represent the SUL. At either background measurement the recording layer moments were aligned perpendicular to the sample plane. At zero field the SUL moments were randomly oriented while at the applied field, the moments were saturated in-plane. The scattering intensities were converted to cross-section units by the direct beam measurement, $d\sigma/d\Omega = I(q)/\Phi_0$ where I(q) is the measured scattering intensity and Φ_0 is the incident flux on the sample.

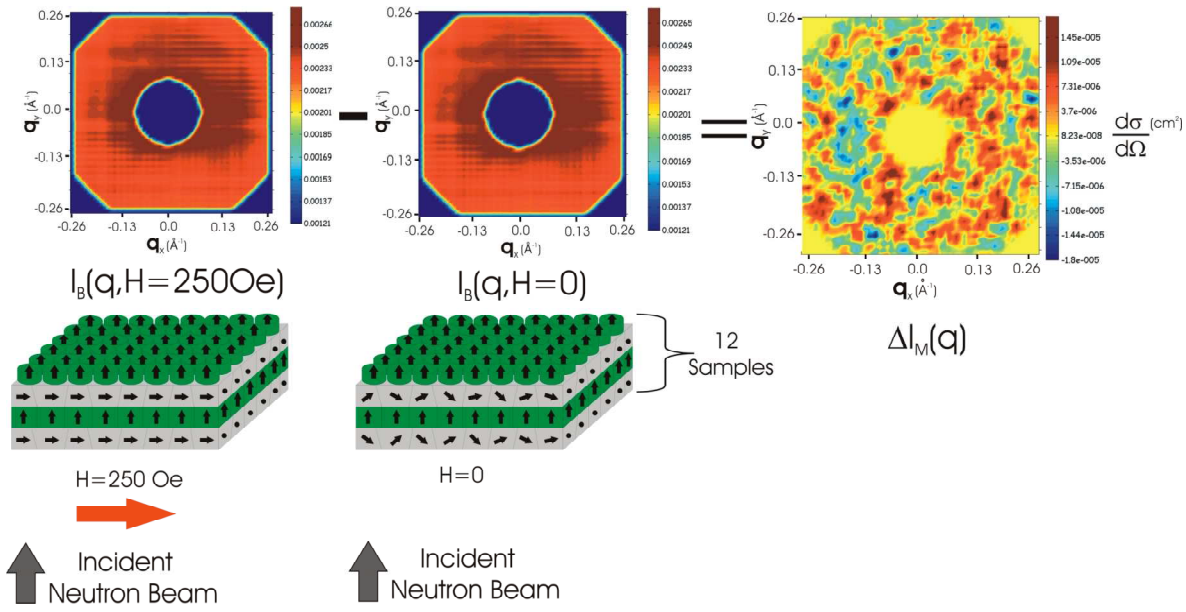

Figure 5.16: The H114 background measurements $I_B(q,H=250Oe)$ and $I_B(q,H=0)$ at the sample detector distance of 1.50 m.The incident neutron beam was normal to the sample plane. The background subtraction gives the magnetic difference plot.

The magnetic difference plot at 1.5 m is shown in Figure 5.17. The azimuthal scattering intensity was extracted within the two-dimensional scattering plane, see the right plot in Figure 5.17. The cosine^2 fit appears to show no magnetic scattering anisotropy within the scattering plane. This result was somewhat puzzling since the saturated SUL sample exhibited a strong anisotropic diffraction pattern. This property was observed in Chapter 4 where the sample, AX1821, showed a strong anisotropic scattering intensity at the in-plane field of 1.0 T. In the case of H114, the weak scattering anisotropy was attributed to the sample's poor scattering statistics. Another possibility relates to the SUL's strong demagnetisation field that rotates the moments out of plane. At zero field the SUL moments were randomly oriented throughout the scattering volume. At the in-plane field of 250Oe, the SUL moments were forced to align along the field direction. Within this magnetised state the demagnetisation field may have prevented the SUL moments from fully saturating. The independent VSM measurement of H114 have suggested that the soft saturated moment was approximately 5% larger than the SANS result at 250Oe. This field difference could account for the large noise encountered in the SANS measurements.

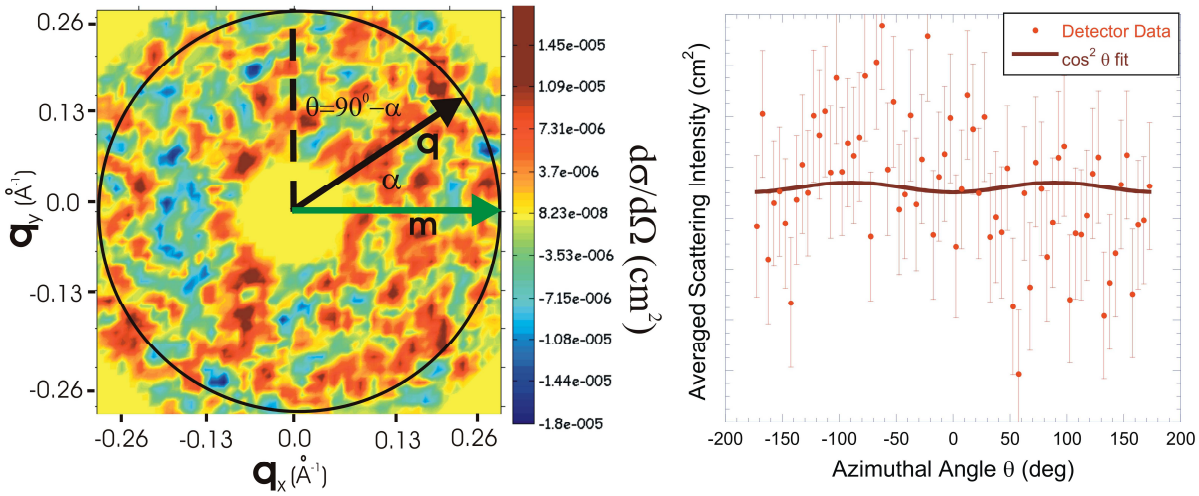

Figure 5.17:The H114 250 Oe magnetic difference plot measured at the sample-detector distance of 1.5 m, which corresponds to the q-range of 0.04 Å^{-1}<$q_{1.5m}$<0.30 Å^{-1}. The moment orientation dependence is expressed by $\sin^2\alpha$. The azimuthal scattering intensity is fitted to the $\cos^2\theta$ function where $\theta=90^0-\alpha$.

The GRASP function ANCOS[2] was used to extract the anisotropic magnetic scattering intensity. The background and magnetic scattering intensities are plotted in Figure 5.18. The background scattering at 250 Oe was a superposition of magnetic and nuclear components. The large majority of nuclear scattering originates from the sample's cryostat. The sample's magnetic scattering originates from the SUL in-plane moments. The nuclear scattering intensity was approximately 100 times the size of the magnetic scattering intensity. This shows that the background scattering was mainly dominated by the nuclear scattering intensity. The magnetic component exhibits no distinct scattering features such as Bragg scattering. In actual fact the SUL does not form an ordered system of magnetic grains. This was due to the amorphous nature of the SUL's magnetic domains. In this case the magnetic scattering was modelled using the Porod function, $I(q)=Aq^{-n}+B$ where A and B represent the scaling constants.

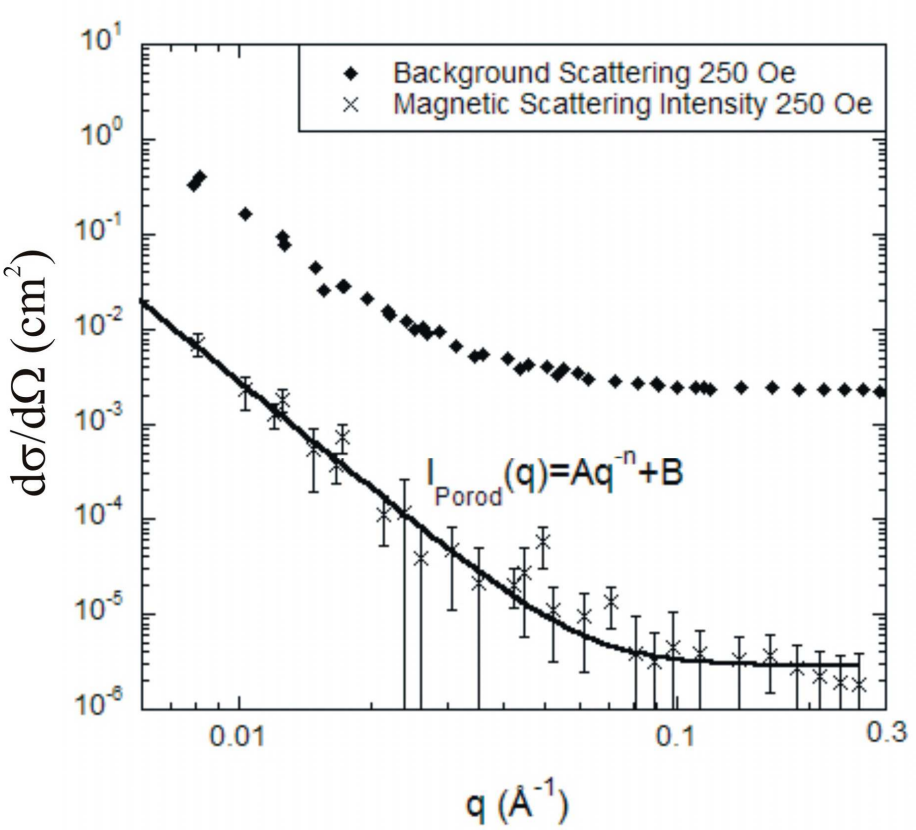

Figure 5.18: The H114 background and magnetic scattering intensity at the applied in-plane field of 250 Oe. The magnetic scattering data is fitted with the Porod function defined by $I_{Porod}(q)=Aq^{-n}+B$.

The SANS foreground of H114 was measured at the applied in-plane field of 2.0 T. The in-plane hysteresis measurements showed that the recording layer saturates at the applied field of 2.0 T. The background scattering was measured at the in-plane field of 250 Oe. The SANS foreground and background diffraction patterns at the q-range of 0.04 $Å^{-1}$<$q_{1.5m}$<0.30 $Å^{-1}$ is shown in Figure 5.19. The sample's magnetised state was depicted for the recording layer (green) and SUL (grey). At the saturation field, the moments within the recording layer and SUL were aligned along the field direction. The diffraction pattern at either field was uniform within the scattering plane. The majority of the scattering originates from the nuclear scattering components such as the sample holder and cryostat. The recording layer's magnetic scattering was extracted by calculating the difference between the foreground I_F(q,H=2.0T) and background I_B(q,H=250Oe) measurements. Since I_B(q,H=250Oe) represents the SANS pattern of a partially saturated SUL then one should expect the magnetic difference plot to contain the residue background component.

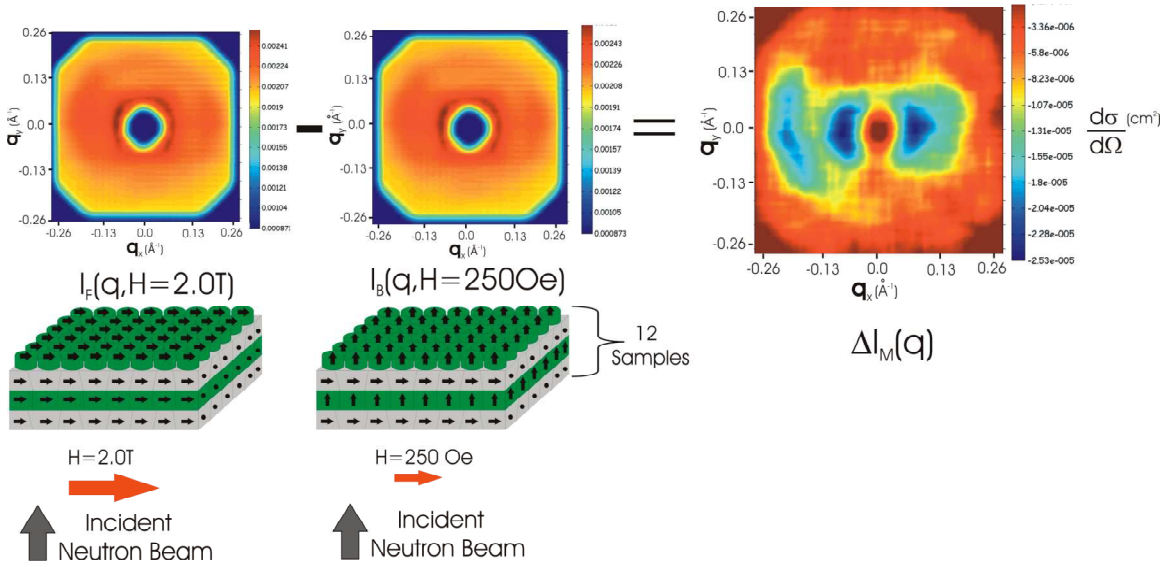

Figure 5.19: The H114 2.0 T foreground and 250 Oe background scattering components at a sample-detector distance of 1.50 m. This distance corresponds to the q range of 0.04 $Å^{-1}$<$q_{1.5m}$<0.30 $Å^{-1}$. The resulting subtraction gives the magnetic difference plot.

The azimuthal scattering intensity was extracted from the magnetic difference pattern. In Figure 5.20(a) the azimuthal data were analysed within the broad q-range of $0.04\ Å^{-1}<q_{1.5m}<0.30\ Å^{-1}$. The magnetic scattering was highly anisotropic within the scattering plane. This scattering behaviour indicates that the recording grain's local magnetisation was fully saturated along the field direction. Note the difference pattern was asymmetric along the negative q_x axis. This effect may have resulted during foreground measurements where the applied magnetic field had slightly twisted the sample out of plane. In Figure 5.20(b) the measurements were performed at the q-range of $0.02\ Å^{-1}<q_{4.0m}<0.10\ Å^{-1}$. Within this q-range, the magnetic structure was investigated at a larger length scale. The magnetic difference plot remains anisotropic about the scattering plane. Hence the local magnetisation at larger length scales remains saturated along the applied field direction.

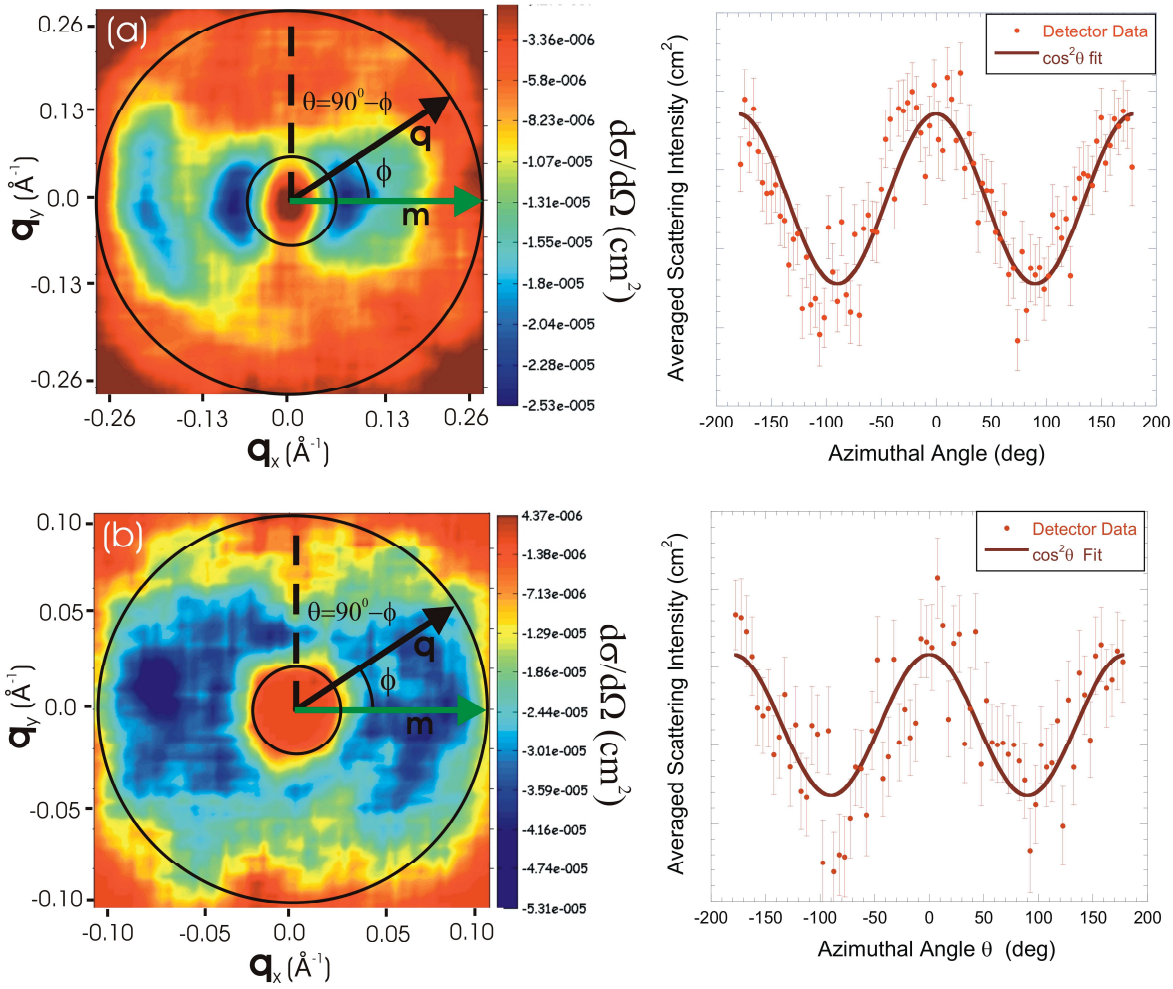

Figure 5.20: The H114 2.0T magnetic difference plot measured at the sample-detector distance of (a) 1.5 m [$0.04\ Å^{-1}<q_{1.5m}<0.30\ Å^{-1}$] and (b) 4.0m [$0.02\ Å^{-1}<q_{4.0m}<0.10\ Å^{-1}$] The azimuthal scattering intensity was calculated over their respective q-range.

The ANCOS^2 function was used to extract the recording layer's magnetic scattering intensity, $I_M^R(q,H=2T)$, and offset, $I_M^R(q,H=250Oe)$. Figure 5.21 compares the foreground and magnetic scattering components at the in-plane field of 2.0T. As was with the background measurements, the large majority of the foreground scattering originates from the sample's cryostat. This background scattering was approximately 100 times the size of the magnetic scattering component.

Within the q_1 range the magnetic scattering appears to originate from the sample's SUL. Ideally the background subtraction should have removed this Porod-type scattering. It would appear that the SANS measurements at 250 Oe underestimated the magnitude of the magnetic background scattering at 2.0 T. The SUL background scattering does not fully saturate at the in-plane field of 250 Oe. Within this q range, the intensity piques at q=0.023 Å^{-1}. The scattering peak may possibly originate from the interference scattering of clustered recording grains. The physics behind this feature is covered later in the chapter. Within the q_2 range the scattering intensity exhibits peaks at q=0.07 Å^{-1} and q=0.13 Å^{-1}. These q-values correspond to the magnetic interference scattering between the recording grains.

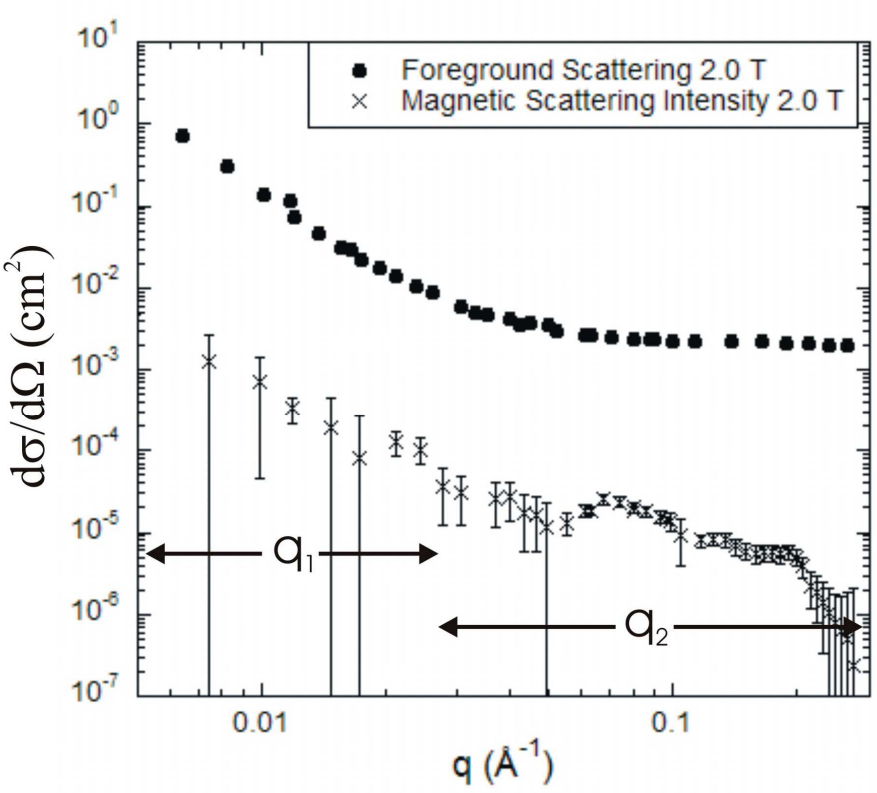

Figure 5.21: The H114 foreground and anisotropic magnetic scattering intensities at the in-plane field of 2.0 T. The q_1-range defines residue scattering from the SUL while the q_2-range represents the dominant scattering intensity from the magnetic recording layer.

The anisotropic magnetic scattering was fitted using the scattering expression equation 4.3. The residue background from the SUL was modelled using the Porod scattering function $I_{Porod}(q)=Aq^{-n}+B$. The recording grain's magnetic structure in reciprocal space was represented by the spherical core-shell form factor expressed by equation 4.5. The interference effects were modelled using the Percus-Yevick structure factor, S(q). Figure 5.22 shows the magnetic scattering at 2.0 T fitted to the spherical core-shell model. The data fit was performed using the non-linear least squares program which gave a closeness of fit $\chi^2<1$. However the scattering model had problems finding a convergent solution to the NLS fitting routine. The output parameters exhibited large statistical errors for $q<0.05$ Å^{-1}. This was attributed to the noisy background scattering near the detector's edge. By setting the Porod input parameters to the *fixed* state one was able to reduce the background fitting errors.

The form factor F(q) extracts the spatial dimensions of the recording grain. The grain's core and shell diameter were 21.6 Å and 70.0 Å respectively with a grain size distribution of 20%. The magnetic scattering contrasts of the core and shell components were $(5.37\pm0.3)\times10^{-7}$ Å^{-2} and $(1.97\pm1.0)\times10^{-9}$ Å^{-2} respectively. The magnetic contrast ratio shows the core was about 200 times the size of its shell component. The relatively small size of the shell contrast suggests that the weakly magnetic shell had a negligible effect on the form factor. It may be possible that the grain's magnetic structure consists only of a solid spherical core of CoCrPt segregated by non-magnetic shell of SiO_2.

In Figure 5.23 the magnetic scattering intensity was re-fitted using the solid sphere model. Table 5.1 lists the output parameters for the Porod, form factor and structure factor functions. For the NLS routine, the input parameters d, ρ, Δη and R were set to the *Free* state. The solid sphere model shows good agreement with the scattering data with a closeness of fit of $\chi^2<1$. The form factor gives a magnetic grain size of 24.8±0.4 Å with a grain size distribution of 16%. The physical (dotted) and magnetic (black core) grain were shown in the figure inset. The magnetic grain size was comparatively small with respect to the physical grain size of 90.0Å [99]. The validity of the solid sphere model is in question since conventional recording media requires that the magnetic grain must be comparable to the physical grain size. If the magnetic grain size were much smaller than the physical counterpart, then the recording media would become thermally active resulting in super-paramagnetic grains.

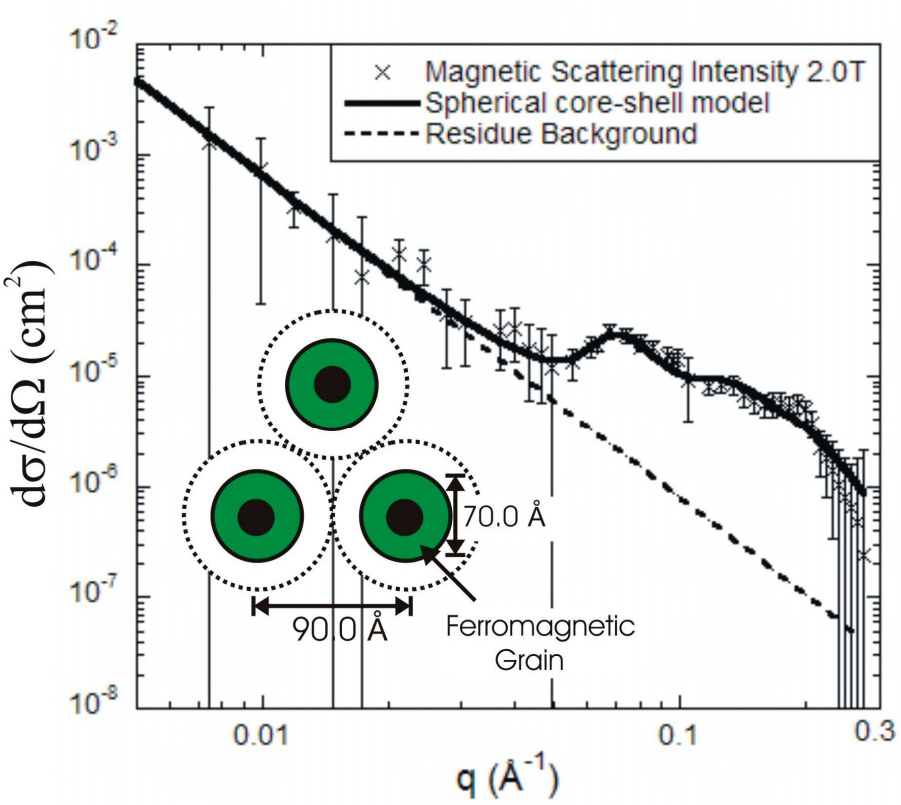

Figure 5.22: The H114 magnetic scattering intensity at the in-plane field of 2.0T fitted to the spherical core-shell model (solid line). The residue background was modelled by the Porod scattering function (dashed). The inset shows the local magnetic dimensions of the spherical core-shell grain.

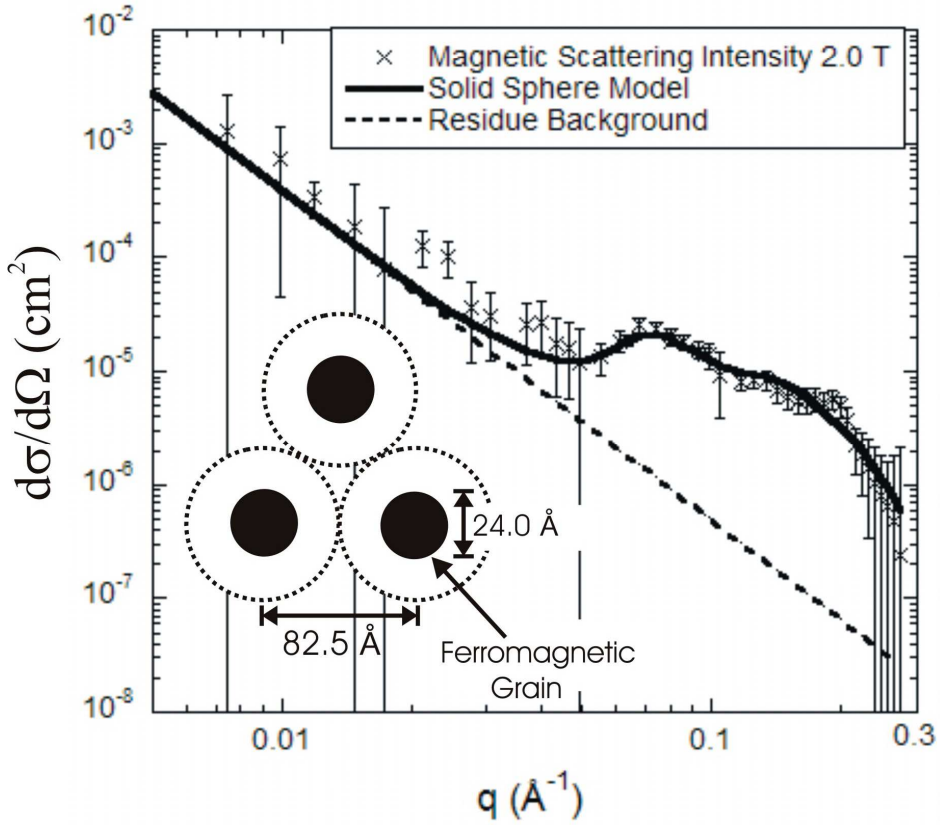

Figure 5.23: The magnetic scattering intensity at the in-plane field of 2.0T fitted to the solid sphere model. The inset shows the local magnetic dimensions of a trio of grains.

The Percus-Yevick structure factor calculates an inter-granular separation of d=82.5±2.0 Å, see Figure 5.24. The magnetic grain size was smaller than the inter-granular separation where $d>2R_s$. This possibly suggests that the magnetic grains were not closed packed (touching) but surrounded by a non-magnetic shell or grain boundary. The grain boundary was mainly composed of SiO_2 that acts to reduce inter-granular exchange coupling. By knowing the grain size and inter-granular separation one can calculate the grain boundary thickness. The approximate thickness of the non-magnetic grain boundary was $t=\{d/2-R\}\approx28.8\pm1.0$ Å. The boundary thickness was considerably larger than the grain boundary of LMRM grains. For example the Cr-enriched grain boundary of the CoCrPtTa medium ranges from 10.0 Å-23.0 Å [14]. These t-values suggest that the perpendicular calculations have overestimated the boundary thickness. The boundary thickness was larger than expected due to the small magnetic grain size.

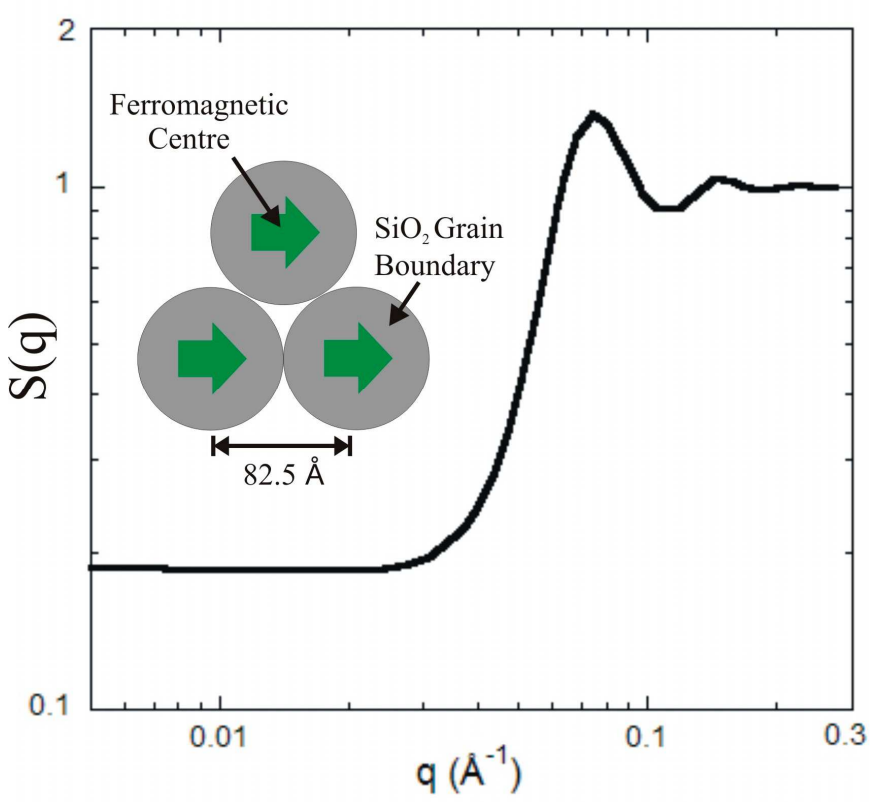

Figure 5.24: The Percus-Yevick structure factor extracted from the magnetic scattering intensity at 2.0 T. The inset shows the local physical dimensions for a trio of grains.

The ANCOS^2 offset represents the magnetic scattering intensity at the in-plane field of 250 Oe. At this small field the granular magnetic moments were oriented perpendicular to the recording layer while the majority of the SUL moments were saturated in-plane. In this sample geometry, the granular moments were oriented parallel to the incident neutron beam, hence the magnetic diffraction pattern was isotropic within the scattering plane. The magnetic scattering from the recording layer was modelled using the solid sphere model. The scattering offset and fit are shown in Figure 5.25. The scattering model fits the offset fairly well with closeness of fit χ^2<1. The form factor gives a magnetic grain size of 21.2±0.40 Å with a gamma-Shultz grain size distribution of 18.8%. Again the magnetic grain was very much smaller than the physical grain size. The Percus-Yevick structure factor shows an inter-granular separation of d=84.9±1.4 Å. For the in-plane field of 2.0 T the structure factor peak was noticeable sharper than then the offset result. The damped structure factor may be due to the increase in the offset's grain size distribution.

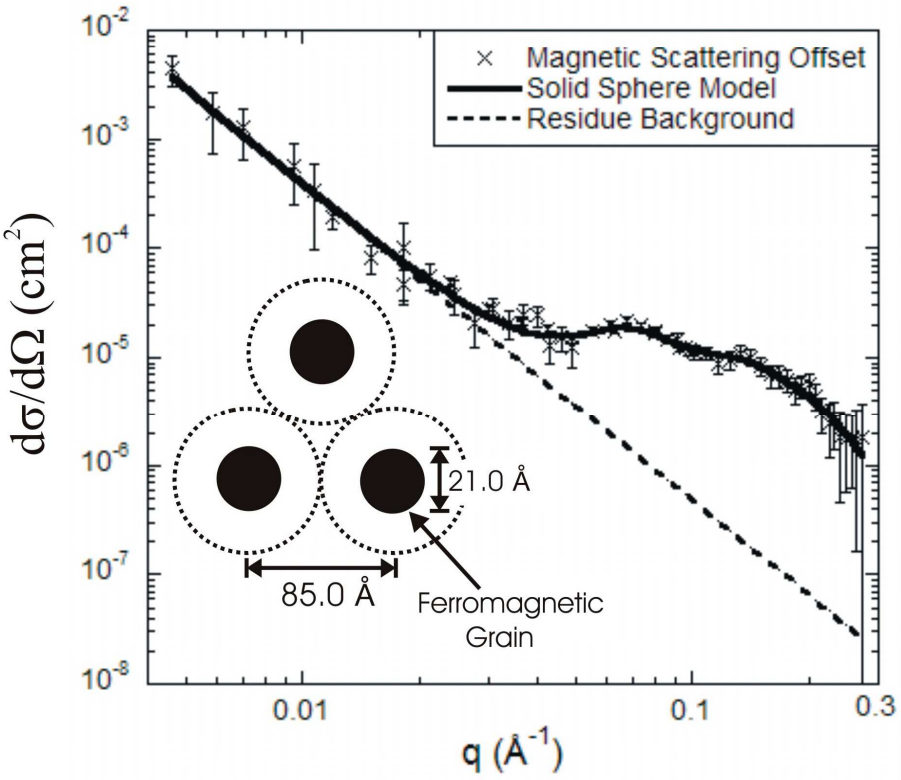

Figure 5.25: The magnetic scattering offset at the in-plane field of 250 Oe fitted to the solid sphere model. The inset shows the local magnetic dimensions for a trio of grains.

Scattering Function	***Description***	***Parameter***	***NLS Switch***	***Value***
S(q)	Grain Separation	d	*Fixed*	82.5 ± 2.0 Å
	Packing density	ρ	*Fixed*	$(9.92\pm0.6)\times10^{-7}$ Å^{-3}
F(q)	Magnetic Contrast	$\Delta\eta^{M}$	*Free*	$(4.51\pm0.3)\times10^{-7}$ Å^{-2}
	Radius	R	*Free*	12.4 ± 0.3 Å
	γ-Distribution Width	σ_R	*Fixed*	2.0 Å
$I_{Porod}(q)$	Porod exponent	n	*Fixed*	2.9
	Scale factor	A	*Fixed*	6.1×10^{-10}
	Background Factor	B	*Fixed*	1×10^{-18}
	Closeness of Fit	χ^2	---	<1.0

Table 5.1: The H114 2.0 T fit parameters for the structure factor-S(q), form factor-F(q) and Porod-$I_{Porod}(q)$ scattering functions.

Scattering Function	*Description*	*Parameter*	*NLS Switch*	*Value*
S(q)	Grain Separation	d	*Free*	84.9 ± 1.4 Å
	Packing density	ρ	*Free*	$(6.60\pm0.3)\times10^{-7}$ Å^{-3}
F(q)	Magnetic Contrast	Δη	*Free*	$(6.44\pm0.4)\times10^{-7}$ Å^{-2}
	Radius	R	*Free*	10.6 ± 0.3 Å
	γ-Distribution Width	σ_R	*Fixed*	2.0 Å
$I_{Porod}(q)$	Porod exponent	n	*Fixed*	2.9
	Scale factor	A	*Fixed*	6.1×10^{-10}
	Background Factor	B	*Fixed*	1×10^{-18}
	Closeness of Fit	χ^2	---	<1.0

Table 5.2: The H114 offset fit parameters for the structure factor-S(q), form factor-F(q) and Porod-$I_{Porod}(q)$ scattering functions.

A further set of H114 SANS measurements was performed at the in-plane fields of 1.3 T and 0.8 T. The ANCOS^2 routine extracted the recording layer's magnetic scattering intensity and phase at the respective magnetic field values. The recording grain's in-plane moment orientation was investigated by plotting the ANCOS^2 phase as a function of q, see Figure 5.26. It was found that the moment orientation, regardless of field strength, averaged along the field direction where the average phase was zero. Within the recording layer the saturation magnetisation was always aligned along the field direction. At fields below saturation, the in-plane moments did not align along a preferred direction of magnetisation. This shows that the sample's in-plane magnetism does not exhibit a shape or magneto-crystalline anisotropy field. Therefore the phase remains constant as a function of q-space. This was not the case for longitudinal media where the grain's easy axis of magnetisation was oriented in-plane resulting in multiple ANCOS^2 phase shifts at the applied fields 0.45 T, 1.38 T and 1.45 T.

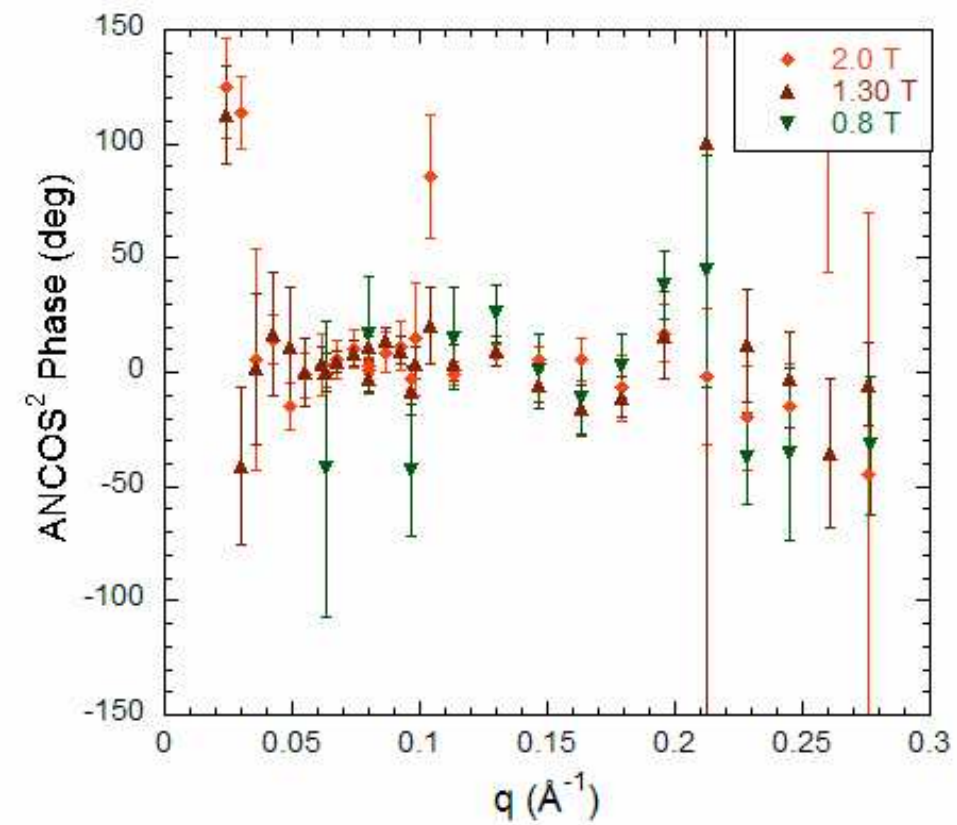

Figure 5.26: The ANCOS^2 phase at the applied in-plane fields of 0.8 T, 1.30 T and 2.0 T. The zero phase refers to a moment orientation along the q_x axis while a $\pi/2$ phase shows a moment alignment along the q_y-axis.

The $ANCOS^2$ phase behaviour exhibited for perpendicular and longitudinal recording grain was understood in terms of the Stoner-Wohlfarth model. In Figure 5.27, the longitudinal recording grain's energy states are plotted as a function of the in-plane moment angle. At remanence, the granular moments were aligned along their easy axis of magnetisation. The magneto-crystalline anisotropy and dipolar fields will determine the direction of the easy axis. Due to the grain's sizeable demagnetisation field, it is not necessarily the case that the easy axis coincides with its c-axis. The recording grain's anisotropy, exchange, dipolar and thermal energies determine the energy barrier height. Application of an in-plane field reduced the energy barrier height thereby increasing the grain's likelihood of switching to an alternate magnetised state. At the saturation field, the energy barrier was breached whereby all granular moments were aligned along the field direction. The SANS studies showed that the diffraction pattern at saturation was highly anisotropic within the scattering plane with no $ANCOS^2$ phase shifts. When the applied field was reduced, the moments began to align along their easy axes. The finite moment orientation factor resulted in the variation between the contrast components $\Delta\eta^M(q_x)$ and $\Delta\eta^M(q_y)$. Therefore the $ANCOS^2$ phase shift was a direct consequence of the grain's in-plane magneto-crystalline anisotropy field.

The perpendicular recording grain's energy states as a function of the moment angle are plotted in Figure 5.28. At remanence, the grain exhibits a strong out of plane magneto-crystalline anisotropy where the easy axis of magnetisation lies parallel to the c-axis. For the perpendicular textured grain, the c-axis lies normal to the sample plane. Upon application of an in-plane magnetic field, the moments begin to align themselves along the field direction. Since the recording grains possessed no in-plane crystalline magneto anisotropy field, the magnetic moments show no preferred alignment within the sample plane. As a result the in-plane energy barrier separating the magnetised states was solely determined by the grain's applied and demagnetisation fields. At the saturation field, the SANS studies showed an anisotropic magnetic diffraction pattern. When the field was reduced, the moments begin to rotate towards their perpendicular easy axes. The moments that remained magnetised in-plane were still aligned along the field direction. In this case, the moment orientation remains unchanged for lower fields. For the low field SANS studies, there was no magnetic contrast variation between the q_x and q_y form factor functions. As a consequence there was no observed $ANCOS^2$ phase shift over the measured q-range.

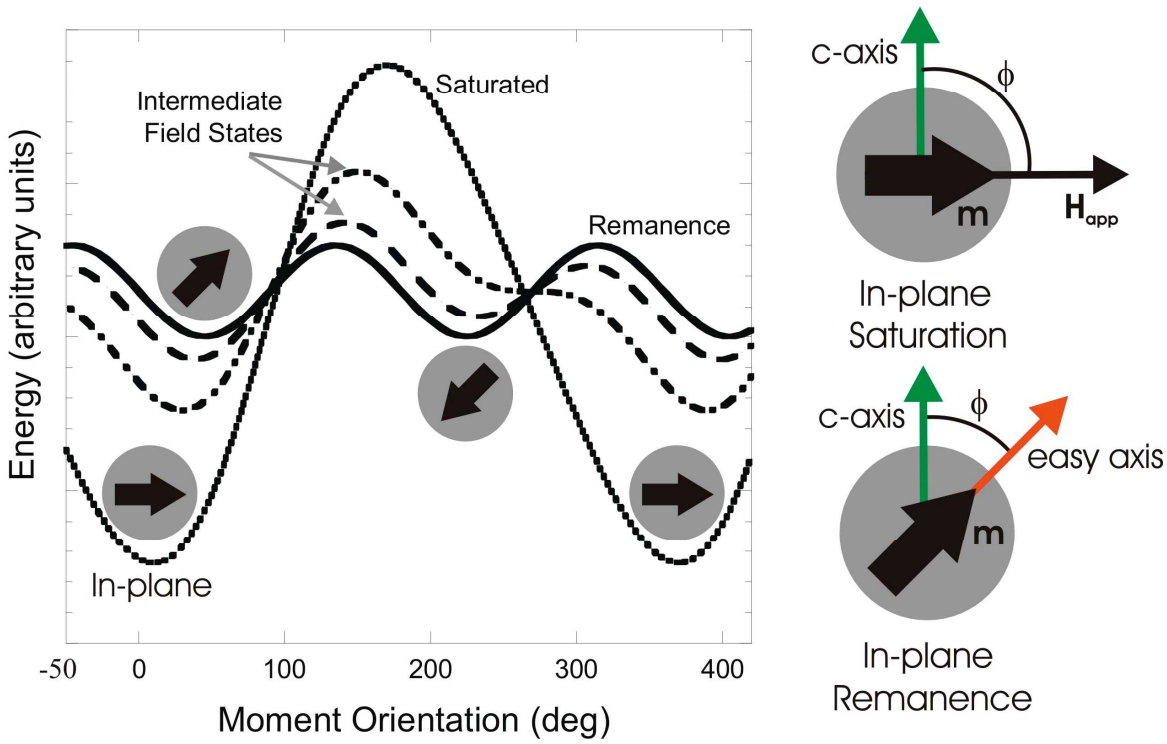

Figure 5.27: The Stoner-Wohlfarth model of a longitudinal magnetic recording grain. The simulations are performed for the in-plane remanent, intermediate and saturated states. At remanence, the recording grains align along their easy axis of magnetisation.

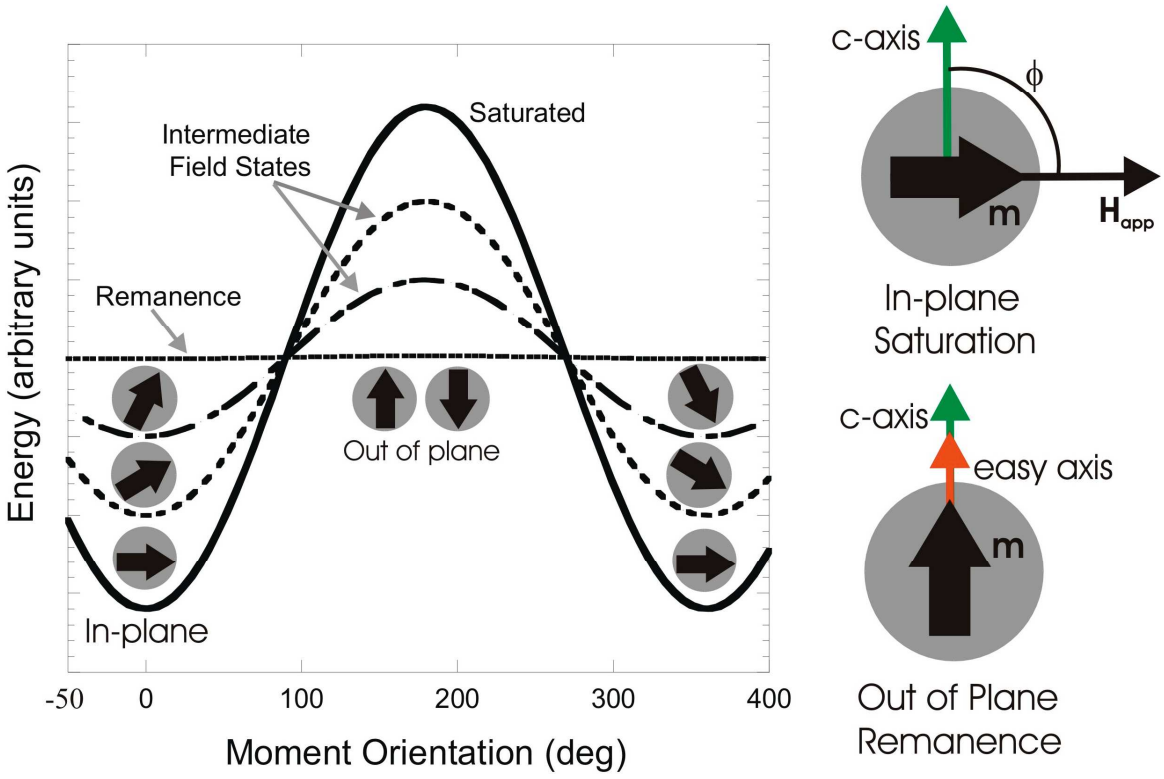

Figure 5.28: The Stoner-Wohlfarth model of a perpendicular magnetic recording grain. The simulations are performed for the out of plane remanent, intermediate and saturated states. At remanence, the recording grains align along their easy axis of magnetisation.

5.4.5 Summary

The magnetic structure of perpendicular recording media was characterised using unpolarised small angle neutron scattering. The recording grain's diffraction pattern was measured at the in-plane fields of 250 Oe, 0.8 T, 1.3 T and 2.0 T. At the applied field of 2.0 T, the recording grains were fully saturated in-plane resulting in an anisotropic magnetic diffraction pattern. The magnetic scattering intensity and offset were modelled using a solid sphere form factor averaged over the gamma-Shultz grain size distribution. The scattering model determined that the granular core was highly enriched with the ferromagnetic cobalt while the shell component was enriched with the non-magnetic substance SiO_2. However the form factor extracted a magnetic grain size that was much smaller than its physical counterpart. The magnetic grain size was too small for a magnetically stable recording media. The diffraction pattern also exhibited interference scattering between the recording grains. The scattering was modelled using the Percus-Yevick structure factor, which was characteristic of an amorphous ensemble of particles with a narrow size distribution.

5.5 Polarised SANS

The previous SANS studies allowed one to extract the magnetic grain size via the magnetic scattering component. It was not possible to characterise the recording layer's physical structure since the magnetic scattering was always superimposed on its nuclear scattering counterpart. Due to this fact the physical structure of the recording layer was characterised using conventional methods such as TEM and small angle x-ray diffraction. However the characterisation technique of polarised small angle neutron scattering (POLSANS) has been developed to measure the recording grain's physical structure. This characterisation technique differs from the unpolarised method by using a polarised incident neutron beam to measure the sample's diffraction pattern. Through polarisation analysis these measurements extract the recording layer's magnetic-nuclear interference term, which is proportional to the nuclear scattering form factor. By using the appropriate scattering model, the form factor extracts useful information on the recording layers's physical properties such grain size and chemical composition. In the following sections, the POLSANS method was used to study the local magnetic and physical structure of the PMRM sample H114.

5.5.1 Instrumentation

The sample H114 was characterised using the using the SANS1 instrument at PSI, Villigen, Switzerland [65]. Sample preparation was similar to the unpolarised measurements performed for the D11 instrument. The sample scattering statistics were improved by stacking 12 sample wafers, total of 24 recording layers, into a single target. The sample pile was encased in aluminium foil and secured in the Al sample holder. The sample holder was lined with cadmium strips, which reduce background scattering from the instrument components. A cadmium mask with an aperture diameter of 1.4 cm was fixed over the surface of the sample pile. The POLSANS experiment requires magnetic fields greater than 1.3 T, hence the H114 sample was magnetised using the Oxford Instruments 11 T cryostat. The scattering measurements were performed in the in-plane and out of plane field geometries as shown in Figure 5.29. Since the cryostat coils were fixed along a particular direction, the magnet must be physically rotated to change the field geometry.

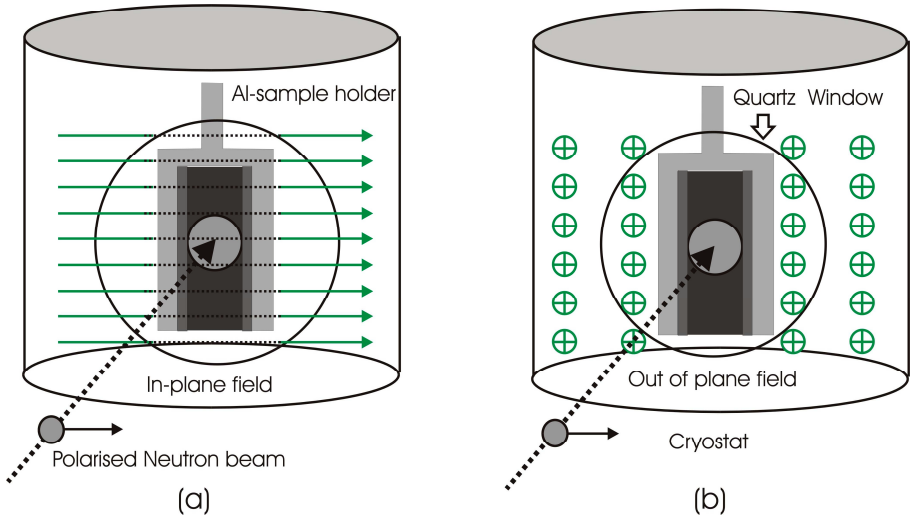

Figure 5.29: The SANS1 11.0 T horizontal cryomagnet used to measure the polarised diffraction pattern for the (a) in-plane and (b) out of plane field geometries.

5.5.2 Measurements

The POLSANS studies of H114 were performed for the in-plane and out of plane geometries. The in-plane geometry was measured at the sample-detector distance of 3.0 m with an average neutron wavelength of 5.0 Å. By performing momentum transfer calculations, the SANS1 instrument spans the q-range of 0.02 $Å^{-1}$<q<0.18 $Å^{-1}$. The polarised measurements consisted of three separate parts (a) zero field transmission $I^{\pm}_{T}$, (b) low field in-plane 250 Oe background scattering $I_B^{\pm}(q)$ and (c) high in-plane field H=3.0 T foreground scattering $I_F^{\pm}(q)$. The solid angle correction was applied to the foreground and background scattering measurements. For purposes of illustration, the polarised foreground scattering intensity was modelled using equation 4.9. The nuclear and magnetic background components were neglected in these simulations. In the left plot of Figure 5.30, the foreground diffraction pattern was shown for the ± spin states. The magnetic moment lies along the q_x axis where the magnetic scattering anisotropy undergoes a phase shift for a change in the spin state |+>→|–>. The right plot calculates the difference between ± foreground intensities.

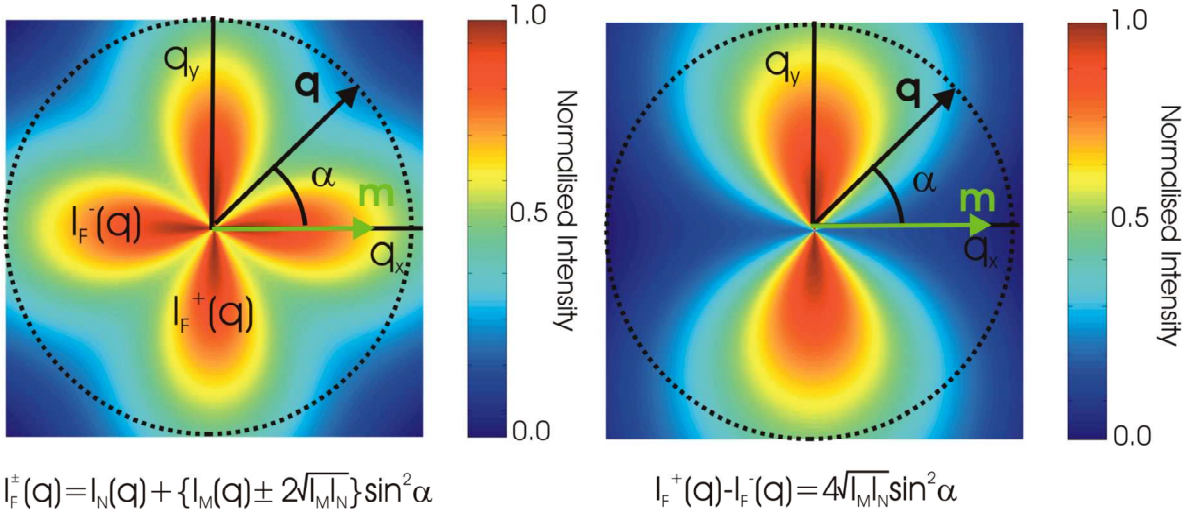

Figure 5.30: The simulated diffraction pattern for the in-plane foreground scattering intensities $I_F^{\pm}(q)$. The anisotropic nuclear-magnetic cross-term is extracted by taking the difference between the ± foreground intensities.

The out of plane field geometry was measured at the sample-detector distance of 2.0 m with an incident neutron wavelength of 5.0 Å. This corresponds to the q-range of $0.02\ Å^{-1}<q<0.27\ Å^{-1}$. The zero field transmission and background measurements were performed as outlined in the in-plane field measurements. The polarised foreground intensity was measured at the out plane fields of 0.0250 T, -0.31 T, -0.57 T and -0.81 T. The out of plane foreground scattering intensity was modelled by using equation 4.9. The moment vector **m** lies perpendicular to the scattering plane hence the foreground expression simplifies to the following, $I_F^{\pm}(q)=I_N(q)+[I_M(q) \pm 2(I_N I_M)^{1/2}]$. In Figure 5.31, the left plot shows an isotropic diffraction pattern for the polarised foreground states. Due to the perpendicular field geometry, the moment orientation factor was unity within the scattering plane. The right figure depicts the nuclear-magnetic interference pattern. Similarly the difference calculation between the polarised foreground intensities results in an isotropic diffraction pattern.

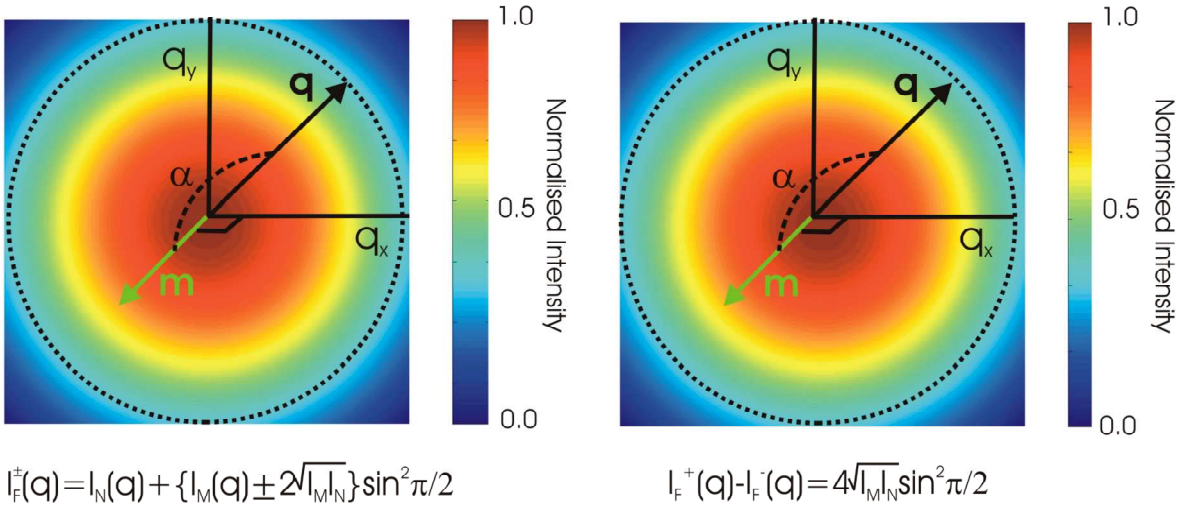

Figure 5.31: The simulated diffraction pattern for the out of plane foreground scattering intensities $I_F^{\pm}(q)$. The isotropic nuclear-magnetic cross-term is extracted by taking the difference between the ± foreground intensities.

5.5.3 Results and Discussion

The sample's foreground scattering intensity was measured for the ± spin states at the in-plane field of 3.0 T. Figure 5.32 shows the diffraction patterns for their respective spin states at the sample-detector distance of 3.0 m. The schematic shows the alignment of the incident polarised neutron relative to the applied magnetic field and sample magnetisation. If the interacting neutron was in the spin up or down state than the applied magnetic field will instantaneously rotate the neutron spin along the field direction. The foreground measurements exhibit distorted diffraction patterns which was attributed to background scattering from the cryostat. The nuclear-magnetic interference pattern was extracted by calculating the difference between the $I_F^+(q)$ and $I_F^-(q)$ foreground scattering intensities. The polarised foreground scattering intensities were converted to cross-section units (cm^2) by normalising the data with respect to the incident beam flux calculation.

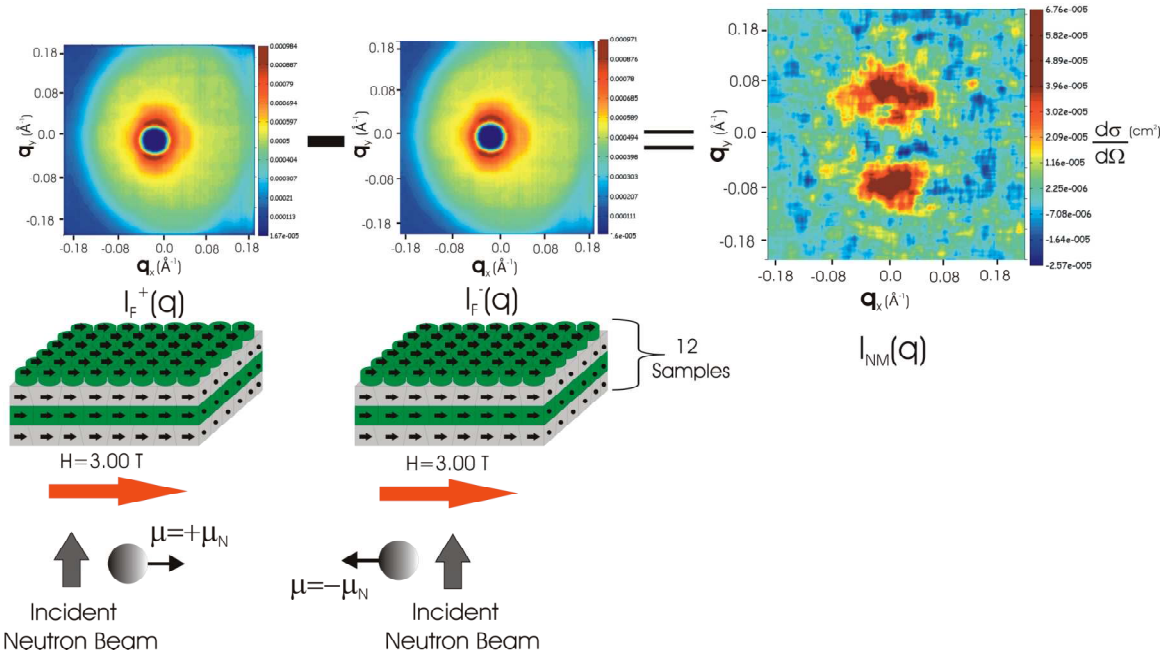

Figure 5.32: The extraction of the nuclear-magnetic interference $I_{NM}(q)$ at the in-plane field of 3.0 T (red arrow). The foreground scattering components $I_F^+(q)$ and $I_F^-(q)$ were measured for the respective ± spin states. The spin state of the incident neutron beam (grey arrow) is represented by the spherical object.

The GRASP routine was used to extract the azimuthal scattering data as a function of $\theta=90^0-\alpha$, see Figure 5.33. The azimuthal scattering data was fitted using the $\sin^2\alpha$ dependence where α is the angle between the **q** and **m** vectors. The q-dependent scattering intensity was described by the following expression $I_{NM}(q)=4(I_N I_M)^{1/2}\sin^2\alpha$. The interference pattern was highly anisotropic about the two-dimensional scattering plane. The difference plot exhibits similar scattering behaviour with respect to the D11 measurements at the applied in-plane field of 2.0 T. The major difference was that the scattering intensity contains no SUL and zero field background scattering components, hence the anisotropic scattering originates solely from the sample's recording layer. Additionally the D11 measurement was purely a magnetic scattering intensity while the interference term was a cross between the nuclear and magnetic scattering components.

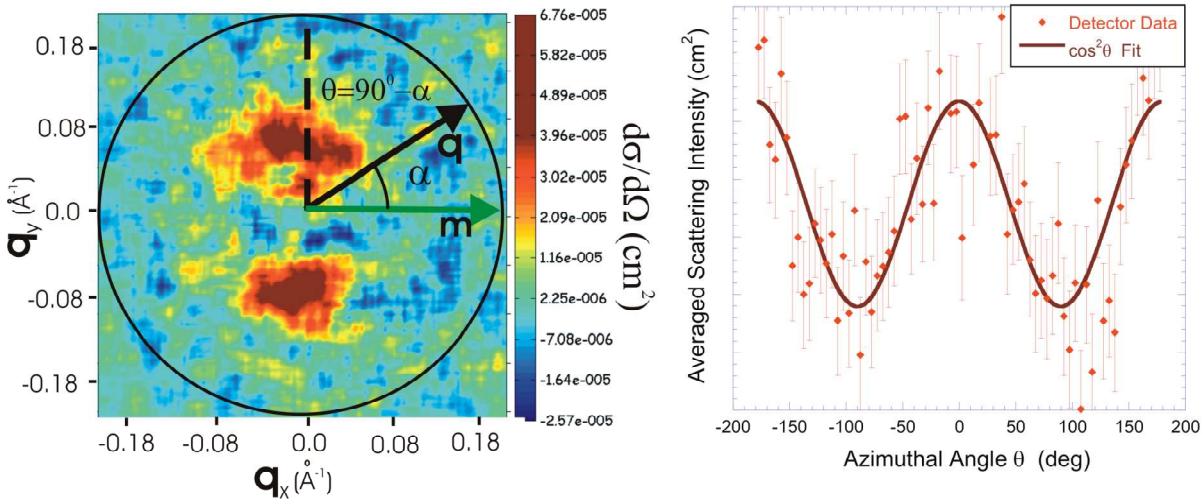

Figure 5.33: The in-plane nuclear-magnetic diffraction pattern for the sample-detector distance of 3.0 m, which corresponds to the q-range of $0.02\,Å^{-1}<q<0.18\,Å^{-1}$. The azimuthal scattering intensity was averaged over the q-plane and fitted with the $\cos^2\theta$ function where $\theta=90^0-\alpha$.

The recording grain's nuclear scattering intensity was calculated using the expression $I_N(q)=I^2_{NM}(q)/\{I_M(q)16\}$ where $I_{NM}(q)$ and $I_M(q)$ represent the interference and magnetic scattering measurements respectively at the applied in-plane field of 3.0 T. It was observed that the magnetic measurements exhibited poor scattering statistics. This was attributed to the weak incident flux of the SANS1 instrument. The scattering statistics were improved by interchanging the magnetic scattering data at 3.0 T with the D11 scattering data at 2.0 T, see Figure 5.23. The magnetic scattering intensities at the fields of 2.0 T and 3.0 T were equivalent since they correspond to the recording layer's in-plane saturation magnetisation. The extraction procedure was further simplified by replacing the magnetic scattering data with the solid sphere fit expressed by the function $I_M(q)=N[<F^2(q)>-<F(q)>^2]+N<F(q)>^2S(q)$. Since the interference scattering contains no SUL background components, the Porod function was subtracted from the magnetic scattering equation. Figure 5.34 plots the nuclear-magnetic interference, magnetic, and nuclear scattering intensities.

The nuclear-magnetic interference exhibits scattering peaks at $q_1=0.025$ Å^{-1} and $q_2=0.065$ Å^{-1}. The first peak originates from magnetic interference scattering between granular clusters. This scattering feature was also observed for the D11 measurements at 2.0 T. The Percus-Yevick calculation gives a cluster separation of 265 Å. The cluster peak also appears on the nuclear scattering intensity, however this feature represents an artifact from the residue magnetic background. The formation of magnetic granular clusters is understood in terms of the recording grain's competing energy components. The grain's energy is a superposition of exchange and Zeeman energies. For the in-plane geometry, the anisotropy energy is zero. As a result the inter-granular exchange energy has a stronger influence between recording grains. It may be possible that the stronger exchange forces are coupling neighbouring recording grains into clusters.

The nuclear scattering component was modelled using a solid cylindrical object of length L and radius R where L>R [54]. Figure 5.35 shows the cylinder fit to the nuclear scattering data. The form factor function gives a grain size of 80.0 Å with an inter-granular separation was of the order of 90.0 Å. The cylindrical length was of the order of 150 Å. These spatial parameters show moderate agreement with independent TEM measurements, however the model poorly fits the scattering data within the low q-range of $q<0.05$ Å^{-1}. The poor fit was attributed to the noisy scattering statistics in and around the beam stop at q=0. The fitting results may be improved by truncating the noisy data sets or by remeasuring the interference pattern at larger detector distances.

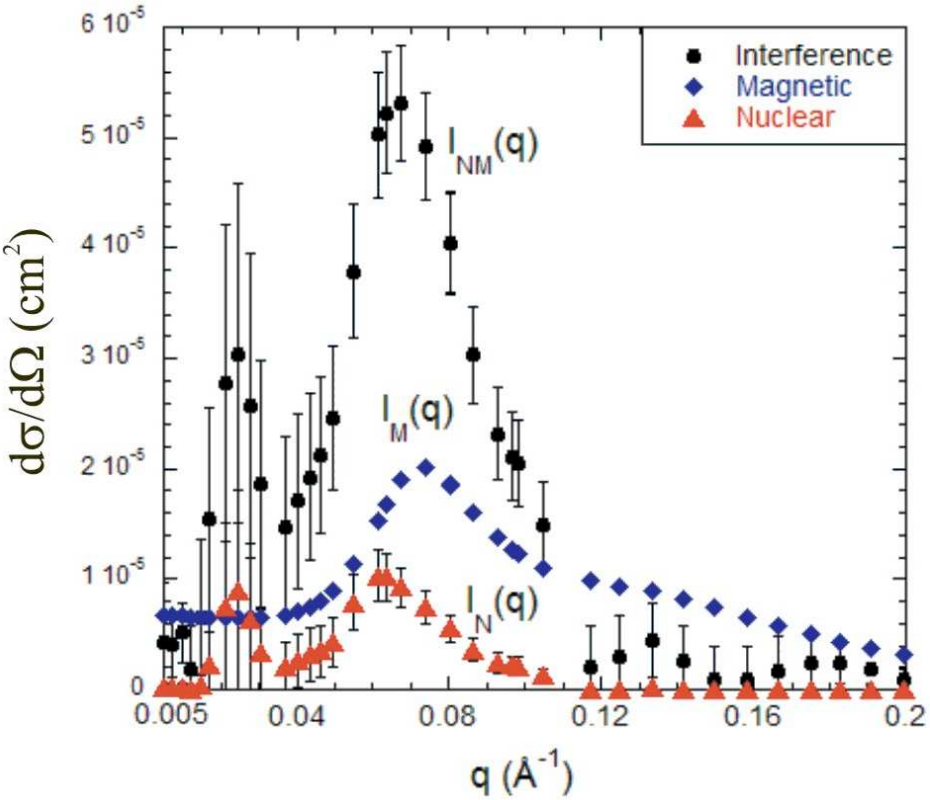

Figure 5.34: The H114 magnetic, nuclear-magnetic interference and nuclear scattering intensities for the in-plane field of 3.0 T.

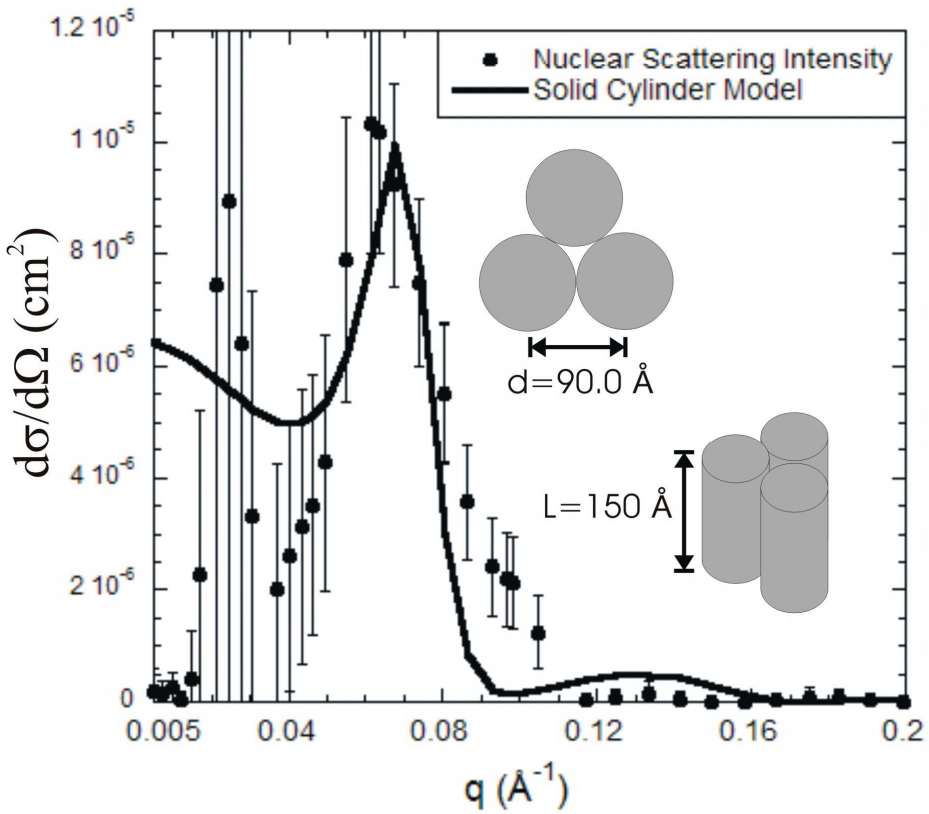

Figure 5.35: The H114 nuclear scattering intensity fitted to the solid cylinder model.

The POLSANS diffraction pattern was measured for the out of plane geometry at the sample detector distance of 2.0 m. The sample-detector distance corresponds to the scattering q range of 0.02 $Å^{-1}$<q<0.27 $Å^{-1}$. The polarised foreground intensities at the out of plane field of 3.0 T is shown in Figure 5.36. The schematic illustrated below the foreground measurement shows the saturation-state of the recording layer and soft underlayer. The incident neutron beam was polarised in the spin up (+) or spin down (-) state. The spin vector will undergo adiabatic polarisation by aligning along the applied field direction. For example when an incident neutron in the spin down state encounters the applied field, the magnetic torque will flip the spin down state parallel to the field direction. The nuclear-magnetic interference scattering was determined by taking the difference between the polarised foreground intensities. Within the scattering plane, the diffraction pattern exhibits an interference ring, which was characteristic of a pseudo-crystalline Bragg peak.

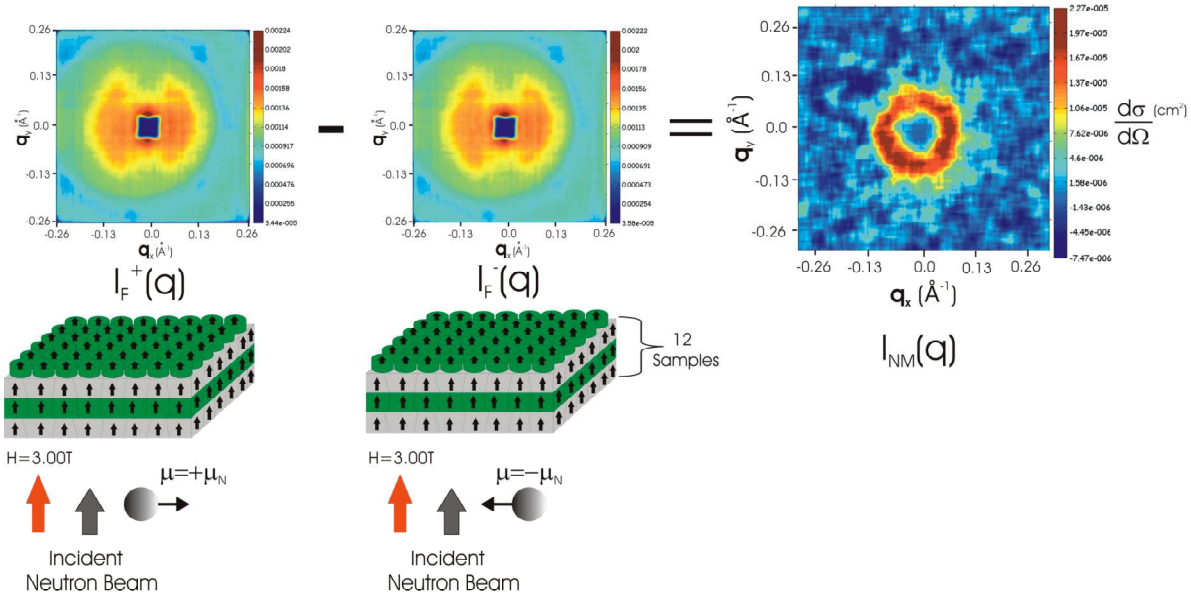

Figure 5.36: The extraction of the nuclear-magnetic interference $I_{NM}(q)$ at the out of plane field of 3.0 T (red arrow). The foreground scattering components $I_F^+(q)$ and $I_F^-(q)$ were measured for the respective ± spin states. The spin state of the incident neutron beam (grey arrow) is represented by the spherical object.

A further set of SANS measurements was performed at the out of plane fields of 0.00250 T, -0.31 T, -0.57 T and -0.81 T. In Figure 5.37 the H114 out of plane hysteresis loop is plotted for the first half of the hysteresis measurement. For each POLSANS measurement, the moment position was numbered on the hysteresis loop. The first position at 3.0 T was extrapolated from the hystesesis measurements where the recording layer saturates at the field 1.3 T. The nuclear-magnetic interference terms for the field range are shown in Figures 5.38 and 5.39. Alongside each diffraction pattern is plotted the radial intensity average, calculated over the q range 0.02 $Å^{-1}$<q<0.27 $Å^{-1}$.

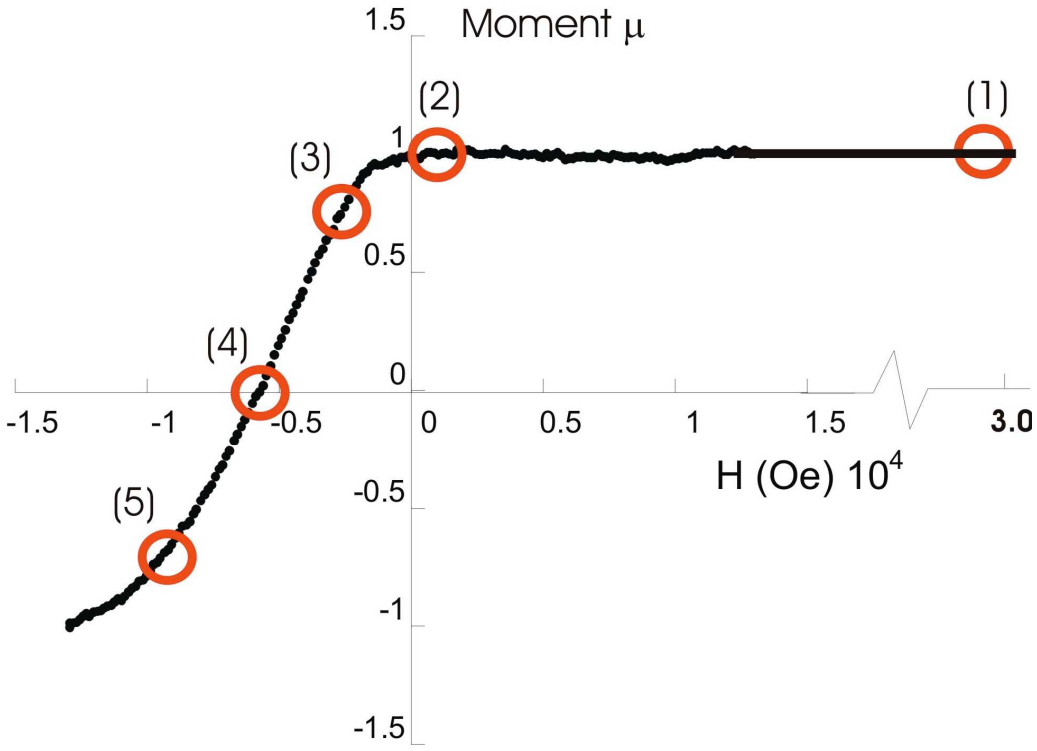

Figure 5.37: The H114 out of plane magnetic hysteresis loop. The red circle marks the hysteresis position of the diffraction measurements at the out of plane fields of (1) 3.0 T, (2) 250 Oe, (3)-0.31 T, (4) -0.57 T and (5) –0.81 T.

The nuclear-magnetic interference term was extracted for the out of plane field of 3.0 T, see Figure 5.38(a). The scattering intensity was positive over the measured q range where $I_F^+(q)>I_F^-(q)$. This scattering condition shows that the neutron's spin up (+) frame was aligned along the applied field direction. The scattering intensity shows a broad diffraction peak at q=0.065 $Å^{-1}$. The P-Y structure factor calculation shows this q-position to correspond to the inter-granular separation of 85.0 Å. At the applied out plane field of 250 Oe, essentially remanence, the interference pattern shows only a slight reduction in scattering intensity with respect to the saturated case. This small reduction was attributed to the decrease in the grain's magnetic scattering contrast. Since the recording grain has a strong perpendicular anisotropy field, the magnetic contrast at saturation and remanence will have similar values. The interference diffraction pattern is illustrated in Figure 5.38(b). The radial intensity plot shows that the interference peak was only slightly smaller than the saturation value.

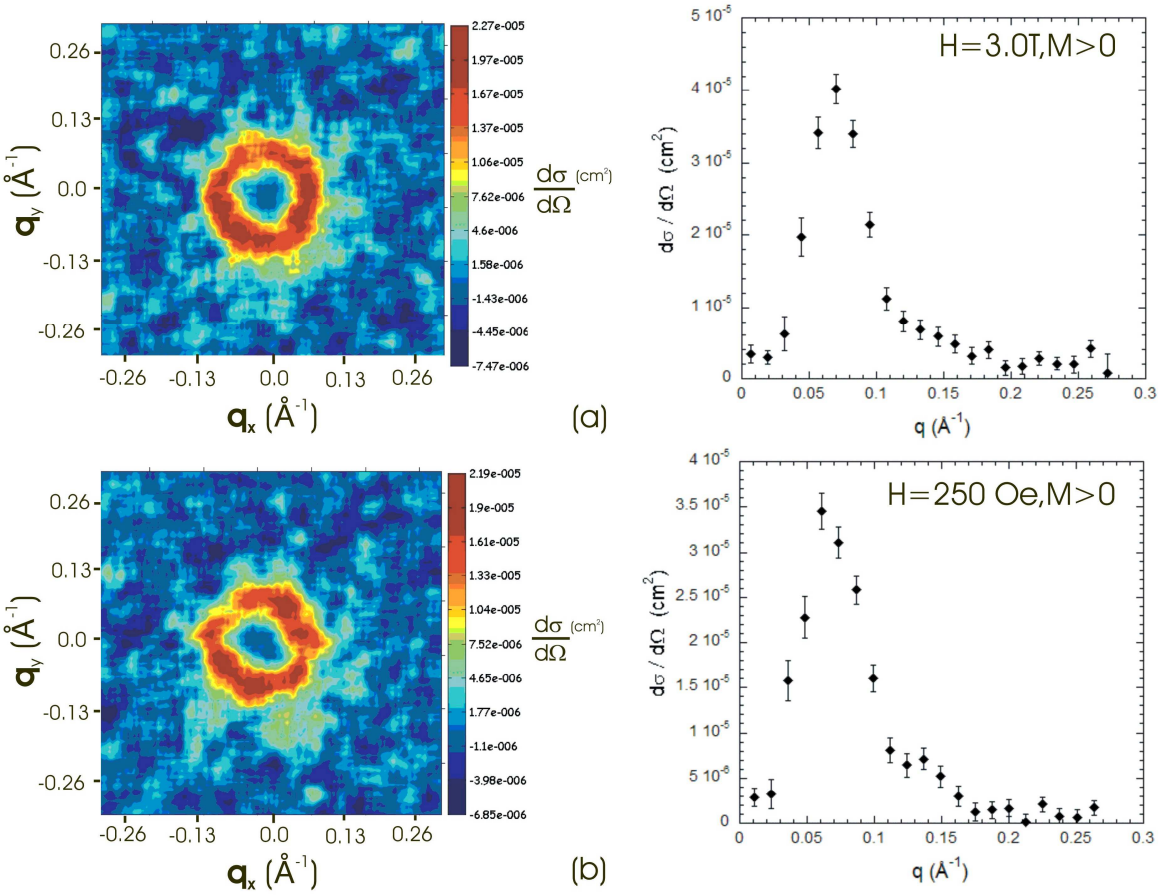

Figure 5.38: The nuclear-magnetic interference term for the out of plane magnetic fields of (a) 3.0 T and (b) 250 Oe. The interference intensity within the scattering plane is plotted as a function q.

The following interference measurements were performed within the hysteresis loop's negative field range of -0.30 T<H<-0.81 T. The neutron spin up state was now aligned along the negative field direction. This results in a relative sign change for the foreground scattering states where $I_F^+(q)<I_F^-(q)$. To compare the scattering data within the neutron's spin up frame, the negative interference term was multiplied by minus one. The interference scattering at H=-0.31 T is shown in Figure 5.39(a). The magnetic scattering component, contained within the interference term, was reduced as the recording grain's magnetisation approaches zero. At the coercive field of H=-0.57 T, the interference scattering shows a negative scattering contrast. This was characteristic of the recording grain's switching behaviour where the magnetisation components begin to align anti-parallel to the applied field direction. At the out of plane field of -0.81 T, the negative interference pattern becomes larger due to increases in the recording layer's out of plane magnetisation, see Figure 5.39(b).

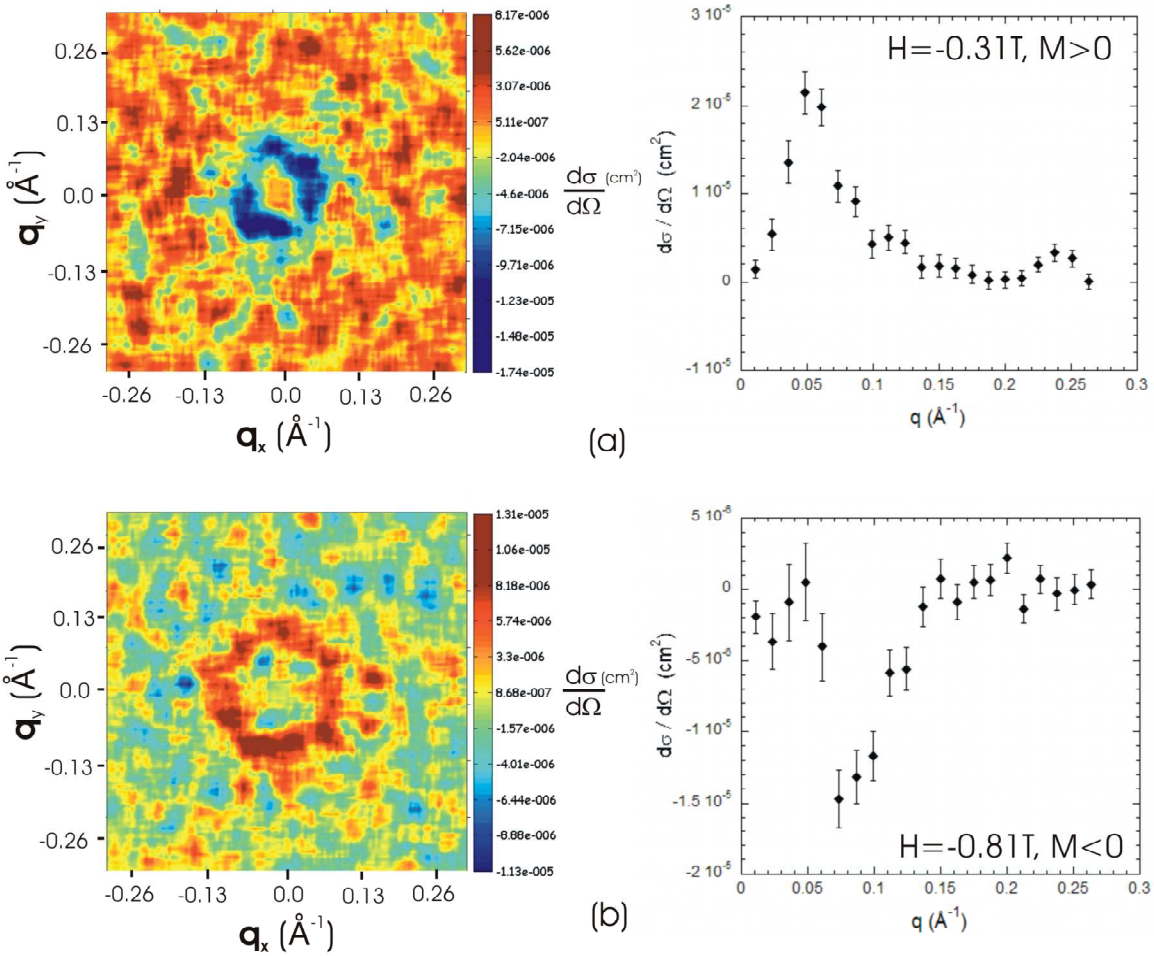

Figure 5.39: The nuclear-magnetic interference term at the out of plane magnetic fields of (a) -0.31 T and (b) -0.81 T. The interference intensity within the scattering plane is plotted as a function q.

The nuclear scattering intensity was extracted from the interference term at the applied out of plane field of 250 Oe. The extraction procedure was similar to the method used for the in-plane measurements. The interference term was expressed as a cross between the nuclear and magnetic intensities defined by $I_{NM}(q)=(I_N I_M)^{1/2}\sin^2\pi/2$. The term $I_M(q)$ expresses the recording layer's magnetic scattering intensity at the out of plane field of 250 Oe. This magnetic scattering component was approximately equal to the offset measurement at the in-plane field of 3.0 T. Similarly the SANS1 scattering statistics were quite noisy. Therefore the offset fit shown in Figure 5.25 was used in place of the SANS1 measurement. The Porod background was subtracted off the offset intensity. The nuclear-magnetic interference and offset terms are plotted in Figure 5.40. The peak at $q=0.065\,Å^{-1}$ characterises the interference scattering between recording grains. At $q<0.023\,Å^{-1}$ the scattering shows no cluster peak as was observed in the in-plane measurement. In this case, the out of plane magneto-crystalline anisotropy energy was much larger than the inter-granular exchange coupling. Hence the magnetic grains do not coalesce into granular clusters.

The nuclear scattering intensity $I_N(q)$ was extracted from the nuclear-magnetic interference term, see Figure 5.41. The nuclear scattering intensity resembles the shape of the interference, however there was a reduction in scattering contrast. The scattering behaviour resembles that of a solid core form factor where the nuclear contrast was uniform over the recording grain. The nuclear scattering data was modelled using a solid cylinder structure with a length L and radius R. The global fit was quite poor in modelling the nuclear scattering data. At low q the form factor fails to fit the sharp drop off in nuclear scattering intensity. The Percus-Yevick structure factor partially fits the interference peak with an average grain size of 86.0 Å. However, the structure factor function cannot properly match the peak width. This was attributed to the overly sharp drop off in scattering intensity at low q. The form factor gives an average grain size of 86.0 Å with a grain size distribution of 6%. The grain size and separation distance compare closely with the physical grain size of 90.0 Å [99].

The nuclear contrast profile was represented by a top-hat wave function. The nuclear scattering length density of the recording grain and grain boundary determines the relative magnitude of these steps. In this case the nuclear scattering length does not appear to vary across the grain boundary interface resulting in a single-phase nuclear scattering. In the following analysis, the validity of the solid cylinder model was tested by calculating the nuclear scattering contrast for the perpendicular recording grain.

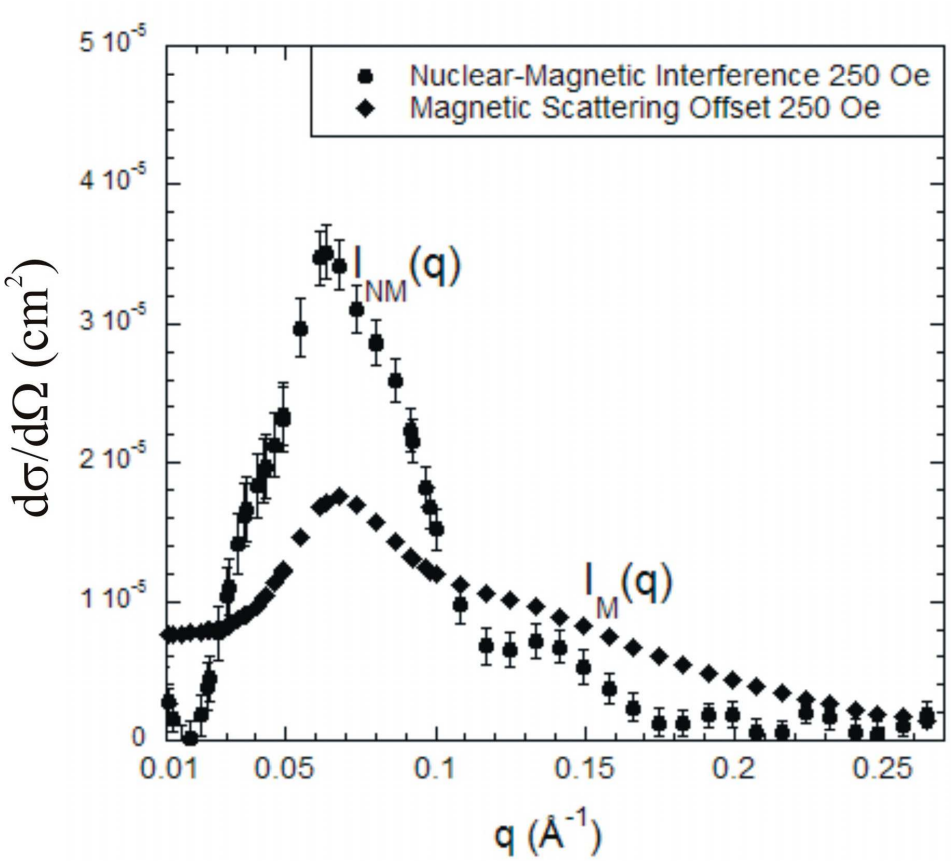

Figure 5.40: The H114 nuclear-magnetic interference and magnetic scattering offset at the in-plane field of 250 Oe.

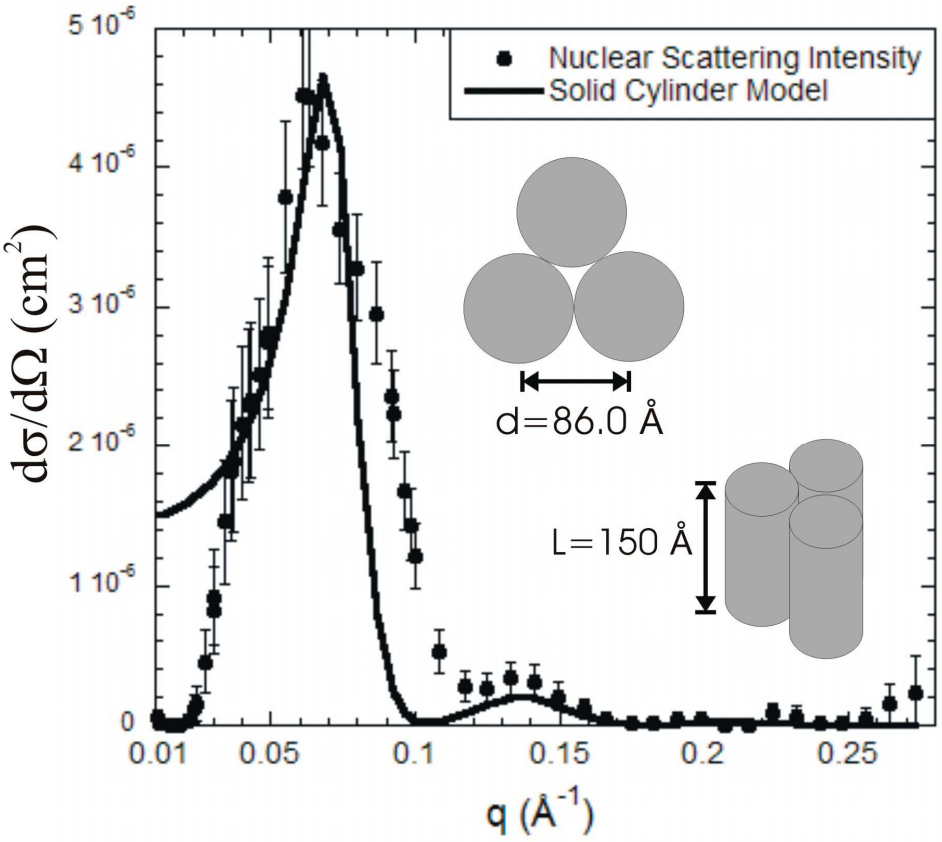

Figure 5.41: The H114 nuclear scattering intensity fitted to the solid cylinder model.

The sample's nuclear scattering contrast was calculated by first extracting the grain's nuclear scattering length density. In energy dispersive x-ray measurements it was shown that the recording grain was composed of a core-shell structure. The core component contains a high fraction of cobalt while the shell component was enriched with SiO_2. It was assumed that the recording grain's core and shell atomic proportions were $Co_{70}Cr_{18}Cr_6–(SiO_2)_2$ and $Co_{10}Cr_{18}Cr_6–(SiO_2)_{22}$ respectively. These proportions give the core and shell components the cobalt percentage of 70% and 10% respectively. The nuclear scattering length density was calculated by the density formula expressed in the previous chapter on polarised SANS, see section 4.5.3. The NIST nuclear scattering length density calculator [91] extracted the core and shell densities of $\eta_c=2.77\times10^{-6}$ Å^{-2} and $\eta_s=6.59\times10^{-6}$ Å^{-2} respectively. In the second stage, the density calculations were used to determine the core and shell nuclear scattering contrasts. The respective nuclear contrast components were expressed by $|\Delta\eta_c|=|\eta_c-\eta_s|$ and $|\Delta\eta_s|=|\eta_s-\langle\eta\rangle|$ where the term $\langle\eta\rangle=\nu_c\eta_c+\nu_s\eta_s$ defines the volume averaged scattering length density. The coefficients ν_c and ν_s represent the core and shell volume fractions respectively where $\nu_c+\nu_s=1.0$.

The relative values of the core and shell contrast components will determine if the nuclear scattering intensity originated from a homogenous particle. The core-shell contrast ratio $\Delta\eta_c/\Delta\eta_s$ was used investigate the recording grain's physical composition as a function of core volume fraction, see Figure 5.42. For small core fractions $\nu_c<0.2$, the contrast ratio shows a non-linear increase which was indicative of a heterogeneous particle with a SiO_2 enriched grain boundary. When $\nu_c\rightarrow0$ and $\nu_s\rightarrow1$ the core contrast value dominates the scattering form factor. As the core volume faction increases to 0.8 the contrast ratio approaches unity. This fraction defines the contrast match between the core and shell components. In this state the recording grain behaves as a homogeneous particle whose scattering form factor was modelled using the solid sphere structure. Figure 5.43 plots the recording grain's nuclear scattering contrast profile for a series of core volume fractions $\nu_c=0.1$-0.9. At small core fractions ν_c, the grain exhibits the core-shell model where the contrast profile traces out a stepped top-hat function over the entire volume. For high ν_c, the recording grain approaches a single top-hat function. In this analysis evidence from SANS measurements and contrast calculations show that the H114 recording grain possesses a uniform scattering contrast for core fractions of the order of $\nu_c\geq0.8$. These results confirm the TEM measurements where the enriched core was segregated by a thin shell of SiO_2.

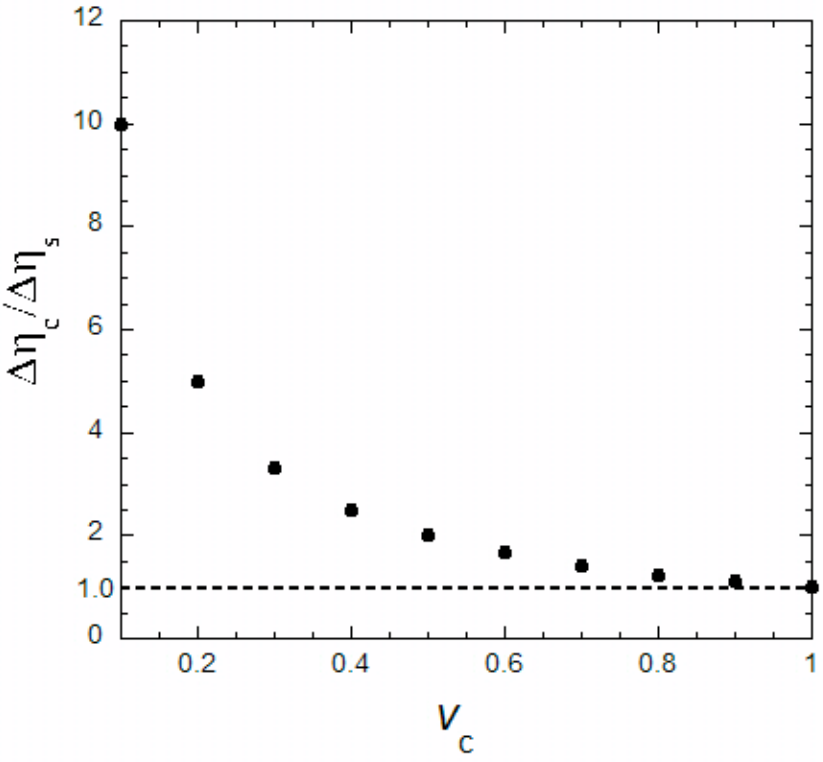

Figure 5.42: The recording grain's nuclear scattering contrast ratio as a function of the core volume fraction v_c. The ratio of unity defines the matching point between the core and shell contrast components.

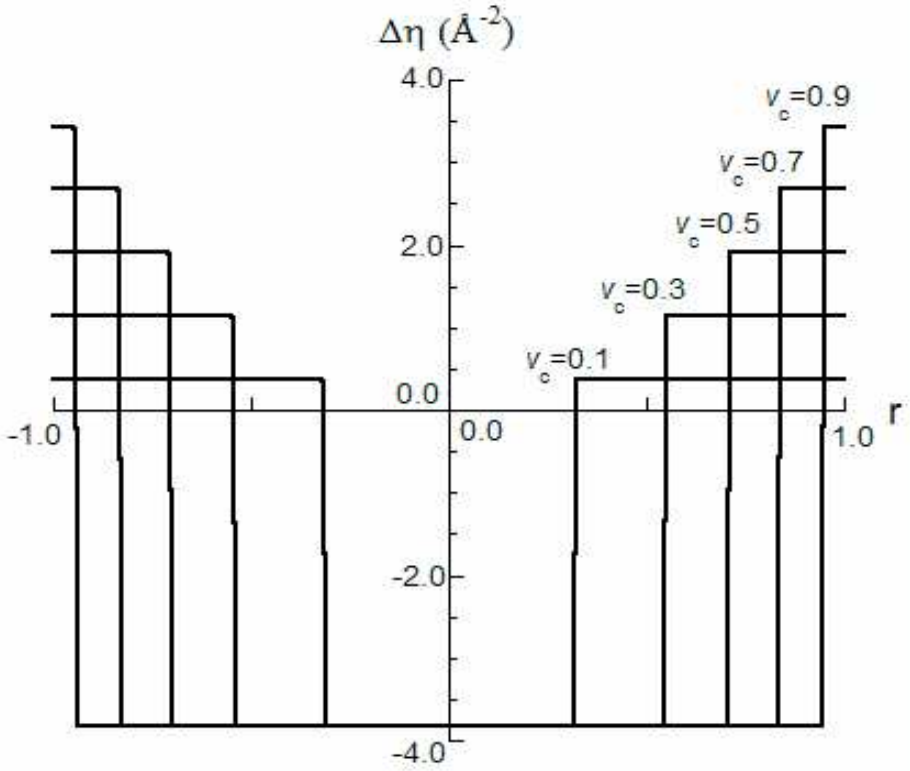

Figure 5.43: The recording grain's nuclear scattering contrast profile at the core volume fraction $0.1<v_c<0.9$ was plotted as a function of radius.

5.5.4 Summary

The characterisation technique of POLSANS was used to study the magnetic and physical structure of perpendicular recording media at the in-plane and out of plane field geometries. In the first experiment, the unpolarised and polarised foreground scattering intensities were measured at applied in-plane field of 3.0 T. At this applied field, the magnetic recording layer was fully saturated in-plane. The unpolarised SANS studies successfully measured the recording layer's anisotropic magnetic diffraction pattern. The magnetic scattering intensity was used to characterise the recording grain's local magnetic structure. The polarised scattering measurements extracted the recording layer's nuclear-magnetic interference pattern. The interference term was proportional to the recording layer's nuclear scattering intensity, which successfully extracted the recording grain's physical length scale and composition.

In the second experiment the polarised scattering measurements were performed at the applied out of plane field of 250 Oe. At this applied field, the magnetic recording layer was saturated perpendicular to the sample plane. The recording grain's nuclear-magnetic interference pattern was determined by calculating the difference between the polarised foreground scattering intensities. The grain's nuclear scattering component was extracted by dividing the nuclear-magnetic interference by its magnetic scattering intensity at the remanent state. It was demonstrated that the nuclear scattering intensity originated from a solid sphere recording grain where the contrast profile was described using the top-hat density function. The solid cylindrical form factor was used to model the physical grain size of the order of 80-90 Å. The grain size was in good agreement with the TEM measurements of these materials.

In the final experiment, the recording grain's magnetic switching behaviour was investigated by using POLSANS studies. The scattering measurements were performed at the out of plane field range -0.8 T<H<3.0 T. At the saturation and remanent fields of 3.0 T and 250 Oe respectively, the nuclear-magnetic interference pattern was isotropic about the scattering plane. The magnetic scattering intensity at either applied field remained virtually unchanged, which was due to the recording grain's strong magneto-crystalline field. At the coercive field of -0.57 T, the interference pattern exhibited a negative magnetic scattering amplitude. The negative scattering value characterised the recording grain's local magnetic length scale-of the order of 90 Å-at the switching field.

5.6 Conclusion

In this chapter, SANS studies have been used to characterise the magnetic and physical structure of CoCrPt-SiO_2-perpendicular recording media. It was demonstrated that the unpolarised SANS experiment could be used to extract the recording layer's magnetic grain size and size distribution function. The sub-granular magnetic structure was modelled using a solid sphere with a diameter of 24.8±0.4 Å with a gamma-Shultz distribution of 16%. In these unpolarised SANS studies, the scattering model extracts a small magnetic grain size with respect to the TEM measurements. If the magnetic grain size is smaller than its physical counterpart, then the recording grain is more prone to thermal activation. This thermally excited state could lead to a magnetically unstable recording media. Future work is required on deriving the scattering form factor that gives a comparable magnetic and physical grain size.

In the latter half of the chapter, the recording layer's sub-granular structure was characterised using the POLSANS technique. It was established through polarisation analysis that the nuclear-magnetic interference was proportional to the recording grain's nuclear scattering intensity. The recording grain was adequately modelled by using the cylindrical structure with a physical grain size of the order of 80-90 Å. However the form factor only partially fits the nuclear scattering intensity. Further work is required on modelling the physical scattering structure of the recording gain. In may be possible to derive the scattering intensity by using the Voronoi construction. The asymmetric cells of a Voronoi pattern represent a more accurate description of the recording grains.

Future experiments are planned for the SANS instruments D22 and SANS1. These experiments are planned to investigate a new set of perpendicular media samples fabricated from a thin Silicon substrate. It is hoped that the Si substrate will reduce the background scattering encountered from the H114 glass-substrate samples. In addition neutron reflectometry experiments are planned to investigate the recording layer and SUL switching behaviour. Further characterisation studies using energy resolved x-ray scattering are planned to investigate the recording layer's physical and magnetic grain size. The advantages of x-ray measurements are the marked increase in photon flux and the ability to spatially correlate the recording grain's physical composition with its sub-granular magnetism

Chapter 6

Ferromagnetic Nanowires

6.1 Introduction

In the last few decades, research and development into patterned media such as self-assembled magnetic nano-structures has attracted considerable interest within the fields of biology and materials science. The applications include cell separation, biosensing, studies of cellular function and magnetic recording media [105,106,107]. The research work into self-assembled magnetic recording media has focused on a cost effective fabrication process that can achieve areal densities in excess of 1 Tb/inch^2.

The patterned magnetic recording media is fabricated through the process known as self-assembly, see top diagram of Figure 6.1. The self-assembly process is driven by a large number of weak interactions such as hydrogen bonding and van der Waals forces. Typically self-assembly is assisted by a molecular or physical template, which secures the ensemble of particles onto the substrate. The bottom figure shows a molecular template where the solvent particles attach themselves to SiO_3 sites. These fabrication processes allow the growth of discrete ferromagnetic structures with very small size distribution. For example fabrication of iron platinum spheres has achieved size distributions of the order of 5% [19,20]. This spatial characteristic gives the patterned media a reduced size distribution over continuous media resulting in an improvement in the signal to noise ratio.

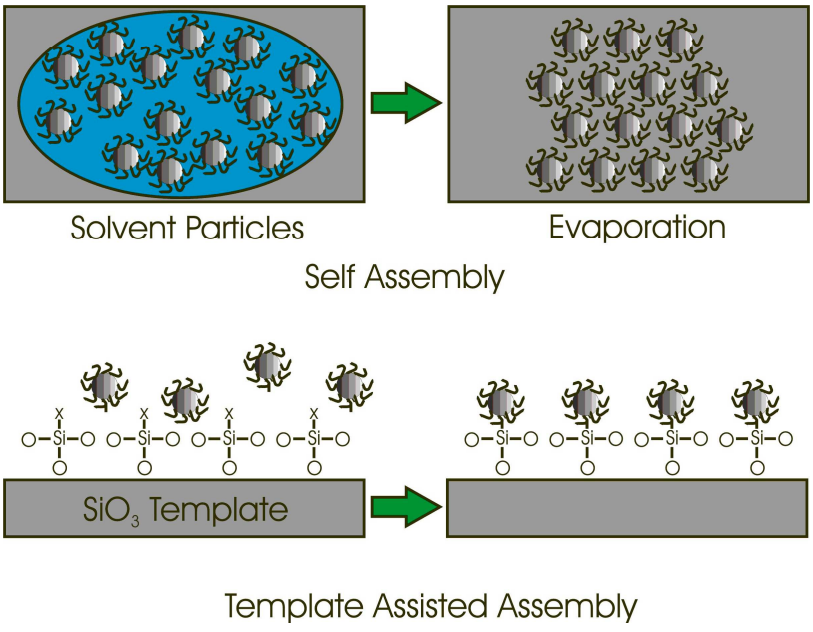

Figure 6.1: Depiction of the self-assembly fabrication process. The top diagram shows the self-assembly by the evaporation of solvent particles. The bottom figure shows template assisted self-assembly using SiO_3 nucleation sites.

The self-assembled structure known as ferromagnetic nanowires is the ideal sample for investigating the magnetic properties of discrete perpendicular recording media. This is mainly due to their relatively cheap fabrication process, which allows the growth of metallic nanowires within a template-assisted assembly of aluminium oxide (anodised). The current research has characterised the nanowire's physical and magnetic properties by using transmission electron microscopy (TEM) and bulk magnetisation measurements respectively [109]. With ongoing improvements to the fabrication process comes the reduction of the nanowire's magnetic volume. In this situation the wires are more prone to demagnetisation fields and thermal activation. These magnetic interactions were better understood by accurately characterising the local magnetism to within a few nanometers. In this chapter, the local magnetism of self-assembled cobalt nanowires was investigated by the characterisation technique of small angle neutron scattering (SANS).

6.2 Physical Microstructure

The self-assembled nanowires were fabricated by electroplating ferromagnetic cobalt onto a nano-porous template composed of anodic aluminium oxide (AAO). Initially the template was composed of a thin film of high purity aluminium (99.99%) with a thickness of 6.0 μm [109]. The electrochemical process known as anodization was used to grow the nano-porous template [110]. The aluminium foil and an electrical conductor act as the anode and cathode respectively. The Al electrochemically reacts with the water molecules to form the growth layer composed of Al_2O_3. Anodization is described by the reaction equation, $2Al+3H_2O \rightarrow Al_2O_3 +6H^-+6e^-$. During formation, the pores begin to take shape within the Al_2O_3 matrix. Figure 6.2 depicts the formation of nanopores within the Al foil. The pore diameter was of the order of 2R=200 Å with an inter-pore separation of d=300 Å. The pore length was approximately L=1.0 μm. The deposition of Co atoms was performed by a two-electrode electrochemical cell under a constant potential of approximately 1.0 V at the temperature of 300 K. The electrolyte $CoS_2O{\bullet}H_2O$ was electrochemically deposited into the porous template. The nanowire's diameter was roughly equal to the average diameter of the cobalt filled pore. Figure 6.3(a) shows a TEM image of cobalt nanowires embedded within the AAO matrix. The nanowires were separated from the Al_2O_3 matrix by using a chemical bath of NaOH. Figure 6.3 (b) shows the TEM image of a separated wire bundle.

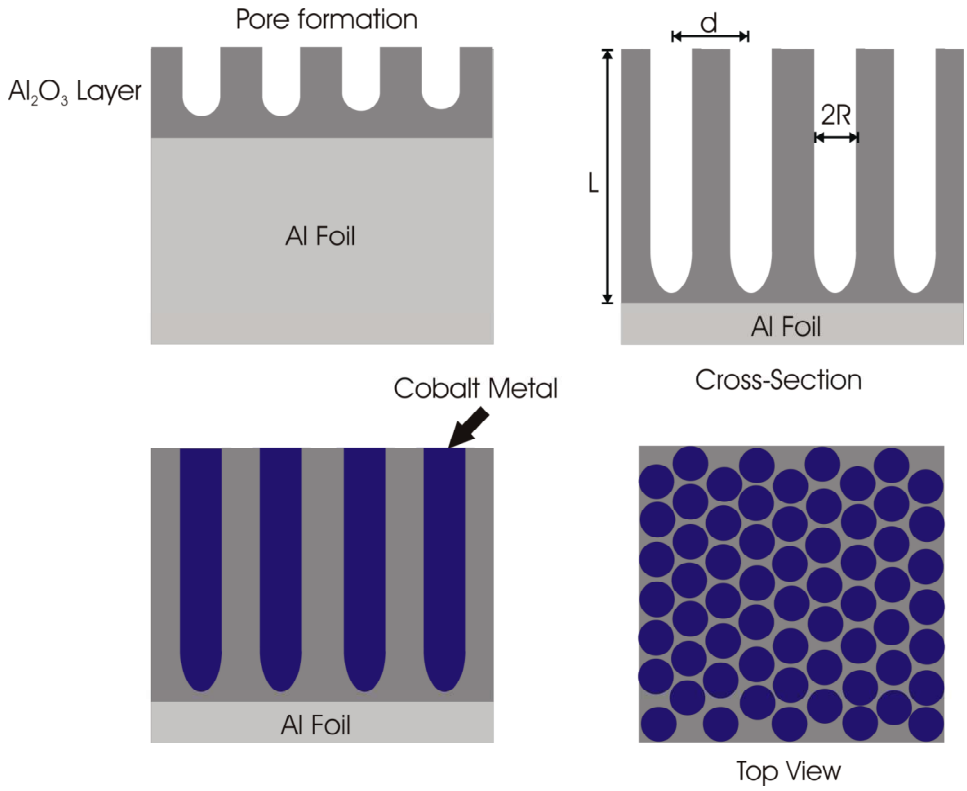

Figure 6.2: The cobalt nanowires Al_2O_3 template. The top figure shows the anodization of Al foil resulting in the formation of nanosized pores. The bottom image shows the porous template electroplated with bulk cobalt.

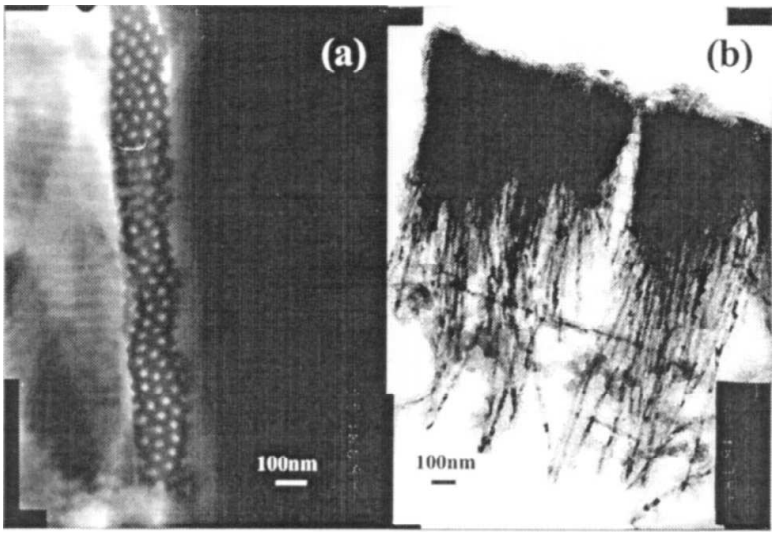

Figure 6.3: The TEM image in (a) shows the top view of Co nanowires embedded in the AAO matrix. The image (b) shows a nanowire bundle that has been removed from the matrix by using a NaOH bath [108].

6.3 Bulk Magnetisation

The cobalt nanowire's bulk magnetisation was characterised using the magnetic hysteresis loop. Figure 6.4 shows the hysteresis measurement for the in-plane (//) and out of plane (⊥) geometries [111]. The out of plane measurement exhibits a large loop area with a squareness of 0.80. Hence at remanence, the nanowire's magnetisation remains perpendicular to the longitudinal axis. This behaviour characterises a strong magnetic shape anisotropy along the nanowire's axis. The shape anisotropy originates from the dipolar field of atomic moments that align themselves along the wire's length dimension. The nanowire does possess a magneto-crystalline anisotropy along the longitudinal axis, however this component was very weak when compared to the shape anisotropy. The coercive field of 1.76 kOe was further evidence of the nanowire's strong shape anisotropy. The in-plane hysteresis gives a squareness of the order of 0.2. The small loop area was indicative of the nanowire's hard-axis of magnetisation. The small remanent and coercive values show the in-plane moments to be susceptible to strong demagnetisation fields.

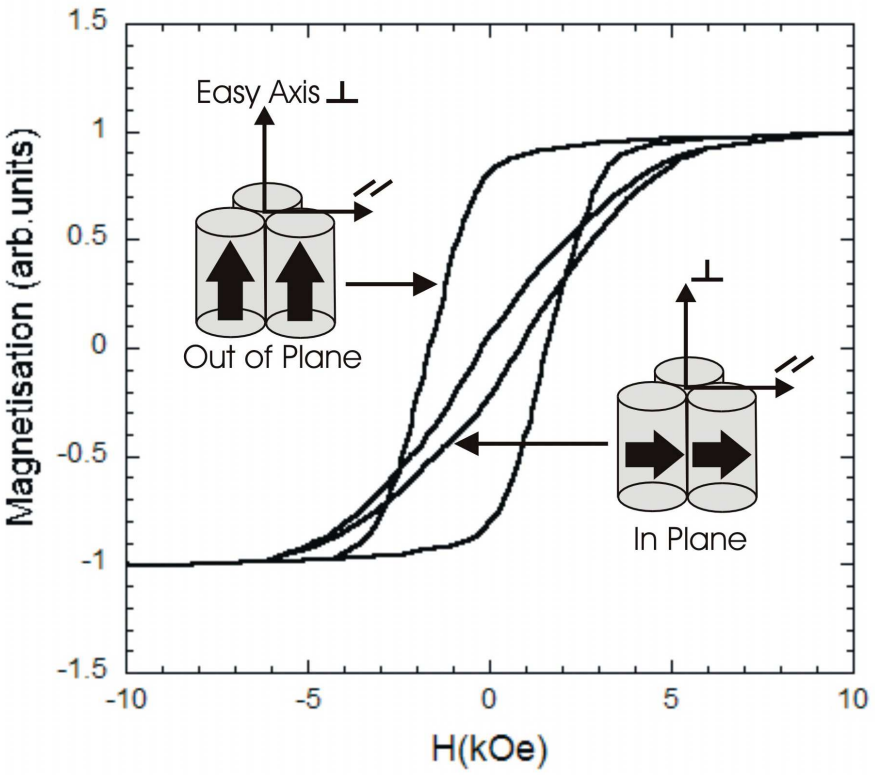

Figure 6.4: The self-assembled cobalt nanowires magnetic hysteresis measurements for the in-plane (//) and out of plane (⊥) configuration [111].

6.4 Unpolarised SANS

The characterisation technique known as unpolarised SANS was used to measure the local magnetisation of the self-assembled cobalt-based nanowires. The TEM images in Figure 6.3 have shown that the nanowires form a columnar structure where the wire length was approximate hundred times the size of it radius so defined L>>R. TEM measurements allow one to devise a scattering model that approximates the physical and magnetic structure of nanowires. In the following sections, the polydisperse ensemble of solid cylinders with radius R, length L and separation distance d was used to model the nanowire's magnetic diffraction pattern at the applied in-plane saturation field of 1.3 T.

6.4.1 Scattering Model

The scattering intensity for a polydisperse ensemble of nanowires was expressed by the following, $I(q)= N\{\langle F^2(q)\rangle-\langle F^2(q)\rangle^2\}+\langle F^2(q)\rangle^2 S(q)$. The structure factor, S(q), was approximated using the hard sphere model [61]. Note the rigorous solution to the structure function involves solving the correlation function for the two-dimensional hard-disc ensemble. There only exists a numerical solution to the hard-disc correlation function, which makes it impractical for fitting scattering data. The hard sphere model gives an exact structure factor that is nearly identical to its two-dimensional counterpart.

The magnetic scattering form factor F(q) was expressed by the Fourier transform of the real space scattering potential defined by the cylindrical top-hat function Π(r). The potential function was zero and unity for r>R and r<R respectively where R is the cylindrical radius. The form factor was expressed by, $F(\mathbf{q})=\Delta\eta(\pi r^2 L)J_1(|\mathbf{q}|r)/|\mathbf{q}|r$, where $\Delta\eta$ is the scattering contrast, L is the cylinder length and $J_1(|\mathbf{q}|r)$ is a first order Bessel function of the first kind, refer to Appendix section 8.1.2. The scattering geometry has the nanowires aligned with the incident beam, hence the **q** vector lies perpendicular to the to wire's longitudinal axis. The scattering intensity was simulated for an ensemble of rigid cylinders, see Figure 6.5(a). The scattering peak at $q=0.04$ Å^{-1} characterises the pair correlations between the cylindrical objects. The form factor intensity decays as a function of $F(q)\propto Aq^{-2}$. It was observed that the scattering model only partially fits the magnetic scattering data at high q. This form factor discrepancy was attributed to the wire's slight misalignment with respect to the incident beam.

The scattering potential for a misaligned cylinder was approximated by the convolution $V(r)=\Pi(r)\otimes\exp(-r/\varepsilon)/r$ where ε represents the decay parameter [112]. The misalignment effectively smoothes out the rigid scattering potential. In Figure 6.5(b), the scattering intensity is plotted for the smoothed cylinder approximation. The Fourier transform of the smoothed cylinder results in a sharper drop off in the scattering intensity, which was proportional to the function Bq^{-4}. The exponential smoothing was equivalent to multiplying the rigid form factor by q^{-1}. The smoothed cylindrical form factor function is expressed by,

$$F_S(q) = \Delta\eta\pi r^2 L \frac{J_1(qr)}{qr} \frac{1}{\sqrt{(1+(\varepsilon q)^2)}}. \qquad (6.1)$$

The decay parameter ε expresses the degree of misalignment with respect to the longitudinal axis. For $\varepsilon\rightarrow 0$ the rigid form factor reduces to perfectly aligned cylinders.

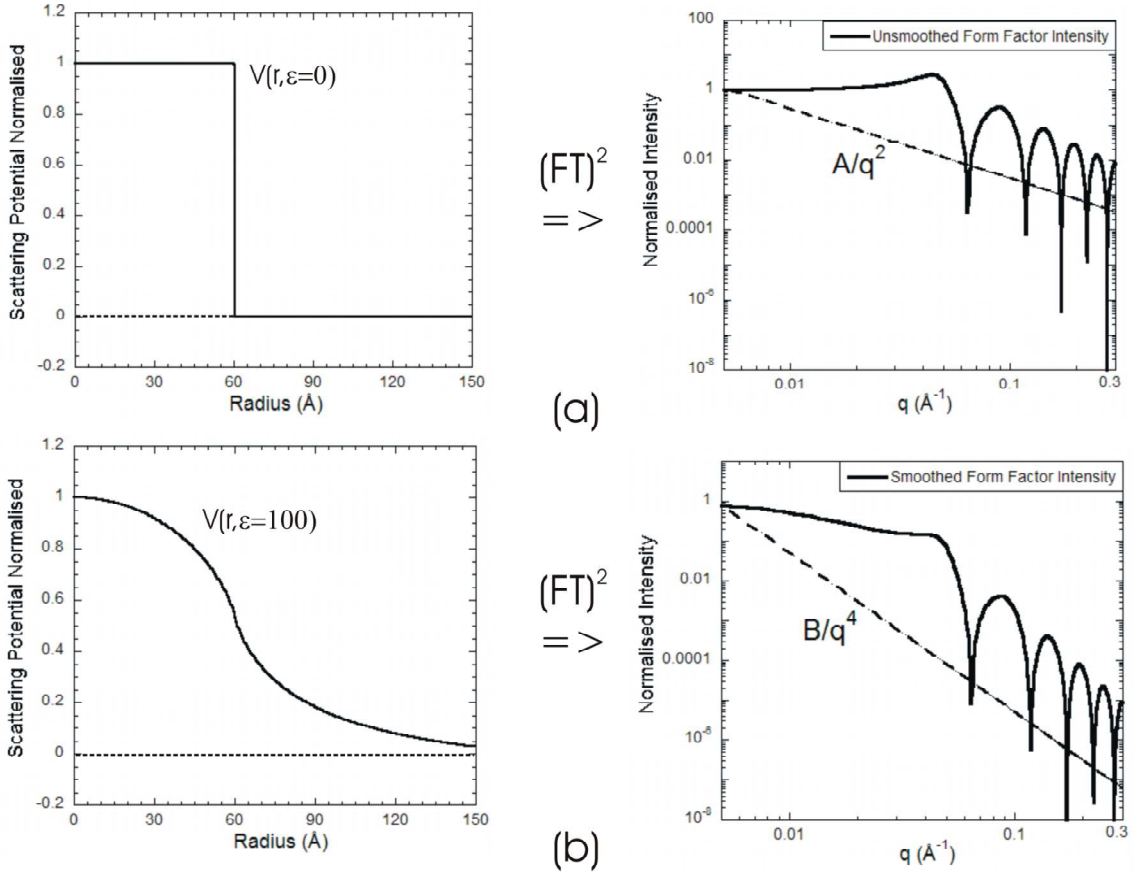

Figure 6.5: The cylindrical scattering potential and its Fourier transform squared $(FT)^2$ for the (a) rigid and (b) smoothed models. The scattering potentials are modelled using the spatial parameters of R=60.0 Å and d=132.0 Å.

6.4.2 Instrumentation

The cobalt nanowires were characterised using the D11 SANS instrument at the ILL, Grenoble France [63]. The sample was fastened to an aluminium sample holder, which was similar to the type used in section 5.4.3 Instrumentation. The sample was inserted between the poles of an electromagnet. Figure 6.6 shows the sample position from the front and top perspectives. This SANS experiment requires one to measure the anisotropic magnetic scattering from an ensemble of nanowires where the sample magnetisation was fully saturated in-plane. According to the in-plane hysteresis plot the sample saturates at fields greater than 1.0 T. The magnetic field of 1.30 T was applied parallel to the sample plane thereby saturating the magnetic moment in-plane.

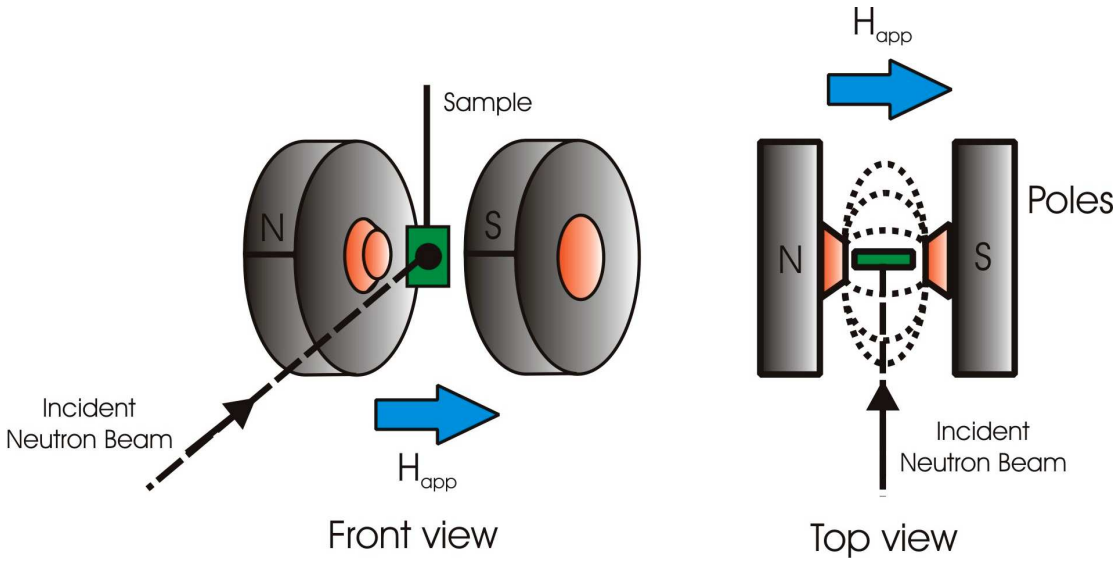

Figure 6.6: The 1.3 T electromagnet used in the SANS measurements. The magnetic field is applied parallel to the sample plane. The incident neutron beam lies normal to the sample's magnetisation.

6.4.3 Measurements

The nanowires's scattering intensity was measured for the sample-detector distances of 1.5, 2.0, 3.5, 8.0 and 16.0 m at the neutron wavelength of 5.0 Å. This range of detector distances corresponds to the q-range of $0.051\,\text{Å}^{-1}<|\mathbf{q}|<0.30\,\text{Å}^{-1}$. The SANS experiment consist of three separate measurements (a) zero field sample transmission intensity I_T, (b) zero field background scattering $I_B(q)$ and (c) applied field foreground scattering $I_F(q)$. The scattering measurements at different detector distances were matched up by applying the solid angle correction while the transmission measurement corrected for the instrument's flux-collimation. The scattering intensity was normalised with respect to the incident flux Φ_{inc}.

The background scattering state was prepared by applying a saturation field perpendicular to the sample plane. The field was then ramped down to its remanent state. This ensures that the sample contains no remanent in-plane magnetisation components. The background scattering intensity was measured at zero field where $I_B(q,H=0)=I_N(q)+I_M^{iso}(q,H=0)$. The nuclear scattering, $I_N(q)$, originates from the cobalt nanowires, aluminium template, sample holder and electromagnet. The magnetic scattering intensity, $I_M^{iso}(q,H=0)$, was isotropic within the scattering plane. This type of magnetic scattering originates from the nanowire's magnetic moments that were aligned perpendicular to the sample plane. At remanence the nanowire's magnetic moments lie parallel to the incident neutron beam. The magnetic scattering within the q-plane was expressed by $I_M^{iso}(q,H=0.0)=I_M(q,H=0)$ where $\mathbf{m}\bullet\mathbf{q}=|\mathbf{m}||\mathbf{q}|\cos(\pi/2)$.

The foreground scattering intensity measured the nuclear and magnetic scattering components for the in-plane saturation field of 1.3 T. The foreground intensity was expressed by $I_F(q,H=1.3T)=I_N(q)+I_M^{aniso}(q)$. The second term defines the anisotropic magnetic scattering intensity, $I_M^{aniso}(q)=I_M(q)\sin^2\alpha$ where α defines the azimuthal angle between momentum transfer and magnetisation unit vectors **q** and **m** respectively. The nuclear scattering was separated from the foreground component by performing a background subtraction. The magnetic difference equation was expressed by the following $\Delta I_M=I_M(q,H=1.3T)\sin^2\alpha-I_M(q,H=0)$. The first term represents the anisotropic magnetic scattering intensity while the second term was known as the magnetic scattering offset. The offset term represents magnetic scattering from the out of plane remanent state.

6.4.4 Results and Discussion

The nanowire's foreground diffraction pattern was measured at the in-plane saturation field of 1.3 T. This applied field was adequate to saturate the in-plane moments as shown in the in-plane hysteresis loop. The background measurements were performed in the remanent state where the magnetic moments were oriented perpendicular to the sample plane. The measured scattering intensity was converted to the differential scattering cross-section by the direct beam correction, $d\sigma/d\Omega=I(q)/\Phi_{inc}$ where I(q) was the foreground or background scattering intensities. Figure 6.7 shows the foreground and background diffraction patterns at the sample-detector distance of 8.0 m. This corresponds to the q range of 0.01 $Å^{-1}$<q<0.04 $Å^{-1}$. The foreground and background measurements show a diffraction ring, which originates from interference scattering of neighbouring nanowires. The wire schematic shows the magnetic structure for the zero field and saturated state. The background subtraction extracted the magnetic difference plot.

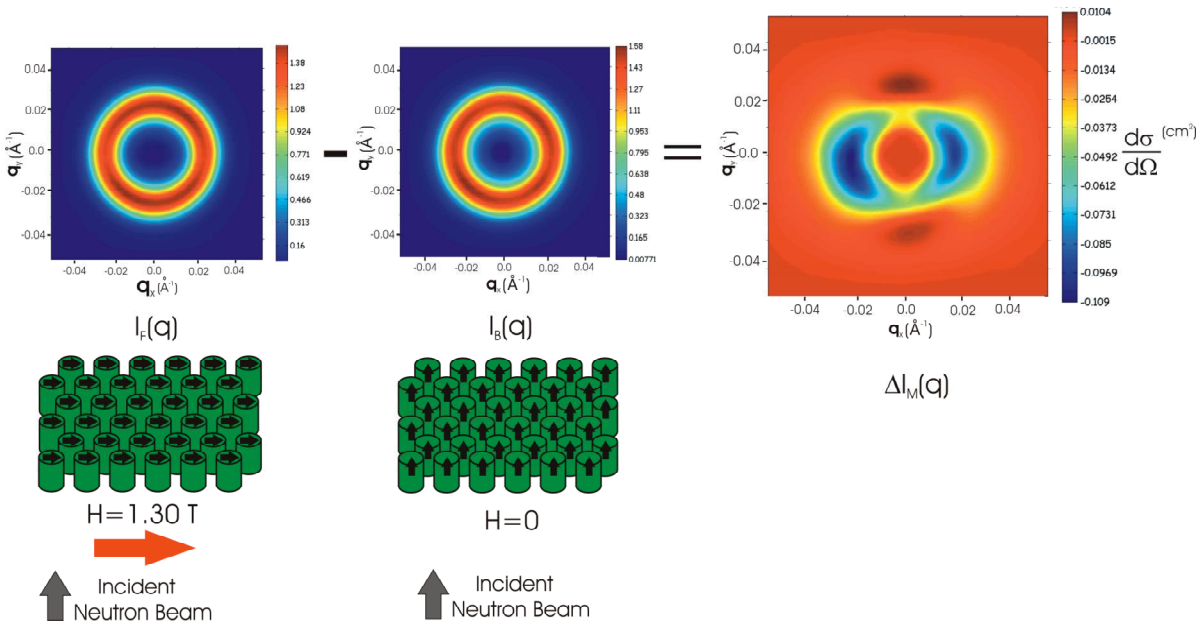

Figure 6.7: The self-assembled cobalt nanowires 1.3 T foreground and background scattering measurements at the sample-detector distance of 8.0 m. The resulting background subtraction gives the magnetic difference plot. The diagrams show the sample's in-plane (x-y) saturated and out of plane remanent states. The incident neutron beam is parallel to the wire's longitudinal axis.

The magnetic difference plot at 8.0 m exhibits a strong anisotropic magnetic scattering within the scattering plane where $\Delta I_M(q_y)>\Delta I_M(q_x)$. The diffraction pattern shows darken red lobes along the q_y-axis. This scattering behaviour was indicative of an ensemble of moments saturated along the q_x-axis. Hence the anisotropic magnetic scattering was expressed by the relation $I_M^{aniso}(q)=I_M\sin^2\alpha$. The difference plot about the x-axis drops below the positive scattering plane represented by dark blue lobes. This region represents the magnetic scattering intensity at the zero field measurement. The GRASP program calculates the azimuthal scattering intensity over the two-dimensional q-plane as a function of $\theta=90^0-\alpha$. The scattering data was fitted using the $\cos^2\theta$ function, see the right plot of Figure 6.8. The difference plots for the remaining detector distances show similar scattering behaviour within the q-plane. Due to the sample's strong demagnetisation fields, the anisotropic magnetic scattering shows no evidence of the ANCOS^2 phase shift.

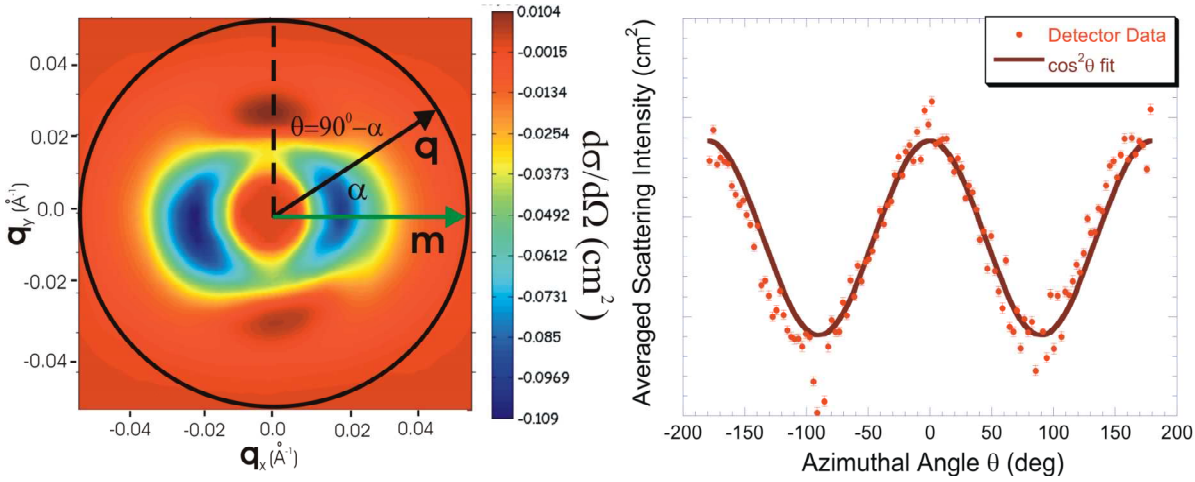

Figure 6.8: The self-assembled cobalt nanowire 1.3 T magnetic difference plot measured at the sample-detector distance of 8.0 m. The azimuthal scattering intensity is calculated over the q range 0.01 Å^{-1} <$q_{8.0m}$<0.05 Å^{-1}. The azimuthal data is fitted by the $\cos^2\theta$ function where $\theta=90^0-\alpha$.

The magnetic scattering intensity was extracted from the difference plot using the GRASP program ANCOS[2], see section 4.3.4 Measurements. In Figure 6.9, the foreground and magnetic scattering components are compared on a log-log scale. The foreground scattering was on average 10 times larger than the magnetic scattering intensity. The larger foreground intensity was attributed to the electromagnet's nuclear background scattering. Instrument components such as the aluminium template and sample holder should only contribute a small fraction to the background component. The foreground intensity shows a sharply defined scattering peak at q=0.023 $Å^{-1}$ which represents interference scattering from the magnetic and nuclear scattering components. For q>0.050 $Å^{-1}$ the scattering intensity decreases as a function of q^{-4} characteristic of the smoothed scattering potential. The foreground intensity tails off to a constant value at q=0.26 $Å^{-1}$. This q-region represents the nuclear scattering from the electromagnet. The magnetic interference peaks mirror their nuclear counterparts with respect to the q position. For q>0.05 $Å^{-1}$ the magnetic scattering decreases as a function of q^{-4} showing a deviation from the constant nuclear scattering background.

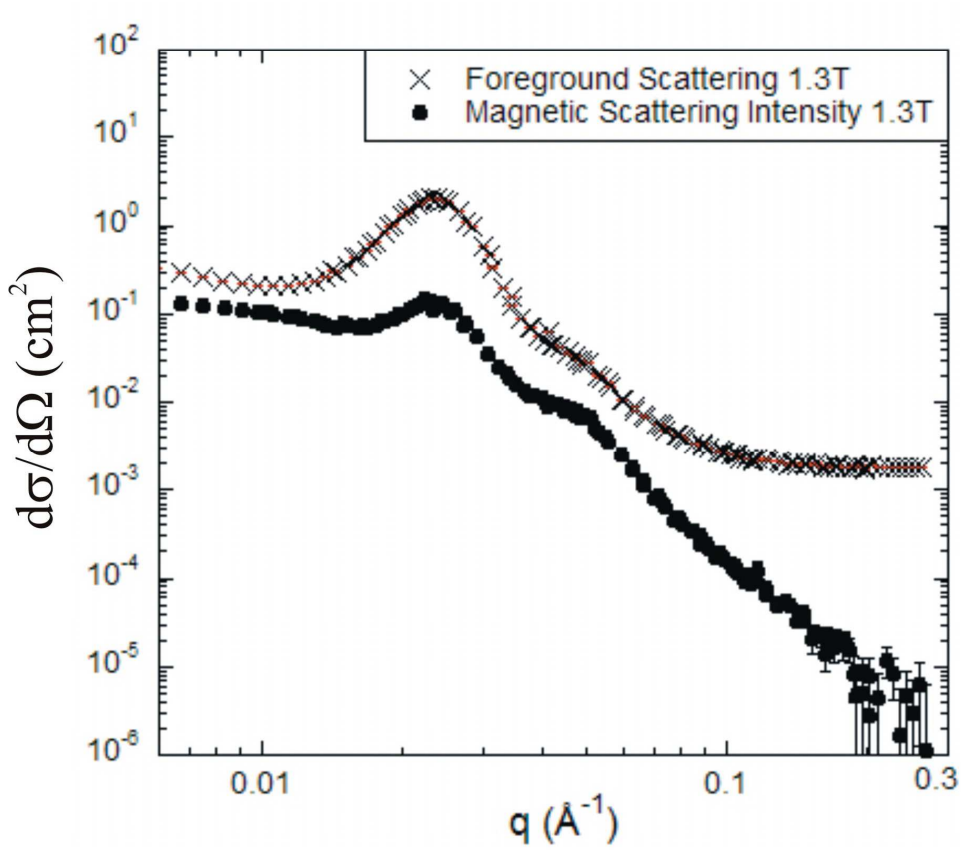

Figure 6.9: The self-assembled cobalt nanowire foreground and magnetic scattering intensity components.

The rigid cylindrical model was fitted to the magnetic scattering data shown in Figure 6.10. The Percus-Yevick structure factor fits the magnetic interference peaks at $q=0.023\,Å^{-1}$ and $q=0.05\,Å^{-1}$. At $q>0.05\,Å^{-1}$ the form factor intensity was observed to deviate from the magnetic scattering by a factor of q^{-2}. The rigid cylinder model fails to predict the q^{-4} scattering behaviour. In this case the nanowires cannot be modelled using the scattering potential for an aligned cylinder. The model must account for the nanowire's misalignment along the longitudinal axis. The magnetic scattering intensity was fitted using the smoothed cylindrical model shown in Figure 6.11. The scattering function shows a closeness of fit $\chi^2=3.0$. Table 6.1 lists the NLS fit parameters for the form factor and structure factor functions.

In Figure 6.12 the structure factor is calculated using the Percus-Yevick model. The wire's average separation distance was 249.0±1.0 Å with a size distribution of 16%. The form factor gives an average wire diameter of 197.2±0.3 Å with a size distribution of 17%. The wire's diameter agrees with the TEM measurement of 200 Å [113]. The nanowire's magnetic scattering contrast was expressed by $\Delta\eta^M=(1.20\pm0.01)\times10^{-5}\,Å^{-2}$. The magnetic contrast was proportional to the nanowire's M_s value at $q=0$. The wire's relative magnetisation was extracted by comparing the contrast with the perpendicular recording grains respective value. The wire's contrast was approximately twenty times the size of the recording grain. The result was much larger than one should expect for bulk cobalt. The recording grain has a $q=0$ magnetisation of $M_s=400.0$ emu/cm^3 while the bulk value was $M_s=1400$ emu/cm^3. This clearly shows that the wire's magnetisation and hence contrast is not twenty times the size of the recording grain.

In Figure 6.13, the scattering potential profile is plotted for the rigid and smoothed cylindrical models. At $\varepsilon=0$ the wires were aligned along the incident beam. When a misalignment was introduced into the system, the scattering potential showed a spatial distortion of $\varepsilon=20.2\pm0.2$ Å. In real space, the smoothed potential results in a sharper decay in q-space thereby fitting the q^{-4} scattering behaviour. Further analysis has shown that the smoothed cylinder derivation was an approximate solution to the scattering potential. It is suggested that the correct scattering potential depends on the nanowire's alignment with respect to the scattering vector. The form factor is expressed by $F(q)\propto J_1(qR\sin\delta)/(qR\sin\delta)\sin(qL\cos\delta)/(qL\cos\delta)$ where δ represents the zenith angle between the **q** and **L** vectors, see Appendix section 8.1.2 for derivation. However this fit was beyond the scope of this thesis.

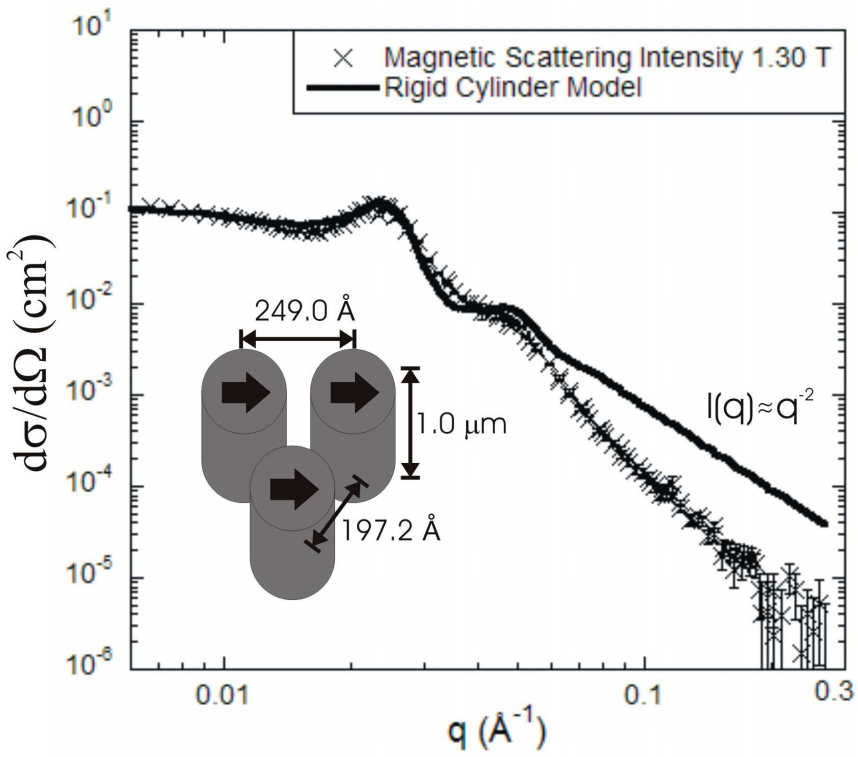

Figure 6.10: The self-assembled cobalt nanowire's magnetic intensity at the in-plane field of 1.3 T fitted to the rigid cylinder model. The inset shows the spatial parameters for a set of aligned cylinders.

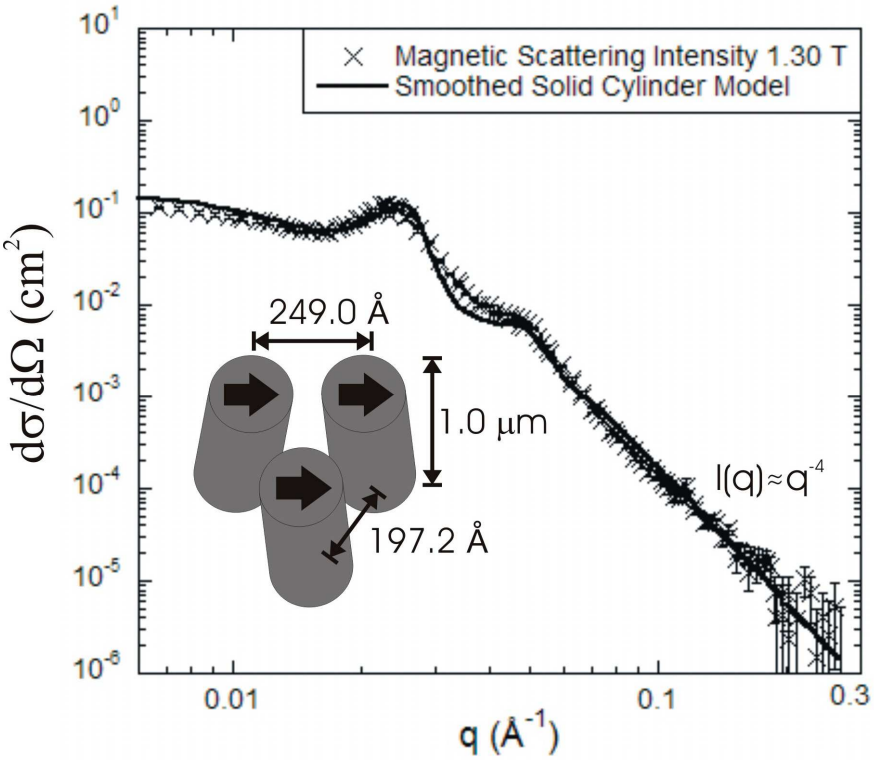

Figure 6.11: The self-assembled cobalt nanowire's magnetic scattering intensity at the in-plane field of 1.3 T fitted to smoothed cylindrical model. The inset shows the spatial parameters for a set of misaligned cylinders.

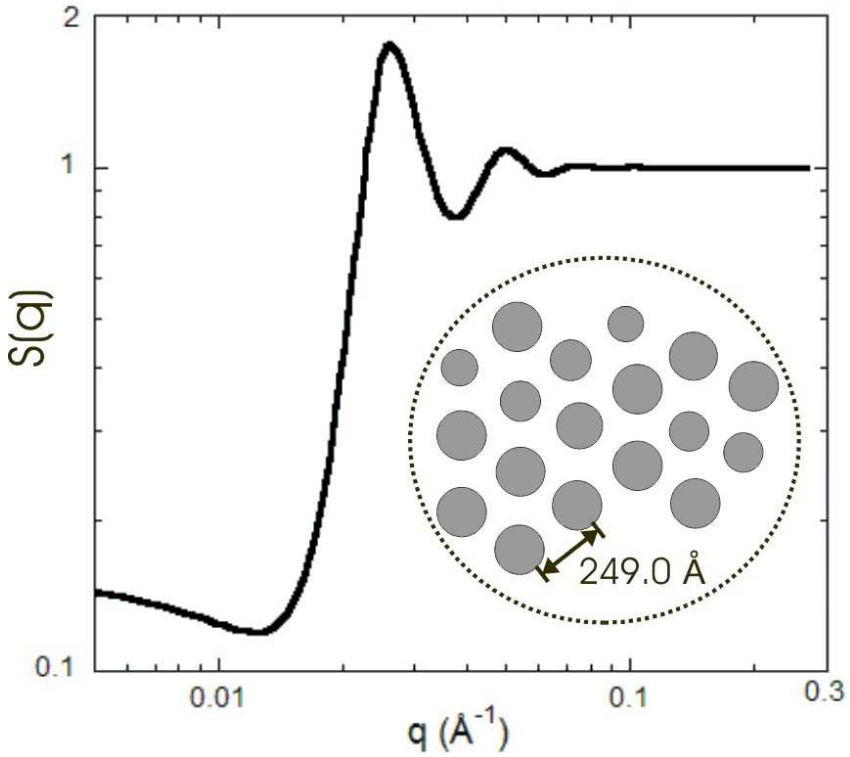

Figure 6.12: The Percus-Yevick Structure factor for smoothed cylinder model. The inset shows the spatial image of the hexagonal ordered cobalt nanowires.

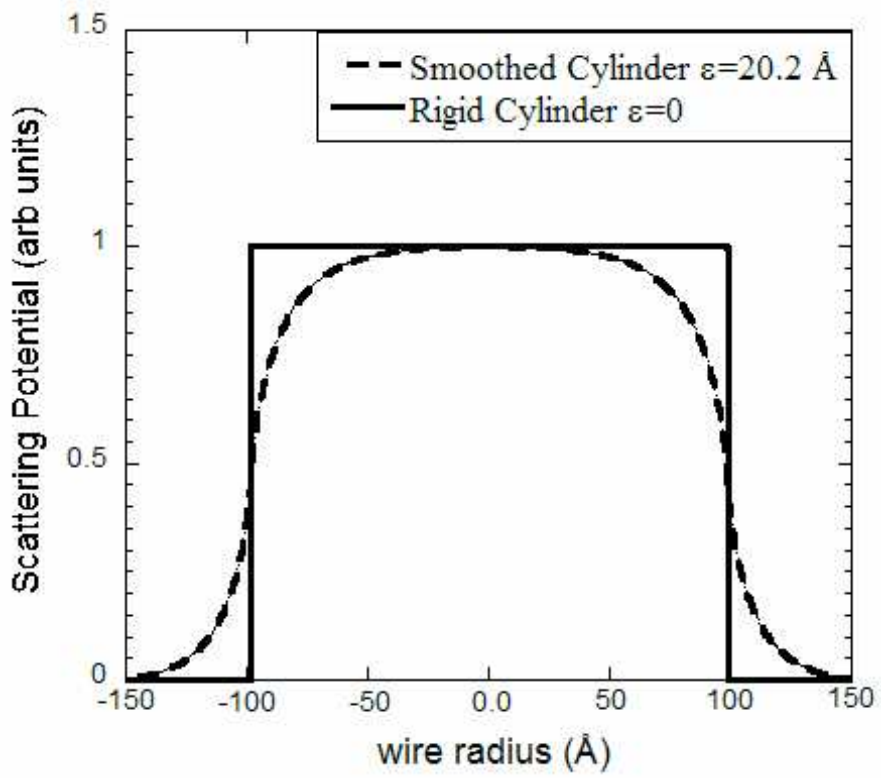

Figure 6.13: The cobalt nanowire's magnetic potential profile as a function of radius for the rigid and smoothed scattering models.

The magnetic offset $I_M(q,H=0)$ at remanence was fitted to the smoothed cylinder model. When the NLS parameters were set in the *Free* state, the cylinder model did not converge to a reasonable set of output parameters. The wire diameter and inter-wire separation were found to be many times the size of their physical counterparts. Due to the offset's weak scattering features, the parameter fit could not determine a convergent solution. The scattering data was refitted using a simplified routine where the input parameters were switched to the *Fixed* state, see Table 6.2. The spatial parameters were assigned to values obtained from the saturated fit. Figure 6.14 shows the magnetic scattering offset fitted to the smoothed cylinder model. The form factor was comparable to the saturated case indicating that the wire's magnetic structure remains unchanged at smaller fields. The interference peak located at q=0.02 $Å^{-1}$ was modelled using the P-Y structure factor. This peak position matches the in-plane value at saturation though the remanent intensity was much weaker than expected. It was known that the nanowire's exhibit a strong out of plane shape anisotropy, hence the remanent peak intensity should be comparable to the saturated case. It was unclear on what caused this reduction in magnetic scattering contrast.

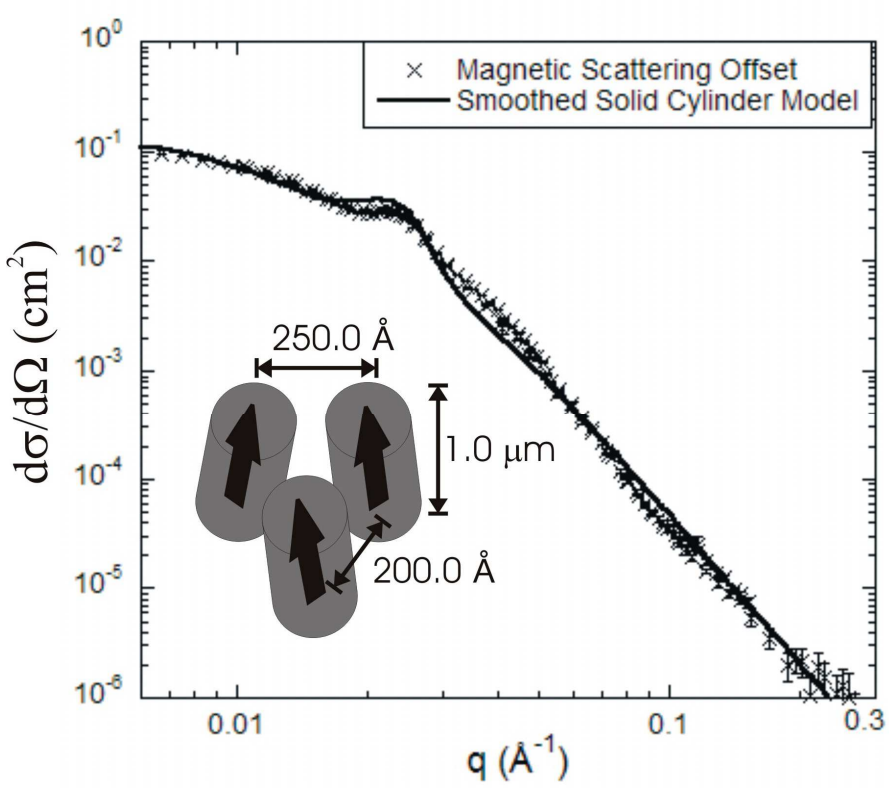

Figure 6.14: The self-assembled cobalt nanowire's magnetic scattering intensity at remanence fitted to the smoothed cylindrical model. The inset depicts the magnetic spatial parameters for a trio of misaligned cylinders.

Scattering Function	***Description***	***Parameter***	***NLS Switch***	***Value***
S(q)	Wire Separation	d	*Free*	249.0 ±1.0 Å
	Packing density	ρ	*Free*	$(4.93\pm0.03)\times10^{-8}$ Å^{-3}
	γ-Distribution Width	σ_d	*Fixed*	40.0 Å
F(q)	Magnetic Contrast	$\Delta\eta^M$	*Free*	$(1.20\pm0.01)\times10^{-5}$ Å^{-2}
	Radius	R	*Free*	98.6 ± 0.3 Å
	γ-Distribution Width	σ_R	*Free*	17.5 ± 0.2 Å
	Decay Constant	ε	*Free*	20.2 ± 0.2 Å
	Closeness of Fit	χ^2	---	3.00

Table 6.1: The cobalt nanowire 1.3 T fit parameters for the structure factor S(q) and form factor F(q).

Scattering Function	***Description***	***Parameter***	***NLS Switch***	***Value***
S(q)	Wire Separation	d	*Fixed*	250.0 Å
	Packing density	ρ	*Fixed*	4.00×10^{-8} Å^{-3}
	γ-Distribution Width	σ_d	*Fixed*	40.0 Å
F(q)	Magnetic Contrast	$\Delta\eta^M$	*Fixed*	3.21×10^{-5} Å^{-2}
	Radius	R	*Fixed*	100.0 Å
	γ-Distribution Width	σ_R	*Fixed*	31.0 Å
	Decay Constant	ε	*Fixed*	19.8 Å
	Closeness of Fit	χ^2	---	---

Table 6.2: The cobalt nanowire remanent fit parameters for the structure factor S(q) and form factor F(q).

The cobalt nanowire's nuclear scattering intensity was extracted by averaging the foreground intensity along the q_x-axis. Since the applied magnetic field saturated the sample along the q_x-axis, there were no magnetic scattering components contained within the nuclear scattering intensity. Figure 6.15 shows the smoothed cylinder model fitted to the nuclear scattering data. The cylinder model shows partial agreement with a closeness of fit χ^2=24.0. Table 6.3 shows the output parameters for the form factor and structure factor functions. The solid cylinder form factor gives an average diameter of 196.0 ±0.4Å with a gamma-Shultz size distribution of 25%. The nanowires's physical structure consists of a cobalt core embedded in an Al matrix, see Figure 6.16. The Al matrix has a weak nuclear scattering contrast, hence the solid cylinder model was a reasonable approximation to the scattering form factor. The Percus-Yevick structure factor gives a pair separation distance of 292.4±0.3Å. The nuclear scattering peak was slightly broader than its magnetic counterpart. This distortion in peak intensity was attributed to the nuclear background scattering from the instrument's electromagnet. In the unpolarised foreground measurement, the nanowire's nuclear scattering intensity cannot be fully separated from the background scattering components.

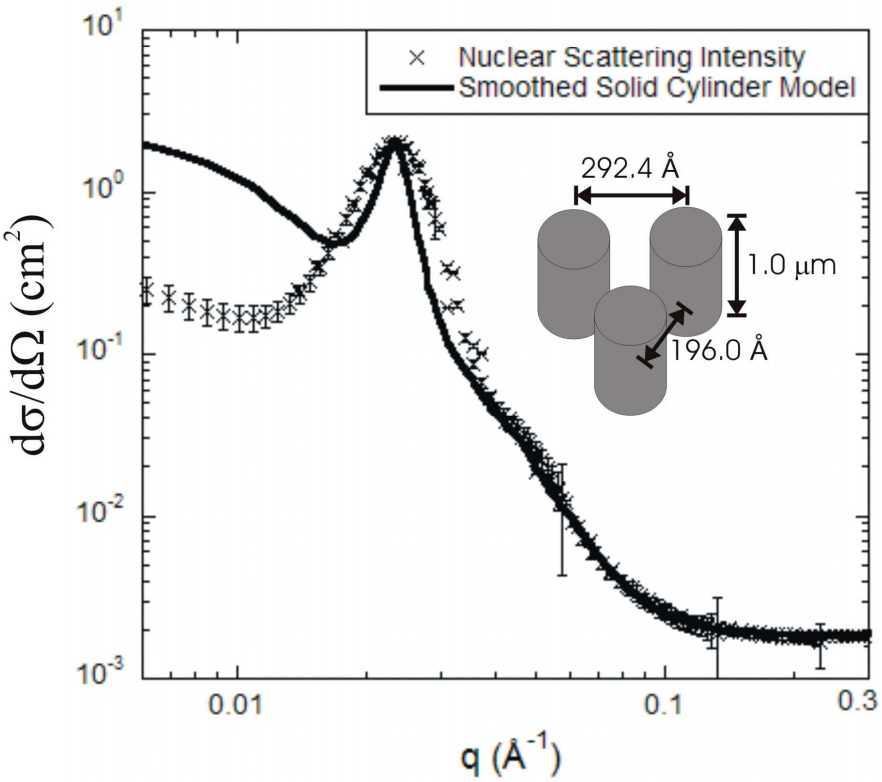

Figure 6.15: The self-assembled cobalt nanowire nuclear scattering intensity fitted to smoothed cylindrical model.

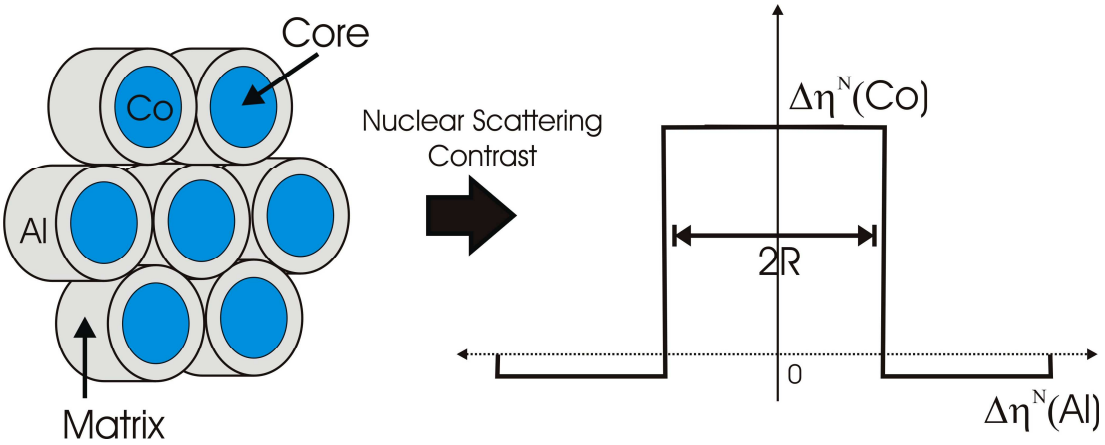

Figure 6.16: The schematic shows the cobalt nanowire's chemical composition and corresponding nuclear scattering contrast. The Al matrix has a weak nuclear scattering length density, hence the core contrast is much larger than the matrix component where $\Delta\eta^N(Co) >> \Delta\eta^N(Al)$.

Scattering Function	***Description***	***Parameter***	***NLS Switch***	***Value***
S(q)	Wire Separation	d	*Free*	292.4 ±0.3 Å
	Packing density	ρ	*Free*	$(3.83\pm0.01)\times10^{-6}$ Å^{-3}
	γ-Distribution Width	σ_d	*Fixed*	40.0 Å
F(q)	Magnetic Contrast	$\Delta\eta^N$	*Free*	$(3.64\pm0.01)\times10^{-4}$ Å^{-2}
	Radius	R	*Fixed*	98.0 ± 0.3 Å
	γ-Distribution Width	σ_R	*Free*	25.0 Å
	Decay Constant	ε	*Free*	37.6 Å
	Closeness of Fit	χ^2	---	24.0

Table 6.3: The cobalt nanowire nuclear scattering fit parameters for the structure factor S(q) and form factor F(q).

6.4.5 Summary

The characterisation technique of unpolarised SANS was used to investigate magnetic and nuclear scattering structure of self-assembled cobalt nanwires. The SANS experiment measured the foreground diffraction pattern at an in-plane saturation field of 1.3 T. The magnetic diffraction pattern at saturation was extracted by subtracting off the nuclear scattering components. It was observed that the magnetic diffraction pattern was highly anisotropic about the scattering plane where the in-plane magnetisation was aligned along the field direction. The magnetic scattering intensity exhibited an amorphous interference peak characteristic of the wire's short-range magnetic order. The nuclear scattering intensity was extracted from the foreground measurement at saturation. The nuclear diffraction pattern was isotropic with the scattering plane. The nuclear scattering intensity showed similar scattering features with respect to the magnetic measurements. The magnetic and nuclear scattering intensities were modelled using the smoothed cylindrical scattering potential. The nanowire's magnetic and nuclear length scales were similar with respect to wire diameter, size distribution and smoothing parameter.

6.5 Conclusion

In this chapter, unpolarised SANS studies were successful in measuring the nanowire's spatial parameters such as wire diameter, inter-wire separation and scattering contrast. For the magnetic length scale, these parameters can be used to determine the sample's areal density and local magnetisation. These properties are important for gauging a sample's potential use as magnetic recording media. The corresponding set of physical parameters, obtained from the nuclear scattering intensity, is useful for characterising the nanowire's chemical composition. For cobalt nanowires this type of measurement is not particularly useful. However, if the sample was alloyed with another element such as platinum then the nuclear scattering contrast could be used to spatially correlate the nanowire's chemical composition. The cylinder model used in this chapter provided an accurate approximation to the nanowire's scattering physics. However, the scattering model was derived using a phenomenological approach, which failed to give an adequate description of the magnetic smoothing effect. Further work is required on deriving the correct magnetic form factor function from first principles.

Chapter 7

Magnetic SANS Simulations

7.1 Introduction

In previous chapters, the local magnetisation of recording media grains and self-assembled nanowires was investigated by using the characterisation technique of small angle neutron scattering (SANS). The diffraction pattern from the magnetised sample was modelled using an analytic scattering function. The magnetic scattering from the discrete object, for example a single recording grain, was represented by the spherical or cylindrical form factor. The interference scattering between grains was simulated using an amorphous structure factor derived from the Percus-Yevick solution for hard spheres. The analytic scattering model was successful in approximating the grain's magnetic spatial parameters such as the grain diameter and scattering contrast. However the analytical scattering function, derived in reciprocal space, represents an ideal snapshot of the grain's local magnetisation. For example the form factor was modelled using a spherical object where in reality the recording grain takes the form of an irregular shaped object. Further insight into the grain's magnetic structure was achieved by simulating the sample's magnetisation map in Cartesian space. Figure 7.1 outlines how a micromagnetic map can be used to extract the sample's magnetic scattering structure. In the following sections, the micromagnetic method was used to study the local magnetic structure of self-assembled nanowires (Chapter 6) and longitudinal magnetic recording media (Chapter 4).

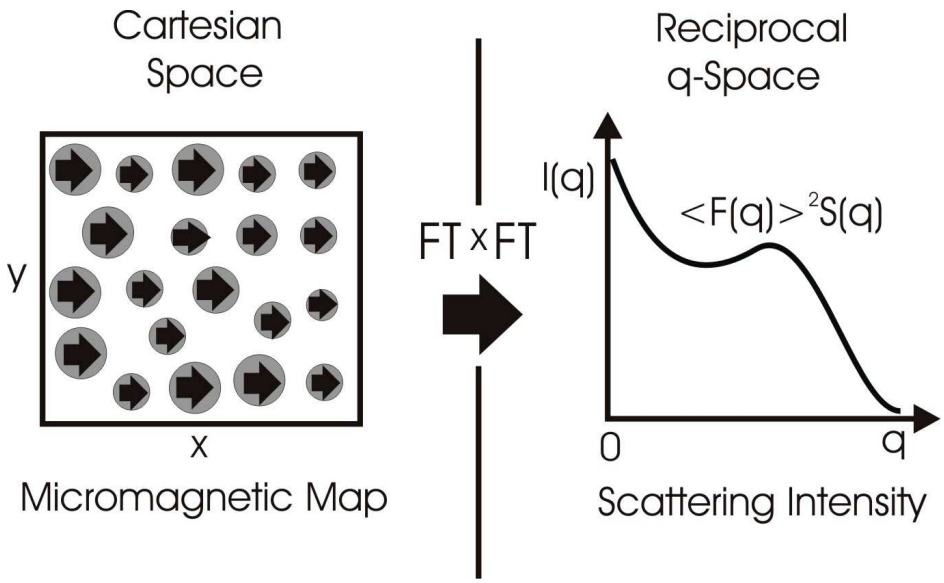

Figure 7.1: The micromangetic map of an ensemble of magnetised grains in two-dimensional Cartesian space. The scattering amplitude is calculated via a Fourier transform (FT) of the micromagnetic map. The scattering intensity by definition is the square of the magnetic scattering amplitude.

7.2 Micromagnetic Method

The sample's local magnetic structure can be represented by a vector array of discrete dipole moments. At the remanent state (H=0), the dipole moments exist in the ground state where each moment aligns along the easy axis of magnetisation. With the application of a strong magnetic field, the moments will minimise their total energy by aligning along the field direction. The moment's response at the remanent or saturated state is described by the micromagnetic method. The total energy of the ith dipole moment $\mathbf{m}_i$ at zero temperature is defined by,

$$E_i = -\mathbf{m}_i \bullet \mathbf{H}_{\mathbf{Zeeman}} - \mathbf{m}_i \bullet \left(\sum_{ij} \frac{-3\mathbf{r}_{ij}(\mathbf{m}_j \bullet \mathbf{r}_{ij})}{r_{ij}^{5}} + \frac{\mathbf{m}_j}{r_{ij}^{3}} \right) + K \sin^2 \phi - J \sum_{ij} \mathbf{m}_i \bullet \mathbf{m}_j . \quad (7.1)$$

The first term represents the moment's Zeeman energy where $\mathbf{H}_{Zeeman}$ is the applied magnetic field. The second term describes the magnetostatic energy resulting from the ith dipole moment interacting with the ensemble's dipolar field. These magnetostatic interactions are linked to the sample's magnetic bulk properties that include domain formation and shape anisotropy. The third term expresses the moment's uniaxial magneto-crystalline anisotropy energy. The angle ϕ defines the direction of the ith moment with respect the crystal's easy axis of magnetisation where K is the anisotropy energy constant. The final term describes the exchange energy between pairs of moments where *J* is the exchange constant.

In magnetic recording media, equation 7.1 describes the energetic terms of the recording grain under coherent rotation. In reality extrinsic properties such as lattice geometry and impurity atoms can damp the spin wave motion. In this case the granular Hamiltonian was approximated using perturbation theory where the magnetic damping energy was small compared to the ground state energy. For most bulk materials this type of calculation was impractical due to the complex nature of the multi-bodied problem. The micromagnetic problem was simplified by using the semi-empirical differential equation known as the Landau-Lifshitz-Gilbert equation (LLG) [114],

$$\frac{d\mathbf{m}_i(t)}{dt} = -\gamma \mathbf{m}_i \times \mathbf{H}_{\mathbf{eff}} - \alpha \frac{\gamma}{m_s} \mathbf{m}_i \times (\mathbf{m}_i \times \mathbf{H}_{\mathbf{eff}}) . \quad (7.2)$$

The LLG equation describes the behaviour of the time dependent moment vector, $\mathbf{m}_i(t)$, immersed in an effective field $\mathbf{H}_{eff}$.

The effective field $\mathbf{H}_{eff}$ is a superposition of magnetostatic, exchange, crystalline anisotropy and Zeeman fields. The leading term of the LLG equation represents the coherent precession of the ith dipole moment. The constant γ defines the moment's gyromagnetic ratio. The second term models the damping effects from the ensemble. The empirical constant α relates to the strength of the damping force. Conventionally the α-constant of a magnetic substance is determined by the characterisation technique of Ferromagnetic Resonance (FMR). The program known as OOMMF [115] illustrates the micromagnetic simulation by solving the LLG equation for a trio of in-plane magnetised discs. The micromagnetic grid was mapped onto the disc trio where the effective field of a single moment was defined by $\mathbf{H}_{eff}=\mathbf{H}_{Zeeman}+\mathbf{H}_{dipolar}+\mathbf{H}_{aniso}+\mathbf{H}_{exe}$. Before the Zeeman field was applied, the disc's easy axis of magnetisation was randomly oriented in-plane. The simulated magnetic hysteresis plot is illustrated in Figure 7.2. The total moment was normalised to its saturation value. The insets show the micomagnetic map at the remanent and saturated states.

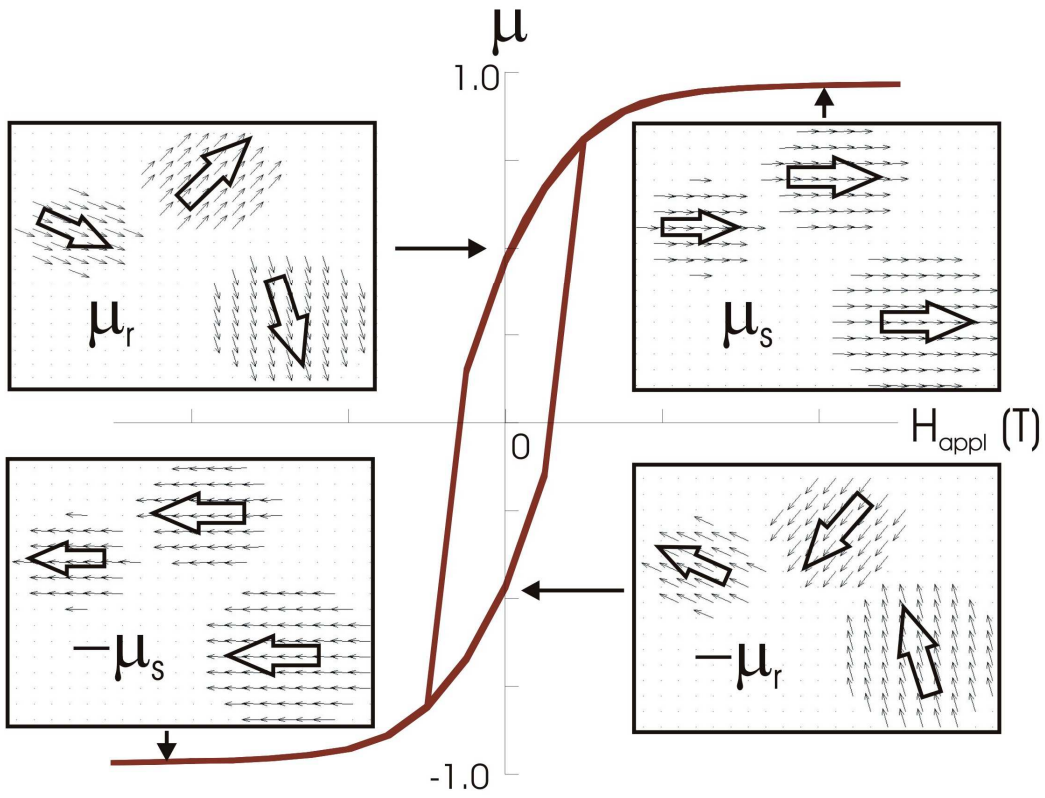

Figure 7.2: The in-plane magnetic hysteresis loop for a trio of magnetised grains is determined by using micromagnetic simulations. The insets show the total normalised moment at the remanent and saturation states. The simulations are performed using the NIST software known as OOMMF.

7.2.1 OOMMF Simulations

The micromagnetic simulations were performed by the NIST software package, Object Oriented Micromagnetic Framework (OOMMF) [115]. The OOMMF package is a graphically based micromagnetic solver that can solve the Gilbert equation for a three-dimensional rectangular grid holding three-dimensional spins. The OOMMF computational engine is based on the C++\TCL programming language. The engine is built around a series of programs known as OOMMF blocks. Each block performs a specific task within the simulation such as defining the rectangular mesh or assigning spin energies. To set-up a micromagnetic simulation, a script file was composed from the required OOMMF blocks listed in Table 7.1. The script file was read into the OOMMF solver which than runs the series of blocks. The simulation performs all calculations in SI units. In this chapter the grain's spatial dimensions were quoted in units of Angstroms.

OOMMF Block	***Description***
Specify Oxs_*ImageAtlas*	Sets up the micromagnetic grid
Specify Oxs_*RectangularMesh*	Sets up a rectangular mesh
Specify Oxs_*UniaxialAnisotropy*	Input uniaxial anisotropy field
Specify_Oxs_*UniformExchange*	Input uniform exchange field
Specify_Oxs_*Demag*	Input demagnetisation field
Specify_Oxs_*Uzeeman*	Input an applied magnetic field
Specify Oxs_*EulerEvolve*	Differential equation solver
Specify Oxs_*TimeDriver*	Time counter

Table 7.1: The micromagnetic simulation is programmed using the TCL script file. The OOMMF compiler runs the script file by executing the above list of block commands.

The first step in the OOMMF simulation was to construct a moment map of the granular ensemble. The OOMMF software sets up the moment grid using the *atlas* block. The box *atlas* defines the grid within a predefined region of space. The size and shape of the ensemble were defined by a subset of regions defined within the box. The geometric shapes such as discs were used to assign moment distribution to the micromagnetic grid. The image *atlas* defines the moment grid via the input of a two-dimensional image of the granular ensemble. The colour image simultaneously defines the magnitude and boundary conditions of each grain. For example an ensemble of ferromagnetic grains embedded in a non-magnetic matrix was represented by an image of black discs superimposed onto a white background. The colour black was assigned a non-zero magnetisation while the white region was set to a zero value. The advantage of the image *atlas* is that one can avoid any complex grid calculations for a large granular ensemble. The image *atlas* becomes especially useful for generating the moment map of magnetic recording media where the ensemble consists of polydisperse magnetic grains. The input image was generated using the programming code known as ROOT [116]. The image file was read into the block, Specify Oxs_*ImageAtlas*, see Figure 7.3. The image was defined within a rectangular box, which was scaled to the dimensions of the ensemble. The following block, Specify Oxs_*RectangularMesh*, sets up the simulations rectangular mesh.

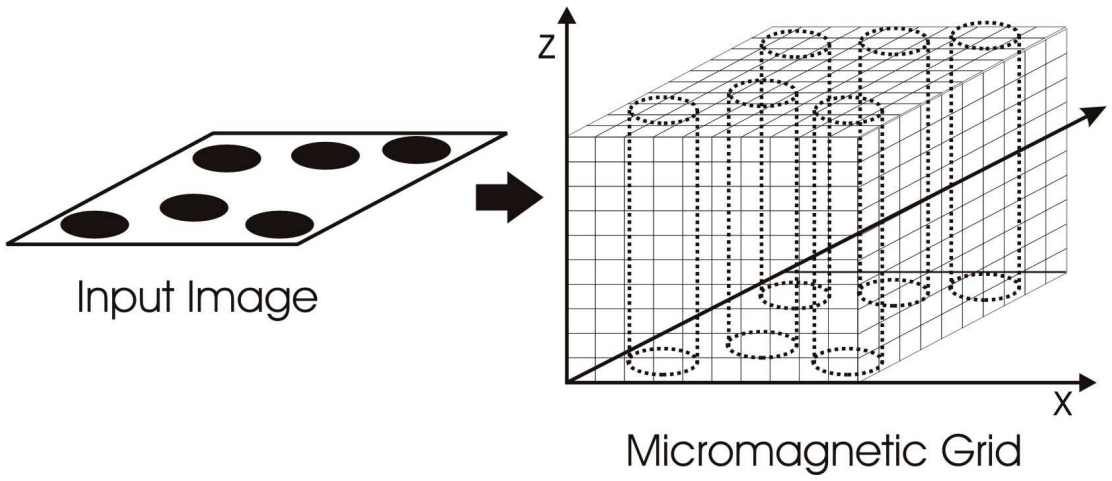

Figure 7.3: The two-dimensional image of an ensemble of magnetic particles embedded in non-magnetic matrix. The OOMMF function Oxs_*ImageAtlas* translates the image map to the micromagnetic grid.

The recording grain was composed of a cobalt-based alloy while the nanowires consisted of bulk cobalt. For either sample the crystalline phase was hexagonal closed packed (hcp). Hence the moment exhibits a uniaxial magneto-crystalline anisotropy. The block, Specify Oxs_*UniaxialAnisotropy*, assigns each dipole moment a magneto-crystalline anisotropy field. The magnitude of the anisotropy field was set by the energy constant K. The direction of the easy axis was defined using an array of unit vectors which was inputted via a data file. The OOMMF exchange calculation was performed using the block Oxs_*UniformExchange*. This block assumes that the exchange force was uniform for its immediate neighbours.

The block, Specify Oxs_*Demag*, calculates the sample's demagnetisation field. The OOMMF calculation assumes that the demagnetisation field was uniform within each cell. The Zeeman field was simulated using the block, Specify Oxs_*Uzeeman*. The field can be set to any direction within the defined atlas. Figure 7.4 shows a two-dimensional micromagnetic grid for a trio of magnetic particles. The OOMMF simulation assigns each magnetic particle with exchange, anisotropy, demagnetisation and Zeeman energies. The LLG equation was solved using the Euler method. The calculations were performed using the block Specify *EulerEvolve*. The final block, Specify Oxs_TimeDriver, controls the time evolution of the simulator. The OOMMF simulation exits when the LLG equation satisfies the following condition $dm_{ave}/dt<<1$.

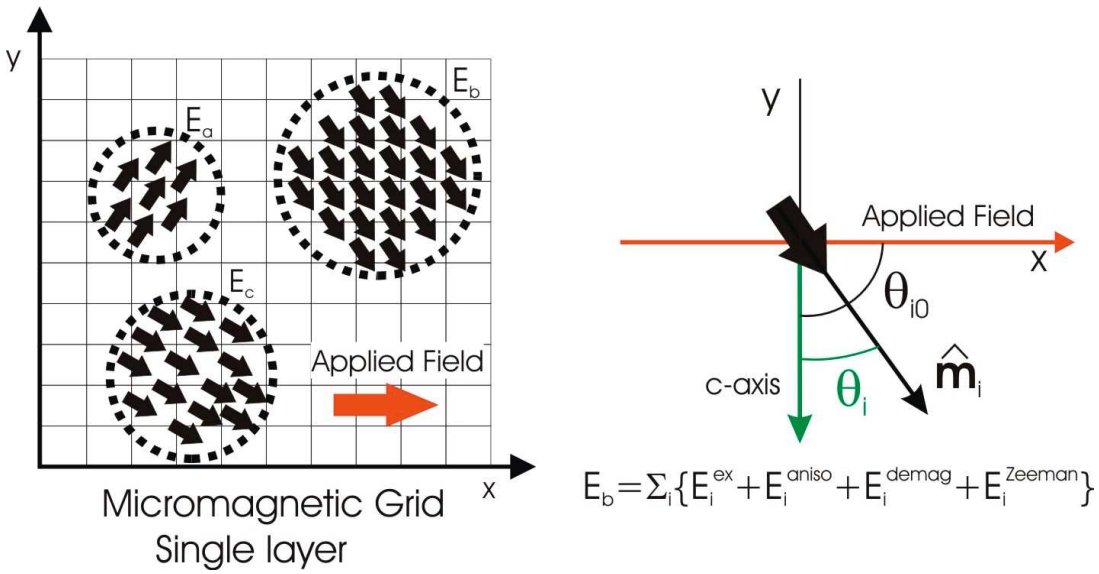

Figure 7.4: The micromagnetic grid shows a trio of in-plane saturated ferromagnetic particles defined by the total energies E_a, E_b and E_c. The particle energy at E_b is a superposition of the ith exchange, anisotropy, demagnetisation and Zeeman energies.

7.2.2 Magnetic Scattering Theory

The micromagnetic simulation generates a moment map of the magnetised body. The moment map contains information on the sample's magnetic grain size and moment orientation. The simulations were compared to the magnetic SANS data by calculating the moment map's Discrete Fourier Transform (DFT) [112]. The magnetic scattering intensity is expressed by,

$$I(\mathbf{q}) = \left|\mathbf{m}(q)[\hat{\mathbf{q}}(\hat{\mathbf{q}} \bullet \hat{\mathbf{m}}) - \hat{\mathbf{m}}]\right|^2 / V . \qquad (7.3)$$

The total moment vector over all reciprocal space is expressed by the Fourier Transform $\mathbf{m}(\mathbf{q})=|\int \mathbf{m}(\mathbf{r})\exp(i\mathbf{q}\bullet(\mathbf{r}-\mathbf{r}_i)d\mathbf{r}|$ where $\mathbf{r}_i$ defines the position of the ith unit cell. In real space the total moment is expressed by the $\mathbf{m}(\mathbf{r})=\Sigma_i\delta(\mathbf{r}-\mathbf{r}_i)\mathbf{m}_i$ where $\mathbf{m}_i$ defines the ith moment per unit cell. The unit vectors $\hat{\mathbf{m}}$ and $\hat{\mathbf{q}}$ define the direction of the total moment and momentum transfer argument respectively. The scattering intensity, equation 7.3 is normalised to the sample volume V. Figure 7.5 illustrates the moment map and the scattering intensity within the Cartesian and reciprocal space respectively.

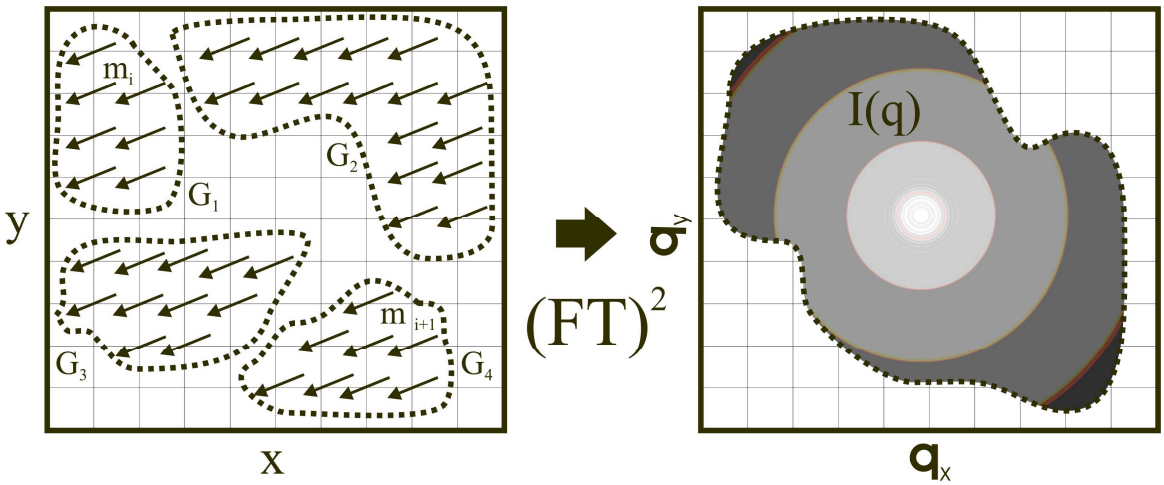

Figure 7.5: The two-dimensional magnetic moment map where m_i, m_{i+1} define the sample's spin moment for the ith unit cell. The sample's total moment in reciprocal space is extracted by calculating the Fourier Transform (FT) of the moment map. The square of the transform is proportional to the diffraction pattern I(q).

7.3 Ferromagnetic Nanowires

In the previous chapter, the unpolarised SANS measurement was used to characterise the local magnetic structure of ferromagnetic nanowires. The sample's foreground measurement was performed in the in-plane geometry where the moments were saturated at an in-plane field of 1.3 T. The SANS diffraction pattern exhibited a strong magnetic scattering anisotropy. This scattering feature was used to separate the nanowire's magnetic scattering intensity from the background scattering components. The smoothed cylindrical form factor was used to fit the magnetic SANS data. It was observed that the magnetic dimensions agreed with the TEM measurements. However a proper physical interpretation of the analytic model was lacking with respect to the smoothed scattering potential. In the following section, micromagnetic simulations were used to study the local magnetisation of ferromagnetic nanowires. In addition these simulations were used to test the reliability of the analytic scattering model devised in Chapter 6.

7.3.1 Simulations

In the micromagnetic simulation, the nanowire's local magnetic structure was modelled using a hexagonal ensemble of cylinders of radius R, length L and separation distance D. The cylinder's radius was set to 100.0 Å with a size distribution of 14%. The approximate length of the cylinder was 10,000 Å. The wire's average separation distance was of order D=240.0 Å. The ROOT compiler was used to input these spatial parameters into a program that generated a polydisperse system of discs. The size distribution was calculated by the Gamma-Schultz distribution function. The output image consisted of red coloured discs populated onto a white background. The red disc represents the ferromagnetic nanowire while the white background defines the sample's non-magnetic AAO matrix. The image was read into the image atlas and mapped onto a rectangular grid. The box dimension was defined by $1550.0 \times 1550.0 \times 10$ Å^3 with a mesh grid of 10 Å per cell. In this case the length dimension was truncated to save time during the simulation run. Truncation of the length component will undoubtedly reduce the nanowire's shape anisotropy and change the orientation of the easy axis. However in the OOMMF simulation the anisotropy constant was independent on the sample's length dimension. This restricts these simulations to in-plane scattering features.

The OOMMF program maps the three-dimensional magnetisation field to red coloured images. The AAO matrix, coloured white, was assigned a zero magnetisation value. The red discs were assigned the saturation magnetisation of metallic cobalt at room temperature $M_s=1.4\times10^6$ A/m [117]. As shown in Chapter 6, the nanowires exhibit a strong out of plane shape anisotropy. This magnetic property was modelled by mapping a perpendicular anisotropy field to micromagnetic grid. The strength of the anisotropy field was approximately 1.0 T. The exchange constant for cobalt at room temperature was set at approximately 3.0×10^{-11} J/m^3 [117]. The Zeeman field was set to the in-plane saturation field of 2.0 T. This Zeeman field value was adequate to align the nanowire's magnetic moments in-plane.

The Euler method for solving differential equations was determined by the block Specify EulerEvolve. The gyromagnetic ratio was set to $\gamma=2.21\text{x}10^5$ m/A•s. The damping constant α for most magnetic materials was much less than one. In order for the OOMMF simulation to reach convergence in a reasonable time period, the α constant was set to unity. The solver exits the simulation when the ensemble reaches a specified tolerance $dm_{ave}/dt<0.01$. The micromagnetic simulations were performed at the remanent and in-plane saturation states. Figure 7.6 depicts the moment maps for the respective magnetised states. The simulations were repeated for an additional fifteen snap shots where each ensemble was randomly shuffled. This procedure was intended to simulate thermal averaging of the ensemble.

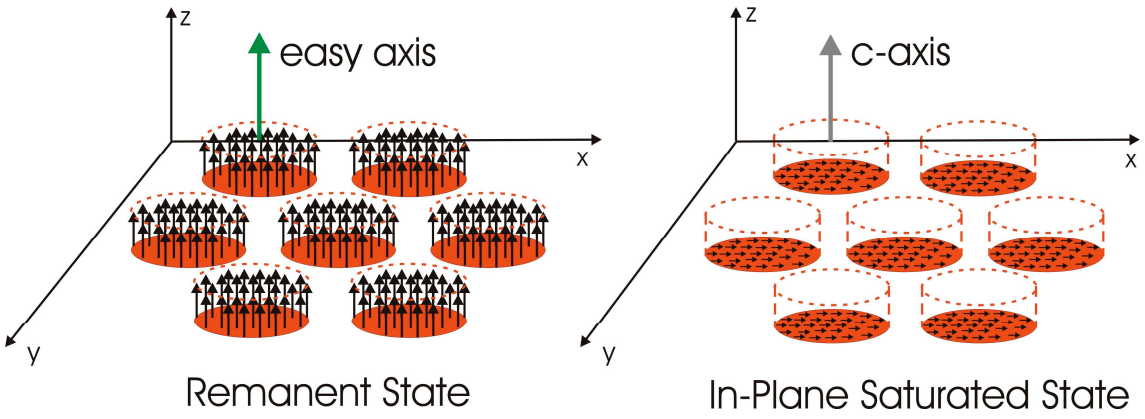

Figure 7.6: The ferromagnetic nanowire moment map for the out of plane remanent and in-plane saturated states. The easy axis of magnetisation and c-axis are oriented along the nanowire's longitudinal axis.

7.3.2 Results and Discussions

The local magnetism of ferromagnetic nanowires was investigated for the remanent state. The magnetic structure was represented by a three-dimensional array of cylindrical objects. The OOMMF program maps an ensemble of spins onto an image plane of red discs where the magnetic moments line parallel to the longitudinal axis. The left-plot of Figure 7.7 shows a snap shot of the hexagonal ensemble within the two-dimensional spatial plane. The out of plane magnetisation was defined by $M_z=V^{-1}\Sigma m_{iz}$ where m_{iz} represents the ith moment on the micromagnetic grid. The set of fifteen OOMMF simulations was converted to q-space via the Fourier transform expressed by equation 7.3. The diffraction pattern was extracted by superimposing the fifteen Fourier images. The right-plot of Figure 7.7 shows the simulated diffraction pattern about the scattering plane. The isotropic diffraction pattern results from magnetic moments aligned perpendicular to the sample plane. It was observed that the diffraction pattern does not exhibit a continuous structure factor ring as shown in the nanowire SANS measurements. In order to simulate the continuous diffraction ring, one must apply azimuthal rotational disorder to the spatial grid.

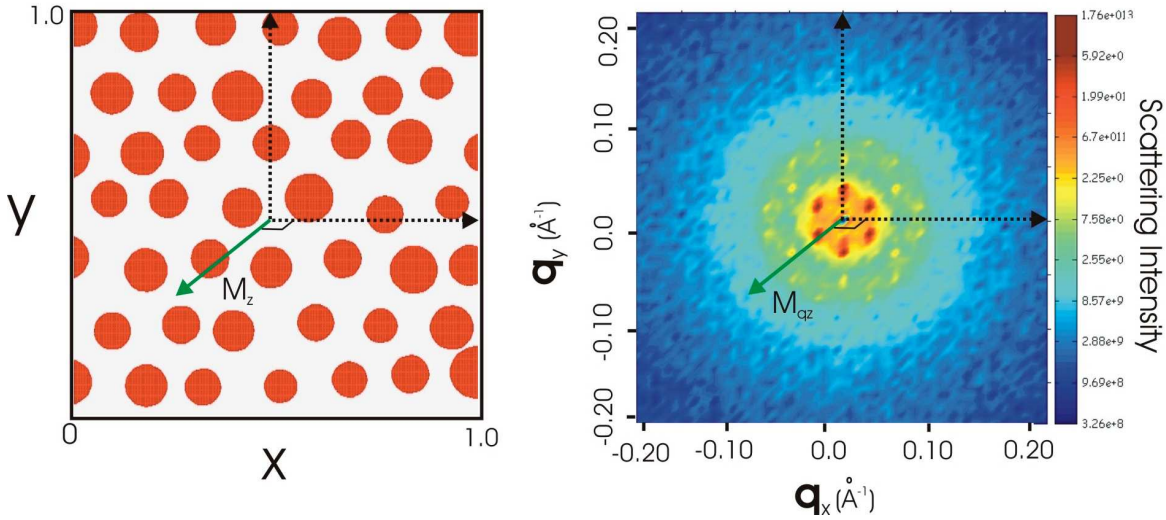

Figure 7.7: The two-dimensional moment map for an ensemble of ferromagnetic discs at remanence. The operation FT×FT of the magnetic moment map gives the SANS diffraction pattern.

The in-plane saturated state was investigated for the hexagonal ensemble of cylinders. The left-plot of Figure 7.8 shows the moment map at the saturated state. The inset magnifies the moment distribution for a pair of cylinders. Within the image plane, the field vectors **M** and $\mathbf{H}_{Zeeman}$ lie collinear. This was due to the strong in-plane magnetic field whereby the magnetic moments were forced to align along the field direction. The OOMMF solver extracts a further set of fifteen moment maps at saturation. The simulated SANS diffraction pattern was highly anisotropy about the scattering plane. This behaviour is highlighted in Figure 7.9 where the azimuthal intensity is calculated for the q range $0.006 Å^{-1} < q < 0.27 Å^{-1}$.

The magnetic scattering intensity was extracted from the SANS simulations, see Figure 7.10. The simulations were compared to the D11 SANS measurements at 1.3 T. The SANS simulation was successful in replicating the position and shape of the amorphous structure factor. However at high q the magnetic scattering deviates from the q^{-4} scattering intensity. In Chapter 6, this scattering feature was corrected by applying a smoothing function to the cylindrical scattering potential. The origin of this smoothing was possibly linked to the wire's misalignment. If this was the case, then the current magnetisation map must account for nanowire's length dimension and its degree of misalignment.

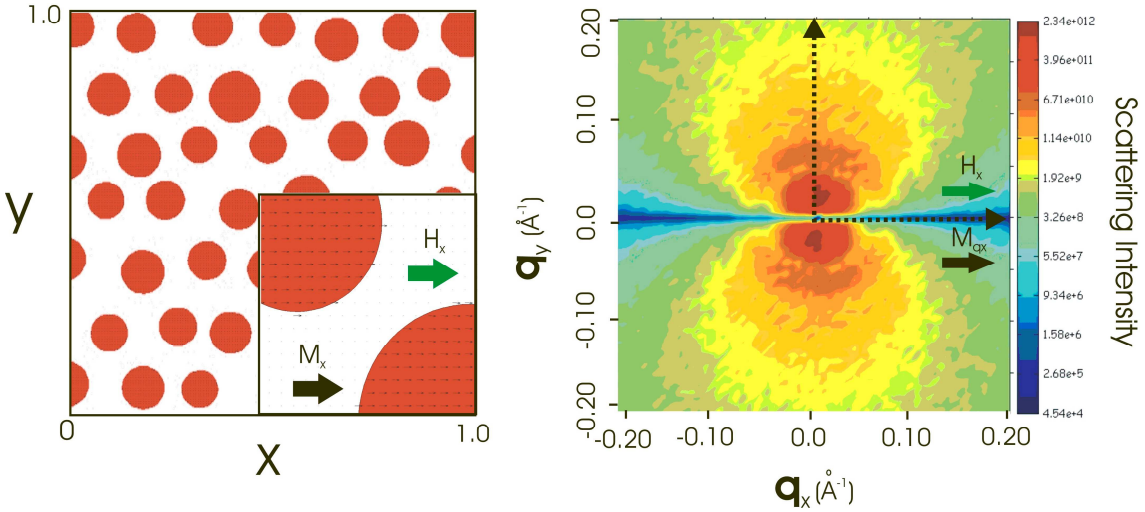

Figure 7.8: The two-dimensional moment map for an ensemble of ferromagnetic discs at the saturated state. The operation FT×FT of the magnetic moment map gives the SANS diffraction pattern.

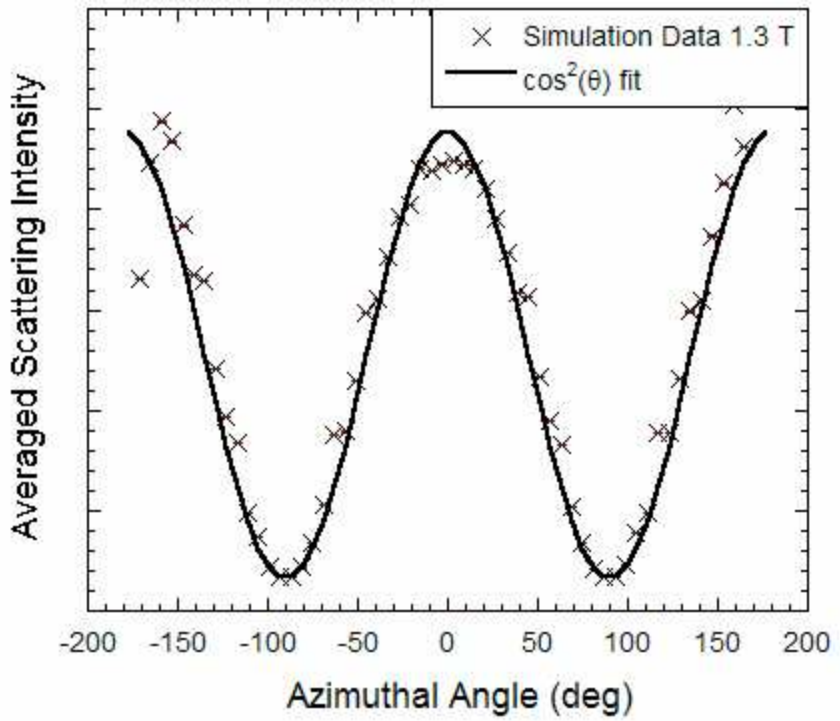

Figure 7.9: The azimuthal magnetic scattering intensity for the anisotropic diffraction pattern calculated over the q range 0.006 $Å^{-1}$<q<0.27 $Å^{-1}$.

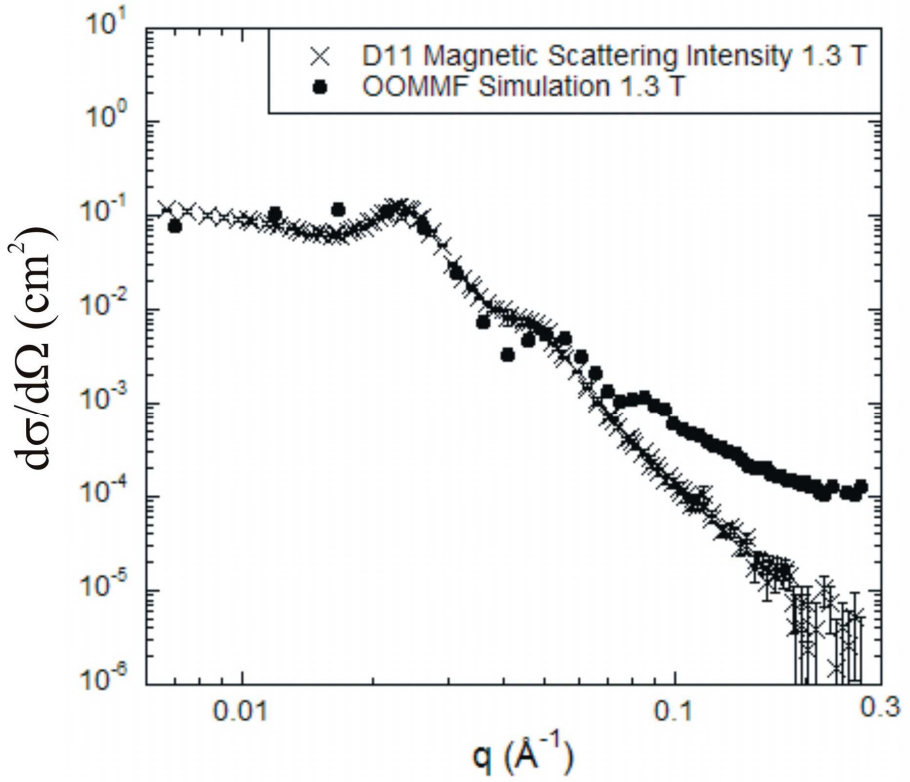

Figure 7.10: The anisotropic magnetic scattering intensity is extracted from OOMMF simulations for the q-range of 0.006 $Å^{-1}$<q<0.27 $Å^{-1}$. The simulation is compared to the D11 SANS measurement at the in-plane field of 1.3 T.

7.3.3 Summary

In this section the nanowires's magnetic structure was modelled using the micromagnetic program OOMMF. At the remanent field the SANS diffraction pattern was isotropic about the scattering plane with a sharply defined structure factor peak. The diffraction pattern was simulated for the in-plane saturated state. The magnetic scattering intensity exhibited a highly anisotropic diffraction pattern about the scattering plane. This effect was a consequence of the strong applied magnetic field that forced all dipole moments to align along the x-axis. The magnetic scattering intensity was compared to the measured scattering data at 1.3 T. The simulation reproduced the shape and position of the structure factor. However at high q the form factor intensity deviated from the scattering data by a factor of q^{-2}. The magnetic scattering model failed to give an adequate explanation for the q^{-4} intensity decay. These micromagnetic simulations were successful in reproducing the nanowire's magnetic scattering features such as moment orientation and interference effects. However the scattering model was over simplified to account for the magnetic smoothing effects encountered in the D11 SANS measurements.

7.4 Longitudinal Magnetic Recording Media

In chapter four the in-plane magnetisation of longitudinal recording media was investigated using magnetic SANS measurements. At the in-plane saturation field of 2.2 T the magnetic diffraction pattern was highly anisotropic about the scattering plane. The magnetic scattering intensity was modelled using a spherical core-shell structure. The cobalt-enriched core was characterised as a high anisotropic ferromagnet while the chromium-enriched shell was identified as a soft ferromagnet. When the applied field was decreased, the magnetic scattering anisotropy varied as a function of q. This scattering property was termed the $ANCOS^2$ phase shift. The phase shift was attributed to the recording grain's magnetic properties such as the magneto-crystalline anisotropy field. In the following section, the micromagnetic simulation was used to model the in-plane saturated state of longitudinal recording media. In the latter half, low field studies were used to study the underlying scattering physics of the $ANCOS^2$ phase shift.

7.4.1 Simulations

The ensemble of longitudinal recording grains was modelled using an array of ferromagnetic cores embedded within a soft ferromagnetic matrix. The physical dimensions of the granular core were determined from magnetic SANS measurements. The average core size was of the order of 53.0 Å with a grain size distribution of 30%. An array of highly disordered cylindrical objects was used to model the microstructure of the ferromagnetic cores, see left plot of Figure 7.11. The program ROOT generates a two-dimensional image of fifty cylindrical objects with a normalised core size of 0.03 and a gamma-Shultz distribution of 30%. The ferromagnetic cores were mapped out using the OOMMF software package. The micromagnetic grid was defined within a rectangular box of dimension 600×600×30 $Å^3$ with a mesh size of 3.0 Å per cell. The image atlas scales the ROOT image to the grid dimensions.

The ferromagnetic cores, coloured red, were assigned a saturation magnetisation of 5×10^5 J/T. It was determined in Chapter four that the recording grain possessed a strong in-plane remanent magnetisation. This magnetic property was modelled by mapping an in-plane uniaxial anisotropy field to each ferromagnetic core where the bulk anisotropy energy density was set to $K_U \approx 300\times10^3$ J/m^3 [118]. This value was typical for longitudinal recording media composed of the alloy CoCrPtB. The cores were saturated along the x-axis by setting the Zeeman field to $\mathbf{H}_{Zeeman}=(2.0\,T, 0, 0)$.

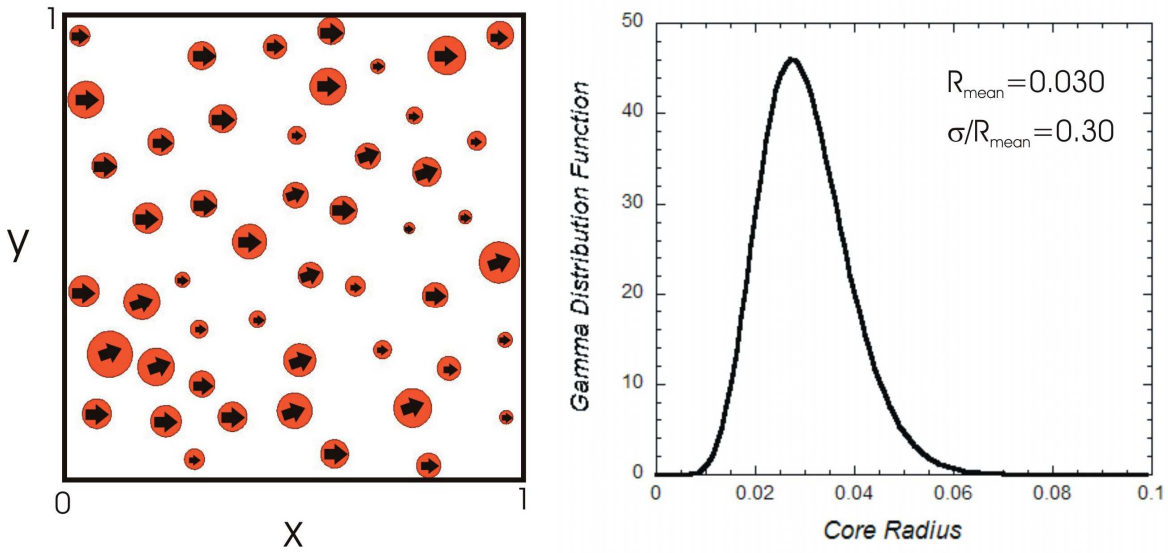

Figure 7.11: The two-dimensional moment map for an ensemble of ferromagnetic cores embedded within a non-magnetic matrix. The core radii are generated using a gamma-Shultz size distribution function.

The soft ferromagnetic matrix was modelled by populating the vector space with paramagnetic moments. In this simulation, the paramagnetic approximation was only valid for small increments in applied field where the soft ferromagnetic response was linear as a function of field. The paramagnetic model neglects thermal effects by assuming the T=0 state. At zero field, the ferromagnetic cores induce a small magnetic moment within the paramagnetic matrix. When an external magnetic field was applied to the matrix, the magnetisation linearly increases as a function of the Zeeman field. The matrix magnetisation is related linearly to the total magnetic field,

$$\mathbf{M}_{matrix}=\chi_{par}(\mathbf{H}_{Zeeman}+\mathbf{H}_{matrix}) \tag{7.4}$$

where χ_{par} is the paramagnetic susceptibility, $\mathbf{H}_{Zeeman}$ is the applied magnetic field and $\mathbf{H}_{matrix}$ is the induced magnetic vector field within the matrix. The field $\mathbf{H}_{matrix}$ was calculated using a monopole system of magnetic charges [119]. The magnetisation for the core $\mathbf{M}_{core}$ and matrix $\mathbf{M}_{matrix}$ components were combined into a three-dimensional magnetisation map shown in Figure 7.12.

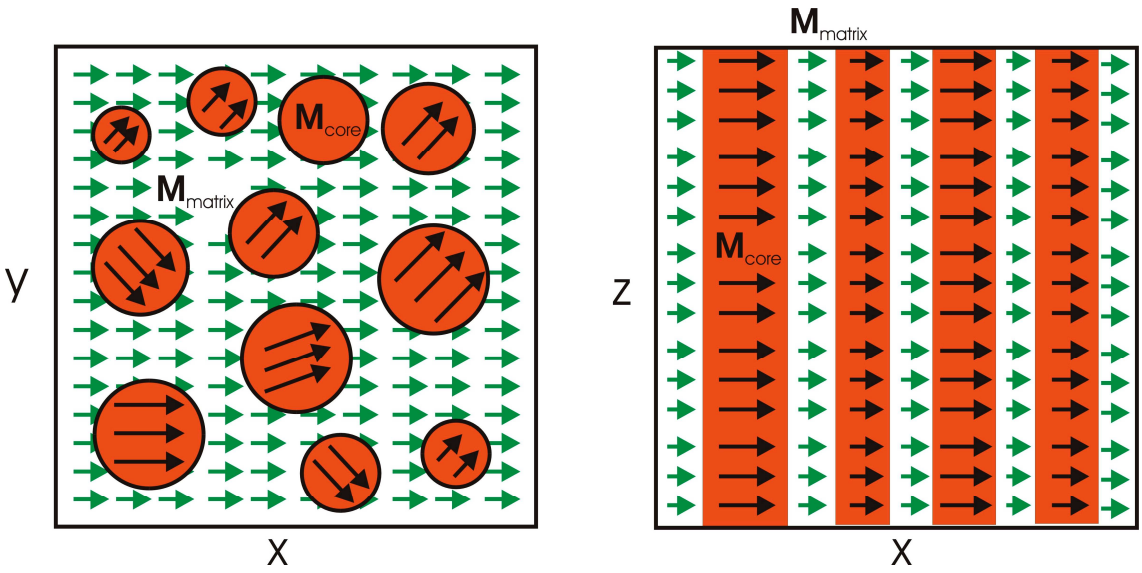

Figure 7.12: The x-y and x-z magnetisation map for the ferromagnetic core (black arrow) and paramagnetic matrix (green arrow).

7.4.2 Results and Discussion

The core and matrix magnetisation components as a function of field were extracted using micromagnetic simulations. The left plot of Figure 7.13 depicts the two-dimensional image of the magnetisation map at the in-plane saturation field of H_x=2.0 T. The core magnetisation $\mathbf{M}_{core}$ was partially aligned along the magnetic field direction. These moment deviations where attributed to the core's strong in-plane anisotropy field. The exchange and demagnetisation fields had little influence on the saturation magnetisation. The paramagnetic magnetisation $\mathbf{M}_{matrix}$ was fully saturated within the spatial plane. Simulations showed that the core magnetisation was less than the matrix component where $|\mathbf{M}_{core}|<|\mathbf{M}_{matrix}|$. In terms of magnetic scattering, the core contrast was smaller than the matrix value. This result disagrees with the Chapter 4 LMRM measurements where the core's magnetic contrast was larger than the shell (matrix) component. It was most likely that the paramagnetic susceptibility of was incorrectly scaled with respect to the ferromagnetic cores.

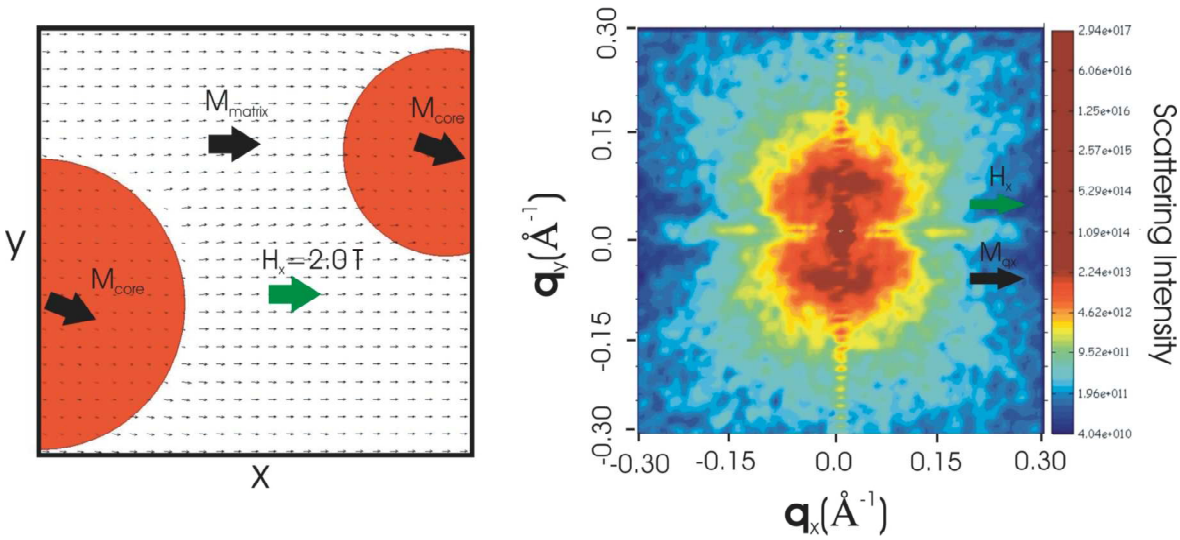

Figure 7.13: The recording grain's two-dimensional magnetisation map for the M_{core} and M_{matrix} components at the in-plane field of 2.0 T. The operation FT×FT of the magnetisation map gives the SANS diffraction pattern.

The magnetic scattering intensity was extracted by calculating the Fourier transform of 15 randomised magnetisation maps. The simulated scattering intensity was calculated by taking the square of the transform. The right-plot of Figure 7.13 shows the magnetic diffraction pattern for the q range 0.02 $Å^{-1}$<q<0.29 $Å^{-1}$. The pattern exhibited pronounced lobes along the y-axis which were characteristic of saturated magnetisation components M_{xi} along the field direction. The diffraction pattern shows yellow diffraction spots along the x-axis. These features originate from the magnetised core's M_{yi} components. The magnetic scattering intensity at the in-plane field of 2.2 T was compared to the simulation results at saturation, see Figure 7.14. At q<0.05 $Å^{-1}$ the scattering intensity shows a plateau which was characteristic of the form factor function near q=0. The simulations shows a peak at q=0.08 $Å^{-1}$ which corresponds to the form factor's core component. The scattering model partially fits the SANS measurements, however there was a slight shift towards smaller q values. This q-shift was due to an incorrectly scaled micromagnetic grid. The simulations can be re-scaled to fit a smaller box size, which would shift the scattering intensity in line with the measured data.

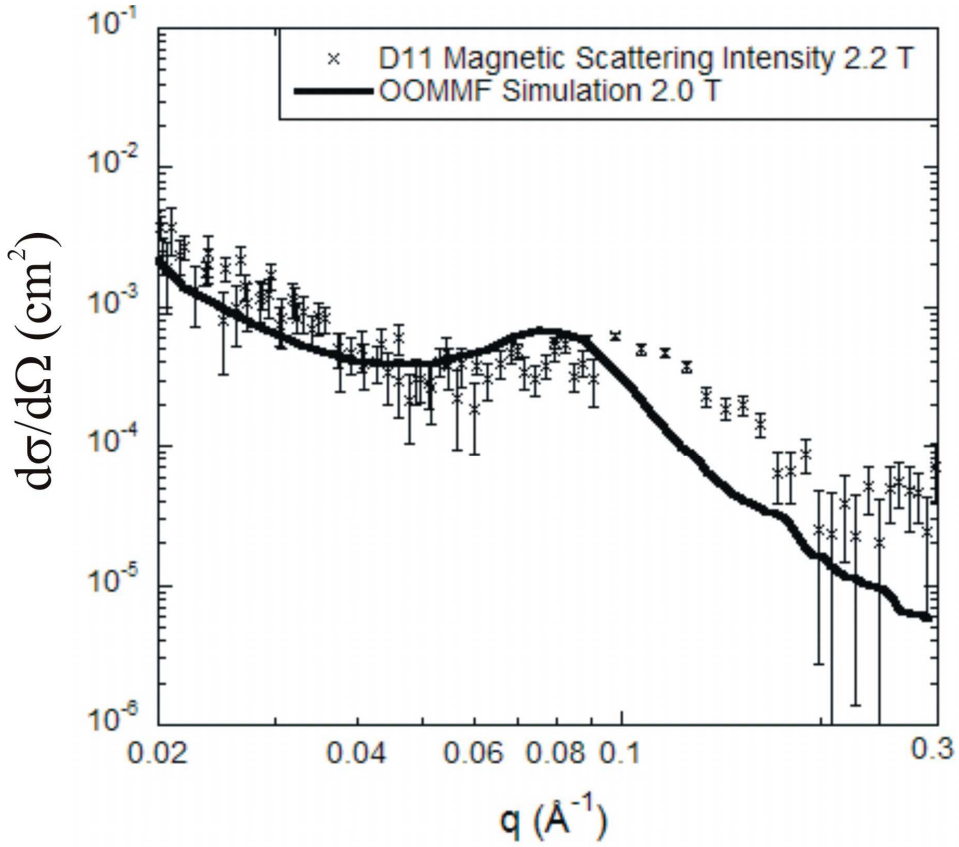

Figure 7.14: The simulated magnetic scattering intensity at H_x=2.0 T (—) compared to the D11 measurement at 2.2 T (x).

When the in-plane field was reduced the matrix magnetisation decreased within the x-y plane. The magnetisation response of core and matrix components is plotted in Figure 7.15(a). The core magnetisation was normalised to unity and remains at its remanent state regardless of the field strength. The matrix magnetisation increases linearly with applied field as expected for a paramagnet. The intersection point, known as the matching field, represents a uniform magnetisation state between the core-matrix components. The matching field was analysed by plotting the magnetisation profile across a magnetic grain, see Figure 7.15(b). The core component was represented by the top-hat function.

The ensemble of longitudinal recording grains was simulated for the low field range of $0.0<H_x<1.7$ T. The magnetisation map of a recording grain is depicted in the left-plot of Figure 7.16. Within the scattering plane, a dashed black circle marks out the boundary between the core $\mathbf{M}_{core}$ and matrix $\mathbf{M}_{matrix}$ components. The variation of $\mathbf{M}_y$ across the grain was defined on the colour plot. The right-plot shows the respective diffraction pattern for the q-range $0.02\ Å^{-1}<q<0.29\ Å^{-1}$. The ANCOS^2 program extracted the scattering intensity and phase as shown in Figure 7.17. The phase was linked to the variation between the x and y magnetisation contrast components. The zero phase condition was expressed by $\delta=0\rightarrow\Delta M_x>\Delta M_y$ while the phase shift occurs when $\delta=\pi/2\rightarrow\Delta M_y>\Delta M_x$.

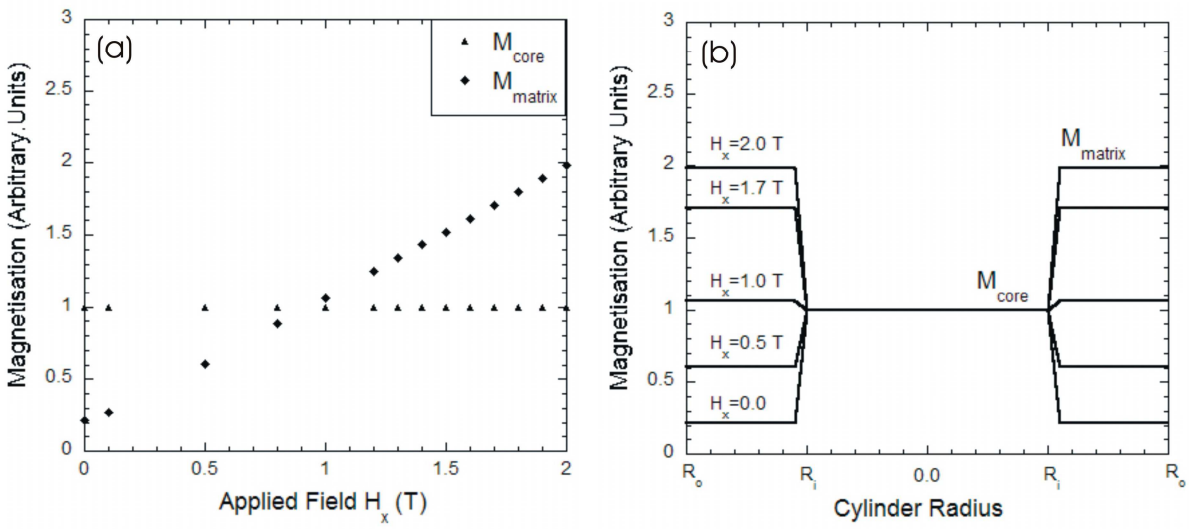

Figure 7.15: The recording grain's core and matrix magnetisation components as a function of (a) in-plane field H_x and (b) outer cylinder radius R_0.

At the in-plane field of 1.7 T the grain's core magnetisation was partially saturated along the field direction. Within the circular boundary, the yellow surface plot gives a variation of $|\Delta\mathbf{M}_y|\approx 0.1$. At the core-matrix boundary the red and blue regions mark out a variation of the order of $|\Delta\mathbf{M}_y|\approx 0.45$. These regions represent a transition from ferromagnetic grain to the paramagnetic matrix. Further out from the core, the variation decays to zero where the applied field has saturated the paramagnetic matrix. The diffraction pattern was anisotropic about the scattering plane though the intensity was slightly distorted along the x-axis. The magnetic scattering intensity exhibits a form factor peak at $q=0.08\,\text{Å}^{-1}$ which compares closely with the SANS simulation at $H_x=2.0$ T. Again this scattering feature originated from the grain's core component. However the simulated scattering exhibits two nodes at $q_1=0.14\text{Å}^{-1}$ and $q_2=0.24\text{Å}^{-1}$. The former node corresponds to the ANCOS^2 phase shift of $\delta_1=90^0$ while the latter q-value represents a shift of $\delta_2=70^0$.

The phase shifts were understood by analysing the grain's magnetic contrast components within the x-y plane. The core and matrix contrast were calculated by $\Delta M_c=|M_c-M_m|$ and $\Delta M_m=|M_m-\langle M\rangle|$ respectively where $\langle M\rangle=1/N\Sigma_i\{M_i\}$ represents the average magnetisation over the ensemble. The core and matrix components were extracted from the magnetisation map of Figure 7.16(a). The core components were $|\Delta\mathbf{M}_x|\approx 0.71$ and $|\Delta\mathbf{M}_y|\approx 0.10$, hence the zero phase condition $|\Delta\mathbf{M}_x|>|\Delta\mathbf{M}_y|$ was satisfied. This contrast variation occurs within the core, hence the zero phase magnetic scattering originates mainly from the grain's ferromagnetic centre. The matrix variation were $|\Delta\mathbf{M}_x|\approx 0.03$ and $|\Delta\mathbf{M}_y|\approx 0.45$ where $|\Delta\mathbf{M}_y|>|\Delta\mathbf{M}_x|$. This condition showed a variation in matrix magnetisation along the y-axis that was responsible for the $\pi/2$ phase shift.

At the field of $H_x=1.4$ T the maximum scattering intensity was oriented along the field direction. The ANCOS^2 phase of $\delta=\pi/2$ now extends over the entire q-range. The core contrasts were $|\Delta\mathbf{M}_x|\approx 0.41$ and $|\Delta\mathbf{M}_y|\approx 0.45$ while the matrix components were $|\Delta\mathbf{M}_x|\approx 0.04$ and $|\Delta\mathbf{M}_y|\approx 0.41$. This shows the core and matrix contrast components have simultaneously satisfied the $\pi/2$ phase condition where $|\Delta\mathbf{M}_y|>|\Delta\mathbf{M}_x|$. The diffraction pattern at $H_x=0.5$ T was highly anisotropy about the scattering plane where the phase has shifted back to zero. When below the matching field, the matrix magnetisation values were much smaller than their respective core components. Hence the core and matrix contrast values will satisfy the zero phase condition $|\Delta\mathbf{M}_x|>|\Delta\mathbf{M}_y|$.

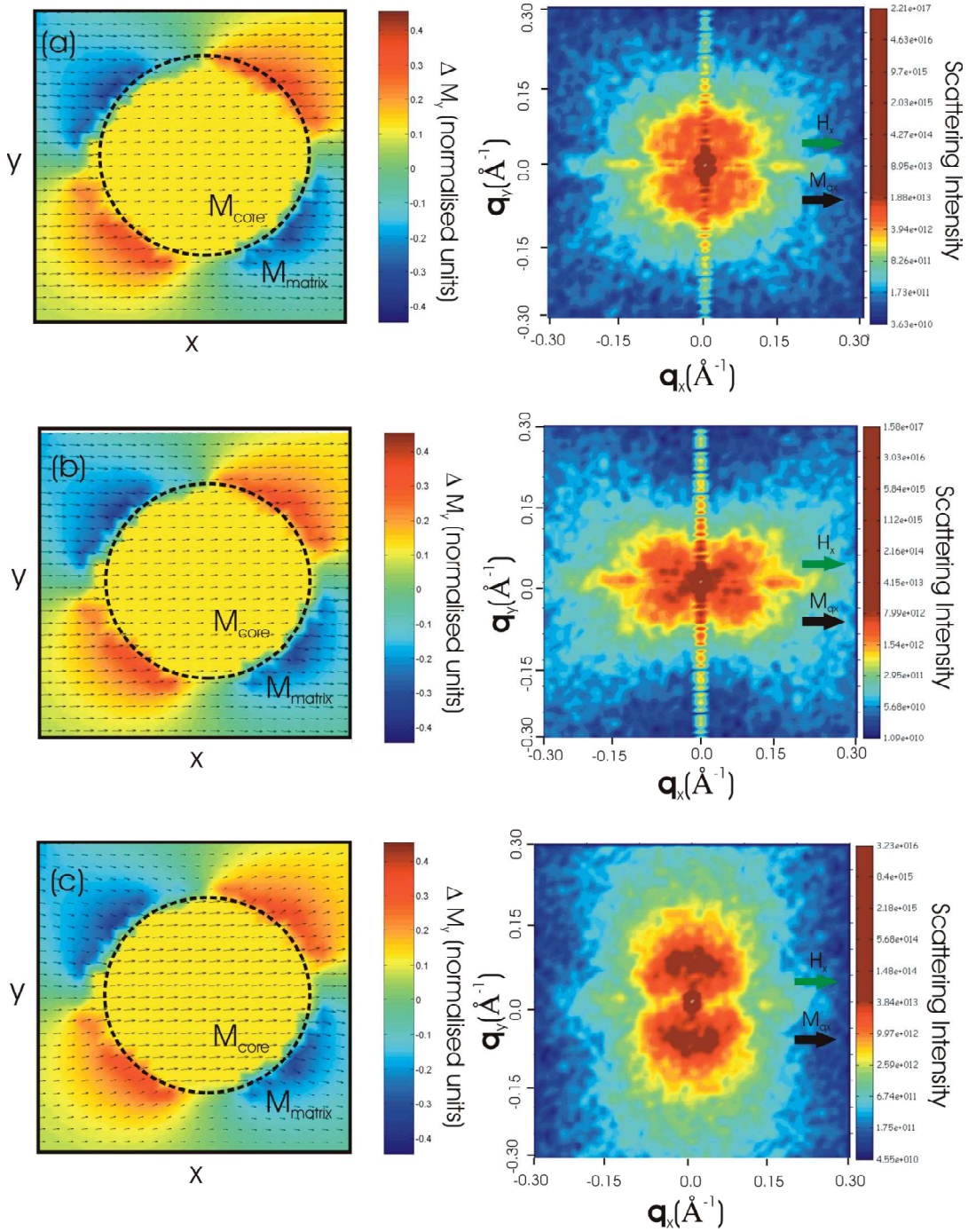

Figure 7.16: The recording grain's magnetisation map is plotted for the in-plane field of (a) 1.7 T,(b) 1.4 T and (c) 0.5 T. The colour countour defines the variation in y-magnetisation across the grain. The magnetic diffraction pattern was calculated for the q-range 0.02 $Å^{-1}$<q<0.29 $Å^{-1}$ at the respective field values.

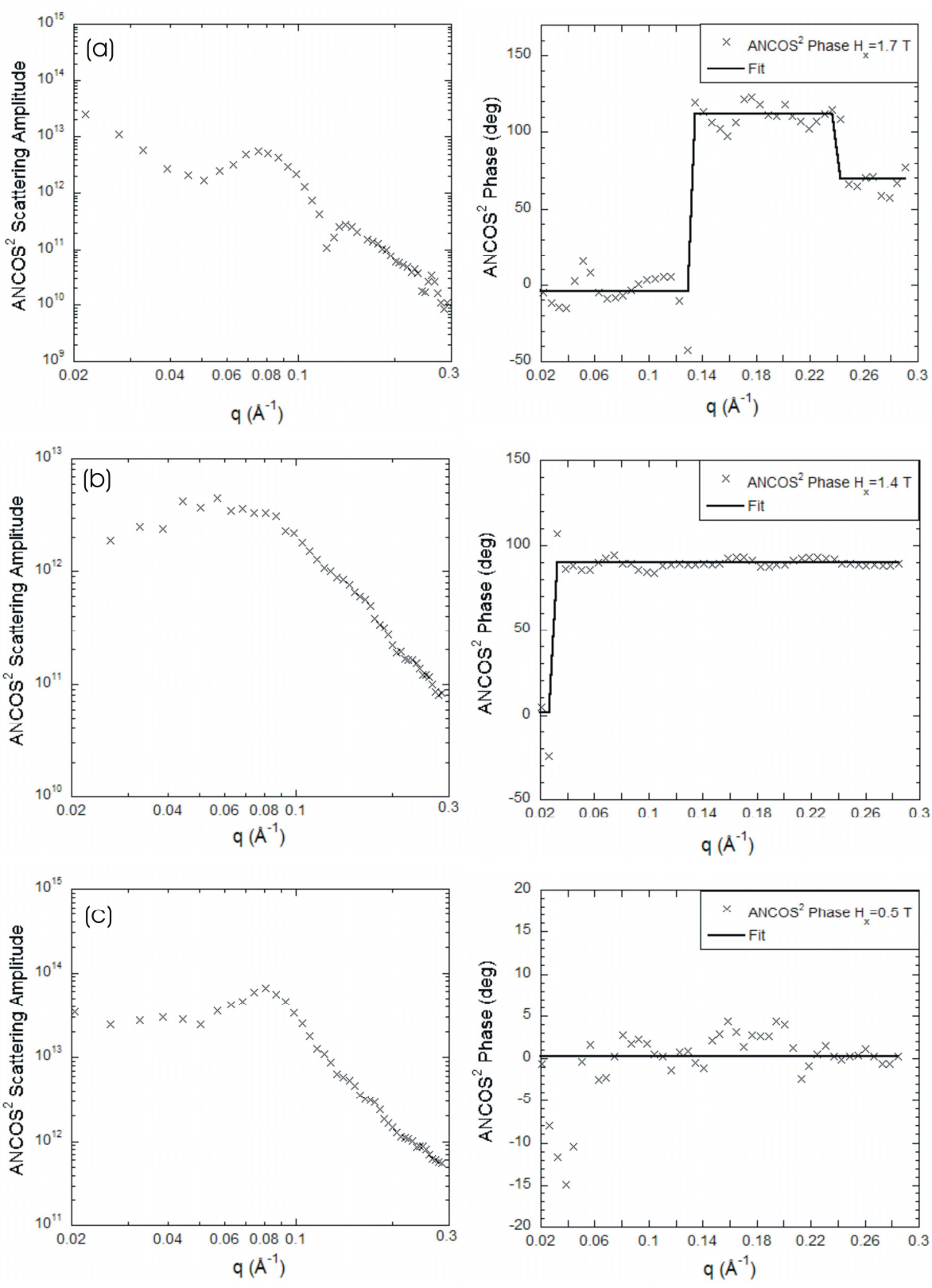

Figure 7.17: The SANS simulation of the ANCOS^2 scattering intensity and phase for the q-range 0.02Å^{-1}<q<0.29Å^{-1} at the in-plane field of (a)1.7 T, (b) 1.4 T and (c) 0.5 T.

7.4.3 Summary

The magnetisation of longitudinal recording media was characterised using micromagnetic simulations. The recording media was composed of a closed packed system of ferromagnetic grains with an average grain size of 106 Å and a size distribution of 30%. The SANS measurements in Chapter 4 determined that the recording grain was composed a hard ferromagnetic core and a soft ferromagnetic matrix. The core component was modelled using a three-dimensional grid of cylindrical objects where each was assigned an in-plane magneto-crystalline anisotropy field. The soft matrix was modelled by using an array of paramagnetic moments.

The core and matrix magnetisation map was extracted for the applied field range of $1.7\,T<H_x\leq 2.0\,T$. The core magnetisation was fully saturated along the field direction though there was a slight moment deviation due to grain's in-plane anisotropy field. The paramagnetic matrix was fully saturated along the field direction. The majority of the core and matrix moments were saturated along x-axis resulting in a highly anisotropic diffraction pattern. The simulated scattering intensity showed moderate agreement with the measured D11 data at 2.2 T.

The core and matrix magnetisation was extracted for the low field range of $0.5\,T<H_x\leq 1.7\,T$. The diffraction pattern at $H_x=1.7\,T$ exhibited anisotropic scattering though the moment orientation was now slightly distorted along the field direction. This intensity distortion corresponded to the $ANCOS^2$ phase shift of $\pi/2$. The phase shift was related to an increase in the matrix contrast components along the y-axis. The diffraction pattern at $H_x=1.4\,T$ exhibited a constant $ANCOS^2$ phase of $\pi/2$ over the entire q-range. In this case the magnetic scattering was dominated from the core and matrix contrast components along the y-axis. The field value at $H_x=0.5\,T$ showed a recovery of zero phase scattering where the scattering originated from core and matrix contrast components along the x-axis.

7.5 Conclusion

In this chapter, we have demonstrated the capabilities of the micromagnetic simulation for investigating the scattering properties of ferromagnetic nanowires and longitudinal recording media. For these simulations the sample's bulk magnetisation was modelled using a three-dimensional micromagnetic grid. The local magnetic structure was represented using an ensemble of cylindrical objects of finite length. The spatial dimensions of these cylinders were obtained through TEM and magnetic SANS measurements. By using the simulation software known as OOMMF, the sample's spatial magnetisation was extracted as a function of applied magnetic field. The SANS measurements were compared to the simulations by calculating the Fourier transform of the micromagnetic grid.

In the first half of the chapter, the micromagnetic method was successful in approximating the nanowire's magnetic scattering intensity at the in-plane saturation field. The simulations were in close support of the magnetic SANS data. This result was important for validating the analytical scattering model derived in Chapter 6. However, the micromagnetic simulations could not fully account for deviations in scattering intensity at high q. It was postulated that this deviation might originate from the nanowire's misorientation within the scattering plane. Future work is required on the current micromagnetic simulation to account for the nanowire's misalignment. This may possibly involve expanding the magnetisation map to multiple layers

In the final section, micromagnetic simulations were successful in studying the magnetic structure of longitudinal recording grains. The recording grain was modelled using a ferromagnetic core and paramagnetic matrix. At the saturation field, the simulations showed moderate agreement with the D11 measurements. However, there were disagreements between the analytic and micromagnetic models. For example at saturation, the local matrix magnetisation was always larger than the core component. This result contradicts the analytic scattering model where the shell magnetisation was always smaller than the ferromagnetic core. For any meaningful comparison between simulation and measurement, the magnetic susceptibility must properly scale the shell magnetisation. The future work involves a detailed analysis of the paramagnetic susceptibility and its agreement with empirical results. In addition further OOMMF simulations are planned to investigate the magnetism of perpendicular recording media such as its recording layer and soft magnetic underlayer.

Chapter 8

Appendices

8.1 The Form Factor

The form factor is a mathematical function in reciprocal space that describes the scattering intensity from a massive target. By definition the form factor is expressed as the Fourier transform of the scattering potential function $\rho(\mathbf{r})$,

$$F(\mathbf{q}) = \int_V \rho(\mathbf{r}) \exp(-i\mathbf{q} \bullet \mathbf{r}) d^3\mathbf{r} \tag{8.1}$$

where the integral is calculated over the target's volume V. The potential function, expressed in real space, contains information on the target's scattering characteristics such as particle size and scattering length density. In the following sections the monodisperse form factor was derived for the spherical and cylindrical geometries.

8.1.1 Sphere

The scattering structure of gases, liquids and amorphous bodies exhibit a high degree of spatial symmetry. In this situation it is adequate to model the scattering structure as a spherical target, see left diagram of Figure 8.1. The spherical scattering potential is defined by the piece-wise function,

$$\rho(r) = \begin{cases} \rho_0 & \text{if } |r| < R \\ 0 & \text{if } |r| > R \end{cases} \tag{8.2}$$

where ρ_0 defines the sphere's uniform scattering potential of a sphere of radius R. The scattering potential defined by equation 8.2 is substituted in the form factor equation,

$$F(q) = \int_0^{2\pi} \int_0^{\pi} \int_0^{R} \rho_0 \exp(-iqr\cos\theta) r^2 dr \sin\theta d\theta d\phi \tag{8.3}$$

Through solving the azimuthal-ϕ and zenith-θ parts of 8.3, the spherical integral is expressed by,

$$F(q) = 4\pi\rho_0 \int_0^{R} r^2 \frac{\sin(qr)}{qr} dr \tag{8.4}$$

The above integral is easily solved using integration by parts. The spherical form factor is given by,

$$F(q) = \frac{4}{3}\pi R^3 \rho_0 \left(3\frac{\sin(qr) - (qR)\cos(qr)}{(qR)^3} \right) \tag{8.5}$$

8.1.2 Cylinder

The scattering structure of elongated particles such as nanopillars and micelles exhibit less spatial symmetry then the case of spherical particles. For this class of materials, the scattering structure is modelled using a cylindrical object with radius R and length L, see right diagram of Figure 8.1. The cylinder is oriented at the angle δ with respect to the scattering vector **q**. The scattering potential is defined using the cylindrical top-hat function,

$$\Pi(\mathrm{r},l)=\begin{cases}\Pi_0 \text{ if } |\,\mathrm{r}\,|<\mathrm{R} \text{ and } -\mathrm{L}/2<l<\mathrm{L}/2\\ 0 \quad \text{if } |\,\mathrm{r}\,|>\mathrm{R} \text{ and } -\mathrm{L}/2<l<\mathrm{L}/2\end{cases} \tag{8.6}$$

where Π_0 represents a uniform scattering potential throughout the cylinder's volume. The cylinder form factor is derived by inserting equation 8.6 into 8.1,

$$\mathrm{F}(\mathrm{q},\delta)=\int_{-\mathrm{L}/2}^{\mathrm{L}/2}\mathrm{d}l\,\exp(-iql\cos\delta)\int_{0}^{\mathrm{R}}\mathrm{r}\mathrm{d}\mathrm{r}\int_{0}^{2\pi}\exp(-i\mathrm{q}\mathrm{r}\cos\phi\sin\delta)\mathrm{d}\phi \tag{8.7}$$

The form factor function is solved by separately transforming the *l* and r-ϕ integrals. The *l*-integral transforms into a sinc function while the r-ϕ integral is solved in terms of a Hankel function transform. The expression of the cylinder form factor is given by

$$\mathrm{F}(\mathrm{q},\delta)=(2\pi\mathrm{R}^2\mathrm{L})\Pi_0\frac{\sin(\mathrm{qL}/2\cos\delta)}{\mathrm{qL}/2\cos\delta}\frac{\mathrm{J}_1(\mathrm{qR}\sin\delta)}{\mathrm{qR}\sin\delta} \tag{8.8}$$

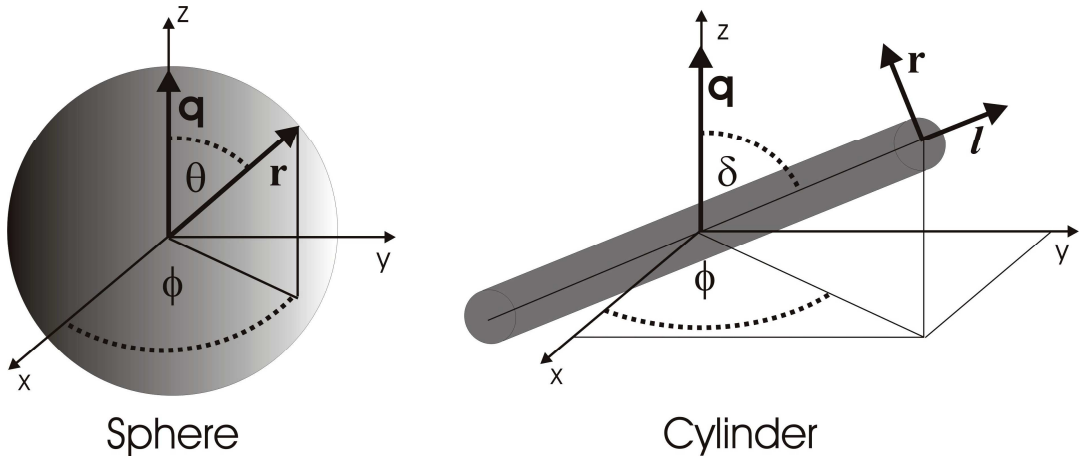

Figure 8.1: The spatial geometry for the spherical and cylindrical form factors.

8.2 The Structure Factor

This appendix derives the structure factor S(q) for an ensemble of monodisperse spheres with bulk density ρ and separation distance *d*. The structure factor determines the linear response of an ensemble of particles interacting via the pair potential $u(\mathbf{r})$ [56] where **r** defines the pair separation variable. In Cartesian space, the system's linear response is described using the total pair correlation function h(**r**). If the system of particles is homogeneous and isotropic than the total correlation function is expressed using the integral equation,

$$h(\mathbf{r}) = c(\mathbf{r}) + \rho \int_V h(|\mathbf{r} - \mathbf{r}'|)c(\mathbf{r}')d\mathbf{r}' \tag{8.9}$$

This equation is defined as the continuous form of the Ornstein-Zernike (O-Z) relation [53,57]. The leading term, known as the direct correlation function, describes the system's short-range pair interactions. The convolution term describes the long-range pair interactions. The concept of the O-Z expression is demonstrated by considering the monatomic liquid system. In Figure 8.1(a) the direct correlation function shows the pair interaction between particles A-B. The total correlation function in Figure 8.1(b) is a superposition of the A-B interaction including the indirect influence of long range interactions A-C and A-D.

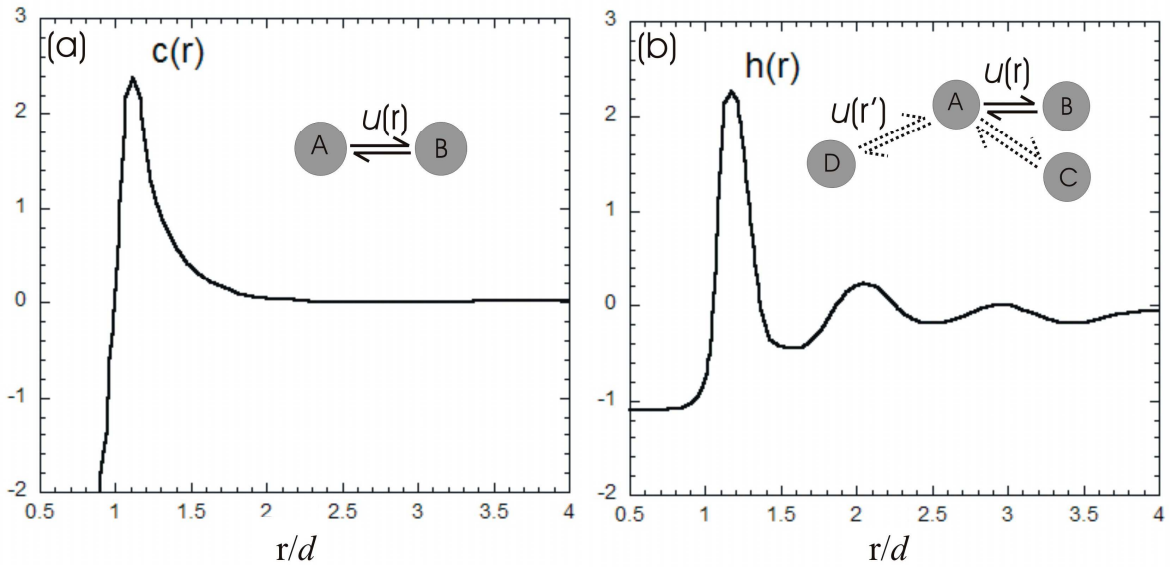

Figure 8.2: The (a) direct correlation function and (b) total correlation function for a monatomic liquid. The inset illustrates the short and long range effects of the pair potential [56].

The direct correlation function is given by the Percus-Yevick (P-Y) approximation [58] for hard spheres first solved by Thiele and Wertheim [59,60],

$$c(\mathbf{r}) = \tau(\mathbf{r})\{\exp(-u(\mathbf{r})/k_B T) - 1\} \tag{8.10}$$

where $\tau(\mathbf{r})$ is the tau pair distribution function. Note the P-Y approximation was derived for the low-density limit, however the theory has proven to be consistent for high-density systems. The total correlation function can be expressed in terms of the tau function,

$$h(\mathbf{r}) = \exp(-u(\mathbf{r})/k_B T)\tau(\mathbf{r}) - 1 \tag{8.11}$$

By substituting equations 8.10 and 8.11 into 8.9 one obtains an integral equation for the tau function,

$$\begin{aligned}\tau(\mathbf{r}) = 1 - \rho\int_V \tau(\mathbf{r}')\{\exp(-u(\mathbf{r})/k_B T) - 1\}d\mathbf{r}' + \\ \rho\int_V \{\exp(u(\mathbf{r})/k_B T)\}\tau(\mathbf{r}-\mathbf{r}')\tau(\mathbf{r}')\{\exp(-u(\mathbf{r})/k_B T) - 1\}d\mathbf{r}'\end{aligned} \tag{8.12}$$

When inserting the hard sphere potential defined by $\{u(r)=\infty,\ r<d;\ u(r)=0,\ r>d\}$ into equation 8.12, the tau function simplifies to the following,

$$\tau(\mathbf{r}) = 1 + \rho\int_{r'<d} \tau(\mathbf{r}')d\mathbf{r}' - \rho\int_{\substack{r'<d \\ |\mathbf{r}-\mathbf{r}'|>d}} \tau(\mathbf{r}')\tau|\mathbf{r}-\mathbf{r}'|d\mathbf{r}' \tag{8.13}$$

Equation 8.13 is solved in terms of a polynomial function via a complex series of Laplace transforms. The direct correlation function is expressed by the piece-wise polynomial,

$$c(r<d) = -\frac{1}{(1-\eta)^4}\left[(1+2\eta)^2 + 6\eta\left(1+\frac{\eta}{2}\right)^2\frac{r}{R} - \frac{\eta}{2}(1+2\eta)^2\left(\frac{r}{R}\right)^3\right], \tag{8.14}$$

$$c(r \geq d) = 0 \tag{8.15}$$

where $\eta = 1/6\pi\rho d^3$ defines the ensemble's packing fraction. By definition the structure factor is expressed as the Fourier transform of h(r)-1,

$$S(q) = \frac{1}{1-\rho c(q)} \tag{8.16}$$

where the integral $c(q) = 4\pi\int c(r)r^2\sin(qr)/qrdr$ represents the direct correlation function in reciprocal space [61].

8.3 Publications

The following list of papers relates to the research covered in the thesis.

1. Neutron Studies of Magnetic Recording Media. S.L. Lee, T. Thomson, F.Y. Ogrin, C.Oates, M.Wismayer, C.D. Dewhurst, R.Cubitt and S.Harkness. Materials Research Society Symposium Proceedings volume **803** (2004).

2. Using small angle scattering to probe the local magnetic structure of perpendicular magnetic recording media. M.P Wismayer, S.L. Lee, T. Thomson, F.Y. Ogrin, C.D Dewhurst, S.M. Weekes and R. Cubitt. Journal of Applied Physics **99**, 08E707 (2006).

3. Micromagnetic simulation of small-angle neutron scattering from magnetic recording media. F. Y. Ogrin, S. L. Lee, M. Wismayer, T. Thomson,C. D. Dewhurst and R. Cubitt and S. M. Weekes. Journal of Applied Physics **99**, 08G912 (2006).

Mat. Res. Soc. Symp. Proc. Vol. 803 © 2004 Materials Research Society GG4.4.1

Neutron Studies of Magnetic Recording Media

S.L. Lee[1], T. Thomson[2], F.Y. Ogrin[3], C. Oates[1,6], M. Wismayer[1], C. Dewhurst[4], R. Cubitt[4], S. Harkness[5]
[1]School of Physics and Astronomy, University of St. Andrews, Fife, KY6 9SS, UK
[2]Hitachi San Jose Research Centre, 650 Harry Road, San Jose, CA 95120 USA
[3]School of Physics, University of Exeter, Exeter EX4 4QL, U.K.
[4]Institut Laue-Langevin, B.P. 156, 38042 Grenoble Cedex 9, France
[5]Seagate Technologies, 47010 Kato Road, Fremont, CA 94538 USA.
[6]AGH School of Science and Technology, al Mickiewicza, 30-059, Krakow Poland.

ABSTRACT

Small-angle neutron studies have been performed on samples of continuous inhomogeneous magnetic recording media. This has allowed the local magnetic structure to be probed at a sub-nanometre resolution, revealing some interesting information about the size and shape of the magnetic grains and their relation to the physical grains.

INTRODUCTION

There have been relatively few neutron studies of the local magnetic structure of continuous magnetic recording media [1,2]. This paucity is in part due to the difficulties of performing scattering experiments on the tiny volumes of magnetic material available in real systems. Experiments have therefore sometimes focused on thick films of related alloys, that lack the dimensions, underlayers and processing history that give thin film recording media their very particular structure and properties.

We have performed a number of studies on longitudinal thin film media intended for use in hard disk drives. These experiments are extremely challenging to perform, due to the small magnetic volume of the active layer (ca. 20 nm) and the large amount of background scattering from the substrate and underlayers. Nonetheless, for those systems where the distribution of grain sizes is relatively narrow, a surprising amount of information can be extracted concerning the local magnetic structure. In this paper we focus on results from one particular material, a CoCrPtB alloy with a grain diameter of around 11nm.

EXPERIMENTAL DETAILS

The samples were sputtered onto Al substrates, beginning with a thick layer of NiP (ca. 1000 nm), followed by a series of non-magnetic seed layers of typical thickness of 10-20 nm, and finally the CoCrPtB layer of thickness 20nm, this layer being capped with 7 nm of carbon. Due to the large amount of metallurgical scattering from microscopic structure at small angles, much of the Al substrate was removed by careful abrasion to reduce this contribution. In order to increase the volume of magnetic material available for scattering, the sample comprised around thirty polished coupons of diameter 18 mm.

The small-angle neutron (SANS) experiments were carried out using the D11 spectrometer at the ILL, Grenoble. The neutrons have both a nuclear and a magnetic scattering cross-section that are roughly comparable in magnitude. However, due to the tiny *magnetic* volume of these samples, the

scattering from the structural disorder dominates the raw scattering data, to the extent that the magnetic signal cannot be extracted simply. However, unlike the nuclear cross-section, which is isotropic, the magnetic signal varies as $I_M \propto \sin^2\theta$, where θ is the angle between the scattering vector and the local direction of the magnetisation. This anisotropy may thus be used to reveal the magnetic scattering in the following way. Firstly a sample is prepared for which the local magnetisation is randomised over 2π (in the plane of the film). The neutrons are incident normal to the plane of the film and are scattering through small angles to give an isotropic pattern containing both a magnetic and a much larger nuclear contribution. A field is then applied to saturate the magnetisation in the plane of the film, which gives rise to an anisotropic magnetic scattering. This can be revealed by subtraction of the zero-field isotropic pattern to remove the nuclear contribution (see Fig.1a). The amount of information that may be extracted is limited by the fact that the zero-field pattern also contains an *isotropic* magnetic contribution. Nonetheless, one can measure the difference in the scattering perpendicular and parallel to the applied field, which may be modelled. This is derived from the amplitude of curves such as that in Fig.1b, showing the angular variation of intensity over a narrow range of the scattering vector. For the case of a magnetically saturated sample the intensity along the field direction goes to zero ($\theta = 0$), so the amplitude of the scattering perpendicular to the applied field can be *uniquely* determined. This was found to be typically 0.1-1% of the total small angle scattering.

RESULTS AND DISCUSSION

In Fig.2a are example data for the magnetic scattering from the sample in an applied field of 1.46 T, which is not quite sufficient to saturate the magnetisation. The solid line is fit to the data of using a model of the general form $I_M = const.f^2(\mathbf{q})S(\mathbf{q})\sin^2\theta$, where the function $f(\mathbf{q})$ is a *form factor* describing the local density of magnetic flux within a magnetic grain (due to the spatially varying

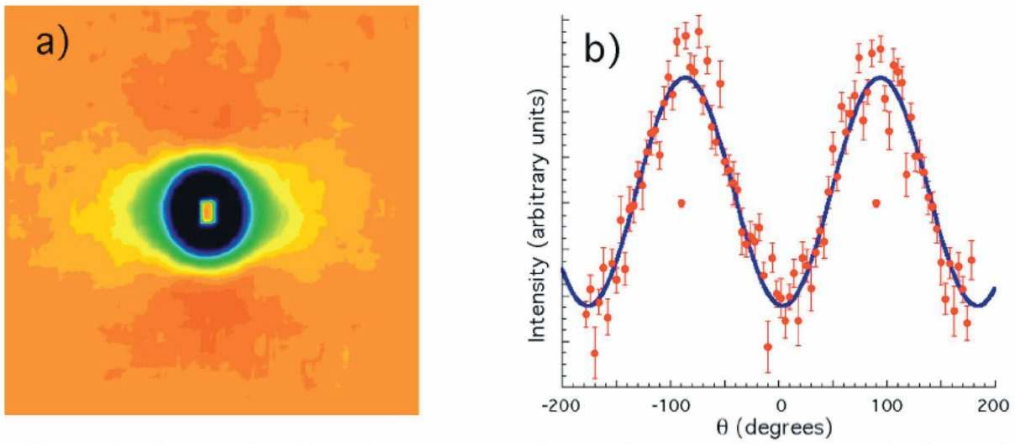

Figure 1 a) An example of the anisotropic magnetic scattering observed from the active layer after removal of the contribution from the nuclear scattering. b) The intensity within a narrow interval of q for the data in Fig.1a, plotted as a function of the angle θ between the scattering vector q and the local direction of the magnetisation. As expected the magnetic scattering varies as $I_M \propto \sin^2\theta$.

magnetisation), $S(\mathbf{q})$ is the *structure factor* that models the spatial correlation of the magnetisation on different grains, and $\mathbf{q}$ is the scattering vector. This is a reasonable way to model the data given a narrow size distribution of particles that are of similar shape and orientation [3,4]. To simplify the analysis $f(\mathbf{q})$ is chosen to be the Fourier transform of a grain of elliptical cross-section, consisting of two concentric shells. This allows for the possibility that magnetisation near the edge of the grains has a different magnitude and direction to that of the central core. This shell model is found to give a much better description of the data over all of the field values measured, from a saturation field of 2.2 T down to a field of 0.45 T corresponding to the closure point of the M-H curve for this material. For simplicity the model assumes that the magnetisation within each shell can be described by an average orientation angle θ, which is valid close to saturation but clearly much less so at lower fields. Nonetheless, fitting the model across the range of applied fields yields remarkable consistency in the length scales extracted, even though the diffraction patterns are very different due to the change in moment orientation.

A slight complication in the analysis arises from the fact that the NiP underlayer is very weakly ferromagnetic, and a change in domain size with applied field gives an additional q^{-n} (n=3.4(1)) contribution to the scattering. This is typical of the Porod scattering expected from randomly distributed inhomogeneities [5], and can be readily observed in the data of Fig. 2b, which shows the scattering from a background reference sample which is identical to the thin film sample under investigation, except that the active CoCrPtB magnetic layer is missing. This additional contribution can easily be distinguished from that due to the active layer due to the simple form, and an additional q^{-n} component is incorporated into the model to account for it. This additional contribution to the much more complex scattering from the active layer can readily be seen by comparing the data to that on a complete sample (Fig. 2a), where it appears as a `linear' contribution to the data at low-q on this

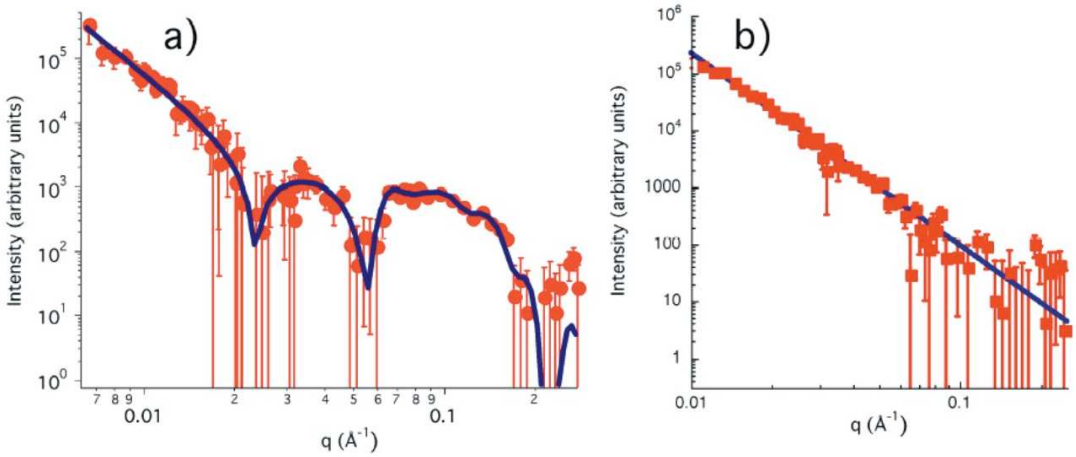

Figure 2 a) An example of the data from the CoCrPtB medium, at a field of 1.46 T, just below saturation. Evidence of the contribution from the NiP layer can be seen as a `linear' contribution at the lowest q-values,These data reveal information about the grain structure both perpendicular and parallel to the field direction, and indicate that the magnetic grains are elongated. The solid line is a fit to the data using the model described in the text. b) The scattered magnetic intensity arising from the NiP underlayer in a background reference sample without an active magnetic layer. The solid line is a fit to the data (see text).

logarithmic scale. For the case of an applied field of 2.2 T, which is sufficient to saturate the magnetisation, the analysis is relatively straight forward, since the magnetic scattering along the field direction goes to zero. Fits to the data using the shell model indicate a core magnetisation that is significantly greater than that of the outer shell. More surprisingly, the extent of the magnetic core (ca. 3.6(1) nm) is much *smaller* than that of the total magnetic grain (ca. 10.6(4) nm), the latter agreeing with the value for the physical grain size of 11nm as determined by transmission electron microscopy (TEM). The spatial correlations are modelled using a Percus-Yevick model for interacting hard spheres [6], which yields an inter-particle separation of 10.8(3) nm, consistent with the diameter of the grains. A schematic of these results is given in Fig. 3a.
Since at saturation the scattering goes to zero along the field direction, no information is available concerning spatial variations parallel to the field. By reducing the field slightly from saturation, transverse components of the magnetisation are allowed to develop which give a contribution to scattering both parallel and perpendicular to the field. In Fig.3b the same data and fit as plotted in Fig. 2a are plotted on a linear scale, showing that, interestingly, the intensity becomes negative over certain regions of q. This reflects the fact that the quantity being plotted is the *difference,* at a given q, between the magnetic scattering perpendicular and parallel to the field, and the latter is non-zero at fields below saturation. The model therefore describes more detail than is apparent from just plots of the modulus of the intensity given in Fig. 2a. The latter is nonetheless useful, since it emphasises the quality of the fit over five orders of magnitude. The fits at this and other fields reveal information about the orientation and anisotropic size of the magnetic grains. In this case the model yields a

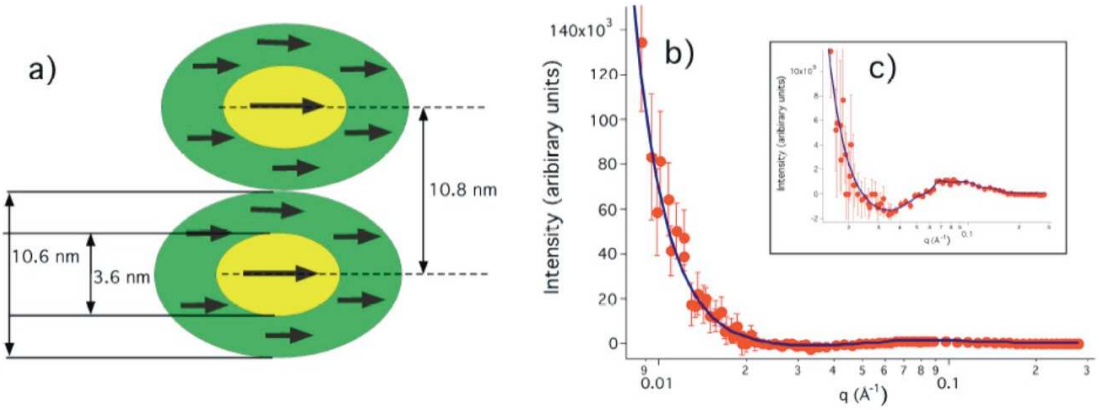

Figure 3 a) A schematic of the magnetic grain determined at a saturating field of 2.2 T. The magnetic grain dimensions for this field can only be determined along a direction perpendicular to the field, and are rather similar to those found at lower fields. The average grain size is given by the fits to the form factor, and the separation of 10.8 nm is given by the Percus-Yevick structure factor. The elongation of the grains along the field direction, in the approximately ratio drawn, is given by the fits to data at lower fields. b) The same data as that of Fig. 2a, taken at 1.46T, but represented on a linear scale. Notice that the intensity appears to be negative over some range of q. This reflects the fact that the data are the *difference* between the magnetic scattering perpendicular and parallel to the field, and the latter is non-zero away from saturation. The solid line is the same fit as in Fig. 2a, which reveals information about the orientation and anisotropic size of the magnetic grains. c) The inset is an expanded region in which the difference plot of intensity is less than zero.

magnetic grain that is elongated along the field direction, with average inter-particle separations of ca. 11.5(5) nm and 10.4(4) nm along directions perpendicular and parallel to the field direction. The occurrence of the much smaller, anisotropic inner core is much more apparent at fields below saturation, and gives rise to some of the sharp features in the magnetic scattering of Fig. 2a. The fits yield an inner core of dimensions 4.0(2) nm and 6.8(3) nm perpendicular and parallel to the field direction, and similarly an outer extent of 8.8 (5) nm and 14.0(3) nm. These results are in broad agreement with those at both higher and lower fields, showing an elongated magnetic grain with an outer dimension close to that of the physical grain (11 nm), but with a much smaller inner core. The systematic errors on fits to data taken at fields below saturation are likely to be larger than those indicated by the fit results, since the model used is less valid in this regime. The aspects of the model that could lead to systematic errors are a) the assumption of concentric shells, and b) the assumption a well-defined direction to describe average of the local magnetisation. The parameters obtained from fits at lower applied fields are also subject to greater uncertainty, since it is only the difference in scattering that is considered. A more sophisticated analysis of the data using numerical simulations is currently underway.

SUMMARY

We have used small angle neutron scattering to investigate the variation of the *local magnetisation* in longitudinal CoCrPtB thin film media by analysing the *anisotropic* component of scattered intensity. There is unambiguous evidence that the magnetisation is much higher within a central core region, which is of *much smaller* extent than the physical grains. This presumably reflects factors such as the compositional variation across the grains and the reduced effective magnetic anisotropy near the surface of the grains. The elongation of the magnetisation along the field direction is also noteworthy. We find that in these small grain (~10 nm) thin film media the basic magnetic entity has a similar extent to the physical grain size. These results should provide interesting input to modelling of the local magnetic structure of these and related systems.

REFERENCES

[1] J. Suzuki *et al.,* Journal of Magnetism and Magnetic Materials **184** 116 (1998).
[2] M. F. Toney *et al.,* Appl. Phys. Lett. **82** (18) 3050 (2003).
[3] W.L. Griffith *et al.,* Phys. Rev. A 35(5) 2200 (1987).
[4] G. Laslaz *et al.,* Phys. Stat. Sol. (a) **41** 577 (1977).
[5] G. Porod, `Small-angle x-rsy scattering', Editors O. Galtter and O. Kratky (Academic Press, London) 1982.
[6] E. Thiele, Journal of Chemical Physics **39** 474 (1963).

JOURNAL OF APPLIED PHYSICS 99, 08E707 (2006)

Using small-angle neutron scattering to probe the local magnetic structure of perpendicular magnetic recording media

M. P. Wismayer and S. L. Lee[a)]
School of Physics and Astronomy, University of St. Andrews, St. Andrews, Fife KY16 9SS, United Kingdom

T. Thomson
Hitachi San Jose Research Center, 650 Harry Road, San Jose, California 95120

F. Y. Ogrin
School of Physics, University of Exeter, Exeter EX4 4QL, United Kingdom

C. D. Dewhurst
Institut Laue-Langevin, BP 156, 38042 Grenoble Cedex 9, France

S. M. Weekes
School of Physics, University of Exeter, Exeter EX4 4QL, United Kingdom

R. Cubitt
Institut Laue-Langevin, BP 156, 38042 Grenoble Cedex 9, France

(Presented on 1 November 2005; published online 20 April 2006)

Small-angle neutron scattering (SANS) has been used to measure the local magnetic structure of perpendicular media consisting of granular CoCrPt–SiO_x thin films. The dimensions of the magnetic structures determined by SANS are consistent with the physical grain sizes suggested by transmission electron microscopy measurements, but yield additional information on magnetic structure *within* the grains, including the existence of a much smaller magnetic core. The results are similar to those recently obtained on longitudinal magnetic recording media, but with the addition of strong interference terms due to the narrower distribution of grain sizes in these samples. © *2006 American Institute of Physics*. [DOI: 10.1063/1.2165798]

The areal density supported by current longitudinal magnetic recording media in hard disk drives (HDD's), ~140 Gbit/in.^{2}, appears close to the limits available from current technologies and families of materials, i.e., from longitudinal CoCrPt-based media.[1] These limits are set by the conflicting requirements that data storage be thermally stable, that data are recorded using the fringe field available from conventional ring heads, and that the medium has an adequate signal-to-noise ratio (SNR). In order to continue to provide greater areal density, HDD's using perpendicular recording, where the medium has a uniaxial anisotropy perpendicular to the film plane, are just starting to become available.[2] The advantage of perpendicular recording is that it allows a soft, high moment magnetic underlayer (SUL) to be incorporated into the structure of the medium. This effectively places the data storage layer directly in the magnetic circuit of the head which, in principle, provides both a greater magnetic field and sharper field gradient during the data write process allowing a higher anisotropy medium to be used.[3]

The structure of a perpendicular medium is significantly more complex than that of a longitudinal medium[4] and hence it is more difficult to determine fundamental magnetic properties. In particular, it is highly desirable to understand the magnetic structure and reversal processes of the data storage layer when incorporated into the complete medium including the SUL. Since the SUL typically accounts for more than 95% of the total medium moment, this presents new challenges.

In this work we use small-angle neutron scattering (SANS) to provide information on the magnetic structure of data storage layers forming part of a complete medium structure. Since neutrons have a magnetic moment, the scattering cross section contains both nuclear and magnetic contributions. SANS is thus able to probe the local magnetic structure at nanometer length scales and SANS results have recently been reported on a number of materials with potential for data storage.[5–9] Of most relevance to this paper are recent reports on longitudinal CoCrPtB media developed for use in high-density disk drives,[8] where a methodology was developed for measuring the extremely small magnetic signals present in the total neutron-scattering cross section. The experiments are extremely challenging, due both to the small magnetic volume of the magnetic recording layer (ca. 15 nm thick) and to the large amount of nuclear background scattering from the substrate and underlayers of the medium. In the present material we have the added complication of an additional *magnetic* signal that arises from the SUL, which must be distinguished from that due to the data storage layer.

The samples were grown by dc-magnetron-sputtering a 15-nm-thick, granular CoCrPt oxide layer onto 65 mm glass substrates. The structure included a 150-nm-thick Co-based SUL onto which a thin seedlayer was deposited prior to the data storage layer. The film stack also included a protective overcoat to inhibit oxidation. In order to obtain sufficient statistics to resolve the magnetic scattering, samples com-

a)Electronic mail: sl10@st-and.ac.uk

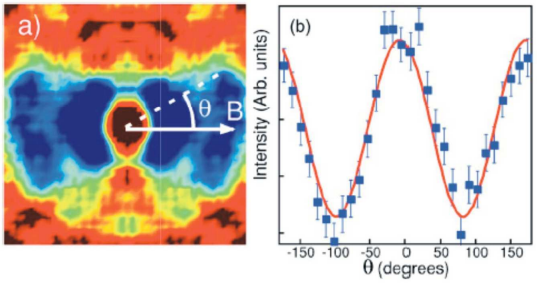

FIG. 1. (Color online) (a) The anisotropic magnetic scattering from the 15 -nm-thick granular CoCrPt–SiO_x layer of the perpendicular recording media samples over a q range of 0.007–0.03 Å^{-1}. The contributions from the nuclear scattering and the SUL have been removed (see text). (b) Angular variation in the scattering plane of the magnetic scattering, fitted to $\sin^2\theta$.

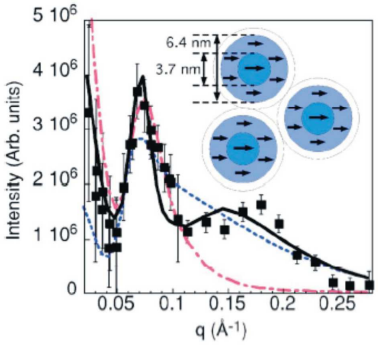

FIG. 2. (Color online) The q dependence of the magnetic intensity from the recording layer at saturation. The solid line represents a fit to the spherical shell model scattering function described in the text. The dashed line is a fit to a solid sphere model with a diameter of 2.5(1) nm; the dot-dashed line is the same model with a diameter fixed to 6.0 nm. Inset: a schematic of the shell model used.

prising a stack of three double-sided substrates were used in these measurements. The SANS experiments were performed using the D11 spectrometer at the Insitute Laue-Langevin (ILL), Grenoble, France.

A magnetic field was applied in the plane of the film and perpendicular to the incident neutron beam. In this geometry the experiment thus probes magnetic structures within the plane of the film. Before each measurement the samples were first rotated through 90° and the magnetization saturated perpendicular to the plane in a field of 2.2 T. This ensured that prior to the measurements the sample was always left in a known state and moreover that in this state the recording layer was magnetically *isotropic* within the plane of the film.

Although the nuclear and magnetic neutron-scattering cross sections are roughly comparable in magnitude, scattering from the structural disorder dominates the raw scattering data due to the much greater volume of nonmagnetic material. However, whereas the nuclear cross section is isotropic, the magnetic signal varies as $I_M(\mathbf{q}) \propto \sin^2\theta$, where θ is the angle between the scattering vector and the local direction of the magnetization, and $\mathbf{q}$ is the scattering vector[9,10] (Fig. 1). This anisotropy in the scattering may thus be used to reveal the magnetic component in the following way, using a method similar to that described in Ref. 8. Firstly, a sample is prepared for which the component of the local magnetization is randomized over 2π in the plane of the film, in this case by saturating the sample perpendicular to the plane and then reducing the field to zero, thus allowing the magnetization to relax. In zero field the neutrons are scattered through small angles to give an isotropic pattern $I(q)=I_M(q)+I_N(q)$ containing both a magnetic and a much larger nuclear contribution. A field is then applied to saturate the magnetization in the plane of the film, so that the magnetic contribution to the scattering now becomes *anisotropic*. Since $I_N(q) \gg I_M(q)$, the variation $I_M(\mathbf{q}) \propto \sin^2\theta$ still cannot be extracted, since the amplitude of $I_M(\theta)$ is small in comparison to the random angular variation of the dominant nuclear scattering $I_N(\theta)$. However, the magnetic contributions are readily revealed by subtraction of the zero-field isotropic pattern in order to remove entirely the nuclear contribution. This image then contains both isotropic (zero-field) *and* anisotropic (saturation field) magnetic contributions, which are easily separated. These contain scattering from both the recording layer and the SUL, but since it is the former in which we are primarily interested an alternative approach is introduced. Following the zero-field measurements additional data are taken at an applied in-plane field sufficiently large to just saturate the SUL yet still small enough to have no appreciable affect on the recording layer, which has a strong perpendicular anisotropy. By taking the difference of any two of these three data sets one can obtain the scattering from the CoCrPt–SiO_x recording layer alone (Figs. 1 and 2), the SUL alone, or from the total magnetic signal. All combinations produce self-consistent results.

We focus here on the anisotropic component of the scattering from the CoCrPt–SiO_x *recording layer*, which reflects the magnetic structure at *saturation*, shown in Fig. 2. We model the data using the approximation $I_M(\mathbf{q}) = \langle f(\mathbf{q})\rangle^2\langle S(\mathbf{q})\rangle + \langle f^2(\mathbf{q})\rangle - \langle f(\mathbf{q})\rangle^2$, where $f(\mathbf{q})$ is a form factor describing the local induction around a magnetic grain, $S(\mathbf{q})$ is the structure factor that models the spatial correlation of the magnetic induction between different grains, and $\langle\cdots\rangle$ denotes the average over the size distribution of the grains. This is a reasonable approximation given the polydispersity and packing density for this system.[11,12] A size distribution of magnetic particle diameters was included using a Gamma-Shultz function, as described in Ref. 9, and the fits yield an effective distribution width $\sigma \sim 0.22$, similar to $\sigma = 0.26(2)$ obtained for the physical grains from transmission electron microscopy (TEM) data. We note that the fits are not strongly sensitive to the precise form of the distribution function.[9] For $S(\mathbf{q})$ an analytical expression for a system of densely packed interacting hard spheres, based on the Percus-Yevick equation,[13] was used. Unlike many simplified treatments, we find it necessary here to include an explicit average of $S(\mathbf{q})$ over the size distribution using the method of Ref. 12, although the more complete treatment of Ref. 11 is found to be unnecessary in the present case. To simplify the analysis $f(\mathbf{q})$ is chosen to be the Fourier transform of an object formed from two concentric shells of magnetization within the plane of the film, thus comprising an inner core and an outer shell

(see inset in Fig. 2). This allows for the possibility that the induction near the edge of the grains has a different magnitude and direction to that of the central core. This shell model is found to fit the data well, whereas a simple solid sphere model is found to provide a poor description of the data (Fig. 2). A cylindrical shell model was also found to fit the data less well, suggesting that the magnetic entities contain less sharp features than the physical grains in which they reside. Both these findings are similar to those obtained from our SANS studies on longitudinal recording media.[8,14] However, in contrast to those results, in the present data we find a strong interference peak in $S(\mathbf{q})$, which is probably more evident here due to the reduced grain size distribution in these samples.[11,12] The peak in $S(\mathbf{q})$ corresponds to an average interparticle separation of 8.5(4) nm, in good agreement with the estimate of the grain size of 7.9(3) nm from TEM. The form factor $f(\mathbf{q})$ indicates an average outer particle diameter of 6.4(2) nm, suggesting a dead (or at least spatially uniform) magnetic region between the grains. This is not unexpected given the inhomogeneous composition of these materials, and the accepted picture of a nonmagnetic grain boundary. However, the less expected result is that within the magnetically active grain there is a much smaller core of higher magnetization, which has a diameter of 3.7(3) nm. Very similar findings for longitudinal recording media have been modeled recently, both analytically and using micromagnetic simulations,[8,14] where it is shown that this outer region can be extremely well described by a softer polarizable magnetic material. However, more measurements are required on these perpendicular recording materials to fully describe the local magnetic structure.

In conclusion, we have succeeded in measuring the local magnetic structure in the active layer of a sample of perpendicular recording media, which represents a considerable experimental challenge. The length scales obtained are in agreement with the measurements of the grain size of the materials, but also reveal a gradation of magnetization across the grain, comprising a central core, a softer outer shell, and nonmagnetic region between the grains. Further field-dependent measurements are planned to explore the nature of these inner and outer magnetic regions.

[1]D. Weller and M. F. Doerner, Annu. Rev. Mater. Sci. **30**, 611 (2000).
[2]A. Takeo and Y. Tanaka, presented at TMRC, August 2005 (unpublished).
[3]Y. Nakamura, J. Magn. Magn. Mater. **287**, 27 (2005).
[4]J. H. Judy, J. Magn. Magn. Mater. **287**, 16 (2005).
[5]M. Toney *et al.*, Appl. Phys. Lett. **82**, 3050 (2003).
[6]T. Thomson *et al.*, J. Appl. Phys. **95**, 6738 (2004).
[7]T. Thomson *et al.*, Appl. Phys. (N.Y.) **96**, 1197 (2004).
[8]S. L. Lee *et al.*, Mater. Res. Soc. Symp. Proc. **803**, GG4.4.1 (2004).
[9]T. Thomson, S. L. Lee, C. Dewhurst, F. Y. Ogrin, C. J. Oates, S. Sun, and B. D. Terris, Phys. Rev. B **72**, 064441 (2005).
[10]J. F. Loffler *et al.*, Phys. Rev. B **71**, 134410 (2005).
[11]W. L. Griffith *et al.*, Phys. Rev. A **35**, 2200 (1987).
[12]W. L. Griffith *et al.*, Phys. Rev. A **33**, 2197 (1986).
[13]E. Thiele, J. Chem. Phys. **39**, 474 (1963).
[14]M. Wismayer *et al.* (unpublished).

JOURNAL OF APPLIED PHYSICS 99, 08G912 (2006)

Micromagnetic simulation of small-angle neutron scattering from magnetic recording media

F. Y. Ogrin[a)]
School of Physics, University of Exeter, Exeter EX4 4QL, United Kingdom

S. L. Lee and M. Wismayer
School of Physics and Astronomy, University of St. Andrews, St. Andrews, Fife KY16, 9SS, United Kingdom

T. Thomson
Hitachi San Jose Research Centre, 650 Harry Road, San Jose, California 95120

C. D. Dewhurst and R. Cubitt
Institut Laue-Langevin, B. P. 156, 38042 Grenoble, Cedex 9, France

S. M. Weekes
School of Physics, University of Exeter, Exeter EX4 4QL, United Kingdom

(Presented on 1 November 2005; published online 27 April 2006)

A micromagnetic simulation of the magnetic morphology of CoCrPtB based longitudinal recording media is used to model small-angle neutron scattering data and provide a quantitative description of the local flux density in these nanostructured magnetic materials. The model addresses several aspects of the experimental measurements and, in particular, explains an unusual increase in scattering along the applied field direction for certain values of the scattering vector **q**. The increased scattering along the field direction results in a change of the phase of the angular variation of the scattering by 90°. This 90° change in scattering phase arises naturally from the influence of stray fields when modeling the media as a heterogeneous alloy consisting of grains with a high saturation magnetization core and a permeable shell. © *2006 American Institute of Physics*.
[DOI: 10.1063/1.2176314]

INTRODUCTION

In studies of nanostructured materials small-angle neutron scattering (SANS) is a very powerful technique for probing local magnetic properties. Scattering due to magnetic flux density can be separated from that due to nuclear potentials by manipulating the magnetic state of the material, for example, by applying a magnetic field so that the magnetic scattering changes while the nuclear scattering remains constant. SANS can provide information on the dimensions of changes in flux density, such as those due to granular or ordered nanoscopic particles, and it can also reveal information on the orientation of the local magnetization vector.[1–4] This is achieved via examination of the scattered neutron intensity as a function of azimuthal angle θ in the scattering plane (for SANS this is perpendicular to the incoming beam), which in our geometry is the easy plane of magnetization and parallel to the film surface. Due to the moment orientation factor in the scattering cross section $[\hat{\mathbf{q}}(\hat{\mathbf{q}}\cdot\hat{\mathbf{m}})-\hat{\mathbf{m}}]$, where $\hat{\mathbf{q}}$ is the momentum transfer unit vector and $\hat{\mathbf{m}}$ is a unit local magnetization vector, magnetic scattering falls to zero as $\hat{\mathbf{q}}$ approaches $\hat{\mathbf{m}}$. For instance, if a sample is uniformly magnetized (e.g., by applying a large external field) the scattering intensity will have an *anisotropic* dependence $I(\theta)\sim\sin^2\theta$, in which the direction of zero intensity will correspond to the orientation of the magnetization within the sample. The **q** dependence of this anisotropic scattering thus gives information on the orientation and spatial variation of the moments, in contrast to magnetometry measurements where this information is lost due to averaging over the volume of the sample. For the experimental configuration discussed here, we can reconstruct the local magnetic structure down to feature sizes of around 1 nm. Recently SANS measurements were reported on CoCrPtB longitudinal recording media sample that displays some intriguing characteristics.[3,5] The data showed that even with the application of a large external field ($H_a > H_k \sim 1.0$ T) in the plane of the sample, over certain q ranges, the angular-dependent scattering intensity changed its phase ϕ from 0° to 90°. Here the scattering intensity is given by $I(\theta)\sim\sin^2(\theta+\phi)$, and H_k is the anisotropy field. The existence of the 90° phase would seem to indicate that in these q ranges there is a significant influence on the scattering from moments that are noncollinear with the applied field. The 90° phase change was found for three different fields above H_k. However, for fields greater than 2.2 T only the 0° phase was observed over the entire q range (0.005–0.3 Å^{-1}). In addition to the appearance of the 90° phase shift, the data also indicated that the local intragranular magnetization has structure. This structure consists of a hard magnetic core which is significantly smaller than the physical grain size and an outer shell of weaker magnetization.[3,5] These observations challenge the view that magnetic grains in the medium are single domains of size comparable to the physical grains.

The phenomenon of scattering with 90° phase shifts of $I(\theta)$ has been observed in other systems.[1–3] In the case of

[a)]Electronic mail: f.y.ogrin@exeter.ac.uk

monodispersed 10 nm Fe particles[1] the change in phase was observed at low fields and dominated the whole q range. An increase in the field led to the recovery of the 0° dependence. The effect was attributed to the existence of an antiferromagnetic phase, thought to result from an oxide layer postulated to form during the fabrication process. A similar result has been also observed recently by Ijiri *et al.*[2] In this case partially oxidized iron nanoparticles have also shown 90° phase shifts. The effect was not observed over the entire q range and could be also manipulated by varying the temperature and magnetic field.

Here we report the simulations of SANS data which show the possibility of a 90° phase dependence of scattering in a granular system of ferromagnetic particles with a modest size distribution (ca. 30%). In comparison to the previously reported results, we demonstrate that the origin of the phase shifts lies in the intragranular magnetic structure and is due to stray fields generated by high saturation magnetization cores at the center of the grains. To illustrate this, we compare the results of simulation with the experimental data obtained on a sample of CoCrPtB longitudinal media. This is a quantitative description of this important signature in the neutron scattering for any material system.

MODEL

In our model the thin film medium is composed of particles (grains), with a Gaussian size distribution, close packed within a single magnetic layer. The particle separation (~12 nm) is approximately equal to the dimensions identified from transmission electron microscopy (TEM) imaging. Using the information from SANS experiments,[3,5] that is, grains are comprised of a central core surrounded by a region of weaker magnetization, we assume that the core occupies a certain fraction of the volume of the grain, with a maximum diameter equal to that of the grain itself. The cores are ferromagnetic, with a strong exchange coupling between moments in the interior of the core. The magnetic anisotropy is taken as uniaxial for each grain, with a random distribution of the principle axis in the plane of the sample. Calculation of the magnetic scattering intensity is performed using the standard Born approximation formalism[6,7] as applied to SANS experiments. The sample plane $(\hat{\mathbf{x}},\hat{\mathbf{y}})$ is positioned perpendicular to the incoming neutron beam, the external magnetic field is applied along the $\hat{\mathbf{x}}$ direction, and the scattering intensity is calculated as a function of momentum transfer vector $\boldsymbol{q}$ in the plane $(\hat{\mathbf{x}},\hat{\mathbf{y}})$ via

$$I(\mathbf{q}) \sim \frac{d\sigma_{\mathrm{mag}}(\mathbf{q})}{d\Omega} = \left| \sum_j l_{\mathrm{mag}} M_j(q)[\hat{\mathbf{q}}(\hat{\mathbf{q}}\cdot\hat{\mathbf{m}}) - \hat{\mathbf{m}}]\exp(i\mathbf{q}\cdot\mathbf{r}_j) \right|^2 / V. \quad (1)$$

Here, l_{mag} is a constant related to the magnetic scattering potential; $M_j(q)=|\mathbf{M}_j(\mathbf{q})|=|\int \mathbf{M}_j(\mathbf{r}-\mathbf{r}_j)\exp(i\mathbf{q}\cdot(\mathbf{r}-\mathbf{r}_j))d\mathbf{r}|$ is the magnitude of the Fourier component of the magnetization vector, where $\mathbf{M}_j(\mathbf{r})$ is the magnetisation of the unit cell j with the position vector $\mathbf{r}_j$; $\hat{\mathbf{m}}$ and $\hat{\mathbf{q}}$ are the unit vectors parallel to $\mathbf{M}_j(\mathbf{r})$ and $\mathbf{q}$, and V is the magnetic volume.

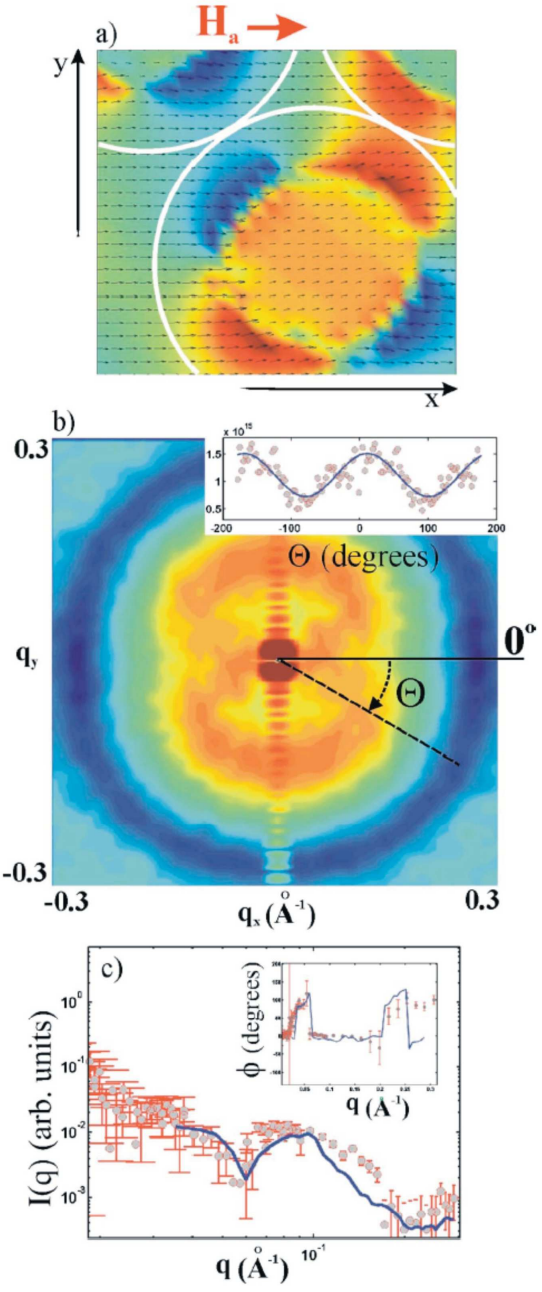

FIG. 1. (Color online) Simulation of magnetic scattering from a longitudinal medium for the case of H_a=1.45 T. Model parameters: Average diameter of particle core, 45 Å; particle separation, 130 Å; saturation magnetization, $M_s=500\times10^3$ A/m; exchange stiffness constant, $A=30\times10^{-12}$ J/m; anisotropy constant, $K_1=410\times10^3$ J/m^3. (a) Simulated magnetic flux density distribution inside and outside the cores. Color demonstrates the variation of y component of **B**. White solid lines indicate grain boundaries. (b) Calculated magnetic scattering intensity $I(\mathbf{q})$ from magnetic flux density distribution shown in (a). Inset shows a 90° phase dependence of $I(\theta)$ at q =0.05 Å^{-1}. (c) Experimental and simulated dependence of the amplitude of the magnetic scattering $I(\theta)$ as a function of q. Inset: Experimental and calculated dependence of the phase $\phi(q)$.

In the calculation, the medium is represented by a rectangular three dimensional (3D) $(200\times200\times10)$ mesh of cells which contain magnetization vectors (one vector per cell). The dimension of a cell is $3\times3\times3$ Å^3. The magnitude and the orientation of $\mathbf{M}_j(\mathbf{r})$ depend on its position. For cells inside the core region, the magnetization is formed by the "spontaneous" moments in the core. These moments are tightly bound by strong exchange coupling, which keep them oriented around the same direction determined by the local uniaxial anisotropy and the direction of the internal field. In the cells outside the core region, the magnetization is formed as a result of the magnetic polarization of the material by the external applied field and the dipolar return field generated by the moments in the cores. Thus the grains in the longitudinal medium can be viewed as a two-phase system, in which one phase is represented by the hard ferromagnetic core region and the other by the surrounding soft paramagnetic-like "shell." In the simplest model, the simulation of the shell is achieved by including a linear magnetic susceptibility for the outer region such that the magnetization around the cores can be then described by the following relation:

$$\mathbf{M}_{\text{ext}} = (\mathbf{H}_D + \mathbf{H}_a)\chi, \tag{2}$$

where $\mathbf{H}_a$ is the external applied field, and $\mathbf{H}_D$ is the dipolar stray field from the moments in the cores. This allows the experimental data to be simulated with surprising accuracy over a wide range of q values and applied fields. The number of particles in our simulation depends on the physical dimensions of the grains, but normally lies in the region from 40 to 60. The calculation of the flux density is performed with the OOMMF micromagnetic simulation program using the parameters given in the caption of Fig. 1. In order to account for the statistical distribution, the scattering calculation is averaged for 15 different configurations.

DISCUSSION

The essential element of this model is that the magnetic scattering is assumed to originate from the spatial variations of all the contributions to the local flux density to which the neutron is sensitive. This includes contributions not only from the cores of the grains, but also from the magnetic material between the cores that is influenced by the long range dipolar fields. Simulations using this model not only predict the correct variation of the phase of the scattering as a function of q, but they also explain quantitatively the evolution of the phase shift pattern as a function of external applied field.

Figure 1 gives the experimental result obtained for a sample of CoCrPtB media measured in an applied field of 1.45 T at room temperature; the result of a simulation based on the above model is also shown. Figure 1(a) shows a simulation of the local flux density inside and around the cores. This demonstrates the dipolar nature of the stray field, which leads to a spatial variation of the y component of the flux density, and which is essentially responsible for the scattering along the external field direction. Note that the x components, which still dominate in real space, have Fourier components that are not significant in this q range and thus do not significantly contribute to the scattering. Figure 1(b) shows the calculated two dimensional (2D) scattering image in the plane $(\hat{\mathbf{x}},\hat{\mathbf{y}})$ and the angle dependence of $I(\theta)$ which follows a $\sin^2(\theta+90°)$ dependence. The amplitude of this dependence is essentially the difference between the contribution to the magnetic scattering from the y and x components of the local field density at the chosen q value. Measuring the amplitude as a function of q gives spatial information about the variations of these components on various length scales. Figure 1(c) contains the experimental and calculated results of $I(q)$. Although the simulated curve does not follow experimental data precisely, which is mainly due to simplifications in the model (e.g., the grain size variation was obtained by Gaussian distribution rather than the more usual lognormal distribution; finite size effects also play a role), the main features of the dependence are well accounted and in very good agreement with the q dependence of the phase ϕ. The inset shows the corresponding dependence of the phase as a function of q. These results are also in very good accord with the analytical calculations produced earlier for the same experimental data.[3]

CONCLUSION

We have demonstrated that the shift from 0° to 90° in the phase of the anisotropic magnetic SANS data, for a field applied in the scattering plane, can be explained by the contribution to the total flux density from a permeable matrix surrounding the cores of the grains when it is influenced by the stray dipolar fields from the cores. We introduced a model which takes into account the overall variations of the flux density in a sample and which calculates the magnetic scattering for the configuration of a SANS experiment. As an example we used experimental results from longitudinal CoCrPtB media, which were simulated using the model. It was shown that in order to obtain a reasonable fit to the data the model must have (i) a significantly reduced diameter of magnetic cores and (ii) there must exist a permeable magnetic medium around the cores of the particles.

ACKNOWLEDGMENTS

The authors would like to acknowledge the support from the University of Exeter Research Fund. We would also like to acknowledge Dr. J. Rowe for help in optimizing the programming code.

[1]J. F. Loffler *et al.*, Physica B **234–236**, 1005 (1997).
[2]Y. Ijiri *et al.*, Appl. Phys. Lett. **86**, 243102 (2005).
[3]S. L. Lee *et al.*, Mater. Res. Soc. Symp. Proc. **803**, GG4.4.1 (2004).
[4]T. Thomson *et al.*, Phys. Rev. B **72**, 064441 (2005).
[5]M. Wismayer *et al.* (in preparation).
[6]*Treatise on Materials and Technology*, edited by G. Kostorz (Academic, New York, 1979), Vol. 15.
[7]J. Weissmuller *et al.*, J. Res. Natl. Inst. Stand. Technol. **104**, 261 (1999).

Bibliography

1. V. Poulsen, "*US PAT No. 661,619 Method of Recordings and Reproducing Sounds or Signals*", (1898).

2. O. Smith, "Some Possible Form of Phonograph", *Electrical World*, Vol **8**, (1888).

3. R. Heinz, *An introduction into Storage Media and Computer Technology*. BASF, (1998).

4. E.Köester and T.C. Arnoldussen, *Magnetic Recording Handbook*, Part 1 Chapter 3 p.101-257.

5. H.N. Bertram, *Theory of Magnetic Recording*, Cambridge University Press (1994).

6. W.C. Bogart, *Magnetic Tape Storage and Handling*, (1995).

7. "DDS Spec Drive DAT Reliability," Computer technology review, **13**, 5 (1990).

8. H. Goldstine, "The Electronic Numerical Integrator and Computer (ENIAC)", *The Origins of Digital Computers*, 359 (1982).

9. A.S. Hoagland, "History of magnetic disk storage based on perpendicular magnetic recording", IEEE Trans Magn. **39**, 1871 (2003).

10. "IBM Archives: IBM 350 disk storage unit", http://www-03.ibm.com/ibm/history/

11. D.A. Thompson, "Thin film magnetoresistor in memory storage, and related applications", IEEE Trans. Magn. **11**, 1039 (1978).

12. D.Weller and A.Moser, "Thermal Effect Limit in Ultrahigh-Density Magnetic Recording", IEEE Trans. Magn. **35**, 4423 (1999).

13. P. Glijer, J.M. Sivertsen, J.H. Judy, "Magnetic force microscopy (MFM) studies of micromagnetic structures of high coercivity CoCrPt/Cr and CoCrPrB/Cr thin films", IEEE Trans. Magn. **31**, 2842 (1995).

14. N. Inaba, M. Futamoto,"Effects of Pt and Ta addition on compositional microstructure of CoCr-alloy thin film media", J. Appl. Phys. **87**, 6863 (2000).

15. E.E.Fullerton, D.T. Margulies, M. E. Schabes, "Antiferromagnetically coupled magnetic media layers for thermally stable high-density recording", Appl. Phys. Lett. **77**, 3806 (2000).

16. M.E Schabes, E.E Fullerton, D.T. Margulies, "Theory of Antiferromagnetically-Coupled Magnetic Recording Media", J. Appl. Phys. (2001).

17. D.Litvinov and S. Khizroev, *Perpendicular Magnetic Recording*, Kluwer Academic, Dordrecht (2005).

18. S.N. Piramanayagam, "Perpendicular recording media for hard disk drives", J. Appl. Phys. **102**, 011301 (2007).

19. S. Sun, C.B. Murray, D. Weller, L. Folks, and Moser, "Monodisperse FePt Nanoparticles and Ferromagnetic FePt Nanocrystal Superlattices", Science **287**, 1989 (2000).

20. T.Thomson, S.L. Lee, M.F. Toney, C.D. Dewhurst, F.Y. Ogrin, C.J. Oates and S.Sun, "Agglomeration and sintering in annealed FePt nanoparticle assemblies studied by small angle neutron scattering and x-ray diffraction", PRB **72**, 064441 (2005).

21. M. Futamoto, N. Inaba, Y. Hirayama, K. Ito, Y. Honda, "Microstruture and micromagnetics of future thin-film media", J. Magn. Magn. Mater. **193,** 36 (1999).

22. J. E. Wittig, T. P. Nolan, C. A. Ross, M. E. Schabes, K. Tang, R. Sinclair, "Chromium segregation in CoCrTa/Cr and CoCrPt/Cr thin films for longitudinal recording media", J. Bentley, IEEE Trans. Magn**. 34,** 1564 (1998).

23. W. Grogger, K. M. Krishnan, R. A. Ristau, T. Thomson, S. D. Harkness, and R. Ranjan, "Quantitative measurement of Cr-segregation in Co(0.8-x)Cr(x)-Pt(0.1)B(0.1) recording media", Appl. Phys. Lett. **80**, 1165 (2002).

24. K. M. Kemner,Y. U. Idzerda, V. G. Harris, V. Chakarian, and W. T. Elam, "Direct observation of Cr magnetic order in CoCrTa and CoCrPt thin flims" J. Appl. Phys. **81**, 1002 (1997).

25. M.F. Toney, K.A. Rubin, Sung-Min Choi and C.J. Glinka, "Small-angle neutron scattering measurements of magnetic cluster sizes in magnetic recording disks", Appl. Phys. Lett. **82**, 3050 (2000).

26. J.B. Kortright, O.Hellwig, D.T. Margulies, E.E. Fullerton, "Resolving magnetic and chemical correlations in CoPtCr films using soft X-ray resonant scattering" J. Magn. Magn. Mater. **240,** 325 (2002).

27. J. Suzuki, K. Takei, Y. Maeda, Y.Morii, "Small-angle neutron scattering study of magnetic microstructures in Co-Cr films", J. Magn. Magn. Mater. **184,** 116 (1999).

28. G. Porod, Kolloid. Z. **124** (1951); **125** 51 and 109 (1952).

29. E.E. Fullerton, O. Hellwig, K. Takano, J.B. Kortright, NIM B, "Soft X-ray magnetic scattering as a probe of recording media", **200**, 202-209 (2003).

30. B.I. Bleaney, *Electricity and Magnetism*, Oxford University Press (1976).

31. S. Blundell, *Magnetism in Condensed Matter*, Oxford Series in Condensed Matter, Oxford University Press (2001).

32. N.W. Ashcroft and N.D. Mermin, *Solid State Physics*, Brooks and Cole (1976).

33. D.H. Martin, *Magnetism in Solids*, London ILIFFE BOOKS LTD (1967).

34. Handbook of Chemistry and Physics, 46 edition.

35. M.Garber and W.B.Henry, "A magnetic susceptibility balance and the temperature dependence of the magnetic susceptibility of copper, silver, and gold, 295^0-975^0", *Can. J. Phys*, **31**, 1595 (1960).

36. M.Höhl, Z. Metallk, **51**, 85 (1960).

37. S.Chikazumi, *Physics of Ferromagnetism*, Oxford University Press (1997).

38. G.T. Rado and H.Suhl, *Magnetism*, "Vol.1 Magnetic Ions in Insulators. Their Interactions, Resonances and Optical Properties", Academic Press, 1963.

39. P. Bruno, *Physical origins and theoretical models of magnetic anisotropy*, Ferienkurse des Forschungszentrums Jülich, Jülich, (1993).

40. A. Amikam, *Introduction to the theory of ferromagnetism* Oxford: Clarendon, (1996).

41. Young, Hugh D., University Physics, 8th Ed., Addison-Wesley, (1992).

42. G.L. Squires, *Introduction to the Theory of Neutron Scattering*, Dover Publications (1978).

43. B. Hammoude, *A TUTORIAL ON SMALL-ANGLE NEUTRON SCATTERING FROM POLYMERS*, NIST, (1995).

44. G.E. Bacon, "Neutron Diffraction", Clarendon Press, Oxford (1975).

45. R.M. Moon, T.Riste and W.C. Koehler, Phys. "Polarization Analysis of Thermal-Neutron Scattering", Phys. Rev. **181**, 920 (1969).

46. J. Weissmuller, A. Michels, J.G. Barker, A. Wiedenmann, U. Erb and R.D Shull, "Analysis of the small-angle neutron scattering of nanocrystalline ferromagnets using a micromagnetics model", Phys Rev. B. **63**, 214414 (2001).

47. C.G. Shull, E.O. Wollan and W.C Koehler, "Neutron Scattering and Polarization by ferromagnetic Materials", Phys. Rev. **84**, 912 (1951).

48. J.L. Yarnell, M.J. Katz and R.G. Wenzel, "Structure Factor and Radial Distribution Function for Liquid Argon at 85 ^{0}K", Phys. Rev. A. **7**, 2130 (1973).

49. P.M. Chaikin and T.C. Lubensky, *Principles of condensed matter physics*, Cambridge University Press, (1995).

50. A. Guinier, *X-Ray Diffraction In Crystals, Imperfect Crystals and Amorphous Bodies*, Freeman and Company, (1963).

51. A. Guinier. *Small-Angle Scattering of X-Rays*, John Wiley & Sons (1955).

52. W.L. Griffith, R. Triolo and A.L. Compere, “Analytical scattering function of a polydisperse Percus-Yevick fluid with Schultz-Γ distributed diameters”, Phys. Rev. A. **35,** 2200 (1987).

53. P.A. Egelstaff, *Introduction to the Liquid State*, Oxford University Press (1994).

54. J.P. Hanson and Schiff, Phys Rev. A **8**, 3096 (1973).

55. L. Verlet, Phys. Rev. **163**, 201 (1968).

56. J.P. Hansen and I. McDonald, *Theory of Simple Liquids*, 2nd Academic Press,(1986).

57. R.J. Baxter, “Method of Solution of the Percus-Yevick, Hypernetted-Chain, or Similar Equations”, Phys. Rev. **138**, 170 (1967).

58. J.K. Percus and G.J. Yevick, “Analysis of Classical Statistical Mechanics by Means of Collective Coordinates”, Phys. Rev. **110**, 1 (1958).

59. E. Thiele, “Equation of State for Hard Spheres”, J. Chem. Phys. **39**, 474 (1963).

60. M.S. Wertheim, “Analytic Solution of the Percus-Yevick Equation”, J. Math. Phys. **5**, 643 (1964).

61. N.W. Ashcroft and J. Lekner, “Structure and Resistivity of Liquid Metals”, Phys. Rev. **145**, 83 (1966).

62. W.L. Griffith, R. Triolo and A.L. Compere, “Analytical structure function of a polydisperse Percus-Yevick fluid with Schultz (gamma) distributed diameters”, Phys. Rev. A. **33,** 2197 (1986).

63. P. Linder, “D11 Instrument characteristics and description”, Web address: www.ill.eu/d11/characteristics (2008).

64. C. Dewhurst, “D22 Instrument Description”, Web address: www.ill.eu/d22/characteristics (2008).

65. J. Kohlbrecher and W.Wagner, “The new SANS instrument at the Swiss spallation source SINQ”, Appl. Cryst. **33**, 804-806 (2000).

66. L. Dobrzynski and K. Blinowski, *Neutrons and Solid State Physics*, Ellis Horwood (1994).

67. K. Ibel, "The Neutron SmallAngle Camera D11 at the HighFlux Reactor, Grenoble", J. Appl. Cryst. **9**, 296-309 (1976).

68. P. Lindner, R.P. May, P.A. Timmins, "Upgrading of the SANS Instrument D11 at the ILL", Physica B **180** & **181**, 967-972(1992).

69. P. Muller, *The Physics of Superconductors,* Spinger (1997).

70. W.Jenks, I.Thomas and J.Wikswo, *SQUIDS*, Encyclopaedia of Appl. Phys. **19**, 457 (1997).

71. S. Foner, "Versatile and Sensitive Vibrating-Sample Magnetometer", Rev. Sci. Instr. **30**, 548 (1959).

72. D.Speliotis, "Getting the Most From Your Vibrating Sample Magnetometer", ADE Technologies (1997).

73. J.M. Florczak and E.Dan Dahlberg, "Detecting two magnetization components by the magneto-optical Kerr effect", J. Appl. Phys. **67**, 7519 (1990).

74. H.F. Ding and H.P. Oepen, "Experimental method for separating longitudinal and polar Kerr signals", J. Magn. Magn, **212** L5-L11 (2000).

75. Z. C. Zhao, "Anomalous hysteresis loops measured by the magneto-optical Kerr effect in a Co/NiO/Cu/Co/Cu structure", J.Appl. Phys. **101**, 016105 (2007).

76. T. Thomson, Longitudinal Magnetic Recording Media (LMRM) samples, Seagate, Fermont, Ca (1999).

77. N.Kaiser, "Review of the fundamentals of thin-film growth", Appl. Optics **41**, 3053 (2002).

78. Li-Lien Lee and D.E. Laughlin, "Effects of Cr Intermediate Layers on CoCrPt Thin Film Media on NiAl Underlayer", IEEE Trans. Magn. **31**, 2728 (1995).

79. C.V. Thompson, "Grain growth in polycrystalline thin films", Mat. Res. Sco. Symp Proc, **341**, 3 (1994).

80. Jack J. K. Chang, Qixu Chen, and Ga-Lane Chen **,** "Nanoroughness effect on Cr growth mechanism", J.Appl. Phys. **81**, 3443 (1997).

81. Bin Lu and David E. Laughlin, "Microstructure of Longitudinal Media, in The Physics of Ultrahigh-Density Magnetic Recording" Springer Series in Surface Sciences, 41, edited by M. Plumer, J. Van Ek, D. Weller and G. Ertl (2001).

82. D.G.Porter and E. Glavinas, "Irregular Grain Structure in Micomagnetic Simulation", J.Appl. Phys. **79**, 4695-4697 (1996).

83. N.I Inaba and M.Futamoto, "Effects of Pt and Ta addition on compositional microstructure of CoCr-alloy thin film media, J.Appl. Phys. **87**, 6863 (2000).

84. M.F. Doerner, T. Yogi, D.S. Parker, "Compositional effects in high density CoPtCr media", IEEE Trans. Magn. **29**, 3667 (1993).

85. SQUID instrument, *The Quantum Design Magnetic Property Measurement System (MPMS)*, San Diego, Ca (1996).

86. T.Thomson, "In-plane VSM measurement of AX1821, AX341 and AX1646", Seagate, Fermont, Ca (1999).

87. T.Pan and G.W.D. Spratt, "Temperature dependence of coercivity in Co-based longitudinal thin-film recording media", J. Appl. Phys. **81**, 3952 (1997).

88. M. Doerner, X. Bian, M. Madison, et al, "Demonstration of 35 GB/in^2 using media on glass substrates", IEEE Trans. Magn. **37**, 103 (2001).

89. C. Dewhurst, "Graphical Reduction and Analysis SANS Program for Matlab, GRAS$_{ANS}$P Software Version 3.4", (2003).

90. W.H. Press, *Numerical Recipes in Fortran*, 2nd Edition (1987).

91. A.Munter, NIST Centre for Neutron Research, "Scattering Length Density Calculator", www.ncnr.nist.gov, (2006).

92. W.B. Zeper, H.W.V. Kesteren, B.A. J. Jacobs, J.H.M. Spruit, and P.F Carcia, J.Appl Phys. **70**, 2264 (1991).

93. A.G. Roy and D.E. Laughlin, "Seed-Layer effect on the microstructure and magnetic properties of Co/Pd multilayers", J. Appl. Phys. **89**, 7531 (2001).

94. M. Albrecht, S. Anders, T. Thomson, C. T. Rettner, M. E. Best, A. Moser, and B.D. Terris, "Thermal stability and recording properties of sub-100 nm patterned CoCrPt perpendicular media", J. Appl. Phys. **91**, 6845 (2002).

95. Ryoichi Mukai, Takuya Uzumaki, and Atsushi Tanaka, "Signal-to-media-noise ratio improvement of CoCrPt-SiO2 granular perpendicular media by stacked Ru underlayer",J. Appl. Phys. **97**, 10N119 (2005).

96. T. Kubo, Y. Kuboki, M. Ohsawa and R. Tanuma, "Crystallographic analysis of CoPtCr-SiO2 perpendicular recording media, with high anisotropy using synchrotron radiation x-ray diffraction",J.Appl. Phys. **97**, 10R510 (2005).

97. Y. Ikeda, Sonobe, G. Zeltzer, B. K. Yen, K. Takano, H. Do and P. Rice, "Microstructure study of CoCrPt/Ti/NiAl perpendicular media", J. Magn. Magn. Mater. 139 **235**, 104-109 (2001).

98. Chun-Tao Xiao, Yuki Inaba and Takehito Shimatsu, "Microstructure, magnetic properties and their seed layer thickness dependencies of granular CoPtCr–SiO_2 perpendicular recording media", Solid State Comm, **144**, 58-80 (2007).

99. T. Thomson, Perpendicular Magnetic Recording Media (PMRM) samples, Hitachi San Jose Research Center, San Jose, CA, USA Fermont, Ca (2003).

100. MOKE Instrument, Hitachi San Jose Research Center, San Jose, CA, USA (2006).

101. VSM Instrument, *The Quantum Design Magnetic Property Measurement System (MPMS)*, San Diego, Ca (1996).

102. T.Thomson, "Out of plane MOKE measurement of H114", Hitachi San Jose Research Center, San Jose, CA, USA Fermont, Ca (2006).

103. T.Thomson, "In-plane VSM measurement of H114", Hitachi San Jose Research Center, San Jose, CA, USA Fermont, Ca (2006).

104. F.Ossart and G.Meunier, "Comparison between various hysteresis models and experimental data", IEEE Trans. Magn. **26**, 2837 (1990).

105. D.H. Reich, M.T. Tanase, "Biological applications of multifunctional magnetic nanowires", J.Appl. Phys. **93**, 7275 (2003).

106. L.Hueso and N.Mathur, "Nanotechnology: Dreams of a hollow future", Nature **427**, 301-304, Jan (2004).

107. B.D. Terris and T.Thomson, "Nanofabricated and self-assembled magnetic structures as data storage media", J.Phys. D: Appl Phys. **38** (2005) R199-R222.

108. H.Zeng and M. Zheng, "Magnetic properties of self-assembled Co nanowires of varying length and diameter", J.Appl.Phys.**87**, 4718 (2000).

109. Y. Peng,T-H. Shen and B. Ashworth, "Magnetic nanowire arrays: A study of magneto-optical properties", J.Appl. Phys. **93**, 7050 (2003).

110. V. Caffarenaa and J. L. Capitaneob, "Preparation of electrodeposited cobalt nanowires", Materials Research **9**, No. 2, 205-208 (2006).

111. Y. Peng, R. J. Zhou, H. L. Li, and Z. J. Chen, Chin. Sci. Bull. **46**, 20 (2001).

112. R.N.Bracewell, *The Fourier Transform and its Applications*, 2nd edition (1986).

113. Y. Peng and T-H. Shen Private Communication ILL May (2004).

114. T.Gilbert, Armour Research Foundation, Report No. 11, (1955).

115. M. J. Donahue and D. G. Porter OOMMF User's Guide, Version 1.0 Interagency Report NISTIR 6376 National Institute of Standards and Technology, Gaithersburg, MD (Sept 1999).

116. R. Brun, F. Rademakers, P. Canal and I. Antcheva, *ROOT*, An Object-Oriented Data analysis Framework. Version 4.04 (2005).

117. P.E. Tannenwald and R. Weber, "Exchange Integral in Cobalt from Spin-Wave Resonance", Phys. Rev. **121**, 715 (1961).

118. Y. Kubuto and L. Folks, "Intergration magnetic coupling and microstructure in CoPtCr, CoPtCrTa and CoPtCrB alloy", J.Appl. Phys.**84**, 6202 (1998).

119. F.Y. Ogrin, Private Communication, University of Exeter March (2006).